Phototrophic iron oxidation and implications for biogeochemical cycling in the Archean Eon

by

Katharine Jean Thompson

BA Microbiology, Cornell University, 2011

A DISSERTATION SUBMITTED IN PARTIAL FULFILLMENT OF
THE REQUIREMENTS FOR THE DEGREE OF

DOCTOR OF PHILOSOPHY

in

The Faculty of Graduate and Postdoctoral Studies

(Microbiology and Immunology)

THE UNIVERSITY OF BRITISH COLUMBIA

(Vancouver)

June 2020

The following individuals certify that they have read, and recommend to the Faculty of Graduate and Postdoctoral Studies for acceptance, the dissertation entitled:
Phototrophic iron oxidation and biogeochemical cycling in the Archean Eon
Submitted by Katharine J. Thompson in partial fulfilment of the requirements for the degree of Doctor of Philosophy in Microbiology and Immunology

Examining Committee:

Associate Professor Sean A. Crowe, Microbiology and Immunology & Earth, Ocean and Atmospheric Sciences

---

Supervisor

Professor Tom Beatty, Microbiology and Immunology

Supervisory Committee Member

Professor Susan Baldwin, Chemical and Biological Engineering

University Examiner

Professor Curtis Suttle, Microbiology and Immunology & Earth, Ocean and Atmospheric Sciences

---

University Examiner

Additional Supervisory Committee Members:

Professor Steven J. Hallam, Microbiology and Immunology

Supervisory Committee Member

Professor Stephen Calvert, Earth, Ocean and Atmospheric Sciences

---

Supervisory Committee Member

Abstract

Banded iron formations (BIFs), which host the world's largest iron ore deposits, formed predominantly through the deposition of ferric iron (Fe[III]) from ferruginous oceans during the Archean Eon. Available evidence suggests that phototrophic iron oxidation (photoferrotrophy) may have played a key role in coupling the carbon and iron cycles during the Archean Eon, depositing BIFs, and, in doing so, underpinned global primary production at this time. To date, however, all known photoferrotrophs form a close association with the ferric iron metabolites they produce during growth. This intimate association calls into question the involvement of photoferrotrophs in BIF deposition, their ability to act as primary producers, and their role in sustaining the biosphere for millions of years. Furthermore, a lack of quantitative knowledge on the growth of photoferrotrophs and the interactions between them and other microorganisms limit our ability to constrain models of BIF deposition and the Archean ocean-atmosphere system as a whole. This dissertation generates new knowledge on extant photoferrotrophy that can be used to inform and constrain models of primary production and BIF deposition during the Archean Eon. I create new knowledge on photoferrotrophy under laboratory conditions and in natural environments through data collected on the physiology and metabolic capacity of pelagic photoferrotroph *Chlorobium phaeoferrooxidans* strain KB01. I also measure process rates and analyze the composition of the microbial community in a ferruginous lake——Kabuno Bay——that is dominated by photoferrotrophy. I subsequently integrate this new knowledge into models that examine the antiquity of nutrient acquisition in the photoferrotrophic Chlorobia and the role of photoferrotrophs as primary producers during the Archean. These models provide an explanation for the formation of BIFs as a by-product of the activity of photoferrotrophic bacteria. Additionally, I demonstrate how photoferrotrophs could have sustained the biosphere, likely fueled microbial methanogenesis, and, therefore, helped to stabilize Earth's climate under a dim early Sun.

Lay Summary

Primitive photosynthesis may have played a fundamental role in the formation of the world's largest iron ore deposits during the first 3 billion years of Earth's history. These iron ore deposits, however, lack evidence for photosynthetic cellular remains that should have been co-deposited with iron. This raises questions about the growth of primitive photosynthetic bacteria in Earth's early oceans. In my thesis, I determine the physical and chemical characteristics of primitive photosynthesis under laboratory conditions and in modern, natural environments. I then apply this knowledge to demonstrate how these photosynthetic bacteria could have thrived in Archean oceans, driving large-scale biogeochemical cycles. My thesis demonstrates that these primitive photosynthetic bacteria could deposit iron ore free of cellular remains and support the growth of other bacteria. Ultimately, this process supports the production of methane, which would have contributed to a greenhouse atmosphere and climate stability under the dim early Sun.

Preface

This work was made possible through the contributions and dedication of many collaborators. Dr. Sean Crowe, as the research advisor was involved in all aspects of this work including experimental design, data analysis and interpretation and writing. Sections of this work are partly of wholly published, in press, or in review. Copyright licenses were obtained and are listed below.

- Chapter 1: Katharine J. Thompson wrote the main text with editorial support from Sean A. Crowe.

- Chapter 2: Katharine J. Thompson wrote the main text with editorial support from Sean A. Crowe. Katharine J. Thompson performed all the laboratory work.

- Chapter 3: Katharine J. Thompson and Sean A. Crowe wrote the main text with input from Rachel L. Simister. Katharine J. Thompson performed all the laboratory work, except the biochemical verification of assimilatory sulfate reduction, which was performed by Sean A. Crowe. Katharine J. Thompson, Rachel L. Simister, and Sean A. Crowe interpreted and analyzed the data with bioinformatic data analysis conducted by Aria S. Hahn. Steven J. Hallam contributed to data interpretation and insights. Editorial support was received from the entire list of authors. The reference for the published paper can be found as follows:

  K. J. Thompson, Rachel L. Simister et al. Nutrient Acquisition and the Metabolic Potential of Photoferrotrophic Chlorobi. Frontiers in microbiology, 8:1212, July 2017.

- Chapter 4: Katharine J. Thompson and Sean A. Crowe wrote the manuscript with detailed input from Paul A. Kenward, Kurt O. Konhauser, Christopher T. Reinhard, and Andreas Kappler. Sean A. Crowe conceived, designed, and directed the study. Sean A. Crowe and Marc Lliós made observations in Kabuno Bay. Katharine J. Thompson performed photoferrotroph cell settling experiments. Tyler Warchola performed cyanobacteria settling experiments. Katharine J. Thompson and Paul A. Kenward conducted electron microscopy imaging of strain KB01. Tina Gauger and Andreas Kappler conducted electron microscopy imaging of strain KoFox. Katharine J. Thompson, Paul A. Kenward, Rachel L. Simister, and Raul Martinez characterized cell surface chemistries. Katharine J. Thompson conducted DVLO modeling. Katharine J. Thompson, Sean A. Crowe, Kohen W. Bauer, and Céline C. Michiels constructed the biogeochemical models. Editorial support was received from the entire list of authors. The reference for the published paper can be found as follows:

K.J. Thompson, P.A. Kenward et. al. Photoferrotrophy, deposition of banded iron formations, and methane production in Archean oceans. Science Advances, 5:eaav2869, November 2019

- Chapter 5: Katharine J. Thompson wrote the main text with editorial support from Sean A. Crowe. Sean A. Crowe and Marc Lliós conducted process rate measurement experiments and made observations in Kabuno Bay. Katharine J. Thompson and Rachel L. Simister developed the bioinformatic pipeline used for metagenome analyses. Katharine J. Thompson performed all the metagenome analyses. Editorial support was received from the entire list of authors.
- Chapter 6: Katharine J. Thompson wrote the main text.

Throughout this dissertation the word 'we' refers to Katharine J. Thompson unless otherwise stated.

None of the work encompassing this dissertation required consultation with the UBC Research Ethics Board.

Table of Contents

Appendices

List of Tables

List of Figures

Acknowledgements

This process has been an incredible experience that began back in Grade 7 when Mr. D asked us to make an oven that could bake real cookies out of cardboard and aluminium foil——in other words the day I discovered that creativity and science went hand in hand with a stomach full of raw cookie dough. There have been numerous people along the way who have encouraged and supported me and honestly there are too many to list! So, instead, here are a few thank yous to those who have made this thesis possible. First, I would like to thank Sean Crowe for giving me a position in his lab. From the first moment we spoke in your office about iron oxidation and the Archean oceans to our current discussion on which model we should construct next, your vast knowledge, experience, and enthusiasm have pushed me to be a better scientist. Thank you for continuing to believe in me and for helping me achieve this dream. Thank you to my "external" committee members Kurt Konhauser, Chris Reinhard, and Andreas Kappler for your ongoing support and willingness to help me pursue my career! I would also like to thank the members of my committee Steven Hallam, Steve Calvert, Tom Beatty, and John Smit for your words of wisdom and support, as well as your diligent edits to my thesis chapters. Thank you to my External Examiner, Professor Alexis Templeton from the University of Colorado Boulder, who reviewed my thesis thoughtfully. A massive thank you to all of the members of the Crowe Lab over the years — Céline Michiels, Ashley Davidson, Jenifer Spence, Julia Huggins, Kohen Bauer, Rachel Simister, Amani Alsufyani, Kanchi Dave, Niko Finke, Arne Sturm, and the many undergraduates –– for your knowledge, willingness to listen, and endless discussions with me on any kind of topic (usually done with a beer in hand). Finally, thank you to all my science and sports friends who gave the outlets I needed to persevere when times were tough –– all those tea breaks and soccer games were just what I needed to get this done!

Dedication

To my parents and sisters for your love, support, and encouragement.

To Tony for your love and unerring patience in the face of “just a few more months”.

Chapter 1

Introduction

Life has interacted with the Earth's surface, effectively altering its chemistry since it first evolved over four billion years ago [1–3]. Across the two billion years that followed life's origin, during the Archean Eon, communities of microorganisms propagated through the use of a variety of inorganic and organic electron donors and acceptors thereby modifying Earth's surface composition, shifting redox balances, and driving biogeochemical cycles [3]. Some of these global-scale processes have been recorded and preserved in the sedimentary rock record, which can be accessed today through geological and geochemical studies. A rich source of information comes from chemical sediments such as carbonates, and for the Archean Eon in particular, banded iron formations (BIFs), which were deposited predominantly between 2.9 and 1.9 billion years ago (Ga) [4]. The quantity of iron present in BIFs, among other indicators, requires that BIFs were deposited from anoxic ferruginous Precambrian oceans, which contained high concentrations of dissolved ferrous iron (Fe[II]) [5]. BIFs likely formed from such ferruginous oceans in response to the oxidation of this Fe(II) and the resulting precipitation and sedimentation of ferric iron (oxyhydr)oxides (Fe[III]) [4, 6, 7]. Many of the models of BIF deposition invoke photosynthesis in the oxidation of ferrous iron from seawater to induce its subsequent precipitation and deposition as mixed valence iron (oxyhydr)oxides and carbonate phases [6–9]. BIFs thus likely record the activity of Earth's early photosynthetic biosphere [6–9].

Two modes of photosynthesis have been implicated in Fe(II) oxidation in the Precambrian oceans (includes the Archean and Proterozoic Eons)——canonical oxygenic photosynthesis by the ancestors of modern cyanobacteria [6] and iron-dependent anoxygenic photosynthesis [7, 8], referred to as photoferrotrophy. While oxygenic phototrophs likely emerged in the Archean [10–12], evidence from studies of geochemical proxies has shown that the partial pressure of oxygen remained very low in the Archean atmosphere (less than 0.001 % of the current value) during BIF

deposition [2, 13–15]. Thus, oxygenic phototrophs at this time were likely restricted to rather small and potentially ephemeral niches, which limited their contribution to global primary production and the flux of O_2 to the atmosphere [11, 16, 17]. Such a low O_2 atmosphere-ocean system likely supported limited rates of Fe(II) oxidation, implying that O_2-driven Fe(II) oxidation was likely a minor contributor to BIF deposition at this time [2, 18, 19]. Conversely, photoferrotrophic bacteria grow using light and Fe(II) to fix CO_2 into biomass and produce Fe(III) as a metabolic by-product [8, 9, 20] and they can do so in the complete absence of oxygen [Eq. 1.1] [20]. Thus, photoferrotrophs, as strict anaerobes, could have thrived in the anoxic Archean oceans, utilizing Fe(II) as their electron donor. As these photoferrotrophs proliferated in nutrient-rich, illuminated surface waters, they could have supported high rates of Fe(II) oxidation and, therefore, generated sufficient Fe(III) (oxyhydr)oxides to deposit BIFs [8, 21].

$$4\,Fe^{2+} + CO_2 + 11\,H_2O + h\nu \Rightarrow [CH_2O] + 4\,Fe(OH)_3 + 8\,H^+ \tag{1.1}$$

This chapter introduces the iron biogeochemical cycle as it pertains to the early Earth, the physiology of photoferrotrophs and the molecular underpinning of this physiology, as well as links between the coupled carbon and iron biogeochemical cycles in modern and ancient environments. It also highlights gaps in our knowledge of photoferrotrophs and their physiology and the resulting uncertainties associated with their role in BIF deposition and biogeochemical cycling in the Archean Eon. Overall, my thesis will create new knowledge on the physiology and metabolic capacity of photoferrotrophy under laboratory conditions as well as on the role of photoferrotrophy in modern ferruginous environments. I have further incorporated this new and quantitative knowledge into numerical models and phylogenetic analyses to test the possible role of photoferrotrophy in BIF deposition and the maintenance of a clement climate, through photoferrotrophs as primary producers, throughout the Archean Eon.

1.1 The marine iron cycle past and present

Archean oceans contained high concentrations of Fe(II) sourced largely from hydrothermal circulation through subsurface ocean crust. Thus, iron in the Archean oceans occurred in ferrous

(Fe[II]) and ferric (Fe[III]) states (Fig. 1.1) [5, 22, 23], wherein solid Fe(III) nanoparticles precipitated from dissolved Fe(II), aggregated, and crystallized to form a suite of Fe minerals (Fig. 1.1) [5, 22, 23]. These Fe minerals are deemed highly reactive as they can be readily reduced both chemically and microbially (Fig. 1.1) [5, 22, 23]. The ratio of collective highly reactive iron minerals (e.g. ferrihydrite and hematite; Fig. 1.1) to the total iron minerals in a given sediment or sedimentary rock can discriminate between whether or not the depositional environment was oxic or anoxic (where a ratio of > 0.38 is indicative of anoxic conditions) [5, 24, 25]. Furthermore, the ratio of highly reactive iron minerals to the quantity of pyritized minerals present in the same sediment or rock can discriminate between whether or not the anoxic depositional environment was ferruginous or sulfide-rich——euxinic (where a ratio of > 0.7 is indicative of euxinic conditions) [24, 25]. Thus, the mineralogy of a given sediment or rock is one of the properties that can be used to diagnose whether the depositional environment for a particular sequence of rock was ferruginous [24]. The ratio of these minerals in samples collected from both marine deposits that are more (e.g. BIFs) or less (e.g. shales) iron-rich, whose ages align with the Archean Eon, reveal that the Archean oceans were almost universally ferruginous [5, 23, 24]. Indeed, models based on the mineralogy of Archean rocks suggest that Fe(II) concentrations could have accumulated to appreciable levels in the oceans (up to approximately 100 μM) [5, 22–24, 26]. The majority of this Fe(II) was likely supplied by hydrothermal vents—through both vents that are concentrated at major mid-ocean ridges (on-axis) and those that extend from the mid-ocean ridges, covering large areas of the ocean floor (off-axis) [5, 23, 24]. The 0.3 Tmol yr^{-1} flux of Fe(II) reconstructed for Archean hydrothermal vent systems [5], however, does not consider off-axis contributions, nor the major differences between the Archean and modern oceans, such as the concentration of sulfate [27]. Thus, this current reconstruction of the fluxes of Fe(II) to the Archean oceans likely underestimates the real magnitude of Fe that accumulated due to the lack of oxidative potential through elements such as oxygen and sulfide.

Extensive and intensive studies of the trace element geochemistry of marine sedimentary rocks [2, 5, 13–15, 28] suggest that oxygen concentrations were as low as 0.001 % present atmospheric level (PAL) during the Archean Eon (Fig. 1.2). Several elements, whose speciation or isotopic composition depends on an oxygen-dependent reaction in their biogeochemical cycles, can be used

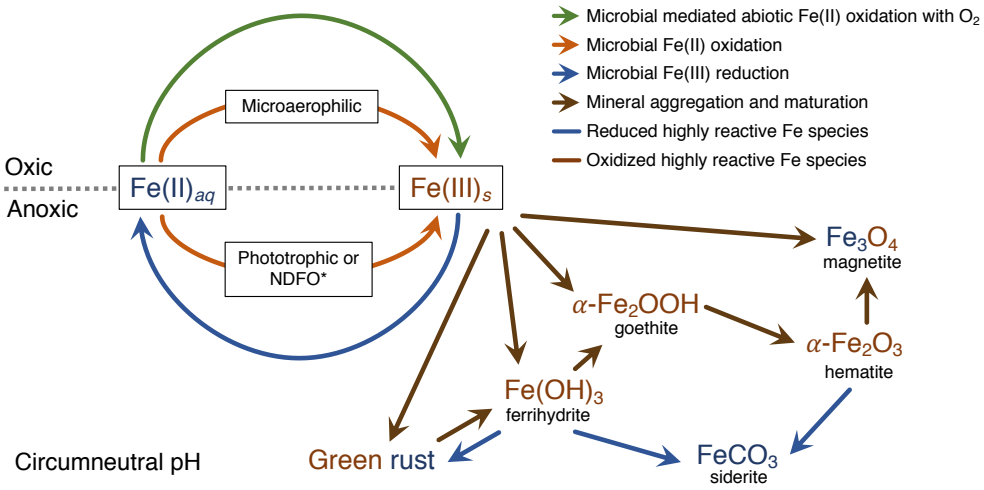

Figure 1.1: *Overview of the iron cycle.* Key abiotic and biotic reactions in the Earth surface iron biogeochemical cycle, including the transition from amorphous Fe(III) minerals to more crystalline Fe(III) and mixed valence iron minerals. *NDFO = Nitrate-dependent Fe(II) oxidation.

as geochemical proxies for the concentration of oxygen in the Archean oceans and atmosphere [28]. For example, the oxidation of land-surface crustal sulfide minerals by oxygen leads to the export of soluble sulfate to the oceans and the subsequent mass-dependent fractionation of the sulfur through microbial sulfate reduction [2, 13–15, 29]. In the absence of oxygen in Earth's atmosphere during the Precambrian, sulfate concentrations in the oceans were very low [27], limiting mass-dependent sulfur isotope fractionation [2, 13–15, 27, 29]. Furthermore, without the increased atmospheric oxygen concentrations needed to form ozone, reactions that result in a mass-independent fractionation of sulfur isotopes (S-MIF)–namely photochemical reactions–would have made up the majority of the sulfur isotopic signal [2, 13–15, 27, 29]. Therefore, the disappearance of S-MIF signals between 2.4 and 2.3 Ga is one of the best known indicators that oxygen concentrations rose in the atmosphere during that time interval [2, 13–15, 30]. While the loss of the S-MIF suggests that atmospheric oxygen concentrations were as low as 0.001 % PAL during the Archean Eon, other elements with oxygen sensitive steps in their biogeochemical cycles signal that temporary oxygen fluxes (so called 'whiffs' of oxygen) could have permeated the otherwise anoxic Archean oceans and atmosphere [16, 31, 32]. For example, the isotopic fractionation patterns of chromium have been linked to the presence of oxygen due to its reaction

with manganese oxides——compounds that are, according to current research, solely produced in the presence of oxygen [16, 33, 34]. The concentration of oxygen in the atmosphere and oceans of the Archean Eon is hotly debated amongst the scientific community [28, 35, 36], and while 'whiffs' of oxygen are certainly plausible, the majority of the Archean oceans likely remained anoxic and ferruginous [5]. Thus, low oxygen meant that Fe(II) was available as an abundant electron donor for both microbial and chemical reactions (Fig. 1.2).

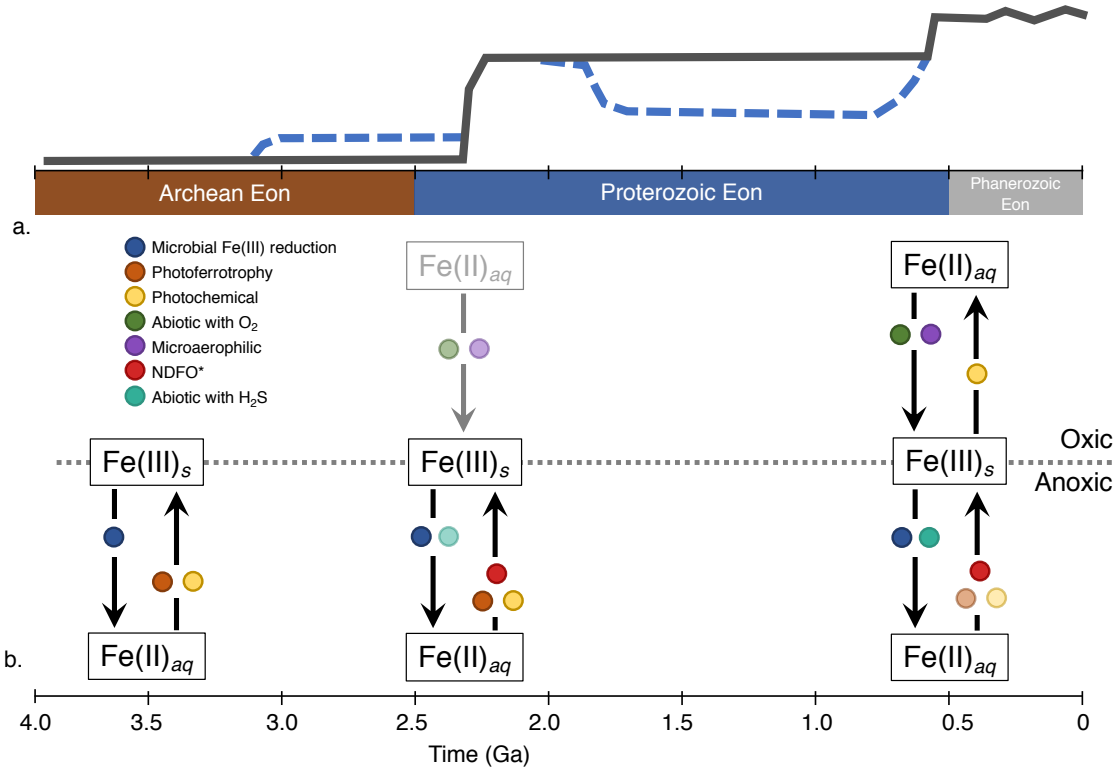

Figure 1.2: *Overview of the iron cycle through time.* Oxygen concentration (a) in the atmosphere relative to the modern oxygen concentration through time when the line represents the canonical oxygen curve and the dashed line represents alternative views, adapted from Lyons et. al., 2014 [28]. Major abiotic and biotic reactions (b) are depicted through the color of the dots and their likely abundance represented by the strength of the color. *NDFO = Nitrate-dependent Fe(II) oxidation.

There are a constrained number of abiotic and biotic reactions that are responsible for cycling and recycling of iron in aqueous environments in the Archean Eon. The lack of atmospheric oxygen in the Archean Eon would have restricted crustal surface sulfide oxidation on the continents and thus the accumulation of soluble sulfate in the oceans [27]. Given that microbial sulfate reduction in the oceans produces sulfide, which is highly reactive with Fe(II) [18, 23], the low concentrations

of sulfate would have further enhanced the accumulation of Fe(II) [5, 15, 37]. Thus, in the absence of oxygen, sulfate or sulfide, there are very few abiotic reactions to transform iron between its two main stable states. One of the few, but likely the most dominant, of these abiotic reactions is the photochemical oxidation of Fe(II) by UV radiation (Fig. 1.1) [38–40]. During the Arhcean Eon, the UV radiation flux would have been unimpeded in the absence of an ozone layer, potentially leading to the anoxic oxidation of Fe(II), present in surface waters, to Fe(III) (oxyhydr)oxides (Fig. 1.2) [38]. While there were minimal chemical reactions to oxidize Fe(II), microbial reactions, such as anoxygenic photosynthetic Fe(II) oxidation, could have played a key role in the Archean oceans (Fig. 1.1, 1.2) [1, 7, 8, 21]. In the absence of dissolved sulfides, the iron cycle could only have been completed through microbial Fe(III) reduction (Fig. 1.1, 1.2). Microbial Fe(III) reduction is an anaerobic process (Fig. 1.1) and, therefore, could have been found throughout the Archean ocean water column and sediments (Fig. 1.2) [41, 42]. Other microbial Fe redox reactions that could have evolved as early as the late Archean Eon, once oxygen concentrations began to rise, including microaerophilic Fe(II) oxidation [43], which couples Fe(II) oxidation to oxygen reduction under low oxygen conditions, and nitrate-dependent Fe(II) oxidation (NDFO) [44], which couples Fe(II) oxidation to nitrate reduction under anaerobic conditions (Fig. 1.1). As both of these microbial reactions require oxygen, with a direct role in microaerophilic Fe(II) oxidation (< 15 μM O_2) and an indirect role in NDFO (wherein oxygen is required for the microbial oxidation of ammonium to nitrate), the magnitude of the role these metabolisms played in the Fe cycle throughout the Archean would have depended on the oxygen flux and could have shifted from minor (Paleoarchean) to appreciable (Neoarchean) (Fig. 1.2). Given the limited number of mechanisms for iron transformation under the Archean conditions, the interplay between the rate of microbial phototrophic Fe(II) oxidation and Fe(III) reduction likely controlled the export of solid Fe(III) (oxyhydr)oxides from the water column.

Unlike the Archean, where Fe was ubiquitous in the oceans and on the continents, the concentration of Fe in the modern environment is limited by the concentration of oxygen [5]. Modern atmospheric oxygen concentrations (21 %) ensures that the oceans are largely oxic with small pockets of anoxia. In the presence of this oxygen, Fe(II) weathered from the continents or supplied through hydrothermal vents on the sea floor in the oceans oxidizes to form Fe(III) mineral

particles that are delivered to the seafloor, buried, and ultimately returned to the mantle through subduction [24]. Thus, dissolved Fe(II) does not accumulate and instead the concentration of Fe in modern seawater is controlled by the solubility of Fe(III) phases [24]. Due to the low solubility of Fe(III) phases, therefore, the total Fe pool in seawater is small and Fe has a short residence time in the modern oceans [5]. Furthermore, the oxygenated atmosphere fosters the production of sulfate on the continents, which accumulates in the global oceans with a modern concentration of 28 mM. These high concentrations of sulfate mean that, in the pockets of ocean anoxia, microbial sulfate reduction to sulfide dominates, resulting in euxinic conditions rather than ferruginous conditions in these anoxic zones [45, 46]. Fe(II) can accumulate in sulfide-free anoxic ocean sediments or in bottom waters of modern stratified lakes where Fe(II) is supplied by hydrothermal vents or Fe-enriched ground waters respectively [47, 48]. The modern biogeochemical iron cycle is, therefore, largely controlled by the availability of oxygen and sulfate, restricting the anaerobic microbial iron reactions to a subset of environments.

Abiotic Fe(II) oxidation, with biologically produced oxygen, dominates the modern marine Fe cycle, while the direct microbial Fe redox reactions that prevailed throughout the Archean Eon are restricted to anoxic marine benthic environments, stratified marine basins (e.g. Chesepeake Bay) and iron-rich stratified lakes. Fe photochemical reactions do occur in the modern surface oceans – either through the photoreduction of Fe(III) bound to organic ligands (Fig. 1.2) [49] or through the photooxidation of Fe(II) (Fig. 1.2) [39]. Given the high concentrations of O_2 in the modern oceans compared to the Archean Eon, however, photochemical Fe(II) oxidation likely plays a minor role in the cumulative Fe(II) oxidation (Fig. 1.2). Conversely, the high concentrations of biologically produced oxygen in the modern oceans guarantees that microbially-mediated abiotic Fe(II) oxidation by oxygen supports most of the marine Fe oxidation (Fig. 1.2), while the high concentrations of sulfide produced through sulfate reduction in anoxic zones and marine sediments contributes to Fe(III) (oxyhydr)oxide reduction (Fig. 1.2). Along with the abiotic reduction of Fe(III) by sulfide, microbial Fe(III) reduction plays a key role in recycling Fe in modern marine sediments, as it is ubiquitous in these anoxic environments [50]. Direct microbial Fe(II) oxidation, whether by anoxygenic photosynthetic, microaerophilic, or nitrate-dependent bacteria, however, is restricted to three different niche environments that are dependent on the

availability of light, oxygen, and nitrate respectively (Fig. 1.1) [20, 43, 44]. These microbial reactions can, therefore, be found in some marine settings, such as in the vicinity to hydrothermal vent systems or in the sediments of coastal marine mud flats, or in Fe-rich freshwater environments, such as pond sediments and stratified lakes. Therefore, the controls on Fe(II) oxidation have shifted through time from predominantly anoxygenic photosynthetic to abiotic, oxygen-dependent Fe(II) oxidation that is mediated by abundant oxygenic photosynthetic organisms (Fig. 1.2). Thus, while the possible Fe reactions have not changed over time, the direct microbial Fe redox reactions have become more restricted as oxygen concentrations have risen in the atmosphere and oceans.

1.2 Extant photoferrotrophy

Despite the small number of known modern environments that have the geochemical conditions and light required for photoferrotrophy, 20 photoferrotrophs, from two different bacterial phyla, have been enriched and isolated into laboratory cultures [20, 48, 51–57]. The first photoferrotrophs, *Rhodopseudomonas* sp. and *Thiodictyon* sp. (Table 1.1), were enriched and isolated from a freshwater pond and marine sediments in Germany in the early 1990's [20]. These were the first bacteria that demonstrated that photosynthetic growth with Fe(II) as the electron donor was biologically and biochemically possible [20]. These organisms were found to grow through both photoautotrophy with ferrous iron as the electron donor as well as photoheterotrophically with succinate or other carbon sources [20]. Following this seminal discovery, many isolates were brought into laboratory culture from a suite of different environments, both marine and freshwater. All but one, however, originated from a benthic source (subset of isolated photoferrotrophs shown in Table 1.1). The singular pelagic strain, Chlorobium phaeoferrooxidans strain KB01, was isolated from one of the few persistently ferruginous lakes that exist today–Kabuno Bay, a sub–basin of Lake Kivu in East Africa [48, 58]. Collectively, extant photoferrotrophs come from three different classes of bacteria (Alphaproteobacteria, Gammaproteobacteria, and Chlorobia), are closely related to other anoxygenic phototrophic members of those classes, and demonstrate polyphyly of the photoferrotrophic trait [35]. Studies with laboratory cultures of photoferrotrophs have produced a wealth of information on their physiology and growth, which ultimately provides a framework

Table 1.1: A summary of some of the isolated photoferrotrophic strains. For a complete list see Bryce et. al. 2018 [57]. References: 1) [20]; 2) [51]; 3) [52]; 4) [54]; 5) [53]; 6) [59]; 7) [55, 60]; 8) [48, 58]; 9) [56]

Class	Strain	Environment (all anoxic)	Location	Reference
Alphaproteobacteria (Purple non-sulfur)	*Rhodopseudomonas palustris*	Marine sediment	Germany	1
	Rhodobacter ferrooxidans strain SW2	Freshwater ponds	Germany	2
	Rhodomicrobium vannielii strain BS-1	Freshwater ditch	Germany	3
	Rhodovulum iodosum	Marine mud flat	Germany	4
	Rhodovulum robiginosum	Marine mud flat	Germany	4
	Rhodopseudomonas palustris strain TIE-1	Fe-rich mat	USA	6
Gammaproteobacteria (Purple sulfur)	*Thiodictyon* sp.	Marine sediment	Germany	1
	Thiodictyon sp. strain F4	Freshwater marsh	USA	7
Chlorobi (Green sulfur)	*Chlorobium ferrooxidans* strain KoFox	Freshwater sediment	Germany	5
	Chlorobium phaeoferrooxidans strain KB01	Kabuno Bay	Democratic Republic of Congo	8
	Chlorobium sp. strain N1	Marine sediment	Denmark	9

for the evaluation of the role of photoferrotrophy in the Fe cycle past and present.

Studies with extant photoferrotrophs have provided a wealth of knowledge on their growth, their response to different environmental conditions, and their characteristic traits. A few studies, to date, have characterized the basic growth patterns of some of the photoferrotrophic isolates. These studies have conducted light microscopy as well as scanning and transmission electron microscopy to determine the internal and external structures of the different photoferrotrophs and the relationship between cell surfaces and the Fe(III) (oxyhydr)oxides they produce as a by-product of their growth (Fig. 1.3). Collectively, these imaging techniques reveal that characterized, benthic, photoferrotrophs form a close association with the Fe(III) particles (Fig. 1.3) [9, 53, 55–57, 61–63]. Indeed, the morphologies of the first isolates were obscured due to encrustation of cells by the Fe(III) metabolites they produced during growth and could only be identified when the isolates were grown with an alternative electron donor [20]. To date, the ability to grow using an alternative electron donor such as an organic carbon compound (e.g. succinate or lactate), H_2, or H_2S has since been demonstrated in all of the characterized photoferrotrophs. Further studies with these same isolates also revealed several differences between the organisms, such as their growth rate in response to changes in the environmental conditions. For example, the photoferrotrophs isolated

from marine environments grow at a higher optimum pH of approximately 7.0-7.3, while those from freshwater environments thrive at a slightly lower pH of approximately 6.5-6.8 [55–57]. Other differences include the growth rates exhibited by different strains at low light intensities with the half-light saturation constants of individual photoferrotrophs falling within a wide range of values (0.25 μmol m^{-2} s^{-1} for *Chlorobium ferrooxidans* strain KoFox to 8 μmol m^{-2} s^{-1} for *Thiodictyon* sp.; [55]). Thus, while photoferrotrophs share the ability to utilize alternative electron donors and known benthic isolates form a close association with Fe(III) particles, there are other notable differences between the individual isolates that likely represent the natural environments in which they originated.

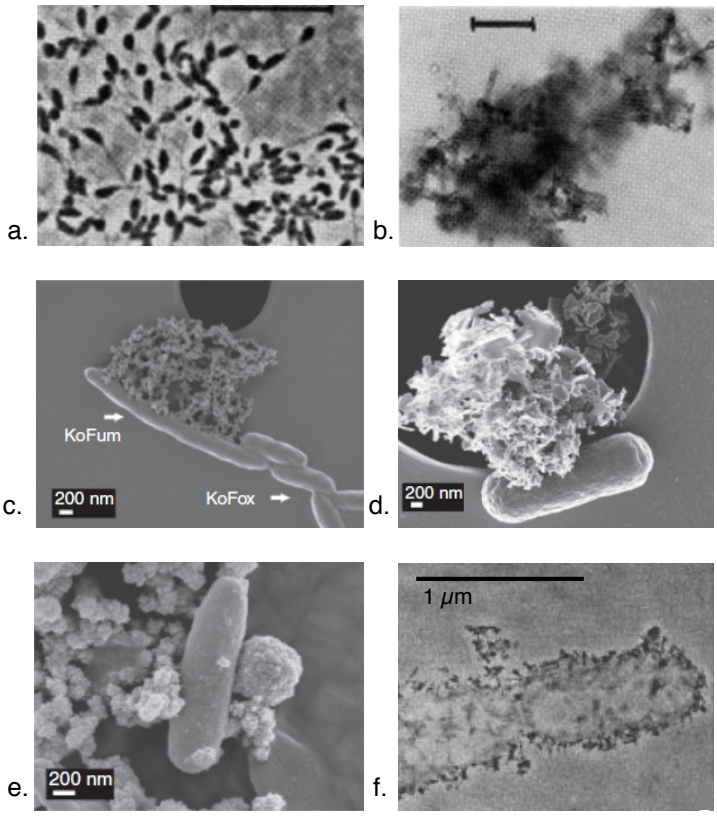

Figure 1.3: *Microscopy, SEM, and TEM images of photoferrotrophic strains.* A microscopy (a) image of the first photoferrotrophic isolate grown with succinate [20], a microscopy image (b) of the first photoferrotrophic isolate grown with Fe(II) [20], an SEM image (c) of *Chlorobium ferrooxidans* strain KoFox grown with Fe(II) [55], an SEM image (d) of *Thiodycton* strain F4 grown with Fe(II) [55], an SEM image (e) of *Rhodobacter ferrooxidans* strain SW2 grown with Fe(II) [55], and a TEM image (f) of *Rhodobacter ferrooxidans* strain SW2 grown with Fe(II) [9].

Ferruginous environments are rare on the modern Earth, yet they provide natural laboratories in which to examine microbial communities under conditions that are similar to those that likely existed in the oceans during the Archean Eon. Given the scarcity of modern, illuminated, Fe(II)-rich pelagic environments, the majority of extant photoferrotrophs that have been studied in laboratory cultures are derived from benthic environments where anoxic conditions persist and Fe(II) is supplied at a rate that supports photosynthetic growth through photoferrotrophy. These environments have included iron-rich fresh-water pond sediments and marine mud flats [20, 51–54, 56]. While these benthic settings yielded the majority of the photoferrotrophs discussed above, their sediment-based and, sometimes (for marine environments), sulfate-rich settings make them poor analogs to the Archean oceans. In the last few years, persistent ferruginous conditions have been discovered in a number of modern lakes, in addition to Kabuno Bay (border of Democratic Republic of Congo and Rwanda): Lakes Matano and Towuti (Indonesia), Lake La Cruz (Spain), Lake Pavin (France), Experimental Lakes Area (ELA; Canada). All of these lakes are stratified and rich in iron due to volcanic activity, weathering of ultramafic (iron-rich) rocks, or groundwater seepage. Detailed studies of the microbial communities and their relationship to the chemical features present in each lake present the opportunity to expand the current knowledge of the role of photoferrotrophs in a ferruginous water column and thus these lakes can inform on biogeochemical cycling under ferruginous conditions, which is extensible to the Archean oceans.

Biogeochemical processes in modern lakes can be interrogated through a combination of geochemical and microbiological analyses. Studies in the aforementioned ferruginous lakes are emerging, providing a wealth of new information on geochemical cycling and microbial community profiles for anoxic, iron-rich water columns [47, 48, 64–68]. Such studies have reported process rates for microbially mediated reactions that occur under ferruginous conditions such as photoferrotrophy, iron reduction, nitrogen cycling, and methane cycling [47, 48, 64–73]. For example, the potential for photoferrotrophy was interrogated through light-based incubation experiments, using a chemical inhibitor for oxygenic photosynthesis, in the chemocline of Kabuno Bay [48]. The lack of change in the rate with and without the inhibitor demonstrates the potential for photoferrotrophy this lake [48]. These process rate measurements provide estimates of the magnitude of key pathways in biogeochemical cycles that are supported by the microbial

community. Additional studies to identify the microbial community members under such ferruginous conditions have been conducted in known ferruginous lakes [47, 48, 64–73]. These data can be further used to inform putative metabolic models of the microbial community (Fig. 1.4) [48]. Most of these studies have identified a large consortium of anoxygenic phototrophs of the class Chlorobia that, based on laboratory experiments with Chlorobia isolates (Table 1.1), are putative photoferrotrophs. While many of these have yet to be confirmed through laboratory growth experiments, photoferrotrophy was confirmed in an isolate from the dominant group of Chlorobia in the Kabuno Bay chemocline (*Chlorobium phaeoferrooxidans* strain KB01 — Table 1.1). To date, therefore, Kabuno Bay is the only known ferruginous water column with a dominant population of confirmed photoferrotrophs likely acting as primary producers. Thus, while studies in modern ferruginous lakes are emerging [47, 48, 64–73], there is little information on the ecology of photoferrotrophs in modern microbial communities that could inform on how community interactions impact iron and carbon cycling in such ferruginous environments, modern or ancient.

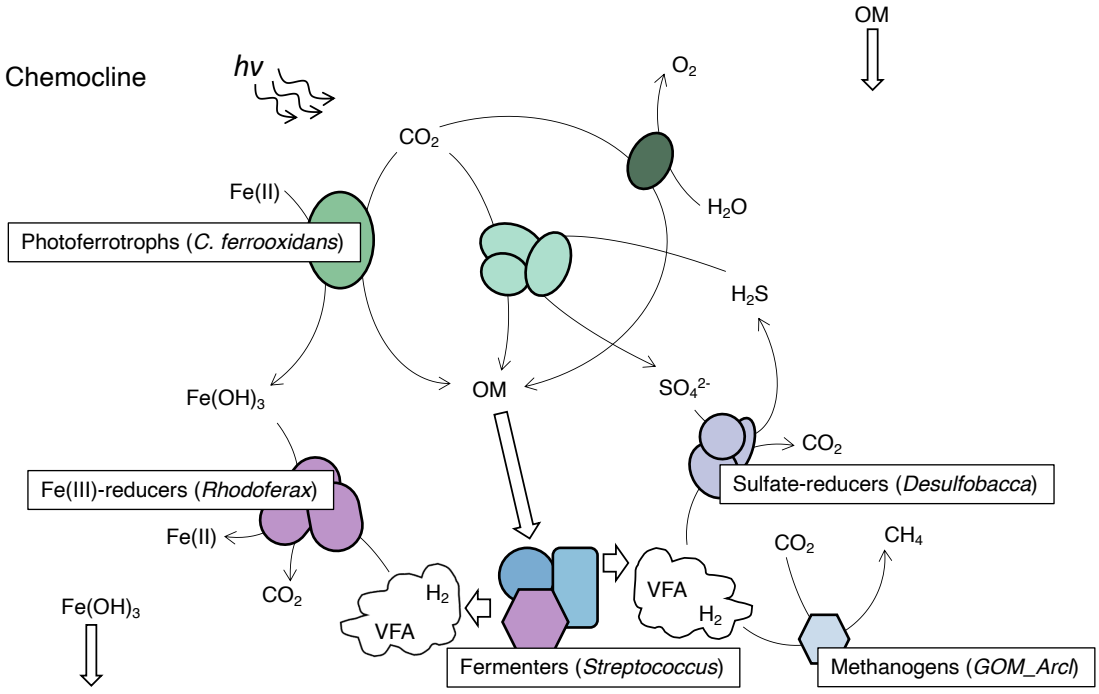

Figure 1.4: *Proposed metabolic model for the microorganism present at the chemocline in Kabuno Bay.* Potential populations of microorganisms are suggested for each metabolism in the white boxes, *hv* denotes light, OM is organic matter, and VFAs are volatile fatty acids. This figure is adapted from Lliros et. al., 2015 [48].

1.3 Photoferrotrophy during the Archean Eon

The sedimentary rock record hosts a wealth of information regarding past ocean environments and the large-scale changes in Earth's surface chemistry that have occurred through time. Sedimentary rocks contains clues to the chemical composition of the oceans and atmosphere in the past. Not only are these deposits useful archives of Earth's history, but they also represent economically viable sources of key elements required for the maintenance and growth of human society. For example, banded iron formations (BIFs) are the world's largest iron ore deposits, which support a substantial amount of global steel production [4, 74, 75]. BIFs are found world-wide with several deposits concentrated in specific regions where Archean and Proterozoic strata still exist, such as the north of Western Australia, the west of South Africa, as well as northeastern North America (Fig. 1.5) [4]. While the size, age, and preservation of each of these deposits varies, they have been sought after, mapped, and geochemically analyzed due, primarily, to their economic value [4, 74, 75]. As a marine sedimentary deposit, BIFs can provide information that can be used to constrain models of Precambrian seawater and atmospheric composition, and for tracking dynamics in large-scale Earth processes such as climate change over time.

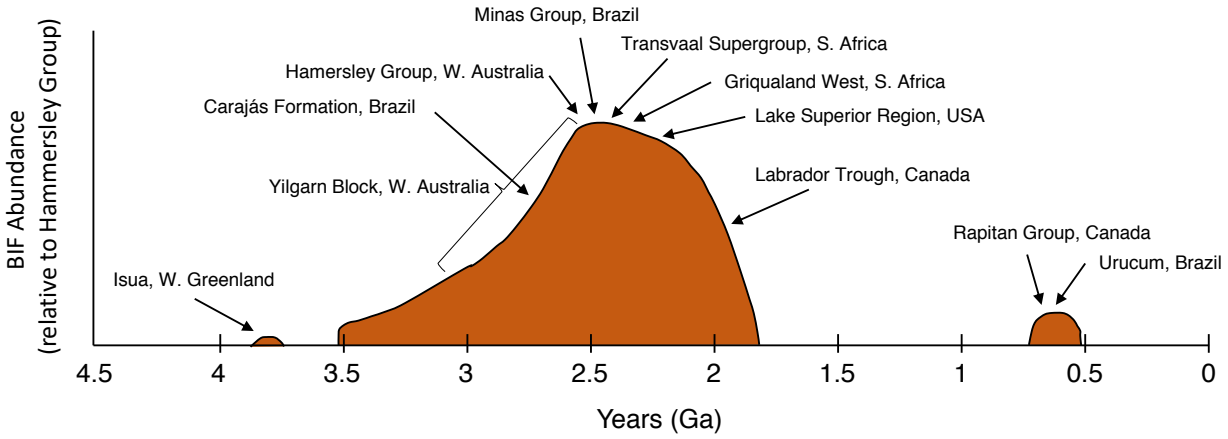

Figure 1.5: *The relative abundance of BIFs versus time (compared to the Hamersley Group BIF volume) where several of the major BIF regions are identified.* Adapted from Klein, 2005 [4], where further formations are delineated.

Banded iron formations were deposited between 3.8 and 0.6 Ga with the majority being deposited during the Archean Eon between 3.5 and 2.5 Ga (Fig. 1.5) [4, 74, 75]. Many BIFs have

very similar bulk chemistry and features which distinguish them from other iron-rich sedimentary rocks, such as ferruginous shales, that were deposited contemporaneously [4]. They contain high weight percent iron (20 to 40 wt. % total Fe) with the remaining balance comprising SiO_2 (43 to 56 wt. %) and minor amounts of other elements such as calcium or magnesium [4]. Furthermore, the iron and silica concentrations typically vary antithetically, which results in banding. BIFs are thus defined as: *"a chemical sediment, typically thin bedded or laminated, whose principal chemical characteristic is an anomalously high content of iron, commonly but not necessarily containing layers of chert [76]"*. While the bulk chemistry of most BIFs is similar, the individual characteristics of each deposit vary depending on depositional processes and/or post-depositional alteration [4]. The majority of BIFs have undergone appreciable metamorphic alteration, which changes their mineralogical composition and makes it difficult to discern the primary mineralogy. Extensive work, however, on the less altered Archean BIFs, such as the Hamersley BIF in the Pilbara region of Western Australia, have led to several hypotheses for their mode of formations [4, 77, 78]. While hotly debated, the general consensus is that BIFs were deposited when large amounts of seawater Fe(II) were oxidized to ferric iron minerals of varying composition [4, 6, 7]. Other research has suggested, however, that ferrous iron minerals, and silicates in particular, were in fact the primary minerals that contributed to BIF deposition, with post-depositional alteration of such primary phases to secondary Fe(III) (oxyhyr)oxides [79–81].

The first attempt to account for the formation of BIFs, postulated by Preston Cloud in early 1970's, involved the oxidation of seawater Fe(II) by molecular oxygen produced through oxygenic photosynthesis, which had accumulated in the oceans and atmosphere following the evolution of oxygenic photosynthetic prokaryotes [6]. This hypothesis was based on analyses of a subset of BIFs, which contained putative nannofossils of eukaryotic algae. Although the so-called microfossils were misidentified as organic remains, Cloud's initial hypotheses remain partially valid as there is now abundant evidence in the rock record for the presence of molecular O_2 in Earth's atmosphere as early as 3.0 Ga [16, 31, 32]. Furthermore, genomic evidence concurs with the sedimentary rock record, suggesting that oxygen-producing cyanobacteria likely evolved during the Archean Eon [10–12]. Despite the likely early evolution of oxygenic photosynthesis and production of O_2 during the Archean Eon, however, further work using proxies has shown that

the atmospheric oxygen content remained very low (less than 0.001 % of current atmospheric O_2) throughout the majority of BIF deposition (Fig. 1.6) [2, 13–15, 18, 19]. These low O_2 concentrations suggest that oxygenic cyanobacteria were restricted to small niche environments on land or in nutrient-rich coastal regions, limiting their contribution to global primary production and the flux of O_2 to the atmosphere [11, 16, 17, 82]. Furthermore, recent modeling, constrained by the rock record and putative ocean and atmosphere O_2 concentrations, demonstrate that the Archean O_2 concentrations could only support a limited rate of abiotic oxidation of Fe(II) [8, 15, 22]. Collectively these studies present evidence that largely rules out O_2 driven Fe(II) oxidation as the primary model for BIF deposition in the Archean Eon [8, 15, 22].

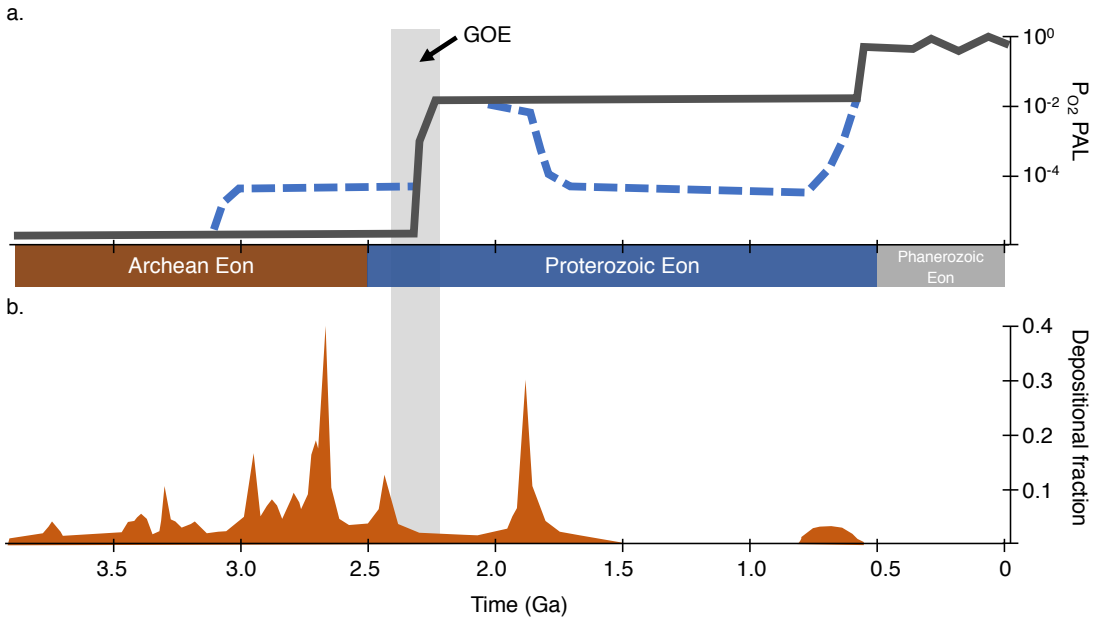

Figure 1.6: *The abundance of BIFs compared to the concentration of atmospheric oxygen over time.* Oxygen concentration (a) in the atmosphere relative to the modern oxygen concentration through time when the line represents the canonical oxygen curve and the dashed line represents alternative views, adapted from Lyons et. al., 2014 [28]. BIF deposition (b) through time represented as the depositional fraction of the rock record at the time of deposition, adapted from Isley and Abbott, 1999 [83].

Three alternative mechanisms for Fe(II) oxidation have been proposed since Cloud's seminal work—anoxic iron oxidation through UV photolysis, the chemical precipitation and subsequent oxidation (via oxygen once it had accumulated in the atmosphere and oceans) of Fe(II) ferroan silicate phases such as greenalite, and anoxygenic photosynthesis. Both the photochemical oxida-

tion and precipitation of primary Fe(II) minerals could have occurred irrespective of biological activity and have thus been proposed as alternatives to biologically mediated Fe(II) oxidation. The photochemical oxidation of Fe(II) has been shown to occur at rates that would indeed have been sufficient to deposit large BIFs [38, 39]. The initial laboratory experiments conducted to test this hypothesis, however, were conducted under conditions that were not analogous to those of the Archean Eon oceans. For example, unlike in modern oceans, the concentrations of bicarbonate [84] and silica [85] were likely present in high concentrations in Archean seawater. Subsequent experiments using similar laboratory, Archean-like conditions have indicated much slower rates of photochemical Fe(II) oxidation as the high concentrations of silica and bicarbonate would have favoured the deposition of ferrous iron silicates and carbonates at rates that grossly exceed those of photochemical iron oxidation [40]. While there is petrographic evidence for primary Fe(II) minerals, such as such as greenalite, in some BIF deposits [79, 81, 86, 87], there is no evidence to support the subsequent transformation of these Fe(II) minerals to the predominantly Fe(III) minerals observed in BIFs today. Indeed, in order to reproduce the mineralogical composition of BIF, these primary Fe(II) minerals would have had to be oxidized by ground water, saturated in oxygen, for several billion years to result in the BIFs that we observe today [88]. It is plausible that this mechanism could have played a small role in transforming some primary Fe(II) minerals in BIFs to Fe(III) minerals, but the magnitude of oxidation required to deposit BIFs is probably unreasonable [88]. Thus, while chemical oxidation could have played a minor role in BIF deposition, biologically mediated photosynthetic Fe(II) oxidation reactions are far more favorable under the anoxic conditions that persisted in the deep oceans for over three billion years of Earth's history during which BIF were formed.

Garrels and Perry [7] originally proposed that anoxygenic phototrophic bacteria used sunlight to directly oxidize ferrous iron (photoferrotrophy) instead of oxygen dependent Fe(II) oxidation in Earth's early oceans. This idea gained considerable traction when Widdel *et. al.* [20] isolated the first photoferrotrophic bacterium (Table 1.1). Anoxygenic phototrophs harness energy from sunlight to fix carbon dioxide into biomass, while an electron from an inorganic electron donor (e.g. H_2, Fe(II), H_2S) [1] replaces the one lost from the photosystem to fix CO_2 into biomass. Photoferrotrophs acquire this electron from Fe(II), producing Fe(III) as a metabolic by-product

[Eq. 1.1], completing the oxidation of Fe(II) in the absence of molecular oxygen [8, 20, 21]. Indeed, laboratory experiments and direct observations from ferruginous water bodies have demonstrated that these photoferrotrophs are capable of oxidizing ferrous iron at high enough rates to support the fluxes of Fe(III) (oxyhydr)oxides needed to deposit even the largest BIFs [8, 21, 47, 48]. While photoferrotrophy provides a compelling mechanism for the oxidation of Fe(II) to support BIF deposition in the complete absence of oxygen, large knowledge gaps limit our ability to conclusively diagnose photoferrotrophs as the causative agents in Fe(II) oxidation and BIF deposition from Archean seawater. For example, a defining characteristic of extant photoferrotrophs is that they associate with the Fe(III) (oxyhydr)oxides that they produce as a by-product of their growth (Fig. 1.3). This association is difficult to reconcile with the very low concentration of organic carbon present in BIF facies [75, 89]. Thus, while BIF deposition may imply photoferrotrophic activity, the known physiology of cultured photoferrotrophs contradicts this theory.

1.4 Problem statement

Available evidence suggests that photoferrotrophs may have played a key role in coupling the carbon and iron cycles during the Archean Eon and, in doing so, underpinned global primary production at this time. To date, however, all known photoferrotrophs form a close association with the ferric iron metabolites they produce during growth. This association calls into question their involvement in BIF deposition and, notably, their ability to act as primary producers, sustaining the biosphere for millions of years. A lack of quantitative knowledge on the growth of photoferrotrophs and the interactions between them and other microorganisms limits our ability to constrain models that can be applied to the conditions from which BIFs were deposited, as well as the Archean ocean-atmosphere system as a whole. The lack of organic matter preserved in BIF and the magnitude of these deposits suggests that they could only have been produced if cells did not associate with the iron (oxyhydr)oxides, since this would result in either microbial iron reduction, precluding BIF deposition, or in the preservation of considerably more organic carbon in BIFs. Such an association between cell surfaces and ferric iron metabolites would

additionally cause the bacteria to sink in the ocean water column, shuttling them out of the photic zone, which would then halt photosynthetic growth. Additionally, there are very little data on the putative growth of photoferrotrophs under the physicochemical conditions that were likely prevalent during the period of BIF deposition, which adds further uncertainty to models in which photoferrotrophs act as primary producers and were the agents of BIF deposition.

Some of these unknowns can now be addressed, however, through laboratory experiments with *Chlorobium phaeoferrooxidans* strain KB01, which can provide critical information on photoferrotrophy, generally, and on the interactions between photoferrotrophs and the microbial consortium they support. Experiments with *Chlorobium phaeoferrooxidans* strain KB01 and studies of the Archean analogue environment from which it was isolated, Kabuno Bay, may provide new insight into key microbe-mineral and microbial community interactions with extensibility to coupled carbon and iron cycling in the Archean Eon. Detailed quantitative knowledge of the growth of *Chlorobium phaeoferrooxidans* strain KB01 and its interactions with other microorganisms are needed to constrain models that aim to reconstruct BIF deposition and the Archean ocean-atmosphere system.

1.5 Dissertation overview

The overall goal of my thesis is to generate new knowledge on photoferrotrophy that can be used to inform and constrain models of primary production and BIF deposition during the Archean Eon. More specifically, I aim to:

i. Explore the physiology and metabolic capacity of pelagic photoferrotroph *Chlorobium phaeoferrooxidans* strain KB01.

ii. Elucidate the role of photoferrotrophs, as primary producers, and determine the flow of organic carbon, from primary production to terminal oxidation, within the microbial community of ferruginous Kabuno Bay.

iii. Construct models of BIF deposition and the role of photoferrotrophs as primary producers throughout the Archean Eon.

Chapter 2: *Chlorobium phaeoferrooxidans* strain KB01 – a pelagic, Fe(II)-oxidizing, anoxygenic, photosynthetic bacterium

The research described herein defines the metabolic potential, physiology, and taxonomy of *Chlorobium phaeoferrooxidans* strain KB01, the first photoferrotrophic bacterium to have been isolated from a pelagic environment. Collectively, this information will provide key information for all three aims (i, ii, iii).

Chapter 3: Nutrient acquisition in *C. phaeoferrooxidans* strain KB01

This chapter examines some of the key nutrient (nitrogen and sulfur) requirements for photoferrotrophy, and the metabolic potential associated with meeting these requirements, using genomic analyses, which were, where possible, verified biochemically. Nutrient metabolism was likely a key aspect for ancient primary production under ferruginous conditions. Therefore, the probable antiquity of these metabolisms, in photoferrotrophic Chlorobia, are tested through phylogenetic analyses (i, iii).

Chapter 4: Photoferrotrophy, deposition of banded iron formations, and methane production in Archean oceans

This chapter elucidates the cell surface chemistry of *C. phaeoferrooxidans* strain KB01 and other phototrophic strains to assess the interactions between these microorganisms and the Fe(III) (oxyhydr)oxides produced as a by-product of either anoxygenic or oxygenic photosynthesis. These results are then combined with a re-evaluation of the Archean iron budget to model the role of photoferrotrophs in BIF deposition (i, iii).

Chapter 5: Carbon flow through microbial interactions under ferruginous conditions

This chapter defines the likely microbial interactions in the ferruginous water column of Kabuno Bay by examining both process rates and the genomic content of the microbial communities, with a particular focus on the photoferrotrophic Chlorobia that dominate the chemocline. The genomic information provides a blueprint for the collective metabolic potential of the microbial community in Kabuno Bay, while the process rate data quantitatively tie this metabolic potential to geochemical outcomes. The microbial interactions through pathways of carbon and iron cycling

will then be used to construct models of microbial interactions that may have played a key role in coupled carbon on and iron cycling during the Archean Eon (ii, iii).

Chapter 6: Conclusion

Chapter 6 presents the overarching conclusions from this body of work and addresses the future directions required to further refine models of carbon and iron biogeochemical cycling in the Archean Eon and the impact on ocean and atmospheric chemistry.

Supplementary Materials

There are supplementary materials for Chapters 4 and 5.

Chapter 2

Chlorobium phaeoferrooxidans strain KB01 – a pelagic, Fe(II)-oxidizing, anoxygenic, photosynthetic bacterium

2.1 Summary

Anoxygenic, photosynthetic, ferrous iron oxidizing bacteria (photoferrotrophs) likely supported the early biosphere through primary production (PP) prior to the emergence and proliferation of oxygenic photosynthesis and the oxygenation of the Earth's surface. Compelling evidence for the activity of photoferrotrophs in the Precambrian oceans comes from the world's largest deposits of ferric iron – banded iron formations (BIFs). Several extant photoferrotrophs have been brought into laboratory culture and their physiology studied to constrain models of primary production and biogeochemical cycling under ferruginous conditions. The extensibility of information from these model organisms to ancient oceans is limited in part due to physiologies adapted to benthic lifestyles. Here we describe the cellular composition, growth kinetics, and nutrient cycling capabilities of a novel photoferrotroph enriched and isolated from a modern ferruginous water column. This photoferrotroph (*Chlorobium phaeoferrooxidans* strain KB01) is distinct from its closely related benthic relative *Chlorobium ferrooxidans* strain KoFox. They have 99 % identity between 16S rRNA genes with only 70 % identity across entire genomes. Strain KB01 grows at a maximum rate of 48 ± 7 fmol cell^{-1} h^{-1} under standard laboratory growth conditions with a high specific affinity for Fe(II) (190,000 L g^{-1} wet cell h^{-1}). These growth rates are higher than those of previously characterized photoferrotrophs and other Fe(II) oxidizing organisms more generally. Strain KB01

has adaptations for growth under low light intensities (0.03-0.05 μmol m^{-2} s^{-1}) and has a high specific affinity for light ($\sim$1,410,000 m^2 s g^{-1} wet cells h^{-1}) likely related to extraordinary per cell concentrations of photosynthetic pigments (BChl e of 1.5 $\pm$ 0.3 pg). While many similar traits can be found in other members of the class Chlorobia, or photoferrotrophs from other lineages, this combination of traits in *Chlorobium phaeoferrooxidans* strain KB01 reveals that they are collectively biologically and ecologically compatible with each other and growth through photoferrotrophy in a pelagic habitat. By extension, such a suite of traits could have been critical to underpinning BIF deposition, PP, and coupled carbon and iron cycling in Precambrian Eons.

2.2 Introduction

Photosynthesis fuels the biosphere by using light energy to transform inorganic carbon to organic carbon in biomass and, on the modern Earth, photosynthesis is responsible for nearly all of global primary production (PP) [90, 91]. In modern aquatic environments, PP is conducted mainly by photosynthetic microorganisms that are either oxygenic, like cyanobacteria and eukaroytic algae [91, 92], or anoxygenic, such as the Chlorobia, Chloroflexi, and some Proteobacteria [93]. Oxygenic photosynthesis by such microorganisms drives a large fraction ($\sim$50 %) of global PP today [90, 91], and has likely contributed to PP since the early Archean Eon, some 3 billion years ago [16, 92, 94]. Anoxygenic photosynthesis, on the other hand, likely sustained the biosphere before the evolution and proliferation of oxygenic photosynthesis and continued to play a key role in PP throughout the Precambrian Eons [1, 11, 35, 93], but is now mostly marginalized to the dispersed and often ephemeral pockets of illuminated anoxia that occur on the Earth's surface today [93]. Multiple modes of photosynthesis using a diversity of electron donors have played exclusive, concurrent, and even synergistic roles in PP and thus in fueling the biosphere throughout Earth's history [1, 47, 48, 95, 96]. In so doing, they have coupled the carbon biogeochemical cycle to the cycles of several other elements, including oxygen, sulfur, and iron [1].

Both oxygenic and anoxygenic phototrophs support biological production by harnessing energy from sunlight to excite electrons, supplied mostly by inorganic electron donors, to drive the endergonic conversion of inorganic carbon dioxide (CO_2) into organic carbon [91]. Unlike oxygenic

phototrophs, whose virtually unlimited supply of electrons is supplied by water, anoxygenic phototrophic bacteria use electrons from both inorganic and organic substances that have lower activities than water in aquatic environments (e.g. sulfide (HS^-), ferrous iron (Fe[II])), and tend only to accumulate to appreciable activities under anoxic conditions [91, 93]. The photosynthetic machinery required to excite these electrons, and to subsequently transport them down an electron potential gradient to generate energy, likely stems from common ancestral genes and has features that are conserved across most photosynthetic lineages [11, 35, 92, 97]. For example, there is structural homology in the photosystem I found in both oxygenic and anoxygenic phototrophs, which suggests common ancestry despite differences in the underlying gene sequences [98]. There is, however, considerable diversity in the nature and configuration of proteins used in harnessing light energy and the types of proteins used in the transport of electrons from an electron donor to inorganic carbon [35], which translate to dramatic differences in the physiology across lineages. While well over 100 oxygenic and anoxygenic phototrophs have been brought into laboratory cultures (DSMZ and ATCC culture collections) – enabling detailed biochemical, genomic and physiological studies – cultures of anoxygenic phototrophs that specifically use Fe(II) as their electron donor (photoferrotrophs) are fewer than 20 [57]. Thus, while studies of these cultured photoferrotrophs have provided a wealth of information on their metabolism, our knowledge of the potential physiological diversity in photoferrotrophy is limited compared to the much better studied oxygenic and sulfur-dependent anoxygenic phototrophs.

Motivation for learning more about photoferrotrophy comes, in large part, from their likely disproportionate role in supporting PP and driving fluxes of matter and energy at global scales throughout Earth's early history. Prior to the advent of oxygenic photosynthesis, PP through anoxygenic photosynthesis would have played a crucial role, for example through climate regulation, in sustaining the biosphere [1, 95, 99]. Anoxygenic photosynthesis, almost certainly evolved prior to oxygenic photosynthesis [11, 35, 93], and anoxygenic photosynthesis would likely have supported a biosphere nearly 2 orders of magnitude more productive than a biosphere devoid of photosynthesis altogether [1]. Earliest evidence for photosynthesis comes from microfossils and isotopic signatures for carbon fixation from as early as 3.8 Ga [100–102]. Elemental budgets for the Precambrian Eons imply that Fe(II) would have been the most available electron donor

for anoxygenic photosynthesis, and thus photoferrotrophy (Eq. 2.1) is widely regarded as the dominant mode of primary production through Earth's early history [1, 7, 21, 82, 103]. Early estimates based on these elemental budgets implied that photoferrotrophy could have supported PP up to about 10 % of modern PP, or 170 to 500 Tmol carbon yr^{-1} [1]. Revised estimates suggest, however, that global PP would have been closer to 1 % modern [99].

$$4\,Fe^{2+} + CO_2 + 11\,H_2O + h\nu \Rightarrow [CH_2O] + 4\,Fe(OH)_3 + 8\,H^+ \tag{2.1}$$

Geological evidence for the role of photoferrotrophs in PP during the Precambrian Eons comes from the preservation of banded iron formations (BIFs), which are enormous sedimentary deposits of iron minerals. Deposition of BIFs was initially attributed to the oxygenation of Precambrian seawater through oxygenic photosynthesis, and subsequent abiotic or biological oxidation of Fe(II) to drive deposition Fe minerals at the seafloor [6]. More quantitative considerations, however, now suggest that oxygen concentrations and likely production rates were, in fact, too low to support the rates of Fe deposition needed to form BIFs [2, 8, 15, 22, 82]. Photoferrotrophy, therefore, is the most likely process to support Fe oxidation at the rates needed to deposit BIF [8, 21], at least in the Archean Eon, prior to the widespread oxygenation of the atmosphere ocean system some 2.3 Ga [2, 104, 105]. Furthermore, while oxygenic photosynthesis likely emerged early in the Archean Eons [16, 92, 94], competition for phosphate between nascent oxygenic phototrophs and photoferrotrophs would have restricted the proliferation of the former until Fe(II) availability declined, likely around 2.3 Ga [85, 96, 106]. Thus, not only did photoferrotrophy likely play a key role in sustaining the early biosphere, it also throttled the pace of Earth's oxygenation through competition with early oxygenic phototrophs [85, 96, 106]. While such roles for photoferrotrophy in the evolution of the Earth system are well supported by available physiological and geological information, as well as models that integrate this information into quantitative frameworks, additional information on the metabolic potential and evolutionary history of photoferrotrophy would facilitate more nuanced and robust reconstructions of Earth's early history.

A number of photoferrotrophs have been brought into laboratory culture and studies of these cultures have progressively improved our knowledge of photosynthetic iron oxidation and

enabled evaluation of the possible role of photoferrotrophs in BIF deposition and PP throughout Earth's history. Early recognition, by geologists, that the oxidation of Fe(II) from low-oxygen or even anoxic seawater was likely needed to support BIF deposition led to the original idea that Fe(II) could be directly oxidized as the electron donor in anoxygenic photosynthesis [7]. The first microorganisms that showed photosynthetic growth with Fe(II) as the electron donor, *Rhodomicrobium* sp. and *Thiodictyon* sp., were enriched and isolated from a freshwater pond and marine sediments in Germany [20]. This was the first time that photoferrotrophy was deemed biologically and biochemically possible [20]. At the same time, experiments with these first photoferrotrophic isolates revealed that Fe(II) is stoichiometrically oxidized at a 4:1 ratio with CO_2 fixed (Eq. 2.1) into biomass thereby directly linking, for the first time, photosynthetic Fe(II) oxidation to biological production [20].

Since this discovery of photoferrotrophy in extant bacteria, a number of additional bacteria with capacity to grow through photosynthetic Fe(II) oxidation have been enriched and isolated from both marine and freshwater environments [52, 53, 55–57]. These isolates come from three different classes of bacteria (Alphaproteobacteria, Gammaproteobacteria, and Chlorobia), are closely related to other anoxygenic phototrophic members of those classes, and demonstrate polyphyly of the photoferrotrophic trait [35]. Laboratory studies of these isolates reveal several characteristic features of photoferrotrophs such as a general ability to grow using alternative electron donors (i.e. organic carbon compounds, H_2S, and H_2) and a tendency to grow through Fe(II) oxidation with close physical association between cell surfaces and the iron (oxyhydr)oxide growth products [9, 53, 55–57, 62, 63]. Notably, laboratory studies have also shown that some extant photoferrotrophs are capable of oxidizing Fe(II) at rates that are high enough to support deposition of even the largest of the Precambrian BIFs [9, 21, 42, 55]. Data from such studies underpins conceptual and quantitative models of BIF deposition and coupled iron and carbon cycling in Earth's early oceans [21, 42, 82, 95, 96, 99, 107–109]. All but one of the photoferrotrophs enriched and isolated to date, however, originate from benthic environments [57], and based on analogy to other photosynthetic bacteria, this suggests that most existing information is only partly extensible to water column processes like BIF deposition. For example, previous studies of benthic and pelagic cyanobacteria have shown that even different species of the same

genus occupy different niche environments (benthic versus pelagic) [110], which is likely due to physiological differences, such as extracellular and cell-surface layers and appendages that allow the benthic microorganisms to remain in their preferred environment through attachment [111–113]. Inferences related to the biogeochemistry of the Precambrian oceans based on the physiology of benthic photoferrotrophs may not, therefore, be entirely accurate and there is a clear need for new knowledge from more appropriate analogue organisms derived from ferruginous pelagic environments.

Chlorobium phaeoferrooxidans strain KB01 was enriched and isolated from the water column of an Fe(II)-rich lake [48] and, since it comes from a pelagic habitat, arguably represents the best modern analogue for the photoferrotrophs that likely underpinned BIF deposition, PP, and coupled carbon and iron cycling in the Precambrian oceans. Strain KB01 was isolated from the ferruginous waters of Kabuno Bay, a permanently stratified sub-basin of Lake Kivu, located in East Africa on the border of the Democratic Republic of Congo (DRC) and Rwanda. On-going volcanic activity in the area surrounding Lake Kivu releases carbon dioxide and methane gas into the lake and its sub-basin, maintaining anoxic bottom waters [114]. Furthermore, ground water enriched in Fe(II) continually feeds Kabuno Bay creating a chemocline that juxtaposes the lower part of the photic zone with Fe(II)-rich water. Strain KB01 was originally referred to as *Chlorobium ferrooxidans* strain KB01 based on analyses of its 16S rRNA gene, which is 99 % similar, and thus indistinguishable by conventional definitions of species-level classification, to benthic photoferrotroph *Chlorobium ferrooxidans* strain KoFox [48]. Subsequent whole genome sequencing, however, revealed that the strains were only 70 % identical at the genome level thus justifying the designation of strain KB01 as its own species and its renaming as *C. phaeoferrooxidans* strain KB01, accordingly [58]. In this paper, we provide the detailed and systematic description of strain KB01 supported by ecological, phenotypic and genotypic information. We further use this information to support the ideas that strain KB01 is a strong analogue of Precambrian photoferrotrophs and that its physiology and metabolic potential is extensible to conceptual and quantitative models of BIF deposition, PP, and coupled carbon and iron cycling in the Precambrian Eons.

2.3 Materials and methods

2.3.1 Strain and growth medium

Chlorobium phaeoferrooxidans strain KB01 was enriched and isolated from the chemocline of ferruginous Kabuno Bay, a sub-basin of Lake Kivu in East Africa [48] and was subsequently grown in serum bottles containing an anoxic (80:20 N_2:CO_2) atmosphere and standard ferrous iron (Fe[II]) – containing growth media as described by Hegler et al., 2008 [55, 115]. The standard growth media [55] was prepared and allocated into serum bottles (100 mL media, 160 mL total volume), with 0.3 g L^{-1} NH_4Cl, 0.5g L^{-1} $MgSO_4{\cdot}7H_2O$, 0.1 g L^{-1} $CaCl_2{\cdot}2H_2O$, 0.6 g L^{-1} KH_2PO_4. After autoclaving, 22 mmol L^{-1} bicarbonate was added along with trace elements (nonchelated trace element mixture), mixed vitamin solution, selenate-tungstate, vitamin B12 (after chapter 183 by Widdel and Bak [116]). Finally, $FeCl_2$ was added and the pH was adjusted to 6.8-6.9 under an N_2/CO_2 atmosphere (80:20). 10 mmol L^{-1} $FeCl_2$ was utilized for the standard media conditions. The 10 mmol L^{-1} media was also filtered after being made to remove any precipitates to confirm that media precipitates did not change the overall growth rates, which resulted in a final Fe(II) concentration of between 2 and 4 mmol L^{-1} for the standard media (results from these experiments not shown). All experiments were conducted in triplicate and sub-samples were taken to track the growth of strain KB01 as described below.

2.3.2 Bioinformatics

rRNA gene comparison The full length 16S rRNA gene for *Chlorobium phaeoferrooxidans* strain KB01 was retrieved from Llirós *et. al.* [48]. Other 16S rRNA sequences were retrieved from members of the class Chlorobia from the Silva online database — version 128 [117, 118]. Only full-length ($>$ 1400 bp) sequences were selected, and then aligned using the default parameters in the package software ClustalX2.1 [119]. To rigorously test the evolutionary history of strain KB01 within the class Chlorobia multiple tree construction methods (Maximum likelihood (ML), Maximum parsimony (MP), and Neighbour Joining (NJ)) were employed. ML, MP, and NJ trees were constructed in MEGA version 7 [120, 121] and all trees bootstrapped 500 times. The phylogeny shown is from the most robust tree construction method, ML, with the bootstrap values

indicated at the nodes. The bootstrap values for the alternative tree construction methods are also shown at the nodes (MP and NJ) and the legend (0.03) delineates the nucleotide substitutions per site over the indicated distance (Fig. 2.3a).

Full genome analyses The strain KB01 genome was subjected to Illumina paired-end library construction and sequenced (MiSeq platform, version 3 chemistry) to generate 16,133,652 paired 250-nucelotide (nt) reads as reported by Crowe et al., 2017 [58]. The quality-filtered reads were subsequently assembled into 116 contigs using the default settings in ABySS 1.3.5 [58, 122]. The full genome for *Chlorobium ferrooxidans* strain KoFox (90.71 % completed) was retrieved from the National Center for Biotechnology Information (NCBI – https://www.ncbi.nlm.nih.gov/) under the accession number NZ_AASE00000000.1. To identify regions with identical nucleotide sequences in strain KB01 and strain KoFox, the contigs of both strains were aligned and compared using MUMmer (nucleotide comparison with nucmer [123]) and visualized using Circos (http://circos.ca/) — Fig. 2.3b. To delineate the likelihood that strain KB01 is a different species from strain KoFox, *in silico* DNA-DNA hybridization was conducted utilizing the Genome-to-Genome Distance Calculator (http://ggdc.dsmz.de/) [124]. To compare the similarities and differences between the higher level pathways in strain KB01 and strain KoFox, open reading frames (ORFs) for both strains were predicted using Prodigal [125]. The predicted ORFs, for both strains, were subsequently annotated using the online tool Kofam Koala [126] that uses Hidden Markov-Models (HMMs) to compare each ORF to those found in the Kyoto Encyclopedia of Genes and Genomes database (KEGG-11-06-18) [127]. The resulting annotations were compared at the pathway level and visualized through a python script as described in Graham et. al., 2018 [128] -– Fig. 2.3c. Other genes — those that are uncharacterized in the KEGG database — were found by retrieving the relevant gene or protein sequences from the NCBI, Pfam [129], or CAZy databases [130]. The sequence or HMM of the gene/protein of interest was then used to search for those gene or proteins within nucleotide and protein predicted ORFs of the strain KB01 genome using BLAST (initial e-value cut-off of 1×10^{-18}, followed by a Bit Score cut-off of 50 [131]) or HMMER's hmmserach function (e-value cut-off of 1×10^{-18} and length cut-off of 50 % [132]).

2.3.3 Analytical techniques

To track the growth of *Chlorobium phaeoferrooxidans* strain KB01 under iron-rich conditions, sub-samples were taken from the serum bottles at the time of inoculation and every day (or as otherwise indicated) for three to four weeks. The first of these sub-samples was analyzed for Fe(II) and Fe(III) concentrations using spectrophotometric methods. Specifically, Fe(II) and Fe(III) concentrations were determined by the ferrozine method and samples were measured directly as well as after being fixed in 1 N HCl — after Voillier et. al., 2000 [133]. Additional sub-samples were taken from these same serum bottles to measure the pigment concentrations. Pigments contents were assayed spectrophotometrically after 24 hour extractions of 1 mL of pelleted cells in acetone:methanol (7:2 v/v) [134]. A full pigment spectrum (from 400 to 700 nm — Fig. 2.2b) was measured for strain KB01. Subsequent samples were measured at 468 nm (BChl *e* soret peak) and 652 (BChl *e* Q_y peak). Pigment concentrations were then used as a proxy for cell abundance. To further confirm the growth of strain KB01, sub-samples were taken from the serum bottles and cells were fixed in gluteraldehyde (final concentration of 0.1 %). After the cells were fixed, they were subsequently stained with SYBR green (0.25 % final concentration) and directly counted in a 96 well plate using a Miltenyi Biotec MACSQuant, with a flow rate of medium. Pigment and cell count sub-samples were also used to track the growth of strain KB01 in media containing alternative electron donors and acceptors.

2.3.4 Microscopy

Light microscopy *Chlorobium phaeoferrooxidans* strain KB01 was grown in standard growth media (10 mM Fe(II), 4.41 mM phosphate), the serum bottles were gently shaken, and then the Fe(III) (oxyhydr)oxides were allowed to settle for 24 hours. Sub-samples, taken at multiple time points throughout the full 200 hours of growth, were collected from the fully mixed serum bottle after shaking and from the water column once the Fe(III) (oxyhydr)oxides had settled. Wet mounts ($\sim$100 μL) were prepared immediately following the sub-sampling and were imaged using a Zeiss Axio Observer compound microscope fitted with an Axiocam camera. A representative image of a water sub-sample of strain KB01 is shown in Fig. 2.1a.

Scanning electron microscopy (SEM) Cells for SEM were grown up to late-log, early-stationary phase in standard growth media (10 mM Fe(II), 4.41 mM phosphate). The cell-Fe(III) oxyhydroxide suspensions were gently shaken and allowed to settle for 24 hours. A 1 mL sub-sample was collected from either the upper portion of the serum bottle, avoiding settled Fe(III) oxyhydroxides, or from the mixed suspension after gentle shaking. The samples were placed on a Nucleopore Track-Etched Membrane from Whatman©. The cells were then fixed with 2.5 % gluteraldehyde buffered with 0.1 M PIPES at pH of 7.4 for 5 minutes. The external cellular structures were preserved using a 1 % osmium tetroxide solution buffered with 0.1 M PIPES at pH 6.8 for 1 hour. Filters were rinsed gently with MQ water and then dried using an ethanol dehydration series. The filters were critical-point-dried using a Samdri795 from Toosimis Research Corporation. Finally, the filters were attached to a stub and coated with 5 nm of iridium to ensure conductivity. The filters were imaged on a Helios SEM. Fe(III) oxyhydroxides and cells were confirmed through energy-dispersive X-ray spectroscopy (EDS) determinations of carbon and iron abundances and multiple points were measured for each surface found. SEM images are shown in Fig. 2.1b, c of the main text.

Transmission electron microscopy (TEM) 10 mL of strain KB01 cells were concentrated by centrifugation at 5000 rpm for 10 minutes. The concentrated 1 mL of cells was subsequently spun at 10 000 rpm for 5 minutes. The final 30 μL cells were then frozen rapidly using a LEICA EM HPM100. The cellular water was replaced with an alcohol mix while in liquid nitrogen; the samples were sliced as thin sections from an epoxy block and placed onto a copper grid. The samples were imaged on an Osiris S/TEM at the 4D labs imaging facility at Simon Fraser University. TEM images are shown in Fig. 2.1d, e, f of the main text.

2.3.5 Fe and light dependency

Fe(II) concentration dependence of Fe(II) oxidation rates To assess the *C. phaeoferrooxidans* strain KB01 growth rate versus the Fe(II) concentration, strain KB01 was grown in standard media (as described above) under optimal conditions except that the media was amended with a range of Fe(II) concentrations (5 μM to 200 μM). The media were subsequently allocated into serum bottles

(100 mL of media, 160 mL total volume) with triplicate bottles at the same Fe(II) concentration. Strain KB01 cells were harvested at mid to late log phase, spun down, washed with 0.1 N NaCl, and inoculated into each serum bottle, with final approximate concentration of 7 x 10^5 cells mL^{-1}. Sub-samples for Fe(II)/Fe(III), pigments, and cell counts were taken every 20 minutes to track Fe(II) oxidation and cellular growth.

Light dependence of Fe(II) oxidation rates To quantify the dependence of Fe(II) oxidation rates on light intensity, strain KB01 was grown in standard growth media (10 mM Fe(II) – as described above) at a range of light intensities. Strain KB01 cells were harvested at mid to late log phase, spun, down, washed with 0.1 N NaCl, and inoculated into each serum bottle with an approximately 2 % inoculum. The serum bottles were placed at different distances, in triplicate, from a 60 W incandescent light bulb with the resulting light intensities being: 0.03, 0.1, 0.25, 0.5, 0.75, 4, and 15 μmol m^{-2} s^{-1} (a range of 1 to 654 lux). Light intensities were measured with an LI-250A light meter equipped with a LI-COR Quantum Sensor. Two negative controls were used: one was inoculated with strain KB01 and incubated in the dark, wrapped in tin foil and the other was an uninoculated control that was incubated at 4 μmol m^{-2} s^{-1}. Sub-samples for Fe(II)/Fe(III), pigments, and cell counts were taken every two to four days to track Fe(II) oxidation and cellular growth.

Kinetic modelling and calculations To calculate the Fe(II) oxidation rate over time under both the standard conditions (described above) and the limiting conditions, a linear regression was applied to the data points where Fe(II) consumption was highest (example shown in Fig. 2.4a). The subsequent rate data from each Fe(II) or light concentration (from the Fe(II) and light limiting experiments) was plotted as a function of Fe(II) concentration or light flux (Fig. 2.5). A non-linear regression was then used to fit a Michaelis-Menten model to the data:

$$R = V_{\max} \cdot \frac{[S]}{k_m + [S]} \tag{2.2}$$

where R is the reaction rate (μM h^{-1}), V_{max} is the maximum reaction rate (μM h^{-1}), k_m is Fe(II) concentration (μM) or light flux (μmol m^{-2} s^{-1}) at half the maximum rate (V_{max}), and [S] is

the substrate concentration (μM for Fe(II) and μmol m^{-2} s^{-1} for light). Cell-specific V_{max} were calculated by dividing the volume specific V_{max} by the cell counts. Specific affinities for Fe(II) and light were calculated using the following equation:

$$Sa = \frac{(\frac{V_{max} \cdot S_{mw}}{V \cdot D \cdot Cells})}{k_m \cdot S_{mw}} \tag{2.3}$$

where Sa is the specific affinity, V_{max} is the cell specific max reaction rate (mol L^{-1} h^{-1}), S_{mw} is the substrate molecular weight (e.g. gFe mol^{-1}), V is the cell volume (cm^3 $cell^{-1}$), D is the cell density (g cm^{-1}), Cells is the cell counts (cell L^{-1}), and k_m is the substrate at half the V_{max} (mol L^{-1}) [135]. The calculations were completed with an average cell density (1.09 g cm^{-3} [136]), while the average cell volume for strain KB01 cells was $\sim$0.17 μm^3. Further calculations included elucidating the cell-specific BChl *e* content of the strain KB01 cells. This was executed by transforming the pigment absorption to concentrations by using the molar extinction coefficient for BChl *e* in Acetone:Methanol (7:2), 41.4 $\pm$ 0.7 L $mmoles^{-1}$ cm^{-1} [137] or 58.6 L g^{-1} cm^{-1} [138], and dividing the concentrations by the cell counts (cells mL^{-1}).

2.3.6 pH, temperature, and vitamin dependence

pH dependence of Fe(II) oxidation rates To quantify the dependence of Fe(II) oxidation rates on pH, strain KB01 was grown in standard growth media (10 mM Fe(II) – as described above) at a range of pH. Final pH values were controlled to 6, 6.4, 6.8, 7, and 7.3 with either 1 N HCl or 1 N NaOH. Strain KB01 cells were harvested at mid to late-log phase, spun down for 5 minutes at 10000 x *g*, washed with 0.1 N NaCl, and inoculated into each serum bottle with an approximately 2 % inoculum. Each pH value was tested in triplicate, along with an uninoculated negative control to confirm a lack of abiotic Fe(II) oxidation. Sub-samples for Fe(II)/Fe(III), pigments, and cell counts were taken every two to four days to track Fe(II) oxidation and cellular growth.

Temperature dependence of Fe(II) oxidation rates To quantify the dependence of Fe(II) oxidation rates on temperature, strain KB01 was grown in standard growth media (10 mM Fe(II) – as described above) at 4, 15, 23, 25, 30°C. The cells were harvested at mid to late log phase, spun,

down, washed with 0.1 N NaCl, and inoculated into each serum bottle with an approximately 2 % inoculum. All temperatures were tested in triplicate, along with an uninoculated negative control to confirm a lack of abiotic Fe(II) oxidation. Sub-samples for Fe(II)/Fe(III), pigments, and cell counts were taken every two to four days to track Fe(II) oxidation and cellular growth.

Vitamin dependence of Fe(II) oxidation rates To quantify the dependence of Fe(II) oxidation rates on the presence of each bio-essential vitamin, strain KB01 was grown in standard growth media (10 mM Fe(II) – as described above) with the regular suite of vitamins and in standard growth media where each of the vitamins had been individually omitted. The individual vitamins that were tested were: aminobenzoic acid, calcium, nicotinic acid, B12, biotin, pyridoxin. Strain KB01 was also tested in media that did not contain any of the listed vitamins. Strain KB01 cells were harvested at mid to late log phase, spun, down, washed with 0.1 N NaCl, and inoculated into each serum bottle with an approximately 2 % inoculum. All media composition were tested in triplicate, along with an uninoculated negative control to confirm a lack of abiotic Fe(II) oxidation. Sub-samples for Fe(II)/Fe(III), pigments, and cell counts were taken every two to four days to track Fe(II) oxidation and cellular growth.

2.3.7 Alternative electron donors and acceptors

To test for strain KB01's ability to grow on alternative electron donors and acceptors, strain KB01 was inoculated into standard growth media (as described above) that had been amended with a diverse set of electron donors and acceptors. All of the organic compounds tested were amended to the media with a final concentration of 4 mM, while 10 mL of H_2 gas (100 %) was added to the headspace of the serum bottles every second day. Strain KB01 cells were harvested at mid to late log phase, spun, down, washed with 0.1 N NaCl, and inoculated into each serum bottle with an approximately 2 % inoculum. Sub-samples for pigments and cell counts were taken every two to four days to track cellular growth. All media composition were tested in triplicate, along with an uninoculated negative control to confirm growth. To test whether strain KB01 could grow phototrophically with an alternative electron donor, strain KB01 was inoculated into standard media amended with glucose or acetate or lactate or unamended with H_2 in the headspace and

these serum bottles were grown under light saturation (15 μmol m^{-2} s^{-1}). To test whether strain KB01 could ferment organic carbon compounds, strain KB01 was inoculated into standard media amended with glucose or acetate or lactate and these serum bottles were wrapped in tin foil in the dark. To test whether strain KB01 was capable of aerobic respiration, strain KB01 was inoculated into standard media, in Erlenmeyer flasks, amended with glucose or acetate or lactate or pyruvate.

2.4 Results

2.4.1 Morphology and pigmentation

Chlorobium phaeoferrooxidans strain KB01 (hereafter referred to as strain KB01) exhibits internal and external cellular characteristics that typify anoxygenic phototrophic Chlorobia. It is relatively small in cell size (length of ~600 nm, width of ~300 nm) with a rod shape that does not visibly exhibit any of the external machinery required for motility, such as flagella and pilli (Fig. 2.1). Strain KB01 divides through binary cell division (Fig. 2.1b) and has few distinctive cell surface features (Fig. 2.1b, c). Transmission electron microscopy (TEM) reveals internal structures such as the chlorosomes—large oval structures bound to the inner membrane that house the pigments needed to capture light and are characteristic of phototrophic members of the class Chlorobia (Fig. 2.1d, e). Ribosomes are clearly visible (Fig. 2.1d, e) along with a well-defined periplasmic space (Fig. 2.1d, e, f), which is similar to those of other members of the class Chlorobia [139]. Members of the class Chlorobia utilize a combination of pigmented carotenoids and bacteriochlorophylls to harness light energy [140–142]. Spectrophotometric measurements indicate that strain KB01 pigmentation includes a carotenoid (smaller peak at about 450 nm) and bacteriochlorophyll *e* (BChl *e*) with peaks at 468 nm – BChl *e* soret peak – and 652 nm – BChl *e* Q_y peak (Fig. 2.2b; [48]), which manifests as a red-brown coloration, visible in cell suspensions (Fig. 2.2a). Under standard growth conditions (as described below), volume specific pigment concentrations rose to approximately 1060 nmol L^{-1} (equivalent to 750 μg L^{-1}; Fig. 2.4b), which, when compared to corresponding cell counts 2.4, yields an average per cell BChl *e* content of 2.1 $\pm$ 0.5 fmol or 1.5 $\pm$ 0.3 pg. Strain KB01 thus exhibits many of the physical properties, internal features, and overall pigmentation that typify the phototrophic Chlorobia.

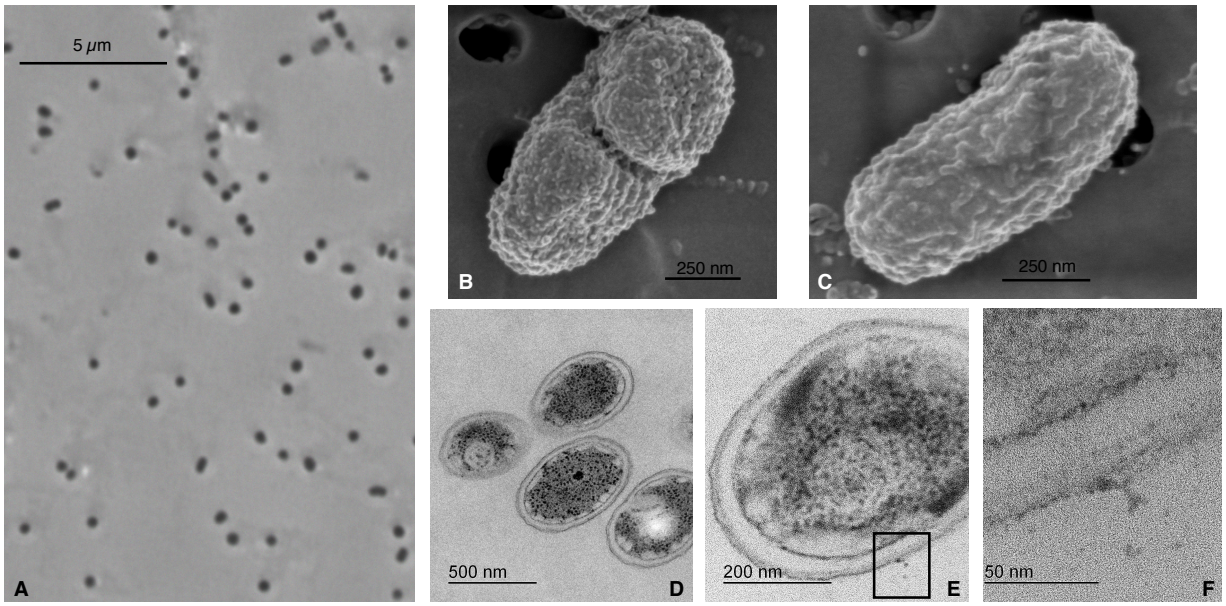

Figure 2.1: *Microscopy images of strain KB01* with optical microscopy (A), SEM (B and C), and TEM (D, E, and F). Note that panel F is a close-up view of the black box in panel E demonstrating a rare instance of Fe(III) particles near the cell wall of strain KB01.

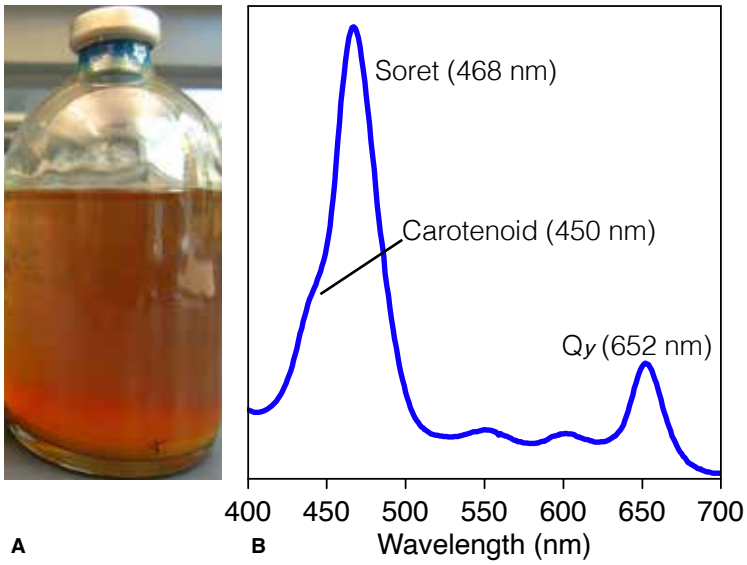

Figure 2.2: *Strain KB01 pigmentation* with a photo of strain KB01 demonstrating its brown/purple pigments (A) and graphical representation of relative abundance of the pigments of *C. phaeoferrooxidans* strain KB01 (B).

2.4.2 Phylogeny and metabolic potential

Strain KB01 is phylogenetically closely related to *Chlorobium ferrooxidans* strain KoFox (grown in co-culture with *Geospirillum* sp. KoFum [53]), but has sufficiently different metabolic potential coded in its genome to define it as a separate species. The whole genome of strain KB01 has been sequenced and deposited in GenBank with the accession number MPJE00000000 [58]. Phylogenetic analyses of the Chlorobia indicate that strain KB01 falls within the *Chlorobium* genus and is most closely related to another Chlorobia photoferrotroph: *Chlorobium ferrooxidans* strain KoFox (Fig. 2.3a). Indeed, the 16S rRNA gene from strain KB01 was 99 % identical to that of strain KoFox. To test whether strain KB01 was sufficiently different from strain KoFox at the genome level to be classified as its own species, the whole genomes of the two organisms were compared in silico. At the nucleotide level, the genome of strain KB01 is 72 % identical to strain KoFox (Fig. 2.3b), while in silico DNA-DNA hybridization [124] conducted between the two strains resolved clear differences between two genomes with only 70-79 % DNA-DNA hybridization, which suggests that the two organisms are different species with a probability of greater than 0.5 (Table 2.1). The GC content difference between the two species was 0.39 %, but the resolution of GC content differences is insufficient to distinguish between two species given that different species often have GC contents that are within 1 % of each other (Table 2.1). Despite strong similarities in phylogenetic marker genes (16S rRNA gene), the genomes of strains KB01 and KoFox are sufficiently different that strain KB01 should be considered its own species.

Table 2.1: Distance metrics using two different formulas between strain KB01 and its closest phylogenetic neighbor, *Chlorobium ferrooxidans* strain KoFox. Note: DDH stands for DNA-DNA hybridization; HSP stands for high-scoring segment pairs.

HSP length/total length			**Identities/HSP length**			**G+C difference**
DDH	Distance	Prob. DDH >= 70%	DDH	Distance	Prob. DDH >= 70%	
64.4 ± 3.8	0.2286	60.86	60.4 ± 2.8	0.0468	52.48	0.39

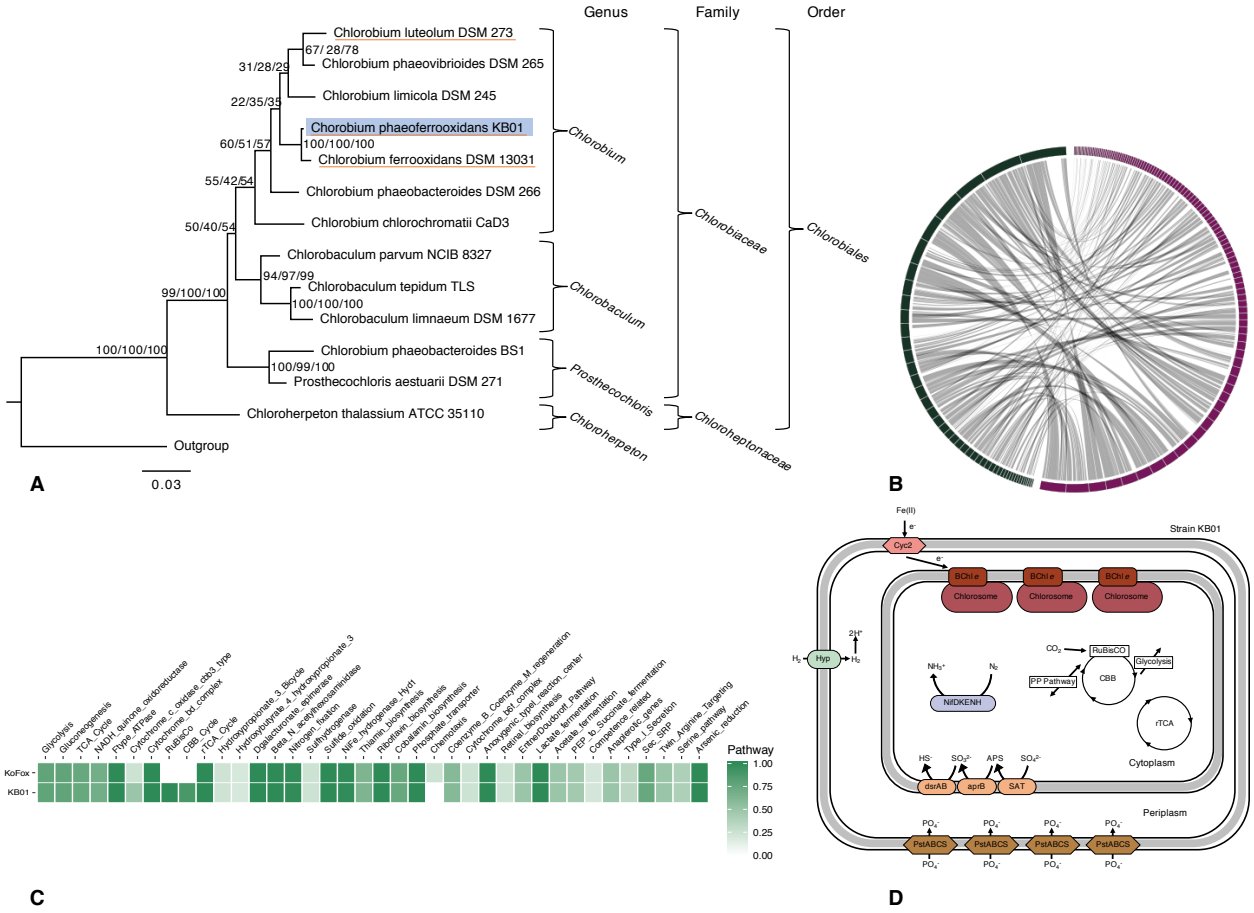

Figure 2.3: *The metabolic potential of strain KB01* with a 16S rRNA gene tree (A) of the class Chlorobia (strain KB01 highlighted in blue) and the photoferrotrophic strains underlined in orange. The tree was computed using three methods — Maximum Likelihood, Maximum Parsimony, and Neighbour Joining and was bootstrapped 500 times for each method with the bootstrap values shown in the above order at each branch. The genome of strain KB01 (purple) compared (B) at the nucleotide level to the genome of *Chlorobium ferrooxidans* strain KoFox (green) where the grey links demonstrates regions that are identical between the two genomes. Strain KoFox and strain KB01 overall pathway comparison (C) where the darker green indicates a more complete pathway (value of 1.00). The major cellular pathways present in strain KB01 (D).

Strain KB01 has much of the same metabolic potential as strain KoFox, but there are some key differences that distinguish the two. To assess such differences in the metabolic potential of both strains, open reading frames (ORFs) for both strains were annotated and compared (Fig. 2.3c). There were several similarities between the two genomes, including the presence of the canonical genes associated with anoxygenic photosynthetic growth in the class Chlorobia (e.g. those for the reverse tricarboxylic acid cycle and electron transport genes such as the inner-membrane bound cytochrome C551). They also shared some genes that are widely distributed across the Chlorobia like those required for nutrient acquisition (e.g. nitrogen fixation) (Fig. 2.3c, d). While the majority of the pathways found in the strain KB01 genome were the same as those found in strain KoFox, strain KB01 also possesses the genes that code for RuBisCo, as well as some of the genes that code for key proteins in the Calvin-Benson-Bassham (CBB) pathway (Fig. 2.3c), which, although more generally known for their role in oxygenic photosynthesis [143], have also been implicated in detoxification pathways in anoxygenic photosynthetic microorganisms [144]. Some of the genes required for these pathways are also found in strain KoFox; however, in strain KoFox the CBB pathway is incomplete and the RuBisCo gene has a nonsense mutation resulting in a premature stop codon and likely an ineffective protein. Like the difference between the two species in the RuBisCo gene, the majority of the variability between the two genomes is due to nucleotide substitutions that do not alter the gene's overall annotation. The two species thus possess similar predicted metabolic potential (Fig. 2.3c) despite a 30 % difference in genomes at the nucleotide level. There are, nevertheless, some differences at the gene and pathway level between the two species that include the number of ORFs attributed to some key pathways. For example, strain KB01 has three more copies of genes associated with phosphate acquisition, such as the gene for the phosphate transport system permease protein (*pstA*) and accessory protein (*phoU*) with four copies found in strain KB01 compared to a single copy of each in strain KoFox. Other differences between the two genomes can be mapped to hypothetical or uncharacterized genes and the number of copies of these genes. Conversely, like strain KoFox, strain KB01 possesses a putative outer-membrane cytochrome ($cyc2_{PV-1}$; Fig. 2.3d) [58] that is homologous to previously identified iron-oxidases in the microaerophilic iron oxidizer *Mariprofundus* strain PV-1 [145]. Combined, these results indicate that strain KB01 is very similar to its relative strain KoFox at the pathway

level, while the differences between the two genomes can mostly be attributed to a combination of single nucleotide substitutions, the number of genes in key pathways (i.e. phosphate uptake), and a number of hypothetical genes.

2.4.3 Electron donor usage, Fe(II) oxidation, and growth

Strain KB01 has very limited capacity to use electron donors other then Fe(II) and electron acceptors apart from CO_2. To determine potential alternative electron donors and acceptors we inoculated strain KB01 into a series of media containing electron donors including glucose, acetate, and hydrogen gas. No photosynthetic growth was detected in any of the media containing organic compounds as the only electron donors. Additionally, no non-photosynthetic growth was detected when organic carbon was added as electron acceptor under both aerobic and anaerobic conditions. While strain KB01 was capable of growth under standard conditions (photoferrotrophically) following exposure to atmospheric oxygen during transfer, no growth was detected under aerobic conditions. This is likely due to abiotic Fe(II) oxidation by oxygen outcompeting the phototrophic growth of strain KB01, although it could also be due to toxicity effects of oxygen on strain KB01 with further experimentation needed to determine if strain KB01 is a strict anaerobe. Notably, despite the presence of key genes for the formation of the hydrogenase complex (i.e. nickel insertion protein HypA) strain KB01 did not grow when hydrogen gas was provided as the sole electron donor for photosynthesis. Collectively these results indicate that strain KB01 grows exclusively through photoautotrophy with Fe(II) as the electron donor and is thus reliant on ferruginous conditions despite the apparent metabolic potential coded in its genome for growth through alternative modes of photosynthesis.

Strain KB01 grew roughly stoichiometrically through Fe(II) oxidation at rates that were dependant on the concentration of Fe(II). During the exponential growth phase (between approximately 70 and 170 hours) under standard conditions — substrate-rich, unfiltered media (see Methods), 10 mM Fe(II), circumneutral pH of 6.8-6.9, room temperature (23 °C), and under light saturation (15 μmol m^{-2} s^{-1}) — strain KB01 oxidized Fe(II) at a rate of 35 $\pm$ 5.3 μM h^{-1} (Fig. 2.4a). Under these same conditions, where 5 mM Fe(II) was oxidized to Fe(III) (oxyhydr)oxides over the course of the full 215 hours, the initial inoculum (1 $\pm$ 0.1 x 10^5 cells mL^{-1}) rose to a final density of 7.2 $\pm$ 1.2 x

10^5 cell mL^{-1} (Fig. 2.4a). During the exponential growth phase, strain KB01 oxidized Fe(II) at a per cell rate of 48 $\pm$ 7 fmol cell^{-1} h^{-1} with specific growth rate of 0.17 $\pm$ 0.002 h^{-1}. Comparing the per cell Fe(II) oxidation rates (in carbon equivalents) to an assumed per cell average carbon content of 1 x 10^{-13} g C, based on the estimate that 50 % of cellular biomass ($\sim$2 x 10^{-13} g [146]) is carbon, results in an $Fe(II)_{oxidized}$ to C_{fixed} ratio in strain KB01 of approximately 6:1. This ratio is close to, and likely within error of, the theoretical and stochiometric value of 4 Fe(II) oxidized per C fixed (Eq. 2.1).

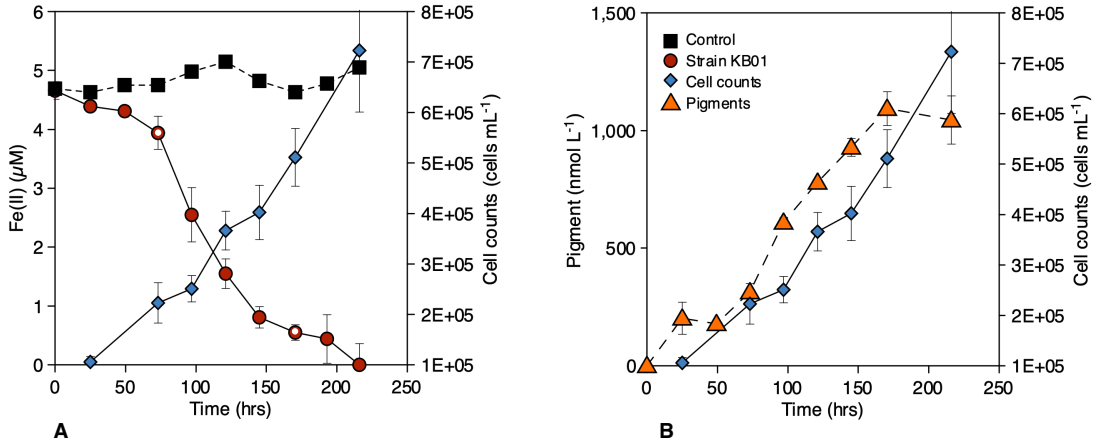

Figure 2.4: *Strain KB01 growth rates* with a growth curve (A) for strain KB01 under optimal growth conditions with Fe(II) oxidation (red circles) compared to a control (black squares) and cell counts (blue diamonds), while pigment concentrations and cell counts for the same growth experiment are shown in (B). The additional circles in (A) delineate the range that was utilized to calculate maximum rates of Fe(II) oxidation.

Fe(II) oxidation by strain KB01 followed first-order reaction kinetics with respect to Fe(II) concentrations and these could be fit with a Michaelis-Menten model (Fig. 2.5a). The change in rates of Fe(II) oxidation as a function of Fe(II) were best fit with a maximum rate (V_{max}) of 43 $\pm$ 7 fmol h^{-1} per cell and a half-saturation constant for Fe(II) (k_m) of 5 $\pm$ 5 μM. To calculate the specific affinity of strain KB01 cells with respect to Fe(II) (Eq. 2.3), the average volume of strain KB01 cells (0.17 μm^3; radius of 0.15 μm and length of 0.6 μm) is combined with an average cell density (1.09 g cm^{-3} [136]) and the number of cells at the end of log phase (7.2 $\pm$ 1.2 x 10^5 cell mL^{-1}) to give a wet cellular biomass of 35 μg L^{-1}. The wet cellular biomass is then combined with the volume specific V_{max} (33 μmol L^{-1} h^{-1}) to give a biomass specific V_{max} of 52 g Fe g^{-1}

wet cell^{-1} h^{-1}. Dividing the biomass specific V_{max} of 52 g Fe g^{-1} wet cell^{-1} h^{-1} by the k_m (5 μM) yields a specific affinity for strain KB01 with respect to Fe(II) of 190,000 L g^{-1} wet cell^{-1} h^{-1}. Rates of photosynthetic Fe(II) oxidation by KB01, and by extension its growth rates, thus depend strongly on Fe(II) concentrations in the low μM range.

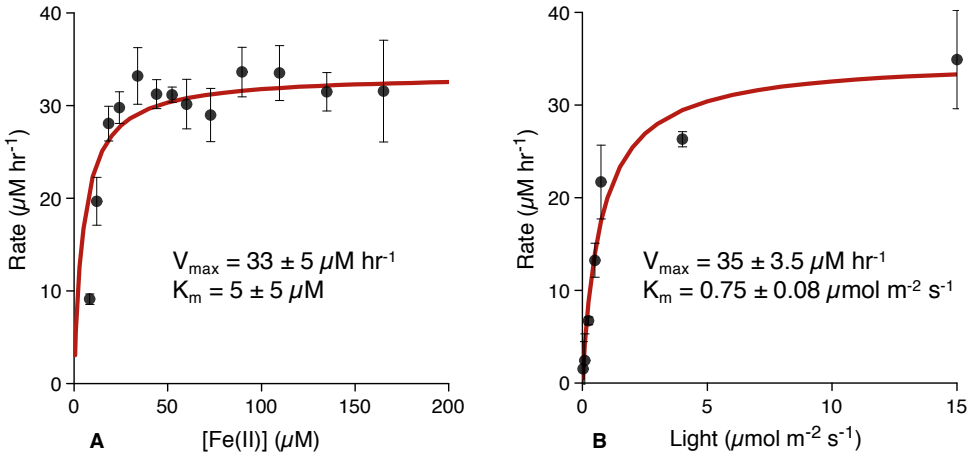

Figure 2.5: *Strain KB01 growth kinetics* with Fe(II) oxidation rates over a range of Fe(II) concentrations (A) and light intensities (B) with the resulting Michaelis-Menten model (red lines) and parameters displayed.

Rates of Fe(II) oxidation and growth by strain KB01 were also dependent on light intensity, pH, and temperature. Strain KB01 was capable of growth at both 15 °C and 30 °C, albeit with slightly longer lag phases and lower growth rates than at 23 °C (Table 2.2). Modelling of the growth rates at these temperatures suggests that strain KB01 is likely capable of growth over a 30 °C temperature range (9 °C to 39 °C – Table 2.2) and although these numbers have yet to be confirmed with empirical data, no growth was detected at 4 °C. Strain KB01 also exhibited similar growth rates (within error) across a pH range of 6 to 7.3 (Table 2.2). Modeling of these growth rates suggests that strain KB01 would be able to grow over a pH range of 4.9 to 8.4 (Table 2.2) with further experiments required to confirm this range. Fe(II) oxidation rates also depended on light availability, which strongly limited Fe(II) oxidation rates below about 2 μmol m^{-2} s^{-1}. The dependence of Fe(II) oxidation rate on light intensity was fit with a Michaelis-Menten model (Fig. 2.5b) where maximal cell specific Fe(II) oxidation rates (49 $\pm$ 5 fmol h^{-1} cell^{-1}) were reached by 5 μmol m^{-2} s^{-1} (light saturation) with a half-light saturation (HLS) value 0.75 $\pm$ 0.08 μmol m^{-2} s^{-1} (Fig. 2.5b). Furthermore, strain KB01 oxidized Fe(II) at light intensities as low as 0.03-0.05 μmol

$m^{-2}\ s^{-1}$ albeit at very slow rates (< 1 μM Fe(II) h^{-1}) (Fig. 2.5b). Rates of Fe(II) oxidation, and again by extension growth, are, thus dependent on pH, temperature and light intensity over a range of environmentally relevant conditions.

Strain KB01 is also capable of growth, albeit at slower growth rates, in the absence of exogenous vitamins, as KB01 possesses the necessary pathways for the biosynthesis of these vitamins. To assess whether strain KB01 could meet its own vitamin requirements, we tested for growth in a series of media prepared with a standard suite of vitamins, but with a single vitamin removed. Growth was possible under all vitamin mixtures, despite the missing vitamins, albeit with longer lag phases and slower growth rates (data not shown). This result is consistent with the complement of vitamin biosynthesis pathways in KB01's genome, such as cobalamin, which is involved in B12 biosynthesis (Fig. 2.3c). Strain KB01 is, therefore, capable of growth when biologically essential vitamins, such as vitamin B12, are scarce or absent, by producing the entire complement of necessary vitamins on its own.

Table 2.2: Strain KB01 bulk growth rates over a range of temperature and pH as well as the predicted range of temperature and pH where strain KB01 should be capable of growth.

Temperature (°C)		15	23	25	30	
Growth rate		23 ± 4	35 ± 1	34 ± 4	30 ± 5	
Predicted temperature range						
Min	Max	R^2				
9 °C	39 °C	0.99				
pH		6	6.4	6.8	7	7.3
Growth rate		33 ± 10	43 ± 12	40 ± 14	40 ± 13	37 ± 11
Predicted pH range						
Min	Max	R^2				
4.9	8.4	0.73				

2.5 Discussion

2.5.1 Characteristic traits of strain KB01

Strain KB01 exhibits genomic traits that differentiate it both from other members of the class Chlorobia and other previously studied photoferrotrophs. Strain KB01, while taxonomically

related to Chlorobium ferrooxidans strain KoFox, 16S rRNA genes are 99 % identical between the two strains (Fig. 2.3a), it only shares 70 % of its genome with strain KoFox (Fig. 2.3b) and can thus be considered a separate species at a probability of greater than 0.5 based on DNA-DNA hybridization (Table 2.1). Some of the genomic differences that distinguish strain KB01's genome from that of its closest relative (Fig. 2.3c), strain KoFox, are the genes associated with the CBB pathway, including the RuBisCo gene, although both are found elsewhere in the class Chlorobia and in anoxygenic phototrophs more broadly [143]. While the RuBisCo gene is most commonly associated with carbon fixation in oxygenic phototrophs, previous studies have suggested that the RuBisCo homologue found in the Chlorobia increases their growth efficiency by reducing oxidative stress [144]. The lack of the RuBisCo gene in otherwise very similar genomes could contribute to the slightly lower per cell Fe(II) oxidation rates seen in strain KoFox compared to strain KB01 (Table 2.3). Given that the lack of the RuBisCo gene in strain KoFox is due to a single nonsense mutation that is not lethal, suggests that the RuBisCo gene is not necessary for photoferrotrophy, at least in benthic strain KoFox. The greater number and extent of redundancy in phosphate transport genes found in strain KB01 (4x greater than in strain KoFox), may reflect its adaptation to low phosphate concentrations in Kabuno Bay [48, 96] and those more generally perceived for modern and ancient ferruginous environments [47, 70, 85, 147]. Additional differences between the two strains include a large number of hypothetical or uncharacterized genes in strain KB01 that do not appear in strain KoFox and further investigation is required to determine their specific functions. Strain KB01 also contains the putative outer membrane cytochrome iron oxidase ($cyc2_{\mathrm{PV-1}}$) that was previous linked to Fe(II) oxidation in microaerophilic Fe(II) oxidizer *Mariprofundus* strain PV-1 [145]. Homologues of the *cyc2* gene have been previously identified in three members of the class Chlorobia, two of which (*C. ferrooxidans* strain KoFox [53] and *C.* sp. N-1 [56]) are capable of photoferrotrophic growth, suggesting its possible role as an outer membrane Fe(II) oxidase. Growth of one of these organisms through photoferrotrophy, *Chlorobium luteolum* DSM 273, however, remains uncertain, and experiments to date [56] suggest it is unlikely. Thus, the role of the *cyc2* may not be specific to Fe(II) oxidation in the Chlorobia. While many of the genes and pathways found in strain KB01's genome are present in other photoferrotrophs and members of the class Chlorobia, the combination and numbers of specific genes, like those involved in

Table 2.3: Physiological information of photoferrotrophic and microaerophilic strains. References: 1) [115]; 2) [55]; 3) [56]; 4) [8]

Organism	Per cell Fe(II) oxidation rate (fmol hr^{-1})	Association to Fe(III) minerals	Enrichment location	Reference
Chlorobium phaeoferrooxidans strain KB01	48 ± 2	No	Kabuno Bay	This work
Chlorobium ferrooxidans strain KoFox	30 ± 1	Yes	Freshwater ditch	1
Rhodobacter ferrooxidans strain SW2	32	Yes	Freshwater pond	2
Chlorobium sp. N-1	0.05 ± 0.001	Yes	Marine sediments	3
Gallionella sp.	1	Yes	Various	4

phosphate acquisition, are characteristic of strain KB01.

Adaptations in strain KB01, such as high concentrations of low-light harnessing pigments may impart ability to grow in low light pelagic environments similar to *Chlorobium phaeobacteroides* strain MN1 and strain BS-1 from the Black Sea [138, 141]. The strain KB01 pigment biosynthesis pathways produce an overlapping carotenoid and bacteriochlorophyll Soret peak that are blue-light shifted compared to those of strain KoFox and many other phototrophs [52, 53, 55, 57, 148]. The blue-light shifted pigments, combined with BChl *e* and its homologues that are found in strain KB01 (Fig. 2.2), are adaptations that promote growth at low light intensities and in deep waters [141]. Indeed, strain KB01 is capable of growth at very low light intensities (0.03-0.05 μmol m^{-2} s^{-1}; Fig. 2.5b) albeit at slow rates (< 1 μM h^{-1}). These low light intensities are comparable to those required for the growth of the community of anoxygenic photosynthetic sulfide oxidizing Chlorobia found in the chemocline of the Black Sea (0.015-0.055 μmol m^{-2} s^{-1}) [138, 149], although the Black Sea Chlorobia are also capable of maintaining biomass under even lower light conditions (< 0.0022 μmol m^{-2} s^{-1}; [138]). The ability of Strain KB01 to grow at low light intensities contributes to its relatively low HLS of 0.75 ± 0.08 μmol m^{-2} s^{-1} (Fig. 2.5b) that is comparable to that of previously characterized photoferrotrophic strain KoFox (0.25 ± 0.12 μmol m^{-2} s^{-1} [55]) and much lower than that of *Chlorobium* sp. N-1 (4.6 μmol m^{-2} s^{-1} [56]). Despite

having a slightly higher HLS than strain KoFox, strain KB01 has a comparable specific affinity for light to strain KoFox ($\sim$1410000 m^2 s g^{-1} wet cells h^{-1} and $\sim$1100000 m^2 s g^{-1} wet cells h^{-1} respectively (Eq. 2.3)), which implies that these two strains have a largely similar capacity to grow under low light conditions. The specific affinities of strains KB01 and KoFox to light likely reflect a more general disposition to growth at low light in the Chlorobia, although there remain few detailed studies of the kinetic relationship between phototrophic growth and light to make rigorous comparisons across the class. Low light adaptation in strain KB01 is also in line with relatively high per cell concentrations of BChl *e* (2.1 $\pm$ 0.5 fmol or 1.5 $\pm$ 0.3 pg), which are higher than the concentration of BChl *e* and *c* measured in Chlorobium limicola (0.05 fmol per cell [150]) and higher than the BChl *a* concentrations measured for aerobic anoxygenic phototrophs in the Chesapeake Bay (0.55 fg per cell [151]). If we consider a range of per cell protein concentrations of 2.8 x 10^{-8} to 3.5 x 10^{-7} μg [47, 152], strain KB01's BChl *e* concentrations (58000 $\pm$ 12000 to 4000 $\pm$ 800 μg mg^{-1} protein) are also orders of magnitude higher than those reported for the Chlorobia strain (BS-1) from the Black Sea [138]. Furthermore, the total BChl *e* concentrations in late-log to early stationary phase strain KB01 cultures (60-800 μg L^{-1}) are similar to those found in Chlorobia dominated chemoclines of meromictic lakes [47, 140]. Adaptations to low light, like high per cell BChl *e* concentrations, may thus be key for the growth of strain KB01 in the chemocline of Kabuno bay, and by extension may allow photoferrotrophic Chlorobia to proliferate in low-light ferruginous chemoclines more generally.

Strain KB01's growth rates under standard conditions are comparable to those of other photoferrotrophic Chlorobia, and higher than those of other Fe(II) oxidizing microorganisms studied to date. At maximum rates of Fe(II) oxidation under standard growth conditions at room temperature (23°C), circumneutral pH (6.8-6.9), and light saturation (15 μmol m^{-2} s^{-1}), strain KB01 oxidized 35 $\pm$ 5.3 μM h^{-1} (Fig. 2.4). These maximum bulk rates are similar to those of other previously characterized photoferrotrophic members of the class Chlorobia such as *Chlorobium* sp. N-1 (32 $\pm$ 0.8 μM h^{-1} [56]) and are faster than those of other chemotrophic Fe(II) oxidizers such as *Gallionella* (1.2 μM h^{-1} [8]). The rate of Fe(II) oxidation decreases with decreasing Fe(II) concentration, following a Michaelis-Menten curve, with a relatively low half-saturation constant (k_m) of 5 $\pm$ 5 μM (Fig. 2.5a) – comparable (within error) to the k_m of anoxygenic sulfide oxidizing

members of the class Chlorobia that have low k_m's compared to other phototrophic sulfide oxidizing microorganisms [153]. Furthermore, strain KB01's low k_m with respect to Fe(II) suggests that the cells have a high affinity for Fe(II). Indeed, strain KB01 has a high specific affinity for Fe(II) of 190,000 L g^{-1} wet cell h^{-1}, which is comparable to microorganisms considered to have extremely high specific affinities for their substrates such as the sulfide oxidizing Gammaproteobacteria of the SUP05/ARTIC96BD lineages that drive cryptic sulfur cycling in oxygen minimum zones [154]. Notably, strain KB01's high specific affinity for Fe(II) is reflected in the per cell phototrophic Fe(II) oxidation rates (48 $\pm$ 7 fmol h^{-1} for strain KB01) that are higher than those of other photoferrotrophic and chemotrophic Fe(II) oxidizing strains (Table 2.3). The high per cell rates of Fe(II) oxidation result in a Fe(II)oxidized to $C_f$ixed ratio of 6:1, which is likely within error of the theoretical and stochiometric ratio of 4:1 (Eq. 2.1). Thus, while many of strain KB01's physiological characteristics are similar to other Chlorobia and strain KoFox in particular, their high cell specific rates of Fe(II) oxidation and resulting high affinity for Fe(II) set strain KB01 apart from other photoferrotrophs studied to date.

Under nutrient limited conditions, strain KB01's per cell Fe(II) oxidation rates are diminished when compared to growth under standard conditions but are still higher than those of other photoferrotrophs and Fe(II) oxidizing microorganisms. For example, when dinitrogen gas is the only available source of nitrogen, strain KB01 has a per cell Fe(II) oxidation rate of 20 $\pm$ 1 fmol h^{-1} [115], which is higher than that of its marine relative *C.* sp. N-1 and fellow photoferrotroph strain SW2 under standard growth conditions (Table 2.3). In addition to growth under nitrogen and sulfate limiting conditions [115], strain KB01 also grew without the addition of exogenous vitamins to its growth medium. This stands in contrast to many modern marine and freshwater microorganisms that do not produce a full complement of vitamins, and instead utilize vitamins that have been excreted by other members of the microbial community (leakage [155]) to support their growth and metabolism [156]. Such metabolic streamlining often confers a competitive advantage at the expense of self-sufficiency. Strain KB01, on the other hand, appears to possess metabolic potential for self-sufficiency both in terms of its ability to acquire nutrients from multiple sources and its capacity to produce a full complement of vitamins. Strain KB01 is also capable of growth at a range of pH (6-7.3; Table 2.2). While this range is comparable to

the range of pH required for the growth of other freshwater photoferrotrophs (5.5-7.5; [55]), strain KB01 has an inferred growth potential over an extended pH range (4.9-8.4; Table 2.2) that, importantly, encompasses the pH range of modern and ancient seawater [56, 157, 158], implying that photoferrotrophy is possible under such conditions.

An important, and distinguishing, trait of strain KB01 is its ability to shed the Fe(III) (oxyhydr)oxides produced as a by-product of its growth [99]. Despite high rates of Fe(II) oxidation and, as a result, Fe(III) precipitation, strain KB01 maintains cell surfaces free of Fe(III) (oxyhydr)oxides (Fig. 2.1). The lack of association allows strain KB01 to remain buoyant in sunlit waters, avoiding sedimentation due to ballasting from associated Fe(III) precipitates [99]. All previously characterized photoferrotrophs have shown some level of association or indeed encrustation by Fe(III) (oxyhydr)oxides, although the degree of association appears to vary depending on the composition of the growth medium (Table 2.3) [9, 63, 99]. Strain KB01 avoids association through the nature of its cell surface functional groups [99], which lead to electrostatic repulsion between the cell surface and Fe(III) (oxyhydr)oxides when these oxyhydroxides carry negative surface charges due to incorporation of anions like silica or phosphate [99]. Such electrostatic repulsion sets pelagic strain KB01 apart from its benthic photoferrotrophic relatives and other benthic photoferrotrophs more generally.

Information on the physiology and metabolic potential of strain KB01 can be further used to predict its rates of growth and metabolism under a range of environmental conditions. Generally, rates of photosynthetic growth are controlled by the availability of electron donor, light and nutrient elements like phosphorus (P) and nitrogen (N). Combining predictive equations that describe the rates of Fe(II) oxidation by strain KB01 as a function of electron donor (Fe(II)), light, and the nutrient P, yields the following:

$$R = V_{\max} \cdot \frac{[Fe]}{k_{\mathrm{mFe}} + [Fe]} \cdot \frac{[light]}{k_{\mathrm{mlight}} + [light]} \cdot \frac{[\mathrm{PO_4^{3-}}]}{k_{\mathrm{mPO_4^{3-}}} + [\mathrm{PO_4^{3-}}]} \tag{2.4}$$

where R is the cell specific rate of Fe(II) oxidation (fmol cell^{-1} h^{-1}), V_{max} is the cell specific Fe(II) oxidation rate (43 $\pm$ 6.6 fmol cell^{-1} h^{-1}), k_{mFe} is the half-saturation constant for Fe(II) (5 $\pm$ 5 μM), k_{mlight} is the HLS constant (0.75 $\pm$ 0.08 μmol m^{-2} s^{-1}), and $k_{mPO_4^{3-}}$ is the half-saturation

constant for phosphate (0.005 μM [96]). This formulation can also be used to calculate growth rates considering the stoichiometry of C_{fixed} to $Fe(II)_{oxidation}$ (0.16:1), which in turn can be used to calculate doubling times based on the amount of carbon content of a cell. Information on the response of photoferrotrophy by strain KB01 to N availability, pH and temperature could, in principle, be considered similarly. In this way, physiological information can be used to model photosynthetic production by strain KB01 across a wide range of environmental conditions and with further information on how the relevant physiology varies across extant and ancestral photoferrotrophs, can be used to reconstruct primary production in the ferruginous oceans of the Precambrian Eons.

2.5.2 Strain KB01 as a model organism for Precambrian PP

Strain KB01 could have deposited the world's largest BIFs with cell numbers that are comparable to those of modern oceanic primary producers, even under nutrient poor conditions. Previous calculations (utilizing the high rates of iron deposition of 1000 m m^{-1} yr^{-1} estimated for the Hammersley group [8, 159, 160]) have estimated that Fe deposition rates of up to 45 mol m^{-2} yr^{-1} were needed to deposit the world's largest BIFs (i.e. Hammersley Basin, Australia). When these Fe deposition rates are combined with the high per cell Fe(II) oxidation rates of strain KB01 (48 $\pm$ 7 fmol h^{-1}), a maximum of 1.1 x 10^3 cells mL^{-1} would be required in the upper 100 m of the Hamersley basin water column (estimated area of 1 x 10^{11} m^2 [8]) to deposit the world's largest known BIF [4]. This number is comparable to previous calculations utilizing the Fe(II) oxidation rates of the environmental community of Chlorobia from Kabuno Bay (1.7 x 10^3 cells mL^{-1} [48]). The modest difference between the two numbers is likely due to differences between the growth rates of a pure culture and those that are part of a larger microbial community. Notably, cell concentration is two orders of magnitude lower than the estimated 5 x 10^5 cells mL^{-1} present in the uppermost 200 m of the modern oceans [146] and is comparable to estimates of the number of primary producing cells per mL in modern near shore and coastal shelf regions (10^3 cells mL^{-1} [161]). Standard laboratory culture media is notoriously nutrient – rich, however, and therefore is unlikely to represent Fe(II) oxidation rates in the nutrient-poor Precambrian oceans. Under nitrogen limiting conditions (dinitrogen as the sole nitrogen source), the per cell iron

oxidation rates for strain KB01 (20 ± 1 fmol h^{-1}) indicate that, under the previously described high iron deposition rates (45 mol m^{-2} yr^{-1} [8]), a maximum of 2.6 x 10^3 cells mL^{-1} would have been required in the upper 100 m of the Hammersley basin water column to deposit the Hammersley BIF [115]. Furthermore, strain KB01 is capable of producing sufficient Fe(III) to have deposited BIFs under low Fe(II) (< 400 μM) and silica-rich (0.6-1.5 mM — comparable to estimated concentrations of silica in the Archean oceans [85]) conditions [99]. Thus, the growth of pelagic strain KB01, under a diverse set of conditions that better mimic those of the Precambrian oceans, supports models for the deposition of BIFs by photoferrotrophs. Additionally, the difference in cell numbers under nutrient rich versus nutrient poor conditions suggests that BIF deposition rates could have scaled with nutrient availability such as biological nitrogen availability.

The genotypic, phenotypic, and ecological information gleaned from *Chlorobium phaeoferrooxidans* strain KB01 suggests that it is a strong analogue of Precambrian photoferrotrophs. Strain KB01 possesses a number of traits, such as a high number of phosphate transport genes or the lack of cell-Fe(III) (oxyhydr)oxide association, that distinguish it from previously characterized photoferrotrophic species that likely promote the proliferation of strain KB01 in low P ferruginous water columns like Kabuno Bay. Furthermore, stain KB01's physical separation from its Fe(III) (oxyhydr)oxide metabolic products allows it to maintain its position within the photic zone of Kabuno Bay's water column. Such traits, combined with characteristics that are ubiquitous throughout the class Chlorobia (i.e. the ability to fix dinitrogen gas under nitrogen limiting conditions), allow strain KB01 to grow efficiently under conditions where nutrients are scarce or limiting. Such nutrient scarcity was likely prevalent under the ferruginous ocean conditions that characterized much of the Precambrian Eons (nitrogen [162], sulfate [27], phosphorus [85]) and thus the ability to acquire biologically scarce essential nutrients would have been key to sustaining appreciable primary production. We argue, therefore, that the physiology and metabolic potential of strain KB01, which underpin its capacity to proliferate in modern ferruginous basins like Kabuno Bay, is broadly extensible to conceptual and quantitative models of PP, coupled carbon and iron cycling, and BIF deposition in the Precambrian Eons. Further support for this claim could come from information that constrains the antiquity of photoferrotrophy in stem group Chlorobia, and the corresponding history of the metabolic potential hosted in strain KB01.

Chapter 3

Nutrient Acquisition and the Metabolic Potential of Photoferrotrophic Chlorobi

3.1 Summary

Anoxygenic photosynthesis evolved prior to oxygenic photosynthesis and harnessed energy from sunlight to support biomass production on the early Earth. Models that consider the availability of electron donors predict that anoxygenic photosynthesis using Fe(II), known as photoferrotrophy, would have supported most global primary production before the proliferation of oxygenic phototrophs at approximately 2.3 billion years ago. These photoferrotrophs have also been implicated in the deposition of banded iron formations, the world's largest sedimentary iron ore deposits that formed mostly in late Archean and early Proterozoic Eons. In this work we present new data and analyses that illuminate the metabolic capacity of photoferrotrophy in the phylum Chlorobi. Our laboratory growth experiments and biochemical analyses demonstrate that photoferrotrophic Chlorobi are capable of assimilatory sulfate reduction and nitrogen fixation under sulfate and nitrogen limiting conditions, respectively. Furthermore, the evolutionary histories of key enzymes in both sulfur (CysH and CysD) and nitrogen fixation (NifDKH) pathways are convoluted; protein phylogenies, however, suggest that early Chlorobi could have had the capacity to assimilate sulfur and fix nitrogen. We argue, then, that the capacity for photoferrotrophic Chlorobi to acquire these key nutrients enabled them to support primary production and underpin global biogeochemical cycles in the Precambrian.

3.2 Introduction

Modern global primary production is supported through oxygenic photosynthesis, which converts sunlight and CO_2 into biomass, fuelling the biosphere and driving fluxes of matter and energy at global scales [163]. Primary production is limited by the availability of nutrients that are essential for growth such as phosphorus, nitrogen, and sulfur [164]. Primary producers thus expend valuable energy to meet their nutrient quotas. In the modern oceans, for example, cyanobacteria can fix nitrogen in the photic zone to support their nitrogen requirements [165]. This in turn provides a competitive advantage that frequently allows nitrogen-fixing cyanobacterial species like *Trichodesmium* to outcompete non-nitrogen fixing species and can lead to cyanobacterial blooms [166, 167]. In addition to their role as primary producers in the modern oceans, cyanobacteria play a key role in the acquisition and redistribution of nutrients [168], driving global biogeochemical cycles since their evolution and proliferation in the Precambrian Eons.

Oxygenic photosynthesis and cyanobacteria emerged early in the Archean Eon [16, 94], evolving from anoxygenic phototrophs [101], which arose as early as 3.8 Ga [169]. Like oxygenic phototrophs, anoxygenic phototrophs fix carbon dioxide into biomass, but instead of water as the electron donor they use a diverse set of inorganic species [e.g., H_2, H_2S, and Fe(II)] to replace electrons transferred from the photosystem to CO_2 [93]. Most anoxygenic phototrophs that grow in illuminated anoxic waters today use reduced sulfur species as their electron donors. During much of Earth's early history, however, reduced sulfur species were likely scarce and the chemistry of marine sediments suggests that the oceans were overwhelmingly iron-rich (ferruginous) for long stretches of both the Archean and Proterozoic Eons [5, 170, 171]. Under these ferruginous conditions, ferrous iron would have been the most abundant and available inorganic electron donor [1]. Models for primary production in these ferruginous oceans suggest that anoxygenic phototrophs using Fe(II) as their electron donor–photoferrotrophs–could have supported up to 10% of modern day primary production before the proliferation of cyanobacteria [1, 85]. Together, the evolutionary history of the photosystem and current knowledge on the history of ocean redox states imply that photoferrotrophs could have played a key role in driving global fluxes of matter and energy throughout the Precambrian Eons.

Compelling, but indirect, evidence for photoferrotrophy during Archean and Paleoproterozoic times comes from the deposition of banded iron formations (BIFs) [7, 8, 21]. BIFs are massive iron ore deposits that were mostly deposited toward the end of the Neoarchean, though their deposition spans from the Eoarchean through to the Neoproterozoic Eras [4]. Classical models for the deposition of iron from seawater to form BIF invoke large-scale oxidation of seawater Fe(II) by oxygen produced as a by-product of cyanobacterial growth and the subsequent precipitation and sedimentation of ferric iron minerals [6, 7, 172]. Oxygen levels through the Archean, however, appear too low to support oxidation of Fe(II) at rates sufficient to sustain the rapid ferric Fe deposition needed to form even some of the apparently small BIFs like the Isua Greenstone belt in Greenland [169]. Instead, Fe(III) could have come from abiotic photochemical iron oxidation through UV photolysis [7, 173], but this also appears too slow to support ferric iron deposition at rates recorded in BIFs [40]. Alternatively, direct photosynthetic iron oxidation through photoferrotrophy could supply ferric Fe to form BIFs [8, 20]. Accepting that oxygen levels were too low to drive Fe(II) oxidation and that UV photolysis appears similarly ineffective, photoferrotrophy may be the only viable mechanism to support appreciable ferric iron deposition and BIF formation. Nevertheless, the role of photoferrotrophs in BIF deposition remains controversial since direct evidence, like lipid biomarkers in BIFs, to diagnose photoferrotrophy, remain elusive. Extant cultures of photoferrotrophic bacteria are thus employed in efforts to further test the possible role of photoferrotrophs in BIF deposition and to identify signals that might be used to diagnose photoferrotrophy in the rock record.

A total of eight enrichments and isolates of photoferrotrophic bacteria have been brought into laboratory collections over the last 30 years. These cultures were largely obtained from a variety of benthic environments, such as marine mud flats and freshwater sediments [20, 51–54], with a single isolate originating from a ferruginous water column [48]. Laboratory cultures of photoferrotrophs are distributed across the Alphaproteobacteria, the Gammaproteobacteria, and the Chlorobi and experiments conducted with these cultures reveal diverse physiological traits that translate to differential growth rates across a wide range of culture conditions [9, 55, 62]. Notably, under modest light availability, many of these cultures grow sufficiently fast to oxidize Fe(II) at rates that would support the deposition of some of the largest BIFs [8, 21]. This gives confidence

in the capacity of photoferrotrophs to deposit BIFs, but laboratory culturing media are notoriously nutrient rich. Natural settings, on the other hand, are typically nutrient poor in comparison [174], and thus the role of photoferrotrophs in both BIF deposition and primary production would have depended on their capacity to grow and acquire nutrients from Precambrian seawater at concentrations almost certainly much lower than typical culture media.

Many laboratory experiments have been conducted with photoferrotrophs from the Alphaproteobacteria and Gammaproteobacteria [9, 55, 62, 175, 176], but the ecological relevance of these groups in natural ferruginous settings is uncertain. In all modern ferruginous environments supporting photoferrotrophy, members of the Chlorobi appear to dominate [47, 48, 67]. Furthermore, most or many extant photosynthetic communities dominated by anoxygenic phototrophs are comprised mostly of Chlorobi [177]. While anoxygenic photosynthesis by the Proteobacteria likely evolved early [101], more recent phylogenomic analyses imply that the original phototrophs belonged to the Chlorobi [142, 178, 179]. The reason for the apparent prevalence of the Chlorobi in modern environments is uncertain, but it is likely related to their ability to grow under environmentally relevant conditions including low nutrient availability and low light [64–66, 138, 180, 181]. Thus, despite the fact that photoferrotrophy by Proteobacteria may be relevant to Precambrian ecosystems, here, we focus our analyses on the Chlorobi because of their apparent ecological prominence in many modern systems and their deeper ancestry compared to phototrophic Proteobacteria.

Both phosphorus and nitrogen often limit photosynthetic activities and primary production in the modern oceans and in freshwater environments [164]. Phosphorus is generally considered the ultimate limiting nutrient on geological time scales as nitrogen can be fixed from the atmosphere when phosphorus is available [182]. Phosphorus is essential for life and is required in phospholipid, nucleic acid, and adenosine tri-phosphate (ATP) biosynthesis. Phosphorus throughout the Precambrian Eons was scarce with seawater concentrations orders of magnitude lower than today [85]. This phosphorus scarcity would have led to low primary production, influencing the ecology and elemental stoichiometry of the photosynthetic primary producers [147]. While phosphorus scarcity likely played an outsized role in shaping the Precambrian biosphere, nitrogen scarcity may have developed locally and transiently throughout the Precambrian Eons [73, 183].

Nitrogen is required to build essential cellular components such as DNA and amino acids. Biologically available nitrogen is supplied to the oceans through rock weathering and volcanism, but ammonium uptake and ultimate burial, however, would have eventually depleted the oceanic bioavailable nitrogen reservoir [184]. In the modern ocean, biological fixation of atmospheric nitrogen keeps pace with phosphate supplies over geologic time scales [185]. Nitrogen fixation is one of the most energetically expensive processes in the metabolic repertoire of life and yet it is distributed across distantly related groups of microorganisms [186, 187]. This underscores the importance of nitrogen fixation to microbial growth and production, is consistent with the early evolution and radiation of nitrogen fixation [32, 188, 189], and exemplifies how the distribution of core metabolic machinery across diverse lineages and functional guilds ensures survival of essential biogeochemical functions over geologic time [3]. While the genomic potential for nitrogen fixation exists within the Chlorobi [142], the capacity of photoferrotrophic Chlorobi to conduct nitrogen fixation and thus support Precambrian marine nitrogen quotas remains untested and unsubstantiated. This leaves our knowledge of the possible ecological role that photoferrotrophs may have played in the acquisition and redistribution of nitrogen and its attendant biogeochemical cycling in the Precambrian oceans entirely unknown.

In addition to phosphorus and nitrogen, sulfur is also essential for life and can limit biological production and growth when scarce [190]. Sulfur on the modern Earth is abundantly available as the fully oxidized sulfate ion due to high concentrations of oxygen in the atmosphere and oceans, which promotes oxidative sulfur weathering and the recycling of sulfur from anoxic marine sediments. During the Precambrian Eons, however, marine sulfate concentrations were much lower [27, 191] likely due to limited oxidative weathering and recycling under low O_2 atmospheres [27, 191–193]. Instead, sulfur was likely scarce and biologically available as low concentrations of sulfate, very low concentrations of sulfide, and possibly organic sulfur [27]. Assimilatory sulfate reduction (ASR), therefore, would have been a key nutrient acquisition pathway, supporting primary production under low sulfur conditions. The genomic potential for ASR has been detected within two members the Chlorobi (*Chlorobium ferrooxidans* and *Chlorobium luteolum* [194]), yet the role of ASR in photoferrotrophic growth remains uncertain. Photosynthetic growth of *C. ferrooxidans* on ferrous iron and without reduced sulfur compounds implies that the

genomic potential for ASR translates into physiological capacity to convert sulfate into biomass sulfur [53]. Given the likely low sulfate and extremely low sulfide concentrations perceived for the Precambrian oceans, ASR may have been absolutely critical for photoferrotrophs to operate as primary producers and contribute to a reservoir of biologically available reduced sulfur compounds in the ocean. The evolutionary history of ASR in the photoferrotrophic Chlorobi has not been explored, nor has sulfate uptake been quantitatively assessed. The role of photoferrotrophs in driving sulfur cycling during the Precambrian remains underappreciated and untested creating another gap in our knowledge of nutrient acquisition and redistribution in the Precambrian oceans.

To address the response of photoferrotrophy to nitrogen and sulfur scarcity, and to create new knowledge relevant to nitrogen and sulfur acquisition and redistribution in the Precambrian oceans, we examined two extant demonstrably photoferrotrophic Chlorobi: benthic *C. ferrooxidans* (grown in co-culture with *Geospirillum* sp. KoFum) [53], and pelagic *Chlorobium phaeoferrooxidans* [48, 58]. We also examined putative benthic photoferrotroph *C. luteolum*, postulated to grow through photoferrotrophy because of its genomic potential for ASR [194]. We verified the capacity of photoferrotrophic Chlorobi to fix inorganic nitrogen and sulfur, and constrained the antiquity of this capacity in the Chlorobi through phylogenetic analyses.

3.3 Materials and methods

3.3.1 Strains and growth medium

Media was prepared after Hegler et. al., 2008 [55], and allocated into serum bottles (100 mL media, 160 mL total volume), with 0.3 g L^{-1} NH_4Cl, 0.5 g L^{-1} $MgSO_4{\cdot}7H_2O$, 0.1 g L^{-1} $CaCl_2{\cdot}2H_2O$, 0.6 g L^{-1} KH_2PO_4. After autoclaving, 22 mmol L^{-1} bicarbonate, trace elements, mixed vitamin solution, selenate-tungstate, vitamin B12, and $FeCl_2$ were added and the pH was adjusted to 6.8-6.9 under an N_2/CO_2 atmosphere (80:20). 10 mmol L-1 $FeCl_2$ was added to all media (regular, NH_4^+ deplete, and SO_4^- poor) — Fe(II) concentrations from 200 μmol L^{-1} to 10 mmol L^{-1} have been shown to produce the same growth rates under nutrient rich conditions. The 10 mmol L^{-1} media was filtered after being made to remove any precipitates, which resulted in a final Fe(II) concentration

of 2 mmol L^{-1} for the standard media and 4 mmol L^{-1} for the NH_4^+ deplete media. The low SO_4^- media was left unfiltered with an Fe(II) concentration of 10 mmol L^{-1}. In the ammonium free media, NH_4Cl was replaced with 0.3 g L^{-1} KCl and an additional 10 mL of N_2 gas was injected into the headspace. In the low sulfate media, 0.0025 g L^{-1} $MgSO_4$ and 0.4 g L^{-1} $MgCl_2$ were added instead of the usual 0.5 g L^{-1} $MgSO_4$. Furthermore, approximately 10 kBq of carrier –free ^{35}S was added to all of the low sulfate cultures. The cultures for the N-fixation experiments were grown in ammonium free conditions once and then transferred into the final experimental bottles. The culture for the ^{35}S experiment was grown up in standard media, spun down and decanted to avoid adding extra sulfate, before the cells were inoculated into the final experimental bottles. All cultures were grown under a constant light intensity of 14 μmol m^{-2} s^{-1}.

3.3.2 Analytical techniques

Spectrophotometric analysis of Fe(II) and Fe(III) concentrations were performed using the ferrozine method; samples were measured directly as well as after being fixed in 1 N HCl — after Voillier et. al., 2000 [133]. Pigments were measured spectrophotometrically after 24 hour extractions of 1 mL of pelleted cells in acetone:methanol (7:2 v/v) [134]. Cells numbers were then obtained using a pigment to cell count conversion factor of 6.3 x 10^{-10} pigment $cell^{-1}$ mL^{-1} for *C. phaeoferrooxidans* and 5.8 x 10^{-10} pigment $cell^{-1}$ mL^{-1} for *C. ferrooxidans*. The cells from the ^{35}S experiment were collected via filtration along with a liquid sample as a background measurement. The filtered samples were subsequently washed with 5 % Trichloroacetic acid (TCA) in order to kill, wash, and dissolve cellular material. TCA precipitates DNA and proteins, leaving only these cellular components on the filter and therefore any counts associated with the filtered samples would indicate ^{35}S that had been incorporated into this cellular biomass [195]. 5 mL of scintillation fluid were added to the ^{35}S samples (1 mL of liquid or the filter) and all samples were counted using a scintillation counter.

3.3.3 Bioinformatics

Genomes of Chlorobia stains used in this paper were retrieved from NCBI under the following accession numbers with the completion percentage of each genome in brackets after the number:

NC_008639.1 (99.45 %), NZ_AASE00000000.1 (90.71 %), NC_007514.1 (97.8 %), NC_009337.1 (98.91 %), NC_010803.1 (99.98 %), NC_002932.3 (97.8 %), NC_011027.1 (98.89 %), NC_007512.1(98.91 %). Genomes were analyzed using MetaPathways V2.5.1, an open source pipeline for predicting reactions and pathways using default settings [196, 197] (https://github. com/hallamlab/metapathways2/wiki) and using the following databases: MetaCyc-v4-11-07-03 [198], Kyoto Encyclopedia of Genes and Genomes (KEGG-11-06-18) [127], SEED-14-01-30 (http://www.theseed.org/), Clusters of Orthologous Groups (COG-13-12-27) [199], Carbohydrate-Active enZYmes (CAZY-14-09-04) [200], and RefSeq-nr-14-01-18 [201] databases. Initially, we identified all sequences with a functional assignment affiliated with nitrogen fixation and assimilatory sulfur reduction using the MetaPathways functional annotation table output.

3.3.4 Phylogenetic trees for nitrogen fixation

Individual NifDKH gene sequences from all organisms outside of the phylum Chlorobia were retrieved from NCBI searches from described strains, concatenated, and then aligned using the package software ClustalX2.1 [119]. To rigorously test the evolutionary history of nitrogen fixation multiple tree construction methods (Maximum likelihood (ML) and Maximum parsimony (MP)) were employed. ML and MP trees were constructed in MEGA version 7 [120, 121] and all trees bootstrapped 500 times. Bootstrap values are indicated at the nodes.

3.3.5 Phylogenetic trees for assimilatory sulfate reduction

CysH and CysD/Sat gene sequences from all organisms outside of the phylum Chlorobia were retrieved from NCBI searches from described strains, using the package software ClustalX2.1 [119]. To rigorously test the evolutionary history of ASR multiple tree construction methods (Maximum likelihood (ML) and Maximum parsimony (MP)) were employed. ML and MP trees were constructed in MEGA version 7 [120, 121] and bootstrapped 500 times. Bootstrap values are indicated at the nodes.

3.3.6 Phylogenetic trees for 16S rRNA

16S rRNA sequences were retrieved from strains used in Nif and ASR gene trees from the Silva online database – version 128 [117, 118]. Only full-length ($>$ 1400 bp) sequences were selected, and then aligned using the package software ClustalX2.1 [119]. To rigorously test the evolutionary history of nitrogen fixation and ASR multiple tree construction methods (Maximum likelihood (ML) and Maximum parsimony (MP)) were employed. ML and MP trees were constructed in MEGA version 7 [120, 121] and all trees bootstrapped 500 times. Bootstrap values are indicated at the nodes.

3.4 Results and discussion

3.4.1 Nitrogen fixation

The process of fixing dinitrogen is kinetically challenging and energetically expensive as it involves overcoming the activation energy required in breaking the triple bond between the two nitrogen molecules. The enzyme necessary for nitrogen fixation, nitrogenase, is a multi-subunit protein that is assembled and regulated by a series of other related proteins. All nitrogenases require a metal ion cofactor – molybdenum, iron, or vanadium – with each cofactor being recruited and incorporated into the nitrogenase by a different set of proteins, Nif, Anf, and Vnf, respectively. Current studies indicate that the majority of nitrogenases depend on the molybdenum ion cofactor for their enzymatic activity (reviewed in Rubio and Ludden, 2008 [202]), while the iron and vanadium dependant nitrogenases may play a role in molybdenum limiting environments [203]. Phylogenetic evidence suggests that the molybdenum-dependant version of the enzyme evolved first [204], which is further supported by the observation that organisms identified as having an iron or vanadium dependant nitrogenase all contain a copy of the molybdenum-dependant nitrogenase [187, 205]. There are up to 25 proteins, depending on the species, required to assemble and regulate the nitrogenase including three conserved structural proteins: NifD, NifK, and NifH. NifH is often used as the marker gene for nitrogen fixation in natural environments, due to its role in the main enzyme structure and in cofactor recruitment. Further phylogenetic information,

however, can be obtained when all three structural proteins (NifDKH) are concatenated due to increased sequence information and the conserved nature of all three proteins. Here we explored these key structural proteins to test for the metabolic potential for nitrogen fixation in the photoferrotrophic Chlorobi. We compare nitrogen fixation in photoferrotrophic Chlorobi to the other members of the phylum Chlorobi and to representatives from all phyla capable of nitrogen fixation to assess the evolutionary history of nitrogenase in relevant to photoferrotrophy in the Chlorobi and to place constraints on the possible role of photoferrotrophs in supplying fixed nitrogen to the Precambrian oceans.

Distribution of nitrogen fixation pathways within Chlorobi

Previous analyses of Chlorobi genomes identified that the metabolic capacity for nitrogen fixation is distributed across the phylum with the exception of the *Ignavibacterium* sp. [142, 206, 207]. *Ignavibacterium* sp. is the deepest branching member of the Chlorobi and the only class of non-photosynthetic organisms in the phylum. Here we show that genes coding for the proteins required for nitrogen fixation are present in the genomes of the photoferrotrophic Chlorobi, *C. ferrooxidans* and *C. phaeoferrooxidans*, putative photoferrotroph *C. luteolum* (Fig. 3.1), and in genomes of all other members of the Chlorobi (data not shown). Specifically, we identified one homolog of each of the molybdenum-dependant nitrogenase proteins in all three photoferrotrophic Chlorobi. No homologs of the alternative vanadium or iron-only nitrogenase proteins were detected (PSI-Blast, expect threshold 10). These results indicate that the photoferrotrophic Chlorobi have the genomic capacity to fix nitrogen. Furthermore, nitrogen fixation is wide spread among the Chlorobi, with all available Chlorobi genome sequences coding the necessary proteins apart from *Ignavibacterium album*.

Biochemical verification of nitrogen fixation

To test for the biochemical capacity to fix nitrogen during photosynthetic growth on Fe(II), nitrogen free (below limit of detection ammonium, ammonia, nitrate, or nitrite) media was inoculated with *C. phaeoferrooxidans* or *C. ferrooxidans*. Both species were also grown in the standard growth medium containing 5.6 mM ammonium [55], for comparison. Both species were able to fix

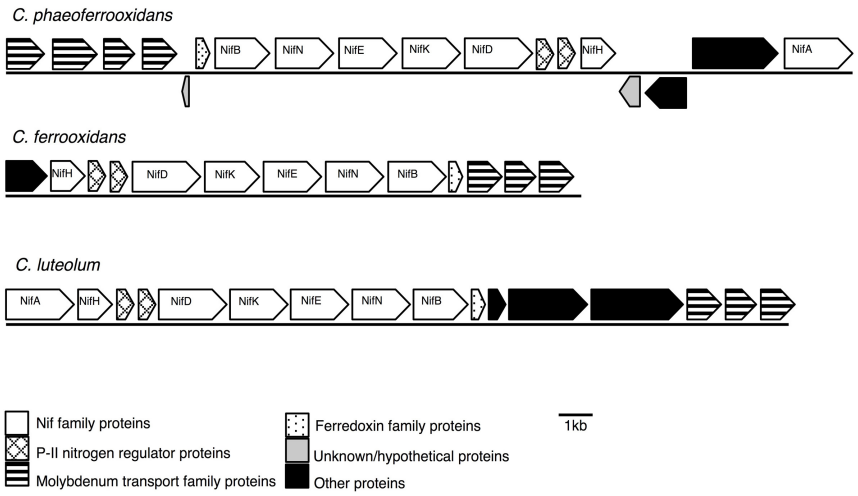

Figure 3.1: *Nitrogenase gene cassettes of the photoferrotrophic Chlorobi*, detailing the position of each gene and the differences and similarities between the gene cassettes.

nitrogen while growing through photosynthetic Fe(II) oxidation with doubling times of 45 and 36 hours for *C. phaeoferrooxidans* and *C. ferrooxidans*, respectively (Fig. 3.2). Fe(II) oxidation rates, during exponential growth phase, were 4.8 $\pm$ 0.33 μM h^{-1} (*C. phaeoferrooxidans*) and 16 $\pm$ 0.56 μM h^{-1} (*C. ferrooxidans*) (Fig. 3.2). Growth under ammonium-rich conditions supported shorter doubling times (15 and 27 hours) and higher rates of Fe(II) oxidation (50 $\pm$ 2.4 μM h^{-1} and 23 $\pm$ 0.7 μM h^{-1}) for *C. phaeoferrooxidans* and *C. ferrooxidans*, respectively (Fig. 3.2). These results indicate that both pelagic *C. phaeoferrooxidans* and benthic *C. ferrooxidans* are capable of using dinitrogen gas as their sole source of nitrogen during growth, but that the need to fix N decreases growth rates.

To further explore the metabolic capacity of photoferrotrophic Chlorobi under both sets of conditions, cell specific Fe(II) oxidation rates were calculated for each species. *C. phaeoferrooxidans* oxidized Fe(II) at 21.2 $\pm$ 1.4 fmol cell^{-1} while fixing nitrogen and 47.8 $\pm$ 2.3 fmol cell^{-1} under ammonium-rich conditions. Conversely, *C. ferrooxidans* oxidized Fe(II) at 30.0 $\pm$ 0.9 fmol cell^{-1} and 29.4 $\pm$ 1.0 fmol cell^{-1} in ammonium free and ammonium-rich media, respectively, with no appreciable difference during N-fixation. The apparent insensitivity of *C. ferrooxidans* to N-availability may be related to the presence of its co-culture partner, *Geospirillum* sp. KoFum. Further experiments with KoFum could help constrain its possible role in N metabolism within

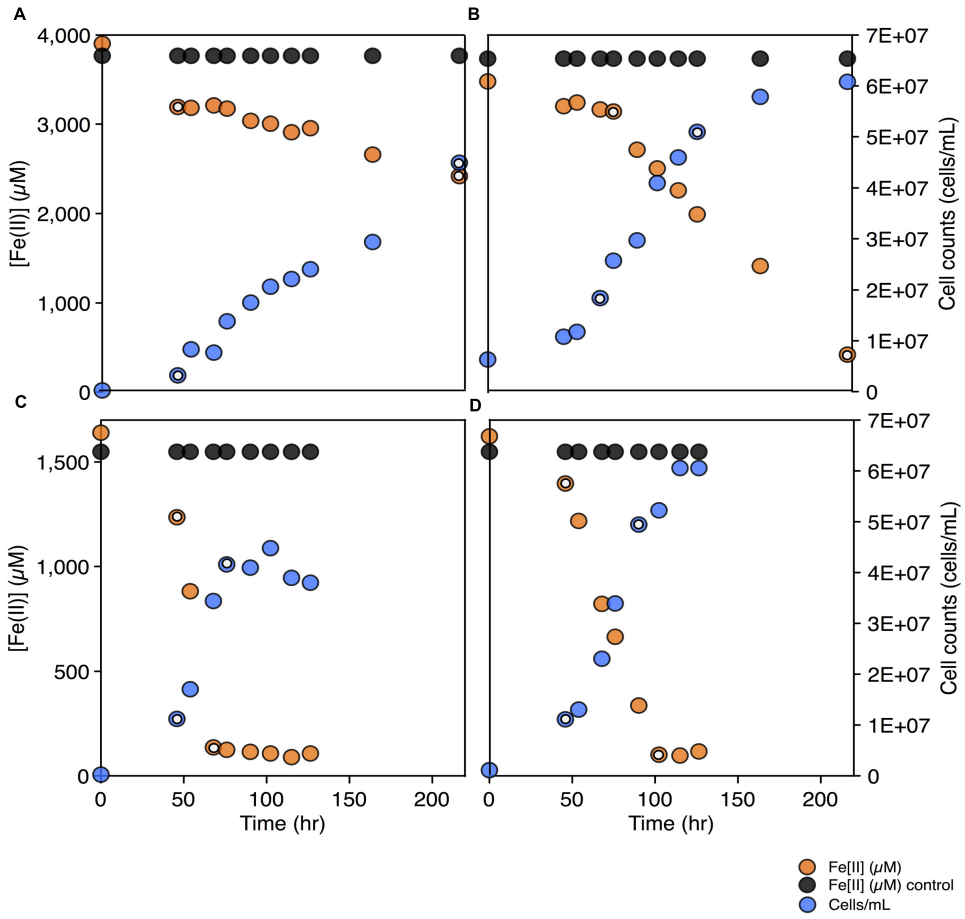

Figure 3.2: *Biochemical verification of Nitrogen fixation* with Fe(II) concentrations and cell counts over time for both *C. phaeoferrooxidans* (A,C) and *C. ferrooxidans* (B,D) under two sets of media: no bioavailable nitrogen – N2 as sole nitrogen source (A,B) and ammonium rich (C,D). Data points used to calculate growth rates and Fe(II) oxidation rates are highlighted in each panel.

the co-culture The observation that *C. phaeoferrooxidans* has lower cell specific growth rates under N scarcity, however, implies lower growth yields during N fixation. Both species are ultimately capable of growth and Fe(II) oxidation while fixing nitrogen but the differential response of cell specific iron oxidation rates to N-scarcity implies that nutrient availability can influence the ecology of photoferrotrophs in the environment.

Evolutionary history of nitrogen fixation in the Chlorobi

To assess the evolutionary history of nitrogen fixation in the Chlorobi we tested for horizontal gene transfer (HGT) within the photoferrotrophic Chlorobi and conducted phylogenetic analyses of Nif

proteins, which we compared to small subunit 16S ribosomal RNA (SSU rRNA) genes. Deviations in the branching orders between these phylogenies would indicate nonvertical inheritance and HGT. To test for horizontal transfer of Nif genes in the photoferrotrophic Chlorobi, we looked for characteristic signatures of HGT within *nif* gene cassettes. Codon adaptation index (CAI) values, a metric used to describe differences in codon usage between specific genes and the genomic background, were calculated for all individual *nif* genes belonging to *C. ferrooxidans*, *C. phaeoferrooxidans*, and *C. luteolum*. All CAI values were greater than the threshold value, 0.70, below which HGT is indicated (Table 3.1). In addition, GC contents of *nif* genes were very similar to GC contents of genomic backgrounds providing no evidence for HGT (Table 3.1). Our analyses also failed to identify tRNAs, transposases, or other genetic elements commonly associated with gene mobility in close proximity (within 5000 bp) to the nitrogenase gene cassette in any of the photoferrotrophic Chlorobi. The general lack of tRNAs or transposases near the *nif* cassettes in the photoferrotrophic Chlorobi, combined with super threshold CAI values and *nif* gene GC contents that are homogenous against genomic backgrounds, imply *nif* gene acquisition through vertical decent.

Table 3.1: Codon adaptation index (CAI) for Chlorobi nitrogenases. Gene length (bp), codon adaptation index (CAI), and GC content (%) for each of the genes in the nitrogenase cassette.

Gene	*C. phaeoferrooxidans*			*C. ferrooxidans*			*C. luteolum*		
	Length (bp)	CAI	GC content (%)	Length (bp)	CAI	GC content (%)	Length (bp)	CAI	GC content (%)
NifB	1275	0.80	52.63	1275	0.76	53.18	1263	0.75	60.89
NifN	1353	0.79	53.22	1350	0.75	53.48	1353	0.74	59.42
NifE	1362	0.79	50.07	1362	0.75	49.63	1362	0.74	57.34
NifK	1383	0.81	53.51	1383	0.73	52.78	1380	0.76	60.14
NifD	1635	0.79	49.54	1635	0.76	49.66	1641	0.77	57.22
PII regulator	378	0.81	50.00	378	0.72	50.00	378	0.72	59.26
PII regulator	357	0.76	49.30	357	0.73	48.74	357	0.70	56.30
NifH	825	0.83	49.58	825	0.79	49.21	825	0.81	59.03

Each parameter was calculated for all three photoferrotrophic Chlorobi, whose whole genome GC contents are: 49.72% for Chlorobium phaeoferrooxidans, 49.9% for C. ferrooxidans, and 58.1% for C. luteolum.

To test the evolutionary history of the *nif* genes in the Chlorobi, we conducted phylogenetic analyses of concatenated NifDKH proteins of all cultured and sequenced Chlorobi that have the genomic potential to fix dinitrogen. The Chlorobi sequences were aligned with selected sequences from the next closest phylum – Bacteroidetes – and the tree was rooted using four

Cyanobacterial species as an out-group (Fig. 3.3). The genus *Chlorobium*, which includes all three photoferrotrophic Chlorobi, the genus *Chlorobaculum*, and the genus *Prosthecochloris* all form monophyletic groups that are collectively part of the phylum Chlorobi clade. Likewise, the Bacteroidetes form a monophyletic group and share a common ancestor with the members of the phylum Chlorobi. Furthermore, when the NifDKH tree is compared to a 16S rRNA tree of the same organisms (Fig. 3.3), all of the genera within the phylum Chlorobi branch in an identical order to those in the 16S rRNA phylogeny. The phylogenetic relationship between the Chlorobi and Bacteroidetes is the same for both NifDKH and 16S rRNA sequences, indicating that the common ancestor to the phyla Chlorobi and Bacteroidetes likely contained a nitrogenase and therefore the ability to fix dinitrogen. *Ignavibacterium* sp., the sole members of the phylum Chlorobi who do not posses a nitrogenase, likely lost the capability to fix nitrogen as the remainder of the Chlorobi and the phylum Bacteroidetes bracket the phylogenetic position of the *Ignavibacterium* sp. Taken together, available data imply vertical decent.

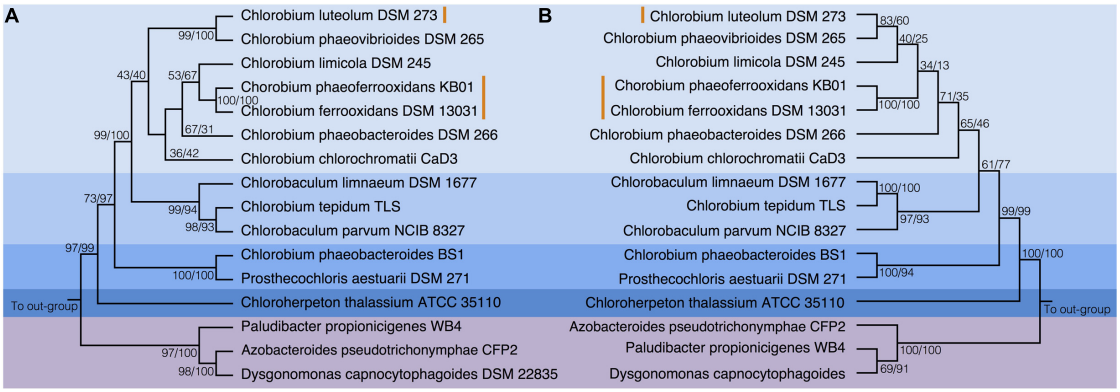

Figure 3.3: *Nitrogenase phylogenies of the Chlorobi and Bacteroidetes.* Phylogenies of the Chlorobi and Bacteroidetes using (A) the concatenated NifDKH proteins and (B) 16S rRNA with bootstrap values shown at each node (maximum likelihood/maximum parsimony). The blue colors delineate the organisms of the Phylum Chlorobi, with each shade representing a different genus, while the purple color delineates the Phylum Bacteroidetes. The orange lines indicate the position of the photoferrotrophic Chlorobi. The trees were rooted with four cyanobacterial organisms. Note: *Azobacteroides pseudotrichonymphae* CFP2 is abbreviated from Candidatus *Azobacteroides pseudotrichonymphae genomovar* CFP2.

Accepting largely vertical descent of NifDKH from the common ancestor of the Chlorobi and Bacteroidetes, NifDKH must have emerged within this line of descent before the divergence of the Chlorobi and Bacteroidetes. The timing of this divergence has been estimated using a whole

genome molecular clock [208] to between 3 and 1.6 Ga, which implies the capacity to fix N in the ancestors of the Chlorobi before this time. Independent N isotope data from metasedimentary kerogen implies N fixation by at least 3.2 Ga [32]. Combined, the evidence for vertical inheritance of NifDKH in the Chlorobi on the taxonomic levels of genus and phylum, the timing of divergence between the Chlorobi and the Bacteroidetes, and the N isotope record, imply that ancestors of modern Chlorobi likely had capacity to fix nitrogen in the iron-rich oceans of the paleoproterozoic and perhaps as early as the mesoarchean eras.

To place N fixation in the Chlorobi, and Bacteroidetes, within the broader context of nitrogenase evolution in general, we conducted further phylogenetic analyses using a greater diversity of organisms. We analyzed the NifDKH phylogeny using two to four representatives from every phylum that had a cultured and sequenced species with previously documented genomic potential for nitrogen fixation (Fig. 3.4). This phylogeny places the Nif proteins found in the Chlorobi and Bacteroidetes in a single clade, supporting their emergence from a common ancestor and the vertical inheritance of NifDKH from this ancestor. The phylogeny of the NifDKH protein is, however, incongruent with that of the 16S rRNA gene from the same organisms (Fig. 3.4). While the Chlorobi and Bacteroidetes group together in both phylogenies, the Spirochetes, Chloroflexi, and Firmicutes also group with the Chlorobi in the NifDKH phylogeny, but belong to distinct clades in the 16S rRNA gene phylogeny. The differences between these phylogenies confound further constraints on the evolutionary history of nitrogenase within the Chlorobi based on phylogeny and add to the overwhelming evidence for horizontal transfer of NifDKH genes [3, 187, 209].

Ecology of nitrogen fixation in Chlorobi, past and present

Members of the phylum Chlorobi underpin biological production in many modern anoxic environments, both sulfidic [181, 210–213] and ferruginous [48, 67], through their ability to harness light energy and fix inorganic carbon into biomass, even at low light intensities [138]. Chlorobi further contribute to biogeochemical cycling in these systems through the acquisition and redistribution of essential nutrients, such as nitrogen. This ecological role would have extended to global scales in the low oxygen Precambrian oceans. Our analyses confirm the genomic potential

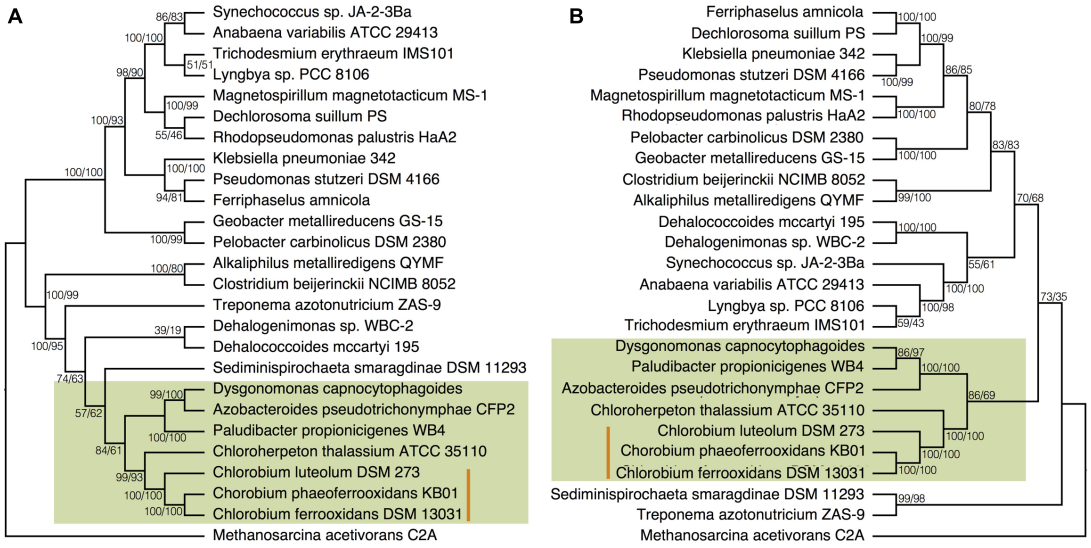

Figure 3.4: *Nitrogenase phylogenies of multiple phyla.* Phylogenies of (A) the concatenated NifDKH proteins and (B) 16S rRNA for two to four representatives of several nitrogen-fixing phyla with bootstrap values shown at each node (maximum likelihood/maximum parsimony). The green color delineates the Chlorobi/Bacteroidetes monophyletic grouping, while the orange line indicates the position of the photoferrotrophic Chlorobi. Note: *Azobacteroides pseudotrichonymphae* CFP2 is abbreviated from Candidatus *Azobacteroides pseudotrichonymphae genomovar* CFP2.

to fix N in all but one of the Chlorobi lineages and directly demonstrate the capacity of the photoferrotrophic Chlorobi to fix dinitrogen as their sole source of nitrogen while oxidizing Fe(II). Rates of Fe(II) oxidation are, however, slower when photosynthetic growth is supported through N-fixation rather than ammonium assimilation. To test the impact of slower rates of Fe(II) oxidation, and therefore growth, on the deposition of BIFs, we ran our cell counts and Fe(II) oxidation rates through the calculation outlined by Konhauser *et. al.*, 2002 [8]. Our data indicates that both photoferrotrophic strains would be capable of generating even the largest BIFs (i.e., the Hamersley BIF) with maximum of $2.44 \cdot 10^3$ photoferrotrophic cells/mL required in the basin. Thus, photoferrotrophic growth coupled to N-fixation could support BIF deposition, even in the face of nitrogen scarcity.

Chlorobium phaeoferrooxidans, and *C. ferrooxidans* exhibit differential responses to N scarcity that manifest in different cell specific Fe(II) oxidation rates and different ratio's between microbial growth (cell doubling times) and Fe(II) oxidation. *C. phaeoferrooxidans* has a cell doubling time to Fe(II) oxidation ratio of 9.4 under N-fixing conditions compared to 0.3 when there is

ample ammonium, whereas *C. ferrooxidans* has comparable ratio's of 2.3 and 1.2 for N-fixing and ammonium-rich conditions comparatively. This differential response indicates that under ammonium-rich conditions *C. phaeoferrooxidans* grows more efficiently (i.e., with a higher growth yield) whereas when N-fixation is required *C. ferrooxidans* grows more efficiently. This creates niches for each microorganism defined by N availability. The differential response also implies that the stoichiometry of Fe-oxidation to biomass production and cell growth is partly decoupled and depends on N availability. Essentially, this decoupling means that more Fe(II) is oxidized to produce an individual cell during growth supported by N-fixation than by ammonium assimilation. Such a decoupling thus requires either the diversion of reducing equivalents (NADH) produced during photosynthesis into compounds not used directly in cell growth, or that cell growth and division requires more fixed carbon during N-fixation. The former could include conversion of N2 to ammines and the biosynthesis of cell exudates, and the latter might include the biosynthesis of cellular proteins needed to conduct N-fixation. Such a decoupling would influence the overall biogeochemical functioning and ecology of ecosystems supported through primary production by photoferrotrophy. The overall activity of the marine biosphere through the Precambrian Eons may thus have been influenced by the availability of fixed N to photoferrotrophs.

3.4.2 Assimilatory sulfate reduction (ASR)

Sulfate ions are biologically inert and organisms expend tremendous energy 'activating' sulfate for three main functions: (1) reduction and incorporation into amino acids; (2) condensation and incorporation into sulfolipids and other small molecules; and (3) for dissimilatory sulfate respiration. In addition to the reduction of sulfate, organisms can acquire organic sulfur compounds like amino acids, and hydrogen sulfide directly from the environment. Acquisition of these reduced sulfur compounds can considerably reduce the expenditure of energy on sulfur acquisition. Here we focus on the first two assimilatory pathways and the capacity for reductive sulfur assimilation in the photoferrotrophic Chlorobi. The proteins required to complete an entire ASR pathway include: CysD, the sulfateadenyl transferase that activates sulfate to form APS; CysN which catalyzes GTP hydrolysis providing the energy needed to adenylate imported sulfate; CysC (a domain of CysN), the APS kinase that phosphorylates APS to PAPS; and CysH, the APS

reductase which reduces the sulfur in APS to sulfite. We have explored the metabolic potential for sulfate assimilation in the genomes of the photoferrotrophic Chlorobi and directly tested sulfate incorporation into biomass.

Distribution of ASR pathways within Chlorobi

Previous analyses of Chlorobi genomes identified the metabolic capacity for ASR in C. ferrooxidans and C. luteolum [194]. Using all currently available genomic information we identified components of the ASR pathways distributed throughout the Chlorobi (Table 3.2). We find that the photoferrotrophic Chlorobi, C. ferrooxidans and C. phaeoferrooxidans, as well as putative photoferrotroph C. luteolum, all possess the necessary proteins for ASR – CysD, CysN/C, CysH – and therefore have the potential capacity to synthesize amino acids from exogenous sulfate (Fig. 3.5). Notably, the presence of both CysD and CysN indicate that sulfate activation to APS in these Chlorobi is coupled to GTP hydrolysis. Sulfate assimilation in the Chlorobi, therefore, offsets the energetic expense associated with sulfate activation. The presence of CysN/C indicates the metabolic potential to phosphorylate APS to PAPS implying that these strains might have capacity to synthesize sulfate-containing compounds like sulfolipids. Finally, while components of assimilatory sulfate metabolisms are more broadly distributed throughout the Chlorobi, genes coding for key components of the pathway are mostly missing implying a lack of capacity for sulfate assimilation outside the photoferrotrophic Chlorobi (Table 3.2). Given the metabolic potential for ASR in the photoferrotrophic Chlorobi, we sought to biochemically verify this process.

Biochemical verification of ASR

Chlorobium phaeoferrooxidans and *Chlorobium ferrooxidans* are both known to grow in media where sulfur is supplied exclusively in the form of sulfate, which directly demonstrates the physiological capacity for sulfate assimilation. We quantitatively tested this capacity by measuring the uptake of ^{35}S labeled sulfate in low sulfate growth media. *C. phaeoferrooxidans*, indeed took up ^{35}S labeled sulfate into TCA extractable biomass, demonstrating assimilatory reduction of sulfate and its incorporation into amino acids. Over the course of these sulfate uptake experiments, *C. phaeoferrooxidans* oxidized 3070 μM Fe(II). This implies the fixation of 770 μM C, based on the 4:1

Table 3.2: Green sulfur bacteria ASR genes. Assimilatory (CysD, CysNC, CysH) and dissimilatory (Sat, AprAB, DsrAB) sulfur proteins present in the genomes of green sulfur bacteria.

Organism	CysD	Sat	CysNC	CysH	AprAb	DsrAB
Chlorobium phaeoferrooxidans KB01	+	−	+	+	−	−
Chlorobium ferrooxidans DSM 13101	+	−	+	+	−	−
Chlorobium luteolum DSM 273	+	−	+	+	−	+
Chlorobium phaeovibrioides DSM 265	+	−	+	−	−	+
Prosthecochloris aestuarii DSM 271	+	−	+	−	−	+
Chlorobium phaeobacteroides BS1	−	+	+	−	+	+
Chlorobium chlorochromatii CaD3	−	+	+	−	+	+
Pelodictyon phaeoclathratiforme	−	+	−	−	+	+
Chlorobium tepidum TLS	−	+	−	−	+	+
Chlorobium phaeobacteroides DSM 266	−	−	−	−	−	+
Chlorobium limicola DSM 245	−	−	−	−	−	+
Chlorobaculum parvum NCIB 8327	−	−	−	−	−	+
Chloroherpeton thalassium	−	−	−	−	−	−
Ignavibacterium album	−	−	−	−	−	−

stoichiometry between Fe(II) oxidation and C fixation observed for *C. phaeoferrooxidans* during growth on Fe(II), and for photoferrotrophic organisms, more generally [20]. A corresponding total of 3 μM S was fixed demonstrating a ratio of 260:1 C to S, which we take as approximately indicative of the S content of *C. phaeoferrooxidans*. There are few data to compare with, but our results suggest that *C. phaeoferrooxidans* has relatively low S quotas compared to aquatic and cultured bacteria (C:S from 10–60) [214] and particulate organic matter from the North Pacific (C:S of 50) [215]. By analogy to *C. phaeoferrooxidans*, photoferrotrophic Chlorobi likely have capacity to fix sulfate into biomass under low sulfate conditions, which they appear well adapted to do based on minimal cellular sulfur quotas in comparison to other bacteria and marine organic material.

Evolutionary history of ASR in the Chlorobi

To test for horizontal transfer of ASR genes to the photoferrotrophic Chlorobi, we searched for characteristic signatures of HGT within the ASR cassettes and conducted phylogenetic analyses of ASR genes, which we compared to 16S rRNA gene phylogenies. The CAI value for each of the ASR genes belonging to *C. ferrooxidans* and *C. phaeoferrooxidans* were all greater than the threshold value, 0.70, below which HGT is indicated (Table 3.3). ASR genes in *C. luteolum*, however, had sub-threshold CAI values, as low as 0.53, indicating possible ASR gene acquisition through horizontal transfer. The GC contents of ASR genes for all three species were very similar to GC

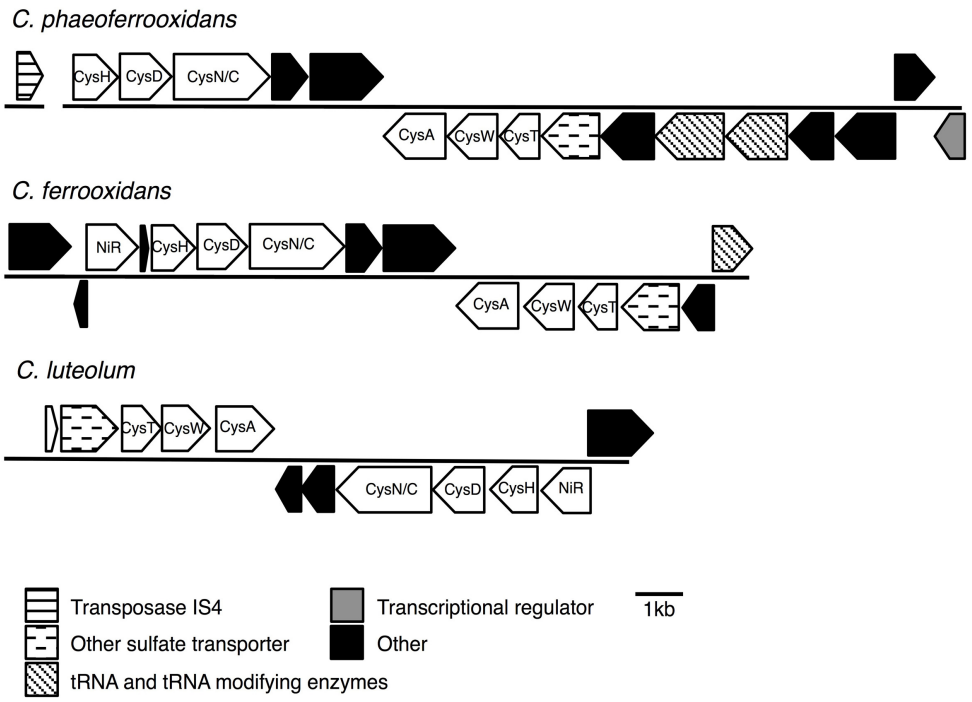

Figure 3.5: *Assimilatory sulfate reduction (ASR) gene cassettes for the photoferrotrophic Chlorobi*, detailing the position of each gene and the differences and similarities between the gene cassettes.

contents of their respective genomic backgrounds, providing no evidence for HGT (Table 3.3). Collectively, these data provide little evidence for the lateral acquisition of ASR gene cassettes in the photoferrotrophic Chlorobi, although the evidence for vertical descent is greater in *C. phaeoferrooxidans* and *C. ferrooxidans* than in *C. luteolum*. A single transposase (Fig. 3.5) was found on a contig adjacent to that hosting the ASR gene cassette in *C. phaeoferrooxidans*. The general lack of tRNAs or transposases near the ASR cassettes in the photoferrotrophic Chlorobi combined with super threshold CAI values and ASR gene GC contents that are homogenous against the genomic backgrounds, implies ASR gene acquisition through vertical decent.

To further test the evolutionary history of ASR, the CysH protein was analyzed to examine the phylogenetic relationship between the proteins used in the photoferrotrophic Chlorobi and ASR in other organisms. The photoferrotrophic Chlorobi grouped together forming a monophyletic clade within the CysH phylogeny (Fig. 3.6). The photoferrotrophic Chlorobi exhibit congruent phylogenies between the CysH protein and 16S rRNA gene (Fig. 3.6), providing further evidence in support of vertical inheritance of the ASR pathway in the photoferrotrophic Chlorobi. The

Table 3.3: Codon adaptation index (CAI) for Chlorobi ASR genes. Gene length (bp), CAI, and GC content (%) for each of the genes in the ASR cassette.

Gene	*C. phaeoferrooxidans*			*C. ferrooxidans*			*C. luteolum*		
	Length (bp)	CAI	GC content (%)	Length (bp)	CAI	GC content (%)	Length (bp)	CAI	GC content (%)
CysH	714	0.78	54.34	714	0.78	54.62	753	0.59	56.97
CsyD	882	0.80	56.12	882	0.78	55.56	915	0.61	57.38
CsyN/C	1800	0.81	54.28	1800	0.77	53.67	1800	0.69	58.06
Siroheme synthase	453	0.81	54.08	453	0.71	52.98	453	0.53	57.17
Uroporphyrin-III C-methyltransferase	1287	0.73	57.96	1287	0.73	55.40	258	0.62	57.36
CysA	1074	0.77	53.26	1074	0.80	52.42	1074	0.67	59.22
CysW	870	0.79	53.22	870	0.79	52.76	870	0.64	58.74
CysT	834	0.79	52.64	834	0.81	53.36	834	0.66	58.03
Sulfate transporter	1020	0.82	53.14	1020	0.79	52.65	1008	0.75	59.52

Each parameter was calculated for all three photoferrotrophic Chlorobi, whose whole genome GC contents are: 49.72% for C. phaeoferrooxidans, 49.9% for C. ferrooxidans, and 58.1% for C. luteolum.

more general evolutionary history of the CysH protein, however, is convoluted given abundant incongruences between the CysH protein and 16S rRNA gene phylogenies. Accepting vertical inheritance of the ASR pathway in the photoferrotrophic Chlorobi and the early divergence of the Chlorobi from other organisms, we hypothesize that gene loss explains the lack of a complete ASR pathways in other photosynthetic Chlorobi and this hypothesis is supported by the partial presence of ASR pathway components across the phylum Chlorobi (Table 3.2).

Ecology of ASR in Chlorobi, past and present

The presence of an ASR pathway in all known photoferrotrophic Chlorobi implies that ASR is advantageous to growth under ferruginous conditions. The lack of the ASR pathway in the canonically sulfur oxidizing Chlorobi makes sense in light of the availability of reduced sulfur compounds in their preferred habitats. The energetic expense of ASR would tend to favor assimilation of reduced compounds when available. Conversely, ferruginous environments are by definition sulfur poor and the availability of reduced sulfur compounds can be limited by the solubility of FeS. Sulfate, therefore, is likely the most abundant and available sulfur source in modern ferruginous environments. The rock record also demonstrates that ferruginous marine conditions persisted throughout much of the Precambrian Eons and reduced sulfur species were likely scarce with the exception of in the apparently ephemeral developments of costal euxinia.

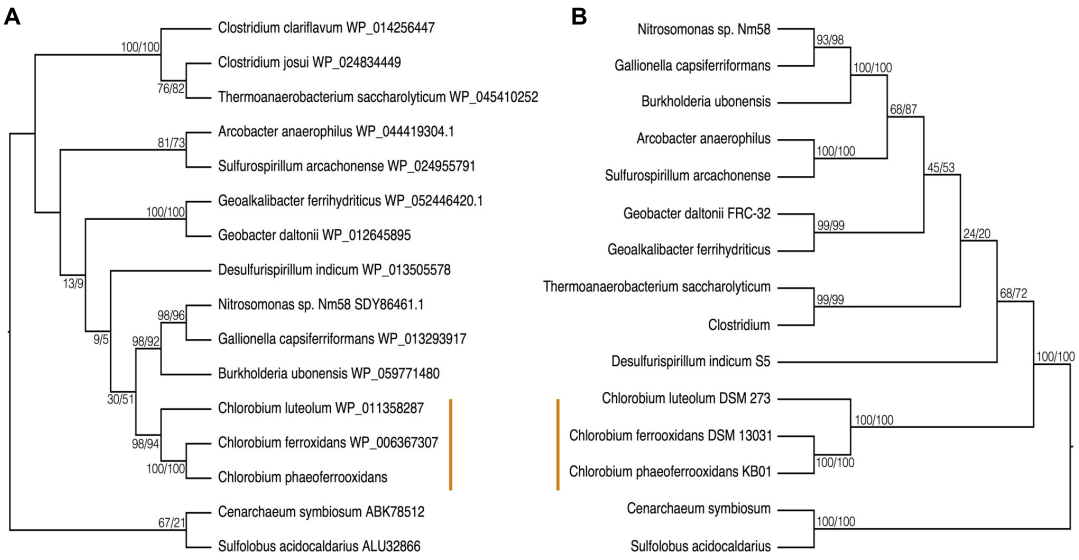

Figure 3.6: *CysH phylogenies of multiple phyla.* Phylogenies of (A) the CysH protein and (B) 16S rRNA with bootstrap values shown at each node (maximum likelihood/maximum parsimony). The orange line indicates the position of the photoferrotrophic Chlorobi. The trees are rooted with two Archaeal species.

ASR may thus have supported sulfur requirements of photoferrotrophic primary producers over long stretches of Earth's history.

The apparent role of ASR in supporting primary production through photoferrotrophy implies that sulfate availability could have been an important control on global productivity. At 28 mM, sulfate is the principle anion in modern seawater, but sulfate concentrations could have been as low as a few μM in the Archean oceans [27]. Nutrients like phosphorus and nitrogen are known to become limiting at such low concentrations. The apparently low sulfur quotas of the photoferrotrophic Chlorobi (260:1, C:S) thus seem well adapted to growth in the low sulfate oceans of the Archean, which would have enhanced productivity in the face of sulfur scarcity.

Under low sulfate conditions dissimilatory sulfate reduction (DSR) would have played a comparatively small role in the remineralization of organic matter in Archean oceans [27]. Qualitatively then ASR would have played an outsized role in the reduction of sulfur and the global sulfur cycle in the Archean oceans, relative to today. We therefore hypothesize that primary production through photoferrotrophy was a key pathway in the production of an organic reduced sulfur pool, which would have provided an important vector for sulfur to Archean sediments. We further

hypothesize that ASR may have predated DSR. Earliest evidence for DSR comes from S-isotope fractionation recorded in 3.47Ga barites [216], whereas photoferrotrophy likely operated as early as 3.8Ga [169] and presumably required ASR. The idea that ASR predates DSR could be tested if homology could be established in enzymes involved in both pathways. Although ASR and DSR serve different functions – sulfate acquisition versus energy transduction, respectively – both pathways actively transport sulfate into the cell and the first enzymes in the pathways are thus analogous. Comparison of amino acid sequences of the first enzymes (CysD and Sat, respectively) in the two pathways indicates a strong degree of homology implying evolutionary relationships between components of ASR and DSR.

To examine the phylogenetic relationships between enzymes that transport sulfate for use in ASR and DSR, we aligned CysD and Sat proteins from the majority of the Chlorobi and a selection of representative microorganisms from diverse phyla. The resulting phylogeny clearly separated amino acid sequences annotated as CysD from those annotated as Sat (Fig. 3.7). Both CysD and Sat appear to support sulfate transport in relation to multiple sulfur metabolisms, but the phylogenetic relationships appear complicated and likely require more detailed analyses. Nevertheless, homology between the two proteins implies a possible evolutionary relationship between ASR and DSR that may inform evolutionary histories and should be tested in the future.

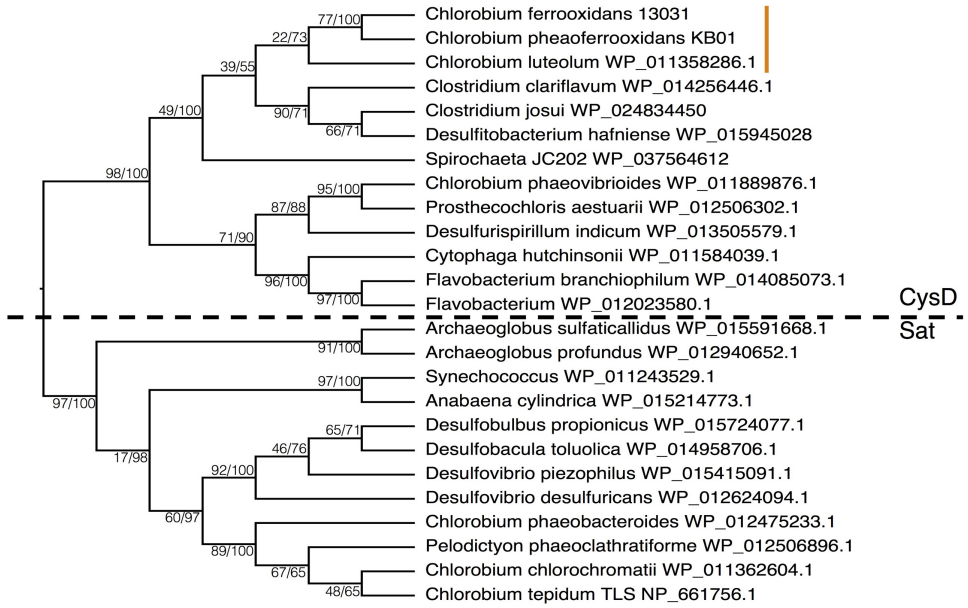

Figure 3.7: *Phylogeny of the Sat/CysD protein* with bootstrap values shown at each node (maximum likelihood/maximum parsimony), to compare the ASR and DSR pathway among a diverse set of organisms. The dashed line delineates the organisms with CysD versus those with Sat. The orange line indicates the position of the photoferrotrophic Chlorobi.

3.5 Outlook

Photoferrotrophy links the C and Fe biogeochemical cycles through coupled CO_2 fixation and Fe(II) oxidation and has likely done so since the early Archean Eon. Models for photoferrotrophic growth in the Archean oceans remain poorly constrained as they are extrapolated from growth rates in nutrient rich laboratory culture media. Here we demonstrate that photoferrotrophic Chlorobi have the physiological capacity to fix inorganic N and S into biomass when availability of these nutrients is low and have likely had this capacity since the Archean Eon. Thus, under N and S limited ferruginous conditions, photoferrotrophy underpins biogeochemical cycling of C, N, S, and Fe. Nutrient availability, however, influences growth and Fe(II) oxidation rates and has consequences for the stoichiometric relationships between C, N, S, and Fe transformations. Undoubtedly, these relationships should be assessed and studied in more detail with additional physiological experimentation and should be applied to further constrain models of photoferrotrophy, biological production, and global biogeochemical cycling in the Archean Eon.

Chapter 4

Photoferrotrophy, deposition of banded iron formations, and methane production in Archean oceans

4.1 Summary

Banded iron formation (BIF) deposition was the likely result of oxidation of ferrous iron in seawater by either oxygenic photosynthesis or iron-dependent anoxygenic photosynthesis—photoferrotrophy. BIF deposition, however, remains enigmatic because the photosynthetic biomass produced during iron oxidation is conspicuously absent from BIFs. We have addressed this enigma through experiments with photosynthetic bacteria and modeling of biogeochemical cycling in the Archean oceans. Our experiments reveal that, in the presence of silica, photoferrotroph cell surfaces repel iron (oxyhydr)oxides. In silica-rich Precambrian seawater, this repulsion would separate biomass from ferric iron and would lead to large-scale deposition of BIFs lean in organic matter. Excess biomass not deposited with BIF would have deposited in coastal sediments, formed organic-rich shales, and fueled microbial methanogenesis. As a result, the deposition of BIFs by photoferrotrophs would have contributed fluxes of methane to the atmosphere and thus helped to stabilize Earth's climate under a dim early Sun.

4.2 Introduction

Banded iron formations (BIFs) host the world's largest iron ore deposits, and they formed predominantly through the deposition of ferric iron (Fe[III]) from ferruginous oceans during the

Archean Eon [4, 83]. Most models for BIF deposition invoke photosynthesis in the oxidation of ferrous iron from seawater to induce its subsequent precipitation and deposition as mixed valence iron (oxyhydr)oxides and carbonate phases [6–9] (see [79] and [81] for alternative models). BIFs thus likely record the activity of Earth's early photosynthetic biosphere [6]. Two modes of photosynthesis have been implicated in Fe(II) oxidation—canonical oxygenic photosynthesis by the ancestors of modern cyanobacteria [6] and iron-dependent anoxygenic photosynthesis [7, 8], referred to as photoferrotrophy. Photoferrotrophic bacteria grow using light and Fe(II) to fix CO_2 into biomass and produce Fe(III) as a metabolic byproduct [8, 9, 20]; they can do so in the complete absence of oxygen [20]. Current literature suggests that such anoxygenic photosynthesis is likely the evolutionary predecessor of oxygenic photosynthesis [11, 35, 93] and Fe(II) oxidation could thus have been driven by photoferrotrophy before the emergence and proliferation of oxygenic photosynthesis [1, 82]. Indeed, models of nutrient cycling in the Archean ocean implicate photoferrotrophs as key primary producers [1, 85] before the rise of atmospheric oxygen 2.4 to 2.3 billion years ago (Ga) during the Great Oxidation Event (GOE) [2, 104, 105]. High methane concentrations in the Archean atmosphere have also been qualitatively attributed to C and Fe cycling associated with BIF deposition [172]. Such an 'upside-down' biosphere [172] in which the reduced products of photosynthesis end up in the atmosphere as methane and the oxidized products are buried as Fe(III) in BIF can, as we show here, be quantitatively and mechanistically linked to the activity of photoferrotrophs in ferruginous Archean oceans.

Observations and models of extant photoferrotrophs demonstrate their capacity to both oxidize Fe(II) at rates sufficient to form even the largest BIFs and support appreciable rates of primary production [1, 8, 21, 48]. Laboratory experiments to date, paradoxically, reveal a tight physical association between photosynthetic ferric iron metabolic byproducts (e.g., Fe(III) (oxyhydr)oxides) and cellular biomass that leads to their co-sedimentation [8, 21, 42]. In the oceans, deposition of Fe(III) along with this photosynthetic biomass would fuel sedimentary respiration that couples oxidation of organic carbon to microbial Fe(III) mineral reduction and converts Fe(III) to dissolved Fe(II) and secondary minerals such as siderite and magnetite [42]. Such sedimentary respiration thus closes the iron redox cycle and precludes the preservation of ferric iron in BIF. Current observations and models, therefore, cannot explain BIF deposition through photoferrotrophy in

light of such co-sedimentation of biomass with Fe(III) and ensuing diagenetic reactions [42, 63]. By contrast, a lack of Fe(III) reduction would lead to the co-deposition of ferric iron in BIF with organic matter at relative concentrations close to the 4:1 stoichiometry of Fe(II) oxidation to C fixation in photoferrotrophy (e.g. 2 wt. % C based on 37 wt. % Fe(III) in Dales Gorge BIF [75]). A compilation of organic matter concentrations and Fe redox states in BIFs, however, reveals that they have very low organic matter concentrations (mean of 0.27 wt. % – Fig. 4.1, A.5 [75, 89]) and contain appreciable Fe(III), with an average Fe redox state of 2.6 (A.1, A.5 [75, 89]). If the iron minerals in BIFs were the product of photosynthesis, then the fate of the corresponding photosynthetic biomass remains entirely enigmatic. Furthermore, regardless of the mode of Fe(II) oxidation, current estimates for the magnitude of hydrothermal Fe(II) fluxes to the Archean ocean appear to be deficient of the mass fluxes needed to sustain BIF deposition [217] and may imply an important role for terrestrial weathering fluxes [22, 218]. We thus combined experiments using modern photosynthetic bacteria with revised theoretical estimates of Fe(II) fluxes to the Archean ocean and box modeling of coupled carbon and iron cycling to show that photosynthetic Fe(II) oxidation could have sustained large-scale, organic-poor, BIF deposition in ocean upwelling systems over hundreds of millions of years.

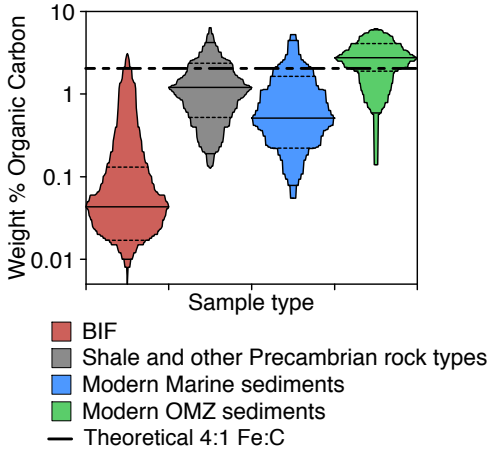

Figure 4.1: *The organic matter concentrations in BIFs, other Precambrian sedimentary rocks, typical modern marine sediments, and oxygen minimum zone (OMZ) sediments.* The solid lines represent the group means while the dotted lines delineate one standard deviation above and below the mean. The black dashed line that spans the figure represents the theoretical organic carbon concentration that would be expected in BIFs deposited by photoferrotrophs (2.04 wt. % C) assuming quantitative co-sedimentation of biomass with ferric Fe. References for this figure can be found in A.5.

4.3 Results and discussion

4.3.1 Separation of biomass and Fe(III)

To explore the fate of biomass and Fe(III) during photosynthetic Fe(II) oxidation, we conducted experiments using *Chlorobium phaeoferrooxidans* strain KB01, a photoferrotrophic bacterium that was isolated from the water column of ferruginous Kabuno Bay, a sub-basin of Lake Kivu in East Africa [48]. We also conducted experiments with *Chlorobium ferrooxidans* strain KoFox——a sediment-dwelling photoferrotroph that tends to associate with Fe(III) (oxyhydr)oxides without becoming encrusted [53, 63], as well as a model marine oxyphototrophic cyanobacterium of the genus Synechococcus. Strain KB01 is the only known photoferrotroph from a pelagic environment [48] and pelagic photoferrotrophs, including those that would have populated Precambrian ferruginous oceans, face a special challenge—they must maintain their position within sunlit waters despite the precipitation of heavy Fe(III) oxyhydroxide metabolic byproducts that have a tendency to adhere to cell surfaces and cause their rapid sedimentation. Most bacteria have negatively charged cell surfaces at neutral pH [219], while Fe(III) (oxyhydr)oxides typically have a positive surface charge at the same pH [220]. This generally leads to a strong attraction between cell surfaces and Fe(III) (oxyhydr)oxides that often manifests as encrustation of bacterial cells and formation of Fe(III) oxyhydroxide-cell aggregates [9, 221].

To test the association between photoferrotrophs and their Fe(III) metabolic byproducts, we grew strain KB01 until late exponential growth phase, gently inverted the cell-mineral suspension to resuspend sedimented Fe(III) (oxyhydr)oxides and cells, allowed the heavy Fe(III) (oxyhydr)oxides to resettle, and determined the percentage of cells that remained suspended (Fig. 4.2a). Experiments conducted in media with reduced phosphate concentrations (3-6 μM), approaching those of modern seawater, but still somewhat higher than sub-μM concentrations found in Precambrian seawater [85], show that 50 % of strain KB01 cells associated with Fe(III) (oxyhydr)oxides, leading to co-sedimentation of biomass and Fe(III) (Fig. 4.2a). While phosphate concentrations were very low in the seawater from which BIFs deposited [85, 222], silica concentrations in Precambrian oceans were high ($\sim$1 mM) [85], and this would have altered the physical and chemical properties of Fe(III) precipitates formed in seawater [222]. In experiments with 1 mM

silica, concentrations implied for Precambrian seawater [85], strain KB01 cells did not associate to, or co-sediment with their Fe(III) oxyhydroxide byproducts (Fig. 4.2a). Instead, almost all of the cells remained suspended (94 $\pm$ 6 %). Likewise, experiments conducted with strain KoFox demonstrated that cell-mineral association was diminished relative to the silica-free experiments, with 72 $\pm$ 7 % of strain KoFox cells remaining suspended (Fig. 4.2a and A.5a). We also grew both strains KB01 and KoFox in their standard growth media containing 4 mM phosphate and no silica, which led to little cell-mineral association for strain KB01 (Fig. 4.2a), and modest association for strain KoFox (A.5a). Detailed electron microscopy revealed that the surfaces of KB01 cells were entirely free from Fe(III) oxyhydroxide precipitates (Fig. 4.3), whereas strain KoFox tended to form multicellular aggregates that variably associated with the mineral precipitates (A.3a). Strain KB01, and to a somewhat lesser extent strain KoFox, thus avoid encrustation with Fe in low P, high Si waters, as well as in standard growth media with high phosphate, remaining suspended despite Fe(III) oxyhydroxide precipitation.

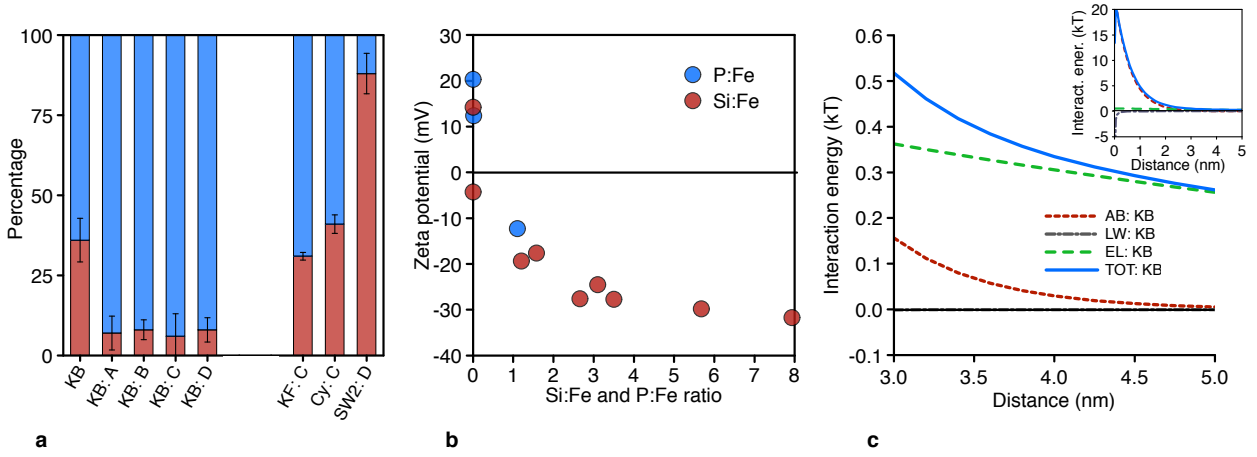

Figure 4.2: *Cell surface characteristics for strain KB01 and the relationship between ferric iron surface charge and medium anions.* The fractions of planktonic (blue) versus sedimented (red) cells (a) for photoferrotrophic strain KB01 under varying geochemical conditions: 400 μM Fe(II) with low P (3 μM) [unmarked], 400 μM Fe(II), low P (3 μM), with 0.6 mM Si [A], 400 μM Fe(II), low P (3 μM), with 1.0 mM Si [B], 400 μM Fe(II), low P (3 μM), with 1.5 mM Si [C], and 10 mM Fe(II) with 4.4 mM P [D]. *C. ferrooxidans* and *Synechococcus* are also shown under the [C] conditions. *Rhodobacter* strain SW2 is shown under the [D] conditions. The zeta potential (b), in mV, of the ferric iron precipitates is depicted with an increasing ratio of Si or P to Fe, where the error bars are all within the data points. Finally, the extended DVLO modeling for strain KB01 (c) with the main graph depicting the interaction energies of the 3 forces (AB – Lewis acid-base; LW – Lifshitz-van der Waals; EL – electrostatic) and the total (TOT – total) for those forces from 3 nm-5 nm, while the inset depicts the forces from 0 nm-5 nm.

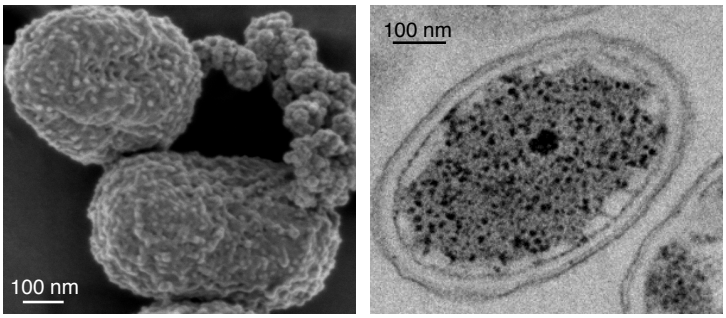

Figure 4.3: *Scanning electron microscopy and transmission electron microscopy image of strain KB01.* Scanning electron photomicrograph (a) and transmission electron photomicrograph (b) of *C. phaeoferrooxidans* strain KB01 revealing various internal and external cell structures as well as a lack of encrustation (a, b) and a rare association with Fe(III) precipitates (a).

We also subjected Synechococcus cells to Fe-Si-rich growth conditions in a similar fashion (Fig. 4.2a and A.5a). Synechococcus associated to a greater extent with the Fe(III) oxyhydroxide products of Fe(II) oxidation than did the photoferrotrophs under these conditions. Such an association was expected, despite the presence of silica, given that oxygen effuses from Synechococcus cells, reacts rapidly with Fe(II), and causes precipitation of Fe(III) (oxyhydr)oxides on the cell surfaces—an association likely maintained due to binding with organic ligands, as observed in many previous environmental and laboratory studies [221, 223, 224]. Photoferrotrophs adapted to pelagic lifestyles thus appear capable of avoiding co-sedimentation with Fe(III) and remain buoyant with the potential for separation of biomass from Fe(III) at larger scales in the environment.

4.3.2 Mechanisms of cell-mineral separation

Surface charge often influences cell-mineral association, or lack thereof, and as solution P:Fe or Si:Fe ratios increased, the surface charge on the Fe(III) (oxyhydr)oxides formed became more negative (Fig. 4.2b) due to the incorporation of P or Si anions into the oxyhydroxide structure [222]. Conversely, Fe(III) oxyhydroxide particles were positively charged under low P or Si conditions, which is consistent with observations of positively charged Fe(III) precipitates in many environments [220]. Strain KB01 cells had strongly negative surface charges (A.4), whereas cells of strain KoFox had near neutral surface charges (A.4), similar to some microaerophillic Fe(II)

oxidizers [225]. This difference in surface charge between strains KB01 and KoFox reflects different cell surface chemistries (A.2), notably an abundance of anionic surface functional groups on strain KoFox with different acid-base behavior than strain KB01 (SI, A.3). Benthic microorganisms, such as strain KoFox, commonly produce surface layers rich in anionic functional groups to facilitate attachment to solid substrates [226] and such anionic surface functional groups tend to strongly bind Fe(III), effectively neutralizing surface charge (A.4). The role of Fe(III) in controlling surface charge on strain KoFox was confirmed by rinsing KoFox cells with reducing agents (sodium dithionite) that liberated Fe(III) and caused a shift in the surface charge to more negative values (A.4). These same rinses had little effect on cells of KB01 (A.4), confirming the role of surface chemistry and Fe(III) binding in controlling association of cells to Fe(III) (oxyhydr)oxides. The direct role of cell surface charges in dictating mineral association and co-sedimentation is also evident from the strong inverse relationship (A.5b) between mineral surface charges and cell-mineral separation.

To assess the biophysical mechanisms that control cell-mineral associations we determined interfacial properties of the cell and Fe(III) oxyhydroxide surfaces and conducted extended Derjaguin–Landau–Verwey–Overbeek (DVLO) modeling to quantify the forces that develop between these surfaces (AppendixA) [225, 227]. DVLO modeling uses measurements of physical surface properties to calculate interfacial forces as a function of distance between surfaces. Our model results revealed that the negative surface charge on strain KB01 indeed led to electrostatic repulsion between its surface and negatively-charged Fe(III) (oxyhydr)oxides (Fig. 4.2c). The more neutral charge on strain KoFox, conversely, led to a weak electrostatic attraction (A.5c). Lewis acid-base and Lifshitz-van der Waals forces were much weaker than the electrostatic forces, but we note that the acid-base properties of strain KB01 lead to repulsion of Fe(III) (oxyhydr)oxides, even without electrostatic effects. Surface charge, therefore, controls cell-mineral association and ultimately like-charged surfaces cause the physical separation of strain KB01, and by extension, other pelagic photoferrotrophs from their Fe(III) oxyhydroxide byproducts. These findings have important implications for BIF deposition and the coupling of carbon and iron cycles in the Archean Eon. We note that while strain KB01 is a derived member of the phylum Chlorobi, its cell surface chemistry is typical for gram negative bacteria [219, 228] and our results are thus

likely extensible to its ancestors and most other gram negative bacteria, with the exception of benthic organisms, like strain KoFox, that have unusual modifications to their cell surfaces. Stem group, pelagic photoferrotrophs in Archean oceans, therefore, most likely possessed cell surface chemistries and interacted with Fe(III) (oxyhydr)oxides much like stain KB01.

4.3.3 Revised Precambrian Fe budgets

Before proceeding to model coupled carbon and iron cycling, we sought to reconcile the possible material fluxes of Fe(II) to the oceans and those needed to sustain BIF deposition [217, 229]. These material fluxes serve as boundary conditions for our models and help tether our results to the geologic record. Peak BIF deposition rates imply an Fe burial flux of 45 mol m^{-2} yr^{-1} over areas greater 10^{11} m^2, or $\sim$4.5 Tmol Fe yr^{-1} [8] and, at steady state, Fe(II) must be actively resupplied to the oceans at this rate through a combination of hydrothermal venting and continental and seafloor weathering. Previous estimates of modern hydrothermal Fe fluxes of $\sim$2 Tmol yr^{-1} (AppendixA), on their own, are insufficient to support steady-state BIF deposition [83, 217, 229] (A.3). These estimates were based on the product of hydrothermal fluid flow and Fe(II) concentrations measured in circulating on- and off-axis fluids [24]. Global Fe fluxes, however, would have been much different in the Archean Eon because of enhanced hydrothermal activity [229, 230], smaller continents [231], reduced seawater sulfate [27, 230], weathering of Earth's crust at low oxygen [2, 16, 28], and pervasively anoxic oceans.

Hydrothermal fluid fluxes to the oceans have been calculated from a variety of geochemical and physical data resulting in a wide range of estimates for these fluxes in the literature. A recent compilation from a number of sources [158], however, provides a synthesis of both on- and off-axis fluid flow as well as a modeled distribution of these values that yields averages (modes) of 5 x 10^{13} and 1.5 x 10^{16} kg y^{-1}, respectively [158]. These values are greater than values considered in previous estimates of modern hydrothermal Fe(II) budgets, implying that modern Fe(II) fluxes to the oceans were underestimated [24]. Archean hydrothermal fluid flow was, furthermore, likely higher than today due to greater heat loss from the Archean lithosphere [217, 232]. Following previous work [217], we thus scaled the updated estimates for modern fluid flow by the ratio of past to modern lithospheric heat loss (AppendixA). This yields estimates for hydrothermal fluid

flow at 2.5 Ga of 1 $\pm$ 0.6 x 10^{14} and 4 $\pm$ 0.6 x 10^{16} kg yr^{-1} for on- and off-axis venting, respectively (A.3). Crucially, these revised estimates for fluid flow increase the possible Fe(II) fluxes to both the modern and Archean oceans.

The concentration of Fe(II) in modern on-axis hydrothermal fluids is $\sim$6 mmol kg^{-1} [24], but this depends on the chemistry of seawater that circulates through seafloor basalts. Notably, high concentrations of sulfate (28 mM) in modern seawater lead to production of hydrogen sulfide in anoxic hydrothermal fluids, and this hydrogen sulfide reacts with Fe(II) to form iron-sulfide minerals that limit the concentration of Fe(II) in efluxing fluids [230]. Sulfate concentrations in Archean seawater were much lower than today due, in part, to the lack of oxidative pyrite weathering on the continents [27]. Models of hydrothermal fluid chemistry, therefore, predict that Fe(II) concentrations in high-temperature hydrothermal fluids were ten-fold higher when seawater was sulfate free versus the modern 28 mM [230], implying that high-temperature vent fluids in the Archean Eon could have had up to 60 mmol kg^{-1} Fe(II). Combining such a high-temperature hydrothermal Fe(II) concentration [230] with revised on-axis hydrothermal fluid flows results in Fe(II) fluxes of 8 $\pm$ 3 Tmol yr^{-1} at 2.5 Ga (A.3) and these are similar to, but smaller than, other recent estimates [95]. The effect of seawater sulfate concentrations on the Fe(II) concentration in lower temperature, off-axis hydrothermal fluids appears less pronounced and so we conservatively consider off-axis hydrothermal Fe(II) concentrations equivalent to today ($\sim$0.75 mmol kg^{-1}) [230]. This results in possible off-axis Fe(II) fluxes of up to 30 $\pm$ 5 Tmol yr^{-1} (A.3). Combining these new estimates for on- and off-axis Fe(II) fluxes, we redefine upper possible limits on hydrothermal Fe(II) delivery to the oceans at 2.5 Ga as $\sim$40 Tmol yr^{-1} (A.3).

In addition to the Fe(II) fluxes from hydrothermal venting, modern continental weathering also contributes Fe to the oceans. We thus assessed the potential delivery flux of continental Fe(II) to Archean oceans taking into consideration the low oxygen atmosphere [28] and smaller continent sizes [231], resulting in a total Fe(II) weathering flux of 5 Tmol yr^{-1} to the oceans (AppendixA). Summing continental weathering and hydrothermal Fe(II) fluxes yields an upper possible global Fe(II) flux of $\sim$45 Tmol y^{-1} to the oceans 2.5 Ga (A.3). This is more than sufficient to deposit BIF at 4.5 Tmol yr^{-1} and is supplied mostly through previously unconsidered off-axis hydrothermal venting. These revised Fe(II) fluxes place upper boundaries on the magnitude of global coupled

carbon and iron cycling, which we explore below using biogeochemical box models.

4.3.4 Modeling Archean marine iron and carbon cycles

We assume that biological production in our model is driven by photoferrotrophy and, while oxygenic photosynthesis could have been active from the Mesoarchean [16, 94], its contribution to primary production may have been small before the GOE due to competition with photoferrotrophs [85, 106]. Nevertheless, discriminating between modes of photosynthesis would have no real effect on our model outcomes since oxygen produced would react with Fe(II) yielding the same 4:1 stoichiometry between iron oxidation and carbon fixation as in photoferrotrophy. Biomass degradation in our model was first channeled through heterotrophic Fe(III) reduction, and then, given the near absence of sulfate in the Archean ocean [27], microbial methanogenesis [27, 42]. We implicitly assumed that both Fe(III) reduction and methanogenesis are preceded by the breakdown of organic matter through hydrolysis, glycolysis, and fermentation. Rates of organic matter breakdown were parameterized based on observations from modern anoxic marine basins [233, 234]. We note, however, that unlike today, the biological pump in the Archean oceans would have operated without ballasting from fecal pellets. Biological production and nutrient cycling in the modern oceans can be divided into three broad oceanographic provinces—open ocean, coastal zone, and upwelling regions [233]. In detail, the distribution and biological activity of these provinces depends on ocean circulation patterns, continental configurations, and nutrient supply, but in the absence of robust constraints on these parameters for the Archean oceans, we assumed that the relative contributions of similar such provinces to biological production scale with continental area and were otherwise similar to the modern. We thus distributed total biological production across these three provinces according to their relative productivities in the modern ocean [233] and scaled continental area from 0-100 % of the modern (Fig. 4.4; AppendixA).

Our results revealed that upwelling provinces support Fe(II) oxidation and Fe(III) oxyhydroxide sedimentation at rates sufficient to deposit even the largest BIFs, such as those of the Hamersley Basin in Western Australia (Fig. 4.5, Table 4.1, AppendixA). Notably, Fe(III) (oxyhydr)oxides, with a relatively high density (3.8 g cm^{-1}) and a tendency to aggregate to larger particle sizes [235], had an average settling velocity of 2 x 10^4 m yr^{-1}. This led to their deposition within a maximum of

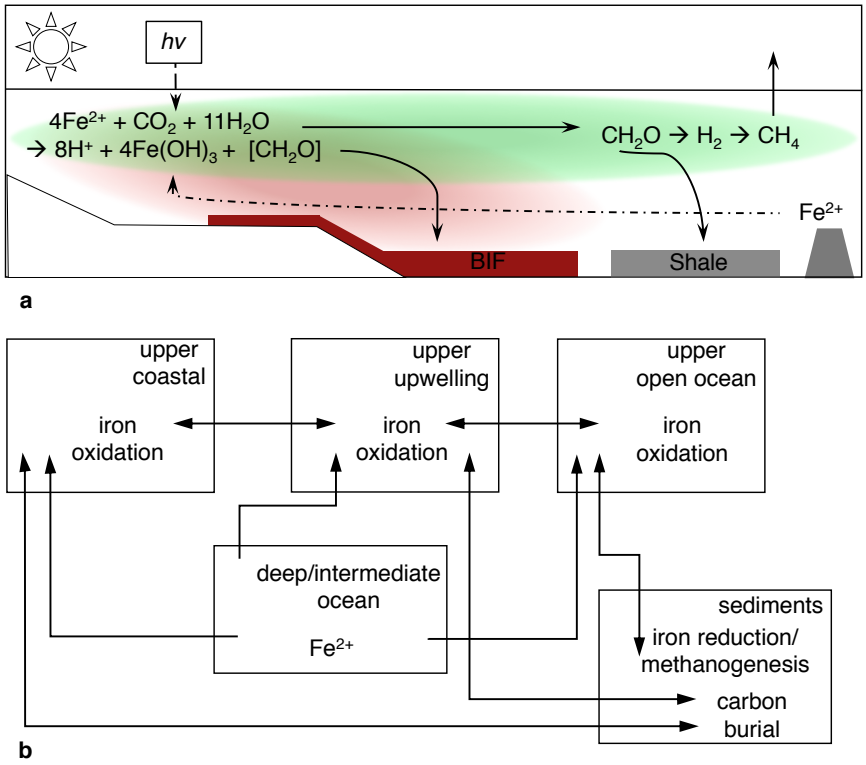

Figure 4.4: *Model of an Archean coastal upwelling zone.* A schematic (a) depicting the cycling of iron and carbon in the model and the boxes (b) that were used to create the model structure, accompanied by arrows demonstrating the fluxes of various biochemical parameters between the boxes.

40 km from their locus of initial precipitation, assuming a 150 m deep water column and current velocities less than 650 m yr^{-1} [233, 236] (A.6, A.4). Furthermore, such localized deposition occurred despite the strong horizontal current velocities that are characteristic of upwelling provinces [233, 236]. In stark contrast, the average settling velocity of biomass not associated with Fe(III) (oxyhydr)oxides was 0.35 m yr^{-1} and biomass can thus be transported distances more than 6000 km——greater than the width of the modern Pacific Ocean (A.6, A.4). Substantial biomass can thus be exported from productive upwelling areas and broadly distributed between oceanic provinces before its deposition. Notably, separation of biomass from Fe(III) (oxyhydr)oxides led to little pelagic and sedimentary Fe-recycling within the upwelling province itself. The small fraction of biomass deposited in upwelling regions fueled diagenesis resulting in both Fe(II) recycling to the water column and the authigenesis of reduced Fe phases such as siderite and magnetite. Siderite can be an abundant component in many BIF [75, 89] and an example carbon isotope

mass balance suggests that 30 % of the siderite in BIFs can be diagenetic with the balance likely representing a primary precipitate (AppendixA). In our benchmark scenario (AppendixA), where 15 % of cells are associated with their Fe(III) byproducts, organic carbon deposition rates could have supported conversion of 10 % of the total Fe(III) deposited to diagenetic siderite. When the diagenetic siderite is combined with primary non-diagenetic siderite, as inferred from the isotopic composition of siderite, the total siderite content of BIFs in our benchmark scenario is as high as 30 %. This combination of primary and diagenetic siderite and remaining Fe(III) (oxyhydr)oxides yielded an average redox state of Fe in BIF of 2.7 and is very similar to that of many siderite-bearing Neoarchean BIFs (A.1, A.5).

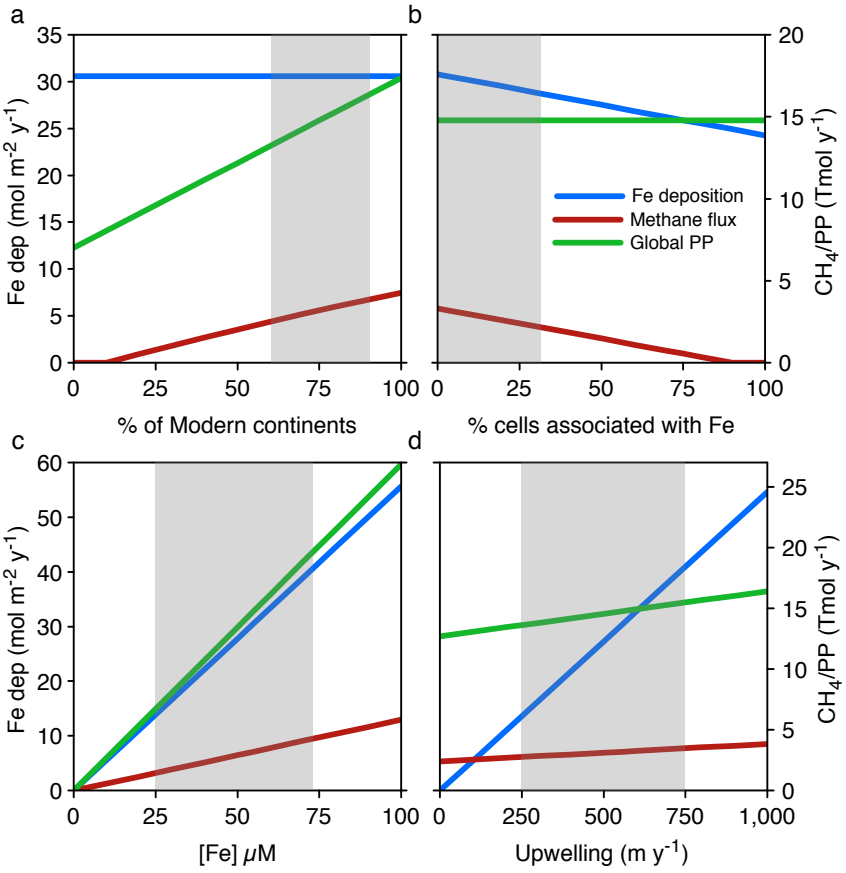

Figure 4.5: *Iron and carbon box model sensitivity results.* Model sensitivity results for varying continent size (a), percentage of cells associated with Fe(III) (oxyhydr)oxides (b), deep ocean Fe(II) (c), and varying upwelling rates in the upwelling provinces (d). Iron deposition rates in the upwelling provinces are depicted on the y-axis, while global rates of primary production and methane production are both shown on the x-axis in Tmol yr^{-1}.

Table 4.1: The low, middle, and high represent the model outputs from the low, middle, and high parts of the ranges depicted by the grey boxes in Fig. 4.5 and A.8. For reference, modern rates of primary production range from 2760 to 3510 Tmol C yr^{-1} [90].

	C PP	C burial	C remin.	C to Fe reduction	C to CH_4 production	Fe recycling	Fe dep. (upwelling province)	Global Fe dep.	Global CH_4
	Tmol C/yr	% of PP	% of PP	% of remin.	% of remin.	Tmol Fe/yr	Tmol Fe/yr	Tmol Fe/yr	Tmol CH_4/yr
2.5 Ga Low	4.5	14.8	85.2	72.6	27.4	11.1	1.0	17.9	0.5
2.5 Ga Middle	14.8	14.7	85.3	49.1	50.9	24.8	9.9	59.1	3.2
2.5 Ga High	22.5	14.6	85.4	41.0	59.0	31.4	17.5	89.9	5.7

Biomass exported from upwelling provinces augmented the biomass produced in the other provinces and drove extensive pelagic and sedimentary Fe-recycling through heterotrophic Fe(III) reduction. As decoupling of biomass from Fe(III) (oxyhydr)oxides in upwelling regions led to excess biomass over Fe(III) in both other provinces, it fueled methanogenesis once Fe(III) had been entirely reduced or was buried as Fe-poor, organic-carbon bearing coastal and deep-sea sediments (Fig. 4.4). Deposition of biomass in these sediments would have led to organic carbon concentrations of between 0.5 and 5 wt. % depending on sedimentation rates of detrital material (SI, A.7). At low sedimentation rates characteristic of deep water environments, organic carbon concentrations are similar to those of the organic carbon-rich shales that deposited throughout the Archean Eon [28].

The globally integrated rates of these processes varied depending on continental area, biomass association to Fe(III) (oxyhydr)oxides, Fe(II) concentrations in the deep ocean, and rates of upwelling (Fig. 4.5). These variables can be constrained to likely ranges based on material fluxes recorded in sedimentary rocks [4, 83, 229], bounds for global cycling [22, 83, 229], and tempered analogies to modern systems [48, 69]——model outputs within these ranges are delineated by the shaded area in Fig. 4.5. Importantly, deep ocean Fe(II) concentrations are constrained to $<$70 μM, similar to earlier estimates of 50 μM based on siderite and calcite solubility [22], because higher Fe(II) concentrations led to global Fe(II) oxidation rates that exceed the revised maximum global

Fe(II) supplies and recycling combined (A.3). Even at these relatively low Fe(II) concentrations (20-70 μM), upwelling provinces could have supported area-specific rates of BIF deposition of up to 54 mol m^{-2} yr^{-1} over areas greater than 10^{11} m^2 (Table 4.1), as needed to deposit the largest of the Archean BIFs [8]. Notably, with decreased cell mineral association, increased continent size, increased deep water Fe(II) concentrations, and increased upwelling rates, Fe(II) consumption could have eventually outpaced even upper limits for Fe(II) supply and this would have led to depletion of deep ocean Fe(II). Within the most likely parameter space, rates of global primary production through photoferrotrophy would have been less than 1 % of modern primary production (Table 4.1) and, in the absence of oxygen and sulfate, the majority of this biomass would have been remineralized through Fe(III) reduction and methanogenesis in the open ocean with the remainder buried in sediments (Table 4.1). Global primary production is limited by P availability over geological time and marine primary production scales with P concentrations in the oceans [237]. Reconstruction of P concentrations in the Archean oceans implied 0.04-0.13 μM [85], which is $\sim$1-4 % of the modern, and sufficient to support our estimates for primary production. Notably, up to 45 % of all remineralized carbon was channeled through methanogenesis and the fraction of remineralization through methanogenesis increased with decreased cell mineral association, increased continent size, increased deep water Fe(II) concentrations, and increased upwelling rates (Fig. 4.5, Table 4.1). Variations in all of these processes thus likely influenced global rates of iron deposition and methane production and could have contributed to the development of differing BIF facies.

The model prediction that methanogenesis would have played a key role in carbon degradation in Archean ferruginous oceans is also supported by other Earth system models [95] and observations from modern ferruginous basins. In Kabuno Bay, East Africa, for example, carbon produced through photoferrotrophy is remineralized through methanogenesis [48] leading to an export of ferric iron from the euphotic zone even under extremely quiescent physical conditions. Likewise, despite abundant Fe(III) (oxyhydr)oxides, as much as 50 % of the carbon degradation in ferruginous Lake Matano is channeled through methanogenesis, rather than Fe(III) reduction [69]. Empirical observations thus point generally to carbon and iron cycling under ferruginous conditions that ultimately leads to methane production even in the absence of the large-scale

advective processes that operate in the oceans. When integrated into a box model of the Archean marine iron and carbon cycles, our observations of cell-Fe(III) oxyhydroxide separation during photoferrotrophy quantitatively describe an Archean biosphere that: (1) accounts for the Fe(III) deposition rates needed to form BIFs; (2) explains the fate of biomass and its absence from BIFs; and (3) provides a strong source of methane to the biosphere.

This model demonstrates that, within the geologically constrained parameter space, global rates of methanogenesis can easily reach 3.2 Tmol yr^{-1} (Table 4.1) and with the near absence of oxygen and sulfate to fuel methane oxidation, most of this methane would be delivered to the atmosphere [29]. Based on new solutions [95] to photochemical models [238], this 3.2 Tmol yr^{-1} biospheric methane flux would support a 10 ppmv methane atmosphere under our benchmark scenario with a possible range of between 1 and 20 ppmv across the likely model parameter space (Table 4.1). While such methane concentrations alone are unlikely to support a warm climate, positive feedbacks with other concurrent modes of photosynthesis, like H_2-based anoxygenic photosynthesis, dramatically increase both biospheric methane fluxes to the atmosphere and atmospheric methane concentrations [95]. Our observations of extant photoferrotrophs, revised global Fe budgets, and models of coupled C and Fe cycling thus support an up-side-down Archean biosphere, similar to that originally proposed by Walker [172], in which the deposition of BIFs leads to a methane-rich atmosphere. Our results further imply that cell-Fe(III) separation augments marine methane production through the breakdown of photoferrotrophic biomass and mechanistically ties biospheric methane fluxes to the deposition of BIF. The role this plays in atmospheric chemistry and greenhouse warming should be tested through further biogeochemical-photochemical modeling efforts.

4.4 Methods

Photoferrotrophic strains and cyanobacteria were grown in basal media [48] and in alternative media (AppendixA and A.1) until late exponential phase. Sub-samples of both Fe(II)/Fe(III) and pigments were used to track the growth kinetics as well as to assess the *in vitro* cellular association to Fe(III). The surface properties of each strain and their metabolic Fe(III) byproducts were assessed

by measuring their surface potential using a Particle Metrix:ZetaView©. The acid-base properties cell surfaces were determined through titrations. Cell surface contact angles were measured for DVLO modelling in three different liquids – water, glycerol, and diiodomethane [225, 227]. Electron microscopies (SEM and TEM) were used to image cell-mineral interactions (AppendixA). The particle sizes of the Fe(III) (oxyhydr)oxides produced by the photoferrotrophic strains were measured using a Mastersizer2000, and these were then used to model the impact of horizontal ocean current velocities on the settling time of both Fe(III) particles and cellular biomass (SI, A.6, A.4). The box model of the Archean marine carbon and iron cycles was designed with three boxes (each representing an oceanic province) to capture variability in fluxes through each box (SI, Fig. 4.4, 4.5, A.8, and Table 4.1).

4.5 Supplementary materials

- Materials and Methods
- Section 1: Cell surface features and acid-base chemistry
- Section 2: Cell-iron surface interaction and extended DVLO modeling
- Section 3: Iron concentration and supply
- Section 4: Physical separation of ferric iron oxyhydroxides and cellular biomass in an ocean setting
- Section 5: Box model of Archean marine carbon and iron cycles
- Section 6: Organic carbon burial and diagenesis
- Table A1: Media concentrations
- Table A2: Cell surface characteristics
- Table A3: Modern and Archean Fe fluxes
- Table A4: Physical separation model results

- Table A5: Data compilations for Fig. 4.1 and A.1
- Fig. A1: BIF redox state
- Fig. A2: Growth curve for *Chlorobium phaeoferrooxidans* strain KB01
- Fig. A3: Additional SEM and TEM images of strains KB01 and KoFox
- Fig. A4: Surface charge of strains KB01 and KoFox
- Fig. A5: Additional cell surface characteristics
- Fig. A6: Fe particle aggregation and physical separation model results
- Fig. A7: Modelled weight % organic carbon
- Fig. A8: Iron and carbon box model sensitivity results

Chapter 5

Microbial community metabolism and coupled carbon and iron cycling in ferruginous environments

5.1 Summary

Models of Precambrian microbial communities and their impact on global geochemical cycles over 3 billion years of Earth's history remain almost entirely conceptual. This is due to a lack of information from environments with biogeochemistry extensible to iron-rich (ferruginous) oceans. Kabuno Bay, a sub-basin of Lake Kivu in East Africa, is one of the few permanently stratified ferruginous environments on the planet today. Process rate measurements and tag sequencing suggest a tight coupling between the primary producing photoferrotrophic bacteria and heterotrophic iron reducers. This tight coupling dictates the export of Fe(III) and the distribution of carbon to other microbial metabolisms, such as methanogenesis. While the role of the photoferrotrophic Chlorobia in Fe(II) oxidation has been established, the pathways through which carbon is channeled from primary production to terminal oxidation, as well as the organisms responsible for each pathway, remain largely unknown. Yet, it is the flow of carbon through these pathways that dictates the relative rates of iron export and methane production in Kabuno Bay. To gain molecular level insight into coupled C and Fe cycling we conducted metagenomic analyses to map metabolic pathways at the population and community level. These pathway-centric analyses highlight the abundance of key genes involved in carbon degradation and fermentation that dominate the overall metabolic potential of the microbial community. They

also elucidate the abundance of multiple modes of photosynthesis coupled to the oxidation of Fe(II), H_2S, H_2, or H_2O. Kabuno Bay hosts largely unknown taxa, such as Candidate phyla MBNT15 and Patescibacteria that predominantly support the C degradation and fermentation pathways in the chemocline. The analyses further highlight previously identified taxa, such as members of the phylum Bacteriodetes, that couple the metabolic potential for C degradation, fermentation, and Fe(III) reduction in individual microorganisms. This tight coupling between C degradation, fermentation, and respiration pathways leads to little carbon leakage for alternative microbial metabolisms, such methanogenesis. Ultimately, our metagenomic analyses reveal mechanistic aspects of coupled C and Fe cycling that likely supported microbial communities across vast stretches of Earth's early history. The metabolic potential and process rates of the microbial community found in Kabuno Bay, thus lays the groundwork for the elucidation of the relationships under the naturally complex ferruginous conditions and can be used to inform models of C and Fe biogeochemical cycling throughout the Precambrian Eons.

5.2 Introduction

Microbial community networks drive global biogeochemical cycles in modern environments and have done so throughout Earth's history [3, 146, 239]. Microorganisms possess the metabolic potential to utilize organic and inorganic substrates for growth resulting in reduction-oxidation (redox) transformations [3]. These redox transformations mediate both large- and small-scale processes in a number of systems on Earth's surface [3, 240], dictating, therefore, the export and import of key substrates to and from modern environments. Through these mechanisms microbial community networks play a key role in processes such as climate regulation [241–243], the availability of bio-essential nutrients [3], and mineralization to form ore bodies [221, 240, 244]. While many studies have been conducted on microbial community networks under a diverse set of modern conditions—both oxic [245–247] and anoxic [248–252]—–very few modern environments are similar to those that prevailed throughout Earth's early history. Modern environments are often oxygen-rich, permeated by ephemeral pockets of anoxia, and this restricts the extensibility of information that can be gleaned from modern environmental microbial communities to the past.

Oceans throughout much of Earth's history were oxygen-free and were, thus, dominated by iron-rich (ferruginous) conditions for much of Earth's first three billion years [5, 22, 23, 83, 170, 171]. Prior to the oxygenation of the Earth's atmosphere and oceans, due to the proliferation and diversification of oxygenic photosynthetic microorganisms [16, 99], atmospheric oxygen concentrations ranged from 0.01 to 1 % of present atmospheric levels (PAL) [2, 15, 28]. Under such reducing conditions, much of the ocean remained anoxic with small bouts of euxinia permeating largely ferruginous conditions [5, 23, 171]. Geologic evidence for these ferruginous conditions comes from the world's largest iron ore deposits——banded iron formations (BIFs)——as well as a plethora of iron-rich deposits, such as ferruginous shales [4, 5, 83, 253]. Data from these deposits combined with models of early Earth oceans indicate that there were high concentrations of ferrous iron (20-100 μM) throughout the Archean Eon and the majority of the Proterozoic Eon [5, 23]. Furthermore, evidence from the isotopic and fossil records [100–102], as well as data from molecular clock reconstructions [12, 254] indicate that microbial communities would have thrived under these ferruginous conditions, thus establishing the biogeochemical cycling of major elements such as carbon and iron [1].

Little is known, however, about microbial community networks and interactions under such ferruginous conditions. Laboratory studies using pure microbial cultures have provided a wealth of information on the metabolic pathways that likely underpinned biogeochemical cycling in Precambrian ferruginous oceans [21, 55, 109, 115]. Pure culture studies, for example, allow us to use information on the physiology of extant microorganisms to make predictions about the possible rates and pathways of key biogeochemical reactions in the Precambrian oceans. These estimated rates can be compared with the material fluxes preserved in the rock record [8, 21, 55, 224]. There are limits to the data that can be collected from pure culture studies, however, as they are constrained to a single bacterium and outcomes are often dictated by the set laboratory conditions. These studies often fail to mimic conditions that are pertinent to the Precambrian Eons and can also misrepresent the growth of an individual microorganism due to excess essential nutrients that accentuate growth or even allow growth where the natural conditions would limit it. Furthermore, pure culture studies fail to capture the relationships between multiple species within a microbial community. To address some of the limits of pure culture studies, studies of

community level processes in modern analogue environments provide real world evidence of biogeochemical cycling under ferruginous conditions and, in particular, reveal coupled elemental cycling through pathways distributed across multiple taxa [48, 64, 68, 70, 71].

Collectively data from both pure cultures and modern analogue environments provide a framework for model-based reconstructions of microbial community processes in the Precambrian oceans [8, 21, 95, 96, 99, 107]. These model-based reconstructions often combine process rates with the inferred processes (from pure culture studies) associated with individual members of the microbial community. These combined data products thus produce conceptual models of the key microorganisms that are integral in the cycling of major elements such as carbon and iron. The framework produced through these conceptual models, however, fails to fully capture the complexity of natural systems and the iterative relationships often needed by members of the microbial community (syntrophy) to complete the biogeochemical cycling of key elements — i.e. carbon. This lack of mechanistic knowledge on microbial community functioning ultimately limits the extent to which models of Precambrian ocean biogeochemical cycling can resolve processes that control key features of the Earth system, like climate. In particular, knowledge on how organic carbon degradation is partitioned between iron reduction and methane production is needed to constrain connections between Precambrian microbial communities and their suggested role in the maintenance of a clement climate [95, 99]. New information on microbial community structure and function under ferruginous conditions is thus needed to improve models of biogeochemical cycling in the Precambrian oceans.

To link the microbial communities in ferruginous lakes to the Precambrian oceans, previous studies have elucidated the community members potentially involved in aspects of carbon cycling and other metabolisms such as methanogenesis and iron reduction through taxonomic identification [48, 64, 68]. Of the ferruginous environments examined, Kabuno Bay is the only one to date with a dominant population of anoxygenic phototrophic iron oxidizing bacteria (photoferrotrophs) acting as primary producers [48, 64, 68]. Examining a microbial community with an established anoxygenic phototroph producing primary carbon is crucial as photoferrotrophs likely supported the microbial biosphere during the Archean before the evolution and proliferation of oxygenic photosynthetic bacteria – the ancestors to canonical cyanobacteria [16, 96, 99]. The identification of

other key taxa such as *Rhodoferax* (laboratory cultures are known iron reducers) and *Desulfobacca* (sulfate reducers) paved the way for a conceptual model highlighting the putative cycling of carbon and iron in Kabuno Bay [48]. While utilizing taxonomy to identify metabolic potential can effectively resolve the abundance and presence of community members, this technique relies on the metabolic potential of laboratory isolates to discern the metabolisms or genomic functions of the microorganisms that are present. As such, the true metabolic potential of the community remains enigmatic. Additionally, aspects of the Kabuno Bay conceptual model——i.e. the microbial consortia responsible for carbon degradation and therefore availability——remain woefully underrepresented. Thus, the overall metabolic blueprint and the presence of this potential within key microbial guilds has yet to be tested.

Here we utilize metagenomic analyses to discern the metabolic blueprint of the microbial populations in Kabuno Bay with specific targeted analyses to demonstrate the mechanism for a tight coupling between the carbon and iron biogeochemical cycles. Specifically, we examined the microbial networks responsible for production of organic carbon (OC) by primary producers, OC degradation, and the coupling of OC to key elements such as iron. Given that carbon and iron processes can be traced through time in the geologic record, elucidating microbial community dynamics under ferruginous conditions can be extrapolated to the past. These analyses, combined with geochemical analyses and processes rate measurements, therefore, provide insight into how microbial populations could have thrived under Precambrian oceanic conditions.

5.3 Materials and methods

5.3.1 Kabuno Bay site description and sampling

Kabuno Bay (KB), a sub-basin of Lake Kivu, is located in the Democratic Republic of Congo (DRC) located at 1.58°-1.70° S, 29.01°-29.09° E in the East African Rift system (B.1). KB is permanently stratified basin with a maximum depth of 120 m and a 10 m sill that connects it to adjacent Lake Kivu. Water samples were collected from multiple depths throughout the water column, with the focus being the oxic-anoxic transition zone, during four sampling trips in February 2012 (rainy season) using a battery-driven peristaltic pump connected to a weighted-double conical intake

through plastic pumping [48]. Water samples were immediately processed for chemical analyses or filtered for molecular analyses [48].

5.3.2 Physio-chemical analyses

Vertical depth profiles of conductivity, temperature, pH, and oxygen were measured in situ with a Hydrolab DS5 (OTT Hydromet, Germany) multiparametric probe [48]. Water samples for iron speciation ($Fe(II)_{aq}/Fe(III)_s$), sulfate (SO_4^{2-}), sulfide (HS^-), and cell counts, were collected at multiple depths and measured as described under analytical techniques. Cylindrical sediment traps with a 0.22 μm filter (diameter of 8 cm) were placed at a depth of 15 m and deployed for 56 hours to capture particulate matter as it settled out of the water column. The filters were kept under anoxic conditions and frozen at -20° until extraction. The particles were subsequently extracted and measured as described in analytical techniques.

5.3.3 Iron oxidation, iron reduction, and sulfate reduction rates

Fe(II) oxidation rates were measured *ex situ* in 100 mL glass syringes that were illuminated with 15 μmol m^{-2} s^{-1} light (supplied by 60 W incandescent light bulb) throughout the incubation. All syringes were amended with 50 μM Fe(II) and half were amended with DCMU, a known inhibitor of photosystem II and oxygenic photosynthesis (3-(3,4-dichlorophenyl)-1,1-dimethylurea or DCMU, 0.5 mg L^{-1}). Sub-samples were collected throughout the course of the incubation to track Fe(II), Fe(III), pigments, and cell counts, which were subsequently measured as described in analytical techniques. Fe(II) oxidation rates were calculated from both the consumption of Fe(II) and production of Fe(III) using a least squares regression through the linear portion of the incubation with the rate of Fe(II) oxidation derived from the slope of the regression. Fe(II) oxidation and Fe(III) reduction rates were also measured through *ex situ* incubations where 100 mL glass syringes were subjected to alternating light and dark cycles. These syringes were amended with 60 μM Fe(II) and subjected to 1 to 3 μmol m^{-2} s^{-1} light during the light cycle. Sub-samples were collected throughout the course of the incubation to track Fe(II), Fe(III), pigments, and cell counts, which were subsequently measured as described in analytical techniques. Rates of oxidation and reduction were calculated from the changes in Fe speciation during the linear

portions of each cycle.

Sulfate reduction rates were measured using $^{35}SO_4^{2-}$. Water was collected in 250 ml glass serum bottles, which were overflowed 3x and capped with blue butyl rubber stoppers with no headspace. Within six hours, ~370 kBq of $^{35}SO_4^{2-}$ was injected into each bottle. The bottles were incubated in the dark and at approximately in situ temperature for 24 hours, after which the incubation was terminated with the addition of 5 ml 20 % zinc acetate. A small portion was collected for sulfate activity measurements. The ZnS produced was filtered onto GFF glass fiber filters, which were well washed with distilled water and frozen. Frozen filters were distilled with 1 N HCl and reduced Cr solution, and the liberated sulfide was recollected in zinc acetate. The activities of the sulfate and ZnS were measured by scintillation counting. This method produced a negligible counting blank in the sulfide activity counts.

5.3.4 Analytical techniques

Sub-samples from both the KB water column and from incubation experiments were analyzed for Fe(II) and Fe(III) concentrations using spectrophotometric analyses. Specifically, Fe(II) and Fe(III) concentrations were measured using the ferrozine method and samples were measured directly as well as after being fixed in 1 N HCl – after Voillier et. al., 2000 [133]. Additional sub-samples were taken from the incubation experiments to measure the pigment concentrations. Pigments were measured spectrophotometrically after 24 hour extractions of 1 mL of pelleted cells in acetone:methanol (7:2 v/v) [134]. Further sub-samples from both the KB water column and from incubation experiments were taken and cells were fixed in gluteraldehyde (final concentration of 0.1 %). After the cells were fixed, they were subsequently stained with SYBR green (0.25 % final concentration) and directly counted in a 96 well plate using a Miltenyi Biotec MACSQuant, with a flow rate of medium.

Sub-samples from the KB water column were analyzed for their sulfate concentrations. Sulfate concentrations were measured using ion chromatography (Thermo Scientific Dionex, ICS-2100) with a Dionex Ion PacTM AS19 RFICTM analytical column (2 x 250 mm). Sample concentrations were quantified by comparing the peak area samples to those of standard solutions. Sub-samples from the KB water column for sulfide measurements were preserved with 5 μL of 20 % (w/v)

zinc acetate per mL of sample. Sulfide concentrations were determined using the methylene blue assay [255], which was calibrated using the standard iodometric titration to determine the specific absorbance of the methylene blue reagent. To measure sulfide, 80 μl of the methylene blue reagent was added was added to 1 mL of sample. The samples incubated with the reagent for 15 minutes and were measured spectrophotometrically at a wavelength of 670 nm.

Fe-speciation measurements were performed on anaerobically preserved and freeze dried sediment samples following the method of Poulton and Canfield [25]. Fe-speciation was conducted on sediment trap material by applying each extraction, described in B.1 [25], directly to filters within the 15 ml centrifuge tube. 0.5 M HCl was substituted in place of the hydroxylamine hydrochloride leach (B.1) so that both Fe(II) and Fe(III) could be determined in this reactive (oxyhydr)oxide fraction. A sub-sample of the 0.5 N HCl extracted fraction [256, 257] was retained and used to measure Fe-speciation on these easily extractable phases spectrophotometrically using the ferrozine assay [133]. The highly reactive, "Fe_{HR}" pool is defined as the sum of (oxyhydr)oxides including ferrihydrite, lepidocrocite, and siderite (Fe_{HCl}, 0.5 N HCl extractable Fe), ferric (oxyhydr)oxides including hematite and goethite (Fe_{Dith}, dithionite extractable Fe), and magnetite (Fe_{Oxa}, oxalate extractable Fe). The non-reactive, "Fe_{NR}" pool is attributed to Fe in silicate minerals (Fe_{Sil}, near boiling 6 N HCl extractable Fe after removal of reactive phases). Fe concentration measurements were performed using a Flame Atomic Absorption Spectrophotometer (Flame AAS). Precision on triplicate measurements was < 1 % (2SD) and our limit of detection was $\sim$0.1 μg g^{-1}. Our extractions dissolved > 92 % of the Fe from the PACS-2 international reference standard.

5.3.5 Flux calculations

To calculate water column Fe fluxes, area specific Fe sedimentation rates were determined by dividing the concentration of Fe captured by the sediment trap in each operationally defined mineral phase (mmol), by the area of the sediment trap (0.005 m^2) and the deployment time to yield Fe fluxes in units of mmol m^{-2} yr^{-1}.

5.3.6 DNA extraction

250 mL of water was collected from each of the five depths throughout the chemocline (10 m, 11 m, 11.25 m, 11.5 m, and 12 m), was filtered through a 0.22 μm filter, and frozen at -20°C . DNA was extracted from the biomass collected on these filters by enzymatic lysis and a phenol:chloroform purification [258]. At the end of the extraction the DNA was washed twice with TE buffer [258] and quality checked through polymerase chain reaction (PCR). The quantity and purity of the final DNA products were verified using a NanoDrop 1000 spectrophotometer (Thermo Scientific) and the Picogreen© (Invitrogen) assay according to manufacturer's instructions (Quant-iT^{TM} dsDNA Assay Kit, 2018). TE buffer (10 mM Tris-HCl, 1 mM EDTA, pH 7.5) was used for diluting the Quant-iT^{TM} PicoGreen© reagent, and for diluting DNA samples.

5.3.7 Metagenome sequencing and assembly

Each water column DNA sample (5 total) was sequenced at the DOE Joint Genome Institute (JGI) where it was subjected to Illumina paired-end library construction and sequenced (HiSeq platform, version 3 chemistry) to generate a total of 95 Gb of paired 150-nucelotide (nt) reads. JGI quality trimmed sequences were assembled *de novo* using the MEGAHIT version 1.2.7 assembly algorithm [259]. All samples were assembled individually. To assess the abundance of each assembled contig within the metagenomic sample, a redefined version of the RPKM (reads per kilobase mapped) calculation was applied to each contig [196]. With each contig's abundance being affected by sequencing depth (may vary between samples) and contig length (longer contigs naturally encompass more reads), this bwa-based version of the RPKM [260] aims to normalize these differences. The RPKM for a given contig is thus:

$$RPKM = \frac{\frac{Readsmappedtocontig}{Contiglength(kb)}}{\frac{Readsmappedtowholemetagenomesample}{10^6}} \tag{5.1}$$

5.3.8 16S rRNA reconstruction

To reconstruct community profiles from the metagenomic sequences, EMIRGE [261, 262] was run on each assembled metagenome utilizing the baseline parameters [261, 262]. The final set of 16S

rRNA gene sequences reconstructed through EMIRGE were subsequently annotated through a comparison with the DADA2 16S rRNA database (Fig. 5.2a; [263]). Other 16S rRNA sequences were retrieved from members of the class Chlorobia from the Silva online database –– version 128 [117, 118]. Only full-length (>1400 bp) sequences were selected, and then aligned using the package software ClustalX2.1 [119]. To rigorously test the evolutionary history of the Kabuno Bay 16S rRNA sequences annotated as class Chlorobia with the database of sequences previously annotated as class Chlorobia, multiple tree construction methods were employed (Bayesian, Maximum likelihood (ML), Maximum parsimony (MP)). ML and MP trees were constructed in MEGA version 7 [120, 121], while the Bayesian tree was constructed in Geneious [264] and all trees bootstrapped 500 times. Bootstrap values are indicated at the nodes and the legend (2.0) delineates the nucleotide substitutions per site over the indicated distance (Fig. 5.2c). To assess the absolute abundance of the members of the microbial community, the relative abundance of each 16S rRNA gene at each depth, generated through EMIRGE [261, 262], was multiplied by the total cell counts for that depth. 16S rRNA genes from the same taxonomic units (e.g. phyla or class) were summed to delineate their representation within the whole community (Fig. 5.2a).

5.3.9 Gene searches

To search for specific genes, open reading frames (ORFs) were predicted for each individually assembled metagenome (5 depths – 10 m, 11 m, 11.25 m, 11.5 m, and 12 m) using Prodigal [125]. To assess the abundance of each of these ORFs, the RPKM value (see above) for the contig that contained each ORF was pulled and assigned to that ORF. These ORFs were subsequently searched for the sequences of genes of interest using either BLAST (e-value cut-off of 1 x 10^{-18}, followed by a Bit Score cut-off of 50 [131]) or HMMER's hmmsearch function (e-value cut-off of 1 x 10^{-18} and length cut-off of 50 % [132]). The described cutoffs were used for all of the genes, with the exception of the 'Paired_CXXCH' which had length cut-off of 100 %. The sequence or HMM model for each gene of interest was pulled from the *Chlorobium phaeoferrooxidans* strain KB01 genome [58], the National Center for Biotechnology Information database (NCBI — https://www.ncbi.nlm.nih.gov/), the Fungenes repository [265], the Pfam database [129], or the CAZy databases [130] The genes of interest, their general function, and the database used to

obtained their sequence or HMM model are listed in B.2. To assess the abundance of a specific gene relative to the overall metabolic potential of the microbial community, the RPKM of a gene of interest was summed for a particular depth, compared to the summed RPKM of the single copy taxonomic marker gene rpoB, and reported as a percent.

5.3.10 Metagenome assembled genomes

To reconstruct population genomes or metagenome assembled genomes (MAGs) the assembled metagenomic contigs were recruited into MAGs using MaxBin version 2.0 [266], with the baseline parameters [266]. The completeness and level of contamination of each MAG was calculated with CheckM version 1.1.0 [267], which uses a set of specific and conserved marker genes to analyze each MAG. The Q-score was calculated for each MAG by subtracting the contamination multiplied by five from the completeness. Only MAGs with a Q-score of greater than 50 were kept for downstream processing. Additionally, the taxonomy of each MAG was determined by comparing the marker genes in each MAG to a genome taxonomy database (GTDB-Tk; [268]). To assess how well the MAGs represented the overall microbial community, the metagenomic trimmed reads from each depth were mapped (bwa-based mapping) to the MAGs recovered from each depth. The read coverage of the MAGs ranged from 3 to 36 % (B.3). The number of MAGs recovered per phyla or class was also compared to the depth integrated absolute abundances of the microbial community (B.6) — MAGs from each of the most abundant groups were recovered albeit not at the same abundances as the microbial community would dictate.

To partition specific metabolisms across the relevant members of the microbial community the same gene searches as described above were conducted within the individual reconstructed MAGs. The abundance of a specific gene or process within the MAGs was determined by summing the RPKMs for the gene of interest from the MAGs alone and comparing it to the sum of the single copy *rpoB* gene from the MAGs. To identify regions with identical nucleotide sequences in genome of *Chlorobium phaeoferrooxidans* strain KB01 and the *Chlorobium* sp. MAG, the contigs of both the strain and MAG were aligned and compared using MUMmer (nucleotide comparison with nucmer – [123]) and visualized using Circos (http://circos.ca/). The whole genome of strain KB01 was retrieved from GenBank with the accession number MPJE00000000 [58]. To examine

the relationship between these pathways in representative, relatively abundant members of the microbial community we selected 30 near or mostly complete MAGs (Table 5.1) some of which were previously implicated as key members of the community [48] and conducted further analyses on the specific pathways present (Fig. 5.4a, 5.4c, 5.5, B.6, B.7, B.8). To compare the similarities and differences between the higher level pathways in 30 of key MAGs from Kabuno Bay, open reading frames (ORFs) for each MAG were predicted using Prodigal [125]. The predicted ORFs were subsequently annotated using the online tool Kofam Koala [126] that uses Hidden Markov-Models (HMMs) to compare each ORF those found in the Kyoto Encyclopedia of Genes and Genomes database (KEGG-11-06-18) [127]. The resulting annotations were compared at the pathway level and visualized through a python script as described in Graham et. al., 2018 [128] -– B.6, B.7.

5.4 Results

5.4.1 Biogeochemical and physical properties of Kabuno Bay

Kabuno Bay is an anoxic and ferruginous (Fe-rich) sub-basin of Lake Kivu located on the border of the Democratic Republic of Congo and Rwanda (B.1). Kabuno Bay is permanently stratified (Fig. 5.1a) with anoxic deep waters (Fig. 5.1b) and this stratification is sustained by volcanic seeps with high concentrations of salts and geogenic gases, as reflected in the high conductivity below 10 m (Fig. 5.1a). These lead to strong density differences between the surface and deep waters that preclude wind or temperature driven mixing. This physical stratification causes chemical stratification, which is revealed, for example, by the disappearance of oxygen to undetectable levels (detection limit of 0.6 μM) below approximately 10 m (Fig. 5.1b) and the accumulation of high concentrations of ferrous iron (Fe[II]), up to 1.2 mM (Fig. 5.1b), and some sulfide (< 10 μM — Fig. 5.1c) in deeper waters. Particulate ferric iron (Fe[III]), accumulates in the upper reaches of the chemocline with concentrations up to 100 μM (Fig. 5.1b), but Fe(III) concentrations decline sharply below 12 m depth (Fig. 5.1b). The strong gradient in Fe(II) and corresponding accumulation of Fe(III) demonstrates net Fe(II) oxidation to Fe(III) between 10 and 12 m, while the decrease in Fe(III) concentrations between 11 and 12 m demonstrates Fe(III) reduction and a partial to closing of the iron cycle in the chemocline. Modest sulfate concentrations persist throughout the water

column (< 600 μM) with a small peak in the chemocline (Fig. 5.1c). Thus, the combination of physical stratification driven by groundwater seeps and the high concentrations of Fe and low sulfide give rise to persistently ferruginous conditions below $\sim$10 m depth and the concentration profiles of Fe(II) and Fe(III) in the upper reaches of the chemocline reveal spatially coupled Fe oxidation and reduction reactions.

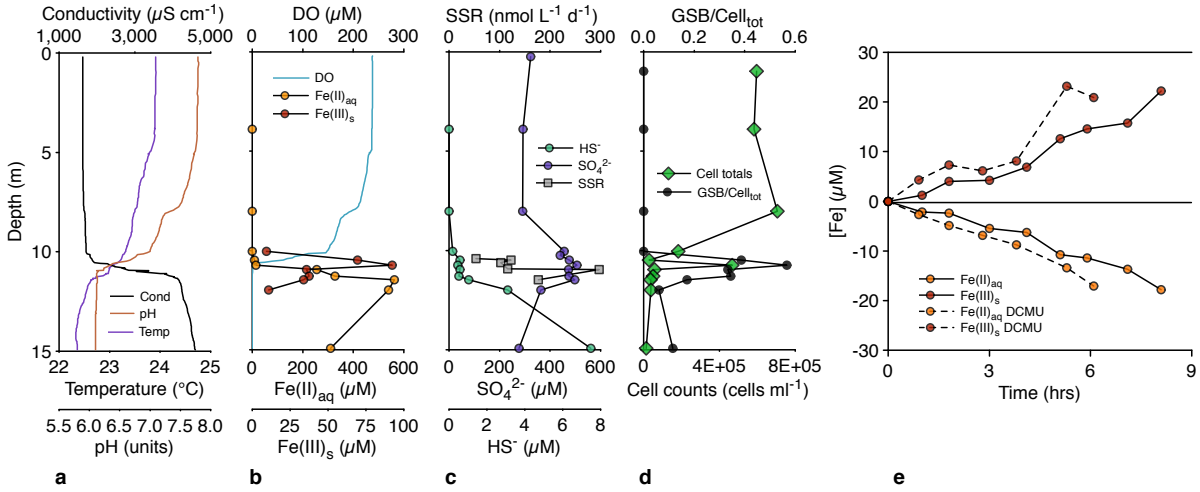

Figure 5.1: *Depth profiles from Kabuno Bay* delineating conductivity, temperature, and pH (a); dissolved oxygen (DO), aqueous ferrous iron ($Fe(II)_{aq}$), and solid ferric iron ($Fe(III)_s$) (b); sulfate (SO_4^{2-}), sulfide (HS^-), and sulfate reduction rates (SSR) (c); cell counts and green sulfur bacteria specific cell counts compared to total cell counts ($GSB/Cell_{tot}$) (d); and phototrophic Fe(II) oxidation over time with and without the oxygenic photosynthesis inhibiter DCMU (e). Note: Light was attenuated to 0.1 % PAR at 10 m during other sampling trips to Kabuno Bay [48]

Much of the Fe(II) oxidation in Kabuno Bay is driven by anoxygenic photosynthesis and is tightly coupled to Fe reduction. Net Fe(II) oxidation rates calculated from both Fe(II) consumption and Fe(III) production agreed well and were $\sim$3 μmol L^{-1} h^{-1} (Fig. 5.1e). Importantly, net Fe(II) oxidation rates were similar in the presence and absence of DCMU (2.4 ± 0.2 μmol L^{-1} h^{-1} without DCMU compared to 3.1 ± 0.4 μmol L^{-1} h^{-1} with DCMU; Fig. 5.1e), a specific inhibitor of photosystem II [269], demonstrating the Fe(II) oxidation is driven entirely by photosystem I through anoxygenic photosynthesis. Comparisons between illuminated and dark phases in parallel incubations revealed both that Fe(II) oxidation is entirely photosynthetic and is also tightly coupled to Fe(III) reduction. In these incubations, gross Fe(II) oxidation rates were 0.5 ± 0.05 μmol L^{-1} h^{-1}, while Fe(III) reduction rates were 0.4 ± 0.04 μmol L^{-1} h^{-1}. Thus approximately 80

% of the Fe(III) produced during oxidation is immediately reduced demonstrating tight coupling between iron oxidation and reduction in Kabuno Bay.

Appreciable particulate Fe(III) and Fe(II) is exported from Kabuno Bay's chemocline, despite the tight coupling between Fe oxidation and reduction in the upper chemocline. Fe speciation measurements of particulate matter exported from the chemocline demonstrate that 97 % of the Fe is present in forms generally considered reactive towards microbial metabolisms and low temperature biogeochemical reactions, and this fraction had an overall redox state of 2.8. An appreciable fraction of this reactive exported Fe (20 %) was thus in Fe(II) phases. The majority of the exported Fe(III) (63 %) was extractable in 1 N HCl, a fraction generally considered abundantly available to microorganisms and often comprised of phases like ferrihydrite [270–272]. Notably, however, the HCl extractable fraction also contained appreciable Fe(II) with an average redox state of 2.7, revealing export of mixed-valence or Fe(II) phases like green-rust or siderite. Additional highly reactive Fe(III) was present as dithionite extractable phases (27 %) like goethite or hematite and oxalate extractable phases (5 %), essentially magnetite [273]. Based on these data, the flux of highly reactive Fe(III) mineral phases from the water column is 0.4 mol m^{-2} yr^{-1}, which is within error of the difference between the Fe(II) oxidation (4.4 $\pm$ 0.4 mol m^{-2} yr^{-1}) and Fe(III) reduction (3.5 $\pm$ 0.4 mol m^{-2} yr^{-1}) fluxes calculated from directly determined rates. These data therefore confirm appreciable export of reactive Fe(III) from the Kabuno Bay euphotic water column, despite the fact that photosynthetic Fe oxidation is tightly coupled to reduction reactions.

Sulfate reduction was also prevalent throughout Kabuno Bay's chemocline, occurring concomitantly with appreciable Fe-reduction, albeit at much lower rates. The rate of sulfate reduction peaked at approximately 11.5 m with a rate of 300 nmol L^{-1} d^{-1} (Fig. 5.1c), which is 40 times lower than the corresponding Fe(III) reduction rates (12000 nmol L^{-1} d^{-1}). The much lower rates of sulfate reduction demonstrate that it can only play a minor role in Fe-reduction. Fe-reduction, therefore, must be directly coupled to microbial respiration. Export of pyrite from the chemocline is 6 mmol m^{-2} yr^{-1} and, compared to depth integrated sulfate reduction rates of 90 mmol m^{-2} yr^{-1}, reveals appreciable S recycling. Thus, sulfate reduction and cycling is active throughout Kabuno Bay's chemocline, where it influences Fe speciation by driving pyrite formation, but it plays a quantitatively minor role in anaerobic respiration compared to Fe-reduction.

5.4.2 Microbial community composition and structure

The microbial community in Kabuno Bay's chemocline is overwhelmingly dominated by anoxygenic photosynthetic bacteria of the class Chlorobia and includes representation from a broad suite of bacterial phyla as well as a limited diversity of Archaea. Microbial community sizes are relatively constant at 10^4 to 10^5 as a function of depth throughout the chemocline (Fig. 5.1d). The population of Chlorobia is well delineated by profiles of BChl *e*, a photosynthetic pigment produced exclusively by members of the class Chlorobia. The distribution of BChl *e* is abruptly truncated by the oxygenated surface waters, peaks at 11 m depth, and decreases in size with increasing depth below this peak as light intensity falls [48]. The taxonomic composition of the microbial community, based on the small subunit ribosomal RNA gene (16s rRNA) (Fig. 5.2a, B.2), reflects the distribution of BChl *e* with the Chlorobia peaking at 11 m (47 % of the whole community; Fig. 5.2a). This is similar to reconstructions of microbial community compositions from amplicon-based community profiling [48]. Likewise, the high relative and absolute abundance, up to 50 % of the community, was also reflected in reconstructions based on other phylogenetic marker genes, such as *recA* and *rpoB* (Fig. B.3a). The rest of the community is mostly comprised of members of 11 other bacterial phyla and Archaea (based on 16S rRNA gene-based reconstructions; Fig. 5.2a). The most striking vertical differences in community composition occur between 10 m and the deeper depths combined, notably the higher abundances of Alphaproteobacteria, Gammaproteobacteria, Actinobacteria, and Cyanobacteria at 10 m (Fig. 5.2a, B.2). Indeed, at 10 m the Gammaproteobacteria make up 60 % of the microbial community compared to only 5 % in the deeper depths (Fig. 5.2a). Below 10 m there is very little depth-dependent structure in the overall community composition, as three main phyla — Bacteriodetes (broken into its three classes — Bacteroidia, Chlorobia, and Ignavibacteria), Candidate phyla MBNT15, and the Patescibacteria dominate at each depth (Fig. 5.2a, B.2). The only exception, in the deeper depths, is the progressive decrease in the relative abundance of the class Chlorobia with increasing depth. The phylum Bacteriodetes is the most abundant phylum (53 %) in the deeper chemocline depths (11 m to 12 m; Fig. 5.2a) and of the three classes that comprise the phylum Bacteriodetes, the members of class Chlorobia were most abundant——representing 36 % of the overall community

in the deeper depths (Fig. 5.2b). Notably, members of the candidate phylum MBNT15 and the relatively unknown Patescibateria made up another 22 % of the deeper chemocline (9 % and 13 % respectively; Fig. 5.2a). Conversely, Archaea represent a maximum of 2 % of the whole microbial community (at 11 m), and 1.6 % of deeper chemocline community (Fig. 5.2a). Thus, the microbial community in the Kabuno Bay chemocline, and in particular the community that populates the deeper chemocline depths, is dominated by few groups, including the abundant Chlorobia.

The dominant organisms representing the class Chlorobia in Kabuno Bay are comprised of 6 distinct taxonomic lineages, most of which are closely related to known photoferrotrophs. Collectively, the 6 distinct lineages of Chlorobia made up to 50 % of the whole community (approximately 2.7 x 10^4 cells mL^{-1}) at 11 m and between 11 and 40 % at the other depths (Fig. 5.2c, B.2). The 5 most abundant lineages form a closely related, but distinct, clade that contains both known photoferrotrophic Chlorobia, *Chlorobium ferrooxidans* str. KoFox and *Chlorobium phaeoferrooxidans* str. KB01, the latter of which was enriched and isolated from Kabuno Bay [48]. This clade is defined by divergence of 0.4 % and these organisms, therefore, would collectively be classified as strains of the same species according to canonical definitions based on identity in 16S rRNA gene sequences. The microbial community in Kabuno Bay is thus largely made up of highly abundant and closely related, but distinct, lineages of Chlorobia with strong phylogenetic affinity to known photoferrotrophs.

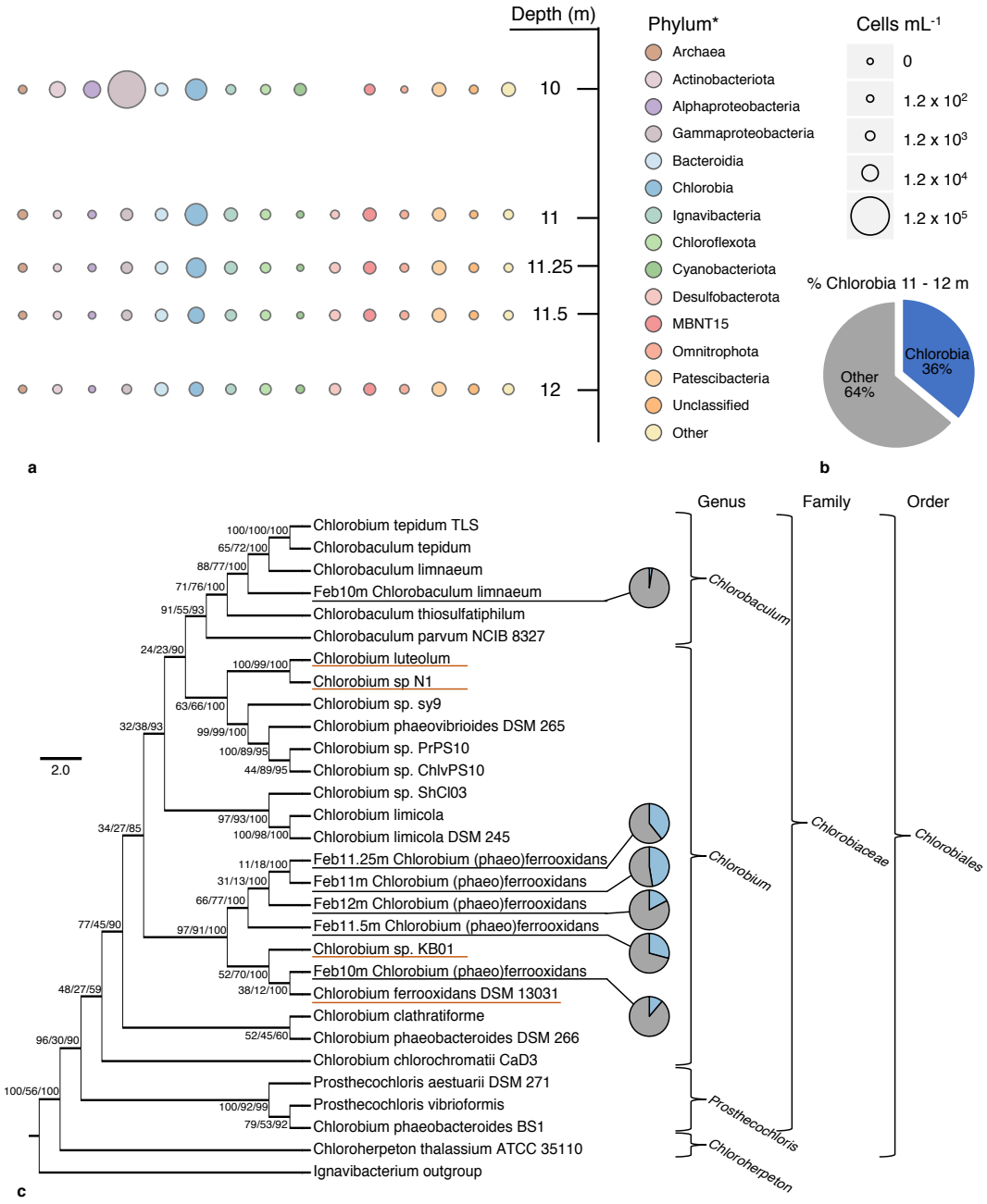

Figure 5.2: *Microbial community composition in Kabuno Bay.* The abundance (cells mL^{-1}) of each phylum (a) based on the reconstruction of the 16S rRNA sequences in the metagenomes. The abundance of the class Chlorobia compared to the rest of the community in the deeper chemocline (11 m to 12 m) (b). Phylogenies of the class Chlorobia 16S rRNA genes and the Chlorobia metagenome reconstructed 16S rRNA genes with bootstrap values shown at each node (maximum parsimony/maximum likelihood/bayesian) (c). Pie charts illustrate the absolute abundance of that individual 16S rRNA gene (blue) compared the whole community for each depth. Photoferrotrophic Chlorobia are underlined in orange. *Phylum Bacteriodetes is shown as its three main classes (Bacteroidia, Chlorobia, Ignavibacteria) and phylum Proteobacteria is shown as two of its classes (Alphaproteobacteria, Gammaproteobacteria).

5.4.3 Photosynthetic and oxidative metabolic potential

The metabolic potential for different modes of photosynthesis exhibited strong vertical structure, with dominance by anoxygenic photosynthesis throughout the chemocline. Genes that are specific to three different modes of photosynthesis — BChl biosynthesis genes (Chlorobia, *BChl_A*), photosystem II (specific to oxygenic photosynthesis, PSII), and reaction center genes (specific to anoxygenic photosynthetic Proteobacteria, *pufM/L*) (Fig. 5.3, 5.4a) – differed in their relative abundance as a function of depth. The collective metabolic potential for photosynthesis, based on the combined relative abundance of these genes, was greatest at 11.25 m (Fig. 5.4a) and was largely due to high relative abundances of the bacteriochlorophyll biosynthesis genes (Fig. 5.3). Indeed, among the photosynthetic genes investigated, the bacteriochlorophyll biosynthesis genes were the most abundant, representing almost 10 % of the total metabolic potential (summed RPKM values for each gene compared to the single copy marker gene *rpoB* — see methods), and up to 20 % of the depth-specific metabolic potential in the mid-chemocline (Fig. 5.3, 5.4a). The depth distribution of bacteriochlorophyll biosynthesis genes was similar to that of the phylogenetic marker genes of the class Chlorobia (Fig. 5.2, B.3a). In contrast, the abundance of the PSII and *puf* genes were very low ($<$ 1 % of the metabolic potential at each depth; Fig. 5.3, 5.4a), but notably, were highest at 10 m and PSII was present throughout the chemocline. Distributions of key photosynthetic genes thus reveal a dominance of photosynthetic metabolic potential by bacteriochlorophyll dependent anoxygenic Chlorobia.

The metabolic potential for electron donor use in anoxygenic photosynthesis was distributed across multiple possible pathways, which were all present at comparable abundances throughout the chemocline. Genes implicated in electron transfer from some inorganic primary electron donors (Fe^{2+} or $S_2O_3{}^{2-}$) to the photosystem include: *cyc2* — putative iron oxidase; *soxB* -– thiosulfate oxidase; *hypA* -– hydrogenase (Fig. 5.3, 5.4a). All three of these genes were found throughout the water column and at comparable abundances, with the abundance of the *cyc2* and *hypA* exhibiting depth distributions (Fig. 5.3, 5.4a) similar to that of the class Chlorobia (Fig. 5.2, B.3a), while the distribution of *soxB* (Fig. 5.3, 5.4a) better reflected that of sulfide concentrations (Fig. 5.1c). Specifically, the *cyc2* genes represented 7 % of the metabolic potential of the whole

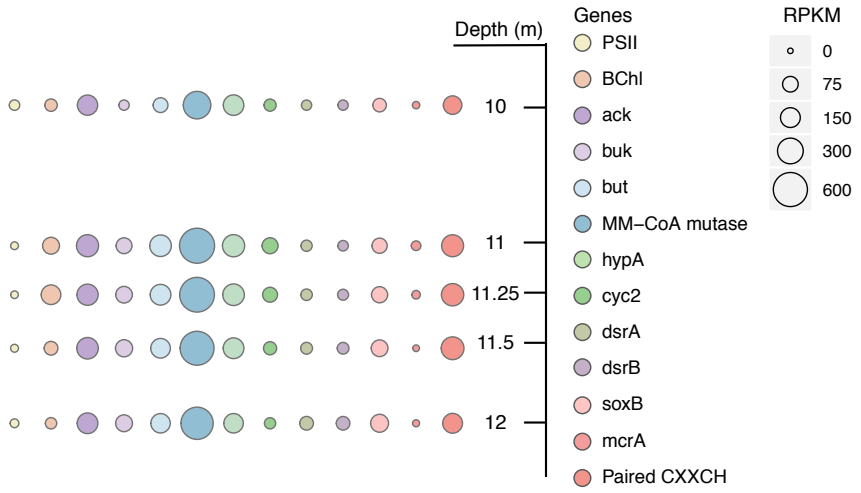

Figure 5.3: *Abundance of key genes predicted to play roles in the biogeochemical cycles in Kabuno Bay* where the size of each bubble represents the total RPKM (Reads per kilobase mapped) for that gene at the specified depth, while the colors delineate each gene.

community, with a peak of 12 % at 11 m (B.4), while *soxB* genes peaked at 12 m and represented 16 % of the community metabolic potential (B.4). The *hypA* genes were the most abundant of the three genes linked to electron donors with a peak of 30 % at 11 m (B.4). The distributions of these genes and those linked to photosynthesis, as described above, resolve metabolic potential for multiple modes of anoxygenic photosynthesis, largely affiliated with the class Chlorobia, throughout the chemocline.

Metabolic potential for multiple modes of photosynthesis is distributed across the genomes of key high- and low-abundance lineages. A large number of high quality population-based metagenome assembled genomes (MAGs) were recovered (Table 5.1) including six individual MAGs that contained the pathways for either anoxygenic or oxygenic photosynthesis. These included three MAGs of Chlorobia, one near-complete MAG closely related to *Chlorobaculum* sp. (Chlorobac_01; 100 % complete, 4.7 % contamination), as well as two partially-complete MAGs (*Chlorobium ferrooxidans* -– Chlorobi_01; 52.8 % complete with no contamination -– and *Chlorobaculum* sp. — 68.3 % complete with 2.2 % contamination) (Table 5.1). All three MAGs contain metabolic potential for anoxygenic photosynthesis including bacteriochlorophyll biosynthesis and carbon fixation genes (Fig. 5.4a, B.7). Both *Chlorobaculum* sp. MAGs contain genes associated with sulfide, thiosulfate, and hydrogen oxidation similar to those identified from

anoxygenic photosynthetic pathways in other members of the *Chlorobaculum* genus (Fig. 5.4a, B.7). The other three, non-Chlorobia, photosynthetic MAGs contained phylogenetic marker genes of three different members the phyla Cyanobacteria (Fig. 5.4a, B.7, Table 5.1; *Neosynechoccaceae*, *Phormidesmiaceae*, and *Pseudanabaena* sp.(Cyano_02)). Like most Cyanobacteria, these photosynthetic MAGs contained necessary genes and pathways for oxygenic photosynthesis (Fig. 5.4a, B.7). Notably, all three of these Cyanobacteria MAGs also contained the genes and pathways for either sulfide/thiosulfate oxidation or hydrogen oxidation (Fig. 5.4a), which indicates that these oxygenic phototrophs also have the metabolic potential for anoxygenic photosynthesis. Metabolic potential for anoxygenic photosynthetic sulfide and hydrogen oxidation in Kabuno Bay is thus present across low-abundance lineages of the Chlorobia and cyanobacteria, whereas the potential for Fe oxidation is absent from all photosynthetic MAGs (Fig. 5.4a).

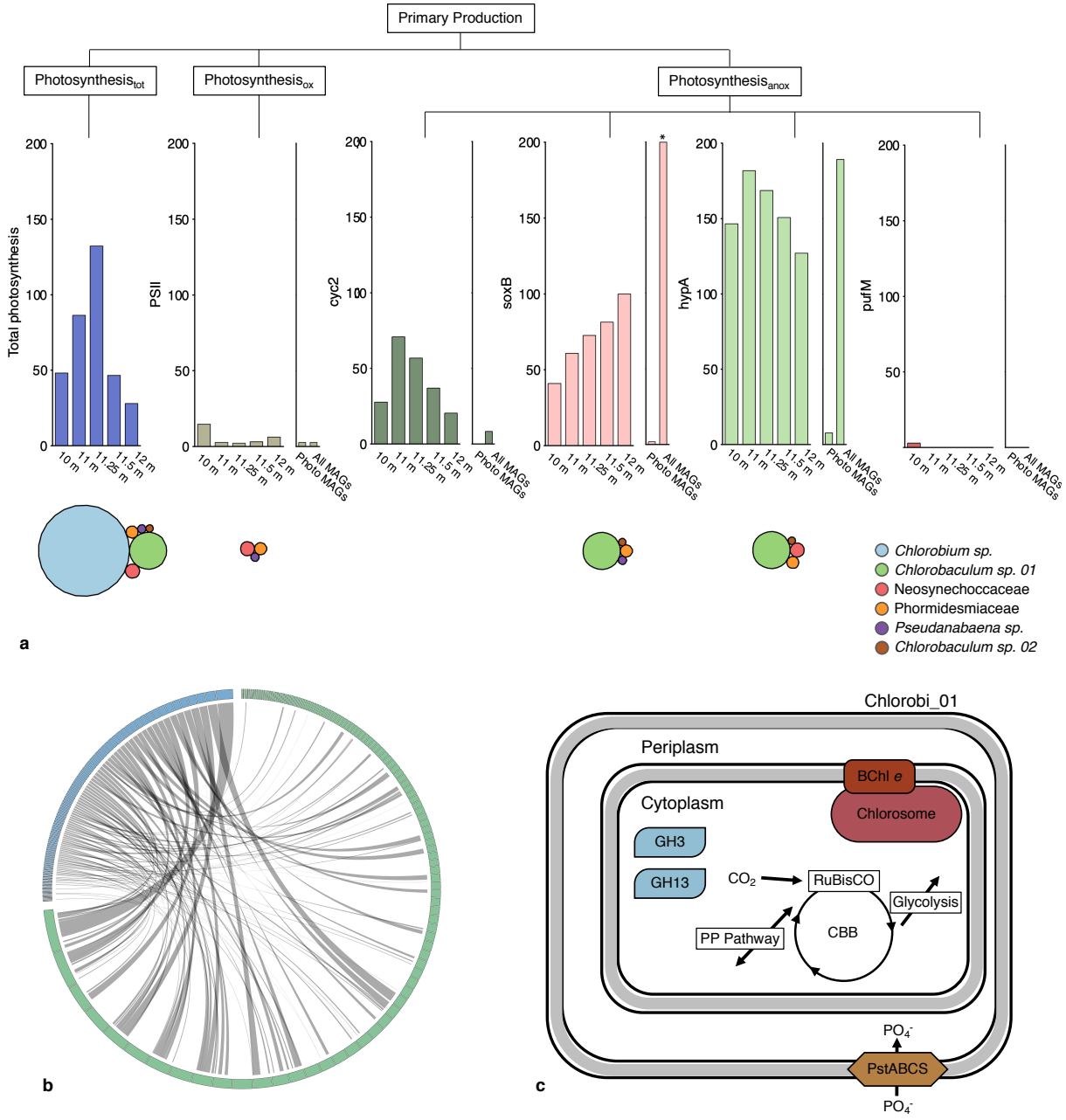

Figure 5.4: *Primary production in Kabuno Bay* with the RPKM of each gene in the bar graph and the MAGs that contain those genes underneath (a). *Chlorobium* sp. MAG (Chlorobi_01) from 10 m (blue) aligned to *C. phaeoferrooxidans* strain KB01 genome (green) where the grey links represent nucleotide sequences greater than 20 nt's with 100 % identity (b). The major pathways found in the Chlorobi_01 MAG (c). Note: the star above the all MAGs for *soxB* is due to the fact that the RPKM of the *soxB* genes in the MAGs extends to 356.

Table 5.1: Extended data from a selection of MAGs including completeness, contamination, and taxonomy. Note: Near-complete genomes (Near) have a completeness $\geq$ 90 % and contamination $\leq$ 5 %; Medium-complete genomes (Medium) have a completeness $\geq$ 70 % and contamination $\leq$ 10 %; Partially-complete genomes (Partial) have a completeness $\geq$ 50 % and contamination $\leq$ 4 %.

Name	Depth (m)	MAG #	Compl-eteness	Contami-nation	Q-score	MAG Type	Network tiers	Average RPKM per MAG	Full taxonomy
Chlorobac_01	10	16	100	4.7	76.5	Near	N/A	4.6	Bacteria;Bacteroidetes;Chlorobia;Chlorobiales;Chlorobiaceae;Chlorobaculum
Chlorobi_01	10	6	52.8	0	52.8	Partial	N/A	27.7	Bacteria;Bacteroidetes;Chlorobia;Chlorobiales;Chlorobiaceae;Chlorobium;Chlorobium ferrooxidans
Cyano_01	10	58	94	2.3	82.5	Near	N/A	0.7	Bacteria;Cyanobacteria;Melainabacteria;Caenarcaniphilales
Cyano_02	10	124	89.8	6.1	59.3	Medium	N/A	0.2	Bacteria;Cyanobacteria;Oxyphotobacteria;Pseudanabaenales;Pseudanabaenaceae;Pseudanabaena
Bact_04	11.5	28	81.9	0.7	78.4	Medium	2,3	3.2	Bacteria;Bacteroidetes;Bacteroidia;Bacteroidales;GWA2-32-17;GWA2-32-17
Bact_05	11.25	32	78.2	0.2	77.2	Medium	2,3	2.9	Bacteria;Bacteroidetes;Bacteroidia;Bacteroidales;GWA2-32-17;GWA2-32-17
Bact_07	11.25	22	85.5	0.2	84.5	Medium	1,2,3	4.8	Bacteria;Bacteroidetes;Bacteroidia;Bacteroidales;TTA-H9
Bact_08	11.5	20	91.3	0.9	86.8	Near	1,2,3	5.0	Bacteria;Bacteroidetes;Bacteroidia;Bacteroidales;TTA-H9
Igna_03	11.25	14	80.7	1.6	72.7	Medium	1,2	8.1	Bacteria;Bacteroidetes;Ignavibacteria;Ignavibacteriales;Ignavibacteriaceae
Igna_06	11.25	7	66.3	1.3	59.8	Partial	1,2	26.2	Bacteria;Bacteroidetes;Ignavibacteria;Ignavibacteriales
Igna_07	12	7	73.6	1.3	67.1	Medium	1,2	8.8	Bacteria;Bacteroidetes;Ignavibacteria;Ignavibacteriales
Lenti_01	11.25	54	96.2	1.6	88.2	Near	3	1.3	Bacteria;Bacteroidetes;Bacteroidia;Bacteroidales;Lentimicrobiaceae;Lentimicrobium
Lenti_02	11.25	12	84	3.1	68.5	Medium	1,2,3	14.7	Bacteria;Bacteroidetes;Bacteroidia;Bacteroidales;Lentimicrobiaceae
Lenti_03	11.5	8	92.7	3.5	75.2	Near	1,2,3	14.8	Bacteria;Bacteroidetes;Bacteroidia;Bacteroidales;Lentimicrobiaceae
MBNT15_01	11.25	8	85.7	1.3	79.2	Medium	1,2	25.1	Bacteria;MBNT15;MBNT15;MBNT15;MBNT15;CG2-30-66-27
MBNT15_02	11.5	4	86.5	0.8	82.5	Medium	1,2	26.1	Bacteria;MBNT15;MBNT15;MBNT15;MBNT15;CG2-30-66-27
MBNT15_04	11.25	18	82.1	4.3	60.6	Medium	1,2	6.0	Bacteria;MBNT15;MBNT15;MBNT15;MBNT15;CG2-30-66-27
MBNT15_07	10	13	92.3	2.5	79.8	Near	N/A	5.8	Bacteria;MBNT15;MBNT15;MBNT15;MBNT15;CG2-30-66-27
Pates_10	11.25	21	59	0	59.0	Partial	2	5.0	Bacteria;Patescibacteria;Gracilibacteria;Absconditabacterales;X112;undefined
Pates_17	12	3	69.3	0.5	66.8	Partial	1	19.4	Bacteria;Patescibacteria;Paceibacteria;Moranbacterales;UBA1568
Pates_20	10	9	69.8	0	69.8	Partial	N/A	13.9	Bacteria;Patescibacteria;Paceibacteria;Moranbacterales;UBA1568
Desulfo_03	11.25	20	97.1	1.3	90.6	Near	1,2,3	5.4	Bacteria;Desulfobacterota;Desulfomonilia;Desulfomonilales;Desulfomonilaceae
Desulfo_04	11.5	19	97.1	1.9	87.6	Near	2,3	5.3	Bacteria;Desulfobacterota;Desulfomonilia;Desulfomonilales;Desulfomonilaceae
Gamma_01	11.25	30	98.1	1.5	90.6	Near	2,3	3.0	Bacteria;Proteobacteria;Gammaproteobacteria;Betaproteobacteriales;SG8-39;2-12-FULL-64-23
Gamma_02	11.5	42	98.3	0.3	96.8	Near	3	1.9	Bacteria;Proteobacteria;Gammaproteobacteria;Betaproteobacteriales;SG8-39;2-12-FULL-64-23
Gamma_03	10	14	77.4	3.5	59.9	Medium	N/A	5.7	Bacteria;Proteobacteria;Gammaproteobacteria;Betaproteobacteriales;Methylophilaceae;Methylopumilus_A
Nitros_01	11.5	38	90	2.7	76.5	Near	3	2.2	Bacteria;Nitrospirota;Thermodesulfovibrionia;Thermodesulfovibrionales;UBA1546
Actino_01	11.5	50	93.6	3	78.6	Near	3	1.8	Bacteria;Actinobacteria;Acidimicrobiia;IMCC26256
Arch_01	10	34	98.9	1.3	92.4	Near	3	1.3	Archaea;Halobacterota;Methanomicrobia;Methanomicrobiales;Methanoregulaceae;Methanoregula
Arch_02	11	16	88	4.7	64.5	Medium	N/A	0.3	Archaea;Microarchaeota;Micrarchaeia;UBA10214

The most abundant photosynthetic MAG, identified as a *Chlorobium* sp., is very similar to *Chlorobium phaeoferrooxidans* strain KB01, previously enriched and isolated from the Kabuno Bay water column. Indeed, the genome of the *Chlorobium* MAG (Chlorobi_01; Table 5.1) is 97 % identical, at the nucleotide level, to the genome of *Chlorobium phaeoferrooxidans* strain KB01 (Fig. 5.4b). Strain KB01 is a photoferrotroph [58, 115] whose genome contains genes (*cyc2*) previously linked to photoferrotrophy [58, 115, 142, 194, 274]. Included in the genes that are identical between the two genomes are some components for nutrient cycling such as the nitrogenase subunits required for nitrogen fixation and phosphate transport genes (Fig. 5.4c, B.6) [115] and components of the pathways associated with autotrophic growth, specifically those which facilitate inorganic

carbon (CO_2) fixation such as those for the Calvin-Benson-Bassham (CBB) cycle (Fig. 5.4c, B.6). The 3 % of the Chlorobi_01 genome that does not match the strain KB01 genome identically is mostly comprised of small contigs with between one and three predicted genes (open reading frames — ORFs). The majority of these ORFs are homologous to hypothetical gene sequences that have been predicted from a variety of microorganisms, none of which are closely related to strain KB01. The Chlorobi_01 genome did not contain the genes for phototrophic sulfide or hydrogen oxidation, nor did it contain the outer membrane cytochrome (*cyc2*). Strain KB01 does host the *cyc2* gene, linked to Fe(II) oxidation, and does have the metabolic potential for thiosulfate oxidation (*soxB*) and hydrogen oxidation (*hypA*) (Fig. B.6). The similarities between the genome sequences of strain KB01 and Chlorobi_01, therefore, indirectly links the metabolic potential for photoferrotrophy and anoxygenic hydrogen oxidation to the dominant Chlorobia lineages in the Kabuno Bay water column.

The metabolic potential for iron, sulfide and hydrogen oxidation was distributed across both photosynthetic and non-photosynthetic lineages, not all of which were well represented in the MAGs. All three functional marker genes (*cyc2*, *soxB*, and *hypA*) were found in greater abundance in the non-photosynthetic MAGs than in the photosynthetic MAGs (Fig. 5.4a). The *cyc2* gene was only found in non-photosynthetic MAGs, but analyses of these sequences revealed high degree of identity to the *cyc2* gene from strain KB01 and these sequences were thus likely present as contaminants in the non-photosynthetic MAGs. While all *soxB* genes were associated with MAGs—found in 28 % of the recovered MAGs—most of these MAGs were non-photosynthetic (Fig. 5.4a). Additionally, the majority of *soxB* genes found in MAGs represented lesser abundant members of the microbial community such as those of the phylum Omnitrophota or class Alphaproteobacteria (Fig. 5.2). Only a fraction of the *hypA* genes were associated with MAGs, and like *soxB*, most of these MAGs were non-photosynthetic (Fig. 5.4a). Thus, while most of the metabolic potential for S oxidation is clearly non-photosynthetic, the metabolic potential for hydrogen oxidation is not fully resolved though MAGs and the distribution between photosynthetic and non-photosynthetic taxa remains somewhat uncertain. The metabolic potential for iron oxidation is entirely unresolved through MAGs but based on *cyc2* sequence analyses is likely hosted almost entirely by the photoferrotrophic Chlorobia.

5.4.4 Carbon breakdown and fermentation

The abundance of genes associated with carbon degradation dominate the overall metabolic potential of the microbial community in Kabuno Bay. Glycosyl hydrolases (GHs), some of which have capacity to hydrolyze complex carbon sources such as cellulose, like GH5, while others are capable of breaking the bond between the sugars and amino acids found in peptidoglycan (GH23) had higher relative abundance than any other functional gene examined (Fig. 5.3, B.3b, B.4). GHs were ubiquitously abundant across all depths in Kabuno Bay (B.3b, B.4). Glycosyl transferases (GTs) were also similarly abundant throughout the chemocline (data not shown). The GHs present were linked to a diverse set of carbon degradation pathways with the most abundant GHs implicated in the degradation of oligosaccharides (GH 2 — 35 % of the total community metabolic potential based on a comparison to the single copy gene rpoB), cellobiose (GH 3 -– 57 %), cellulose (GH 5 -– 38 %), starch (GH 13 -– 150 % and GH 57 -– 33 %), peptidoglycan (GH 23 -– 78 %), and other polysaccharides (GH 74 -– 77 %). The majority of the most abundant GHs exhibited some depth-dependent structure with a peak in abundance at 11 m (Fig. B.3b, B.4), where the most abundant GH (GH13) reached almost 200 % (twice as many copies of GH 13 as copies of the single copy gene *rpoB*) (Fig. B.4). GHs, and by extension the metabolic potential for carbon breakdown, thus represent an extremely abundant component of microbial community metabolism in Kabuno Bay.

The metabolic potential for fermentation pathways was prevalent throughout the chemocline, albeit at lower relative abundances than those of the complex carbon breakdown pathways. Of the fermentation pathway genes, MM-CoA mutase, required for fermentation of glucose to succinate and propionate (converting phosphoenolpyruvate——PEP——to oxaloacetate) had the highest depth-specific abundance (up to 95 % at 11 m depth) as well as the highest overall abundance (75 %) (Fig. B.4). The abundance of pyruvate kinase (pk – converts PEP to pyruvate) is roughly a mirror image of the MM-CoA mutase (Fig. B.4), with its lowest abundance (30 %) at 11 m depth. Pyruvate dehydrogenase (converts pyruvate to acetyl-coA, releasing CO_2), in contrast, had very little depth-dependent structure, with about 50 % of the overall metabolic potential represented by this pathway at every depth. The other fermentation pathways queried represented smaller

portions of the overall metabolic potential (Fig. 5.3) with acetate production (acetate kinase — *ack*) and butyrate production (butyryl-CoA transferase — *but*) at 25 and 20 percent, respectively (Fig. B.4). While the metabolic potential for diverse fermentation pathways is abundant and widely distributed across depth in Kabuno Bay, none of the described genes or pathways are as abundant as those required for complex carbon breakdown as described above.

The metabolic potential for complex carbon degradation and fermentation pathways is ubiquitous across the microbial community and well represented in the MAGs. Genes for both hydrolysis and fermentation were found in the majority of the high-quality MAGs (Q-score of greater than 50 — see methods) with GH's present in 93 % and fermentation genes present in 68 % of the recovered MAGs, respectively. Furthermore, the taxonomy of these MAGs matched the taxonomy of some of the most abundant members of the microbial community including members of the candidate phyla MBNT15 and phylum Bacteroidetes——namely those of the family Lentimicrobiaceae (Fig. 5.2a, 5.5, Table 5.1). A subset of MAGs that represents all the most abundant classes within the microbial community (Fig. 5.2a, Table 5.1) and includes the most abundant MAGs recovered (relative abundance based on the average RPKM of a MAG compared to the total RPKM of the MAGs; Table 5.1 — see methods) exemplify the distribution of the major carbon breakdown and fermentation pathways across prevalent microbial community members (Fig. 5.5, B.7). For example, the starch and other polysaccharide degradation pathways (identified through genes such as the d-galacturonate epimerase) are found in highly abundant community members such as members of the phylum MBNT15 (MBNT15_01; Fig. 5.5, B.7), whereas the peptidoglycan breakdown pathways (identified through genes such as the beta-N-acetylhexosaminidase) are found mostly in the *Lentimicrobiaceae* MAGs (Lenti_03; Fig. 5.5, B.7). A detailed schematic representation of the characteristic pathways found in two examples of these relatively abundant near complete MAGs ($\geq$ 90 % complete and $\leq$ 5 % contaminated), MBNT15_01 and Lenti_03, is shown in Fig. 5.5. While some carbon breakdown pathways appear to be taxonomically restricted, many genes from a diverse set of fermentation pathways were present in almost all the MAGs selected (Fig. 5.5, B.7). A notable exception are the Patescibacteria MAGs, which contain limited metabolic potential and either possessed the genes for complex carbon breakdown or fermentation (B.7). Collectively, these data demonstrate ubiquity of the complex carbon breakdown and fermentation pathways

across diverse lineages and highlight the partitioning of some metabolic potential within specific taxa.

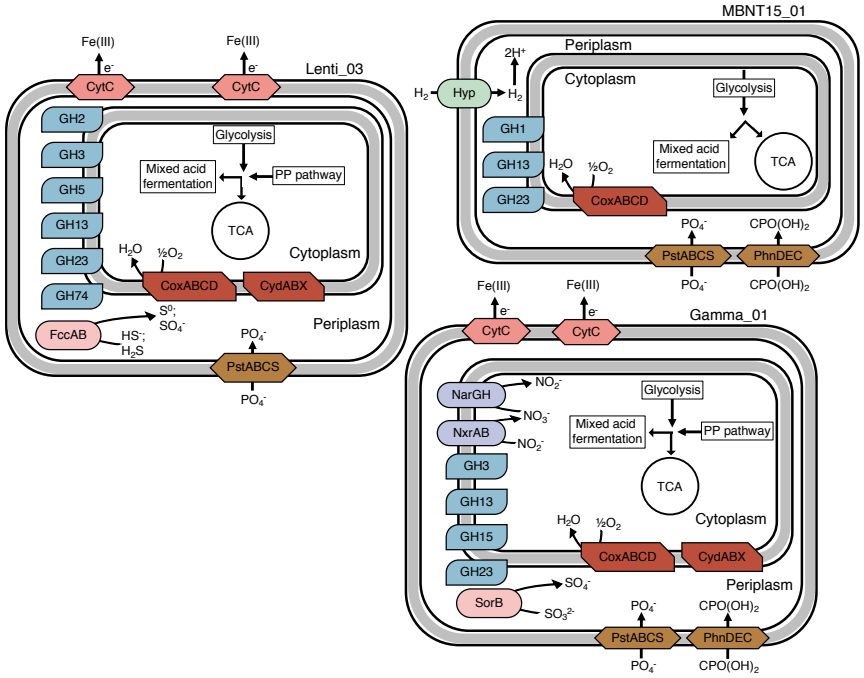

Figure 5.5: *A representation of the metabolic potential for three MAGs* including an abundant fermenter (MBNT15_01), a potential Fe(III) reducer with the metabolic potential for multiple carbon degradation pathways (Lenti_03), and a potential Fe(III) reducer with the metabolic potential for fewer carbon degradation pathways (Gamma_01). The description of each gene listed in found in B.2.

The microbial community in Kabuno Bay has the metabolic potential to channel degradation of complex carbon compounds through fermentation products to CO_2 and CH_4 via a metabolic network with a suite of non-unique, apparently redundant pathways (Fig. 5.6). The upper tier of the network contains a subset of abundant MAGs that possess the genes for the acquisition and breakdown of complex carbon compounds such as disaccharides or larger more complex carbon molecules (e.g. cellulose). This tier comprised 11 different taxa (including six taxonomically distinct MBNT15 MAGs and five Patescibacteria MAGs; Fig. 5.6) whose collective abundance represented 8 % of the total microbial community (average MAG RPKM compared to the RPKM of single copy gene *rpoB* for the whole community). The hydrolytic pathways hosted principally, but not exclusively, in these organisms ultimately produce glucose through the breakdown of complex carbon compounds. The middle tier of the network hosts the MAGs with the metabolic

potential to perform mixed acid fermentation, channelling the glucose produced in the upper tier into a number of fermentation pathways. This tier was comprised of seven different phylogenetic groups, with the majority of the same MAGs from tier 1 present (25 out of 30) and with a single Gammaproteobacteria MAG representing the only new class distinct from the top tier (collective abundance of 7 % of the total microbial community; Fig. 5.6). Notably, many of the same MAGs were present in both tiers with metabolic potential for processing more than one substrate or the production of more than one product (Igna_06, Lenti_02, Lenti_03; Fig. 5.6). For example, the *Lentimicrobiaceae* MAGs had the metabolic potential to degrade all four types of complex carbon compounds examined as well as all four major fermentation pathways (Fig. 5.6). Other MAGs were present on both tiers but contained fewer potential pathways (e.g. MBNT15_01, MBNT15_02; Fig. 5.6). For example, the MBNT15 MAGs contained the pathways required for cellobiose and peptidoglycan degradation as well as those for glucose fermentation to propionate and CO_2 but lacked the other carbon degradation and fermentation pathways present in other community members (Fig. 5.6). Thus, while members of the phylum MBNT15 are abundant throughout the water column (Figure 2), their growth options are restricted in comparison to members of the phylum Bacteroidetes (e.g. *Lentimicrobiaceae*). A broad suite of taxa, notably including *Lentimicrobiaceae*, *Ignavibacteriaceae*, MBNT15, and Patescibacteria thus have metabolic potential to drive conversion of complex carbon compounds to glucose, and some, *Lentimicrobiaceae* and *Ignavibacteriaceae* for example, to continue this conversion to fermentation products. Another suite of taxa, notably MBNT15 and Patescibacteria have metabolic potential to exclusively ferment glucose to select VFAs and hydrogen.

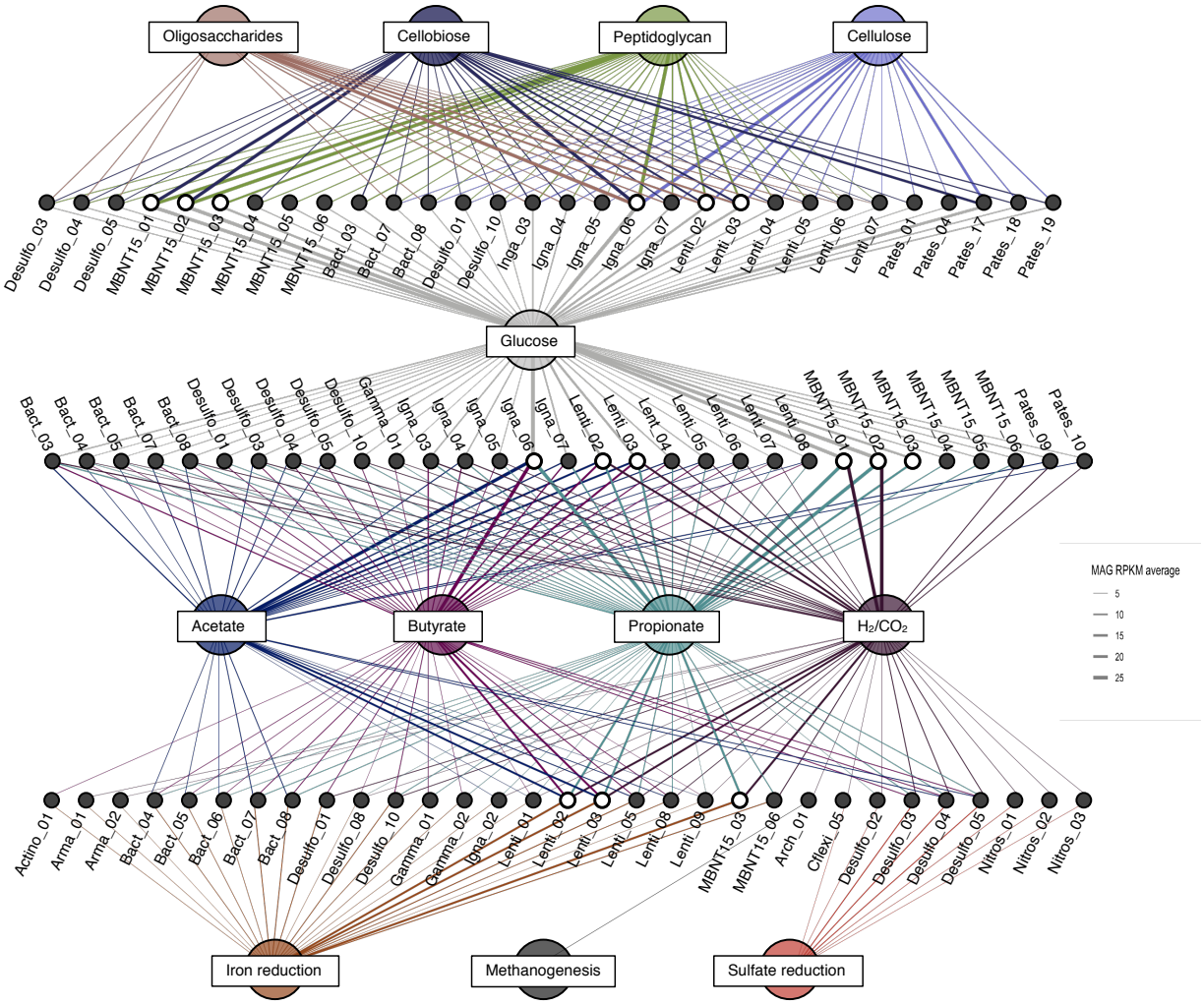

Figure 5.6: *Flow of carbon compounds through the metabolic pathways found in each MAG.* Tier 1 have the potential to degrade complex carbon molecules to glucose, tier 2 encompasses fermenters, and tier 3 has those with the metabolic potential for terminal electron processes. Key MAGs discussed in the text are highlighted with the white circles (e.g. Lenti_03).

5.4.5 Iron reduction, sulfate reduction, and methanogenesis

The metabolic potential for iron reduction in Kabuno Bay was greater than that of any of the other modes of respiration. Outer membrane heme binding cytochrome genes linked to iron reduction represented the largest portion of the microbial community respiratory metabolic potential (roughly 30 % throughout the mid-chemocline depths of 11, 11.25, and 11.5 m – B.4). The sulfate reduction genes were much less abundant (peaking at 6 %) and, notably, their gene abundances follow the same depth-dependent distribution as sulfide concentrations in Kabuno Bay (Fig. 5.1c, B.4). The metabolic potential for methanogenesis, however, was very low (<1 % relative abundance) throughout much of the chemocline with a small peak (2 %) at 11 m (B.4). Overall, respiratory metabolic potential linked to iron reduction (total of 25 % of the whole microbial community) dominated over the other anaerobic microbial respiration pathways throughout the water column.

The metabolic potential for iron reduction and sulfur metabolism was found in a subset of specific taxa that were well represented in the MAGs. Putative iron reduction genes were found in 15 % of the high quality MAGs, whereas those of sulfate reduction were found in 7 % of the MAGs. Notably, there was very little overlap in the taxonomy of the MAGs that housed the metabolic potential for each of these pathways. For example, iron reduction genes were found in MAGs affiliated with the most abundant classes (e.g. Bacteriodia, Ignavibacteria, and MBNT15; Fig. 5.5, 5.6, B.7) as well as some classes that are known to contain iron reducers (i.e. Gammaproteobacteria; Fig. 5.5, 5.6, B.7), whereas the majority of the metabolic potential for sulfate reduction was found in MAGs representing three classes of the phylum Desulfobacterota (Fig. 5.6, B.7, B.8). The metabolic potential for methanogenesis was only found in one MAG (Arch_01; Table 5.1, Fig. 5.6, B.7, B.8), which was classified as a *Methanoregula* sp. (Table 5.1). The overall discrete allocation of redox pathways to several exclusive taxa differs from the comparably generic distribution of carbon degradation and fermentation pathways. Key and relatively abundant members of the microbial community are thus responsible for iron respiration, while less abundant members are implicated in sulfate respiration and methanogenesis.

Metabolic potential for both respiration of iron and sulfate was distributed across taxa with

metabolic potential for the use of a broad range of electron donors including both complex carbon compounds and simple volatile fatty acids, as well as hydrogen. A subset of MAGs with metabolic potential for iron and sulfate respiration make up the final tier of the microbial network (Fig. 5.6) and represent a relatively smaller portion of the overall microbial community than the organisms comprising the upper tiers (4 % compared to 8 % and 7 % for tiers one and two respectively). While MAGs in this lower tier were obligate with respect to their terminal electron acceptor, many had metabolic potential to use a suite of different electron donors including the fermentation products produced by the second tier (Fig. 5.6). Notably, some MAGs (e.g. Lenti_03, Desulfo_03; Fig. 5.5, 5.6, B.8, Table 5.1) exhibited metabolic potential to acquire and degrade multiple fermentation products or even all four of the main fermentation products (acetate, butyrate, propionate, and H_2). Furthermore, many of these MAGs were also found in tier 1 and thus contain the metabolic potential to directly degrade complex carbon compounds (Fig. 5.6). These MAGs, with multiple pathways, were often the more abundant members of the microbial community (e.g. members of the phylum Bacteroidetes——Ignavibacteria and Bacteroidia, which includes the *Lentimicrobiaceae*; Fig. 5.2a). Other, lesser abundant, MAGs were generally restricted to the use of only one fermentation product, such as the sulfate reducing Nitrospirota MAG (Nitros_01; Fig. 5.6, Table 5.1). Metabolic potential for the use of a broad suite of electrons is thus a key trait for many of the anaerobic iron and sulfate respiring microorganisms in Kabuno Bay.

5.5 Discussion

5.5.1 Primary production in Kabuno Bay

Phototrophic Fe(II) oxidation, supported by phototrophic members of the class Chlorobia and independent of oxygen, is the dominant form of photosynthesis and primary production in the Kabuno Bay chemocline. Net phototrophic iron oxidation rates of 3.1 $\pm$ 0.4 μmol L^{-1} h^{-1} (Fig. 5.1e), in the presence of an inhibitor of oxygenic photosynthesis (3-(3,4-dichlorophenyl)-1,1-dimethylurea; DCMU), suggest that anoxygenic photosynthetic bacteria are active at 11 m. High concentrations of BChl *e* pigments [48], ratios of GSB specific cell counts versus total cell counts (Fig. 5.1d), and rates of anoxygenic photosynthetic carbon fixation [72] further indicate that

there is a large population of anoxygenic phototrophs throughout the Kabuno Bay chemocline. Indeed, members of the class Chlorobia, known anoxygenic phototrophs [141, 142, 275], are the most abundant taxa throughout the deeper chemocline depths (36 % of the whole community; Fig. 5.2b). The most abundant members of the class Chlorobia identified form a clade within the genus *Chlorobium* with two other known photoferrotrophic bacteria (Fig. 5.2c; [48, 53, 55, 58])–—*Chlorobium phaeoferrooxidans* strain KB01 and *Chlorobium ferrooxidans* strain KoFox—–one of which (strain KB01) was previously isolated from the Kabuno Bay water column [48, 58]. A partial MAG, taxonomically identified as Chlorobium sp., was 97 % identical at the nucleotide level to the genome of strain KB01 (Fig. 5.4b) and possessed several genes and pathways indicative of anoxygenic photosynthesis (Fig. 5.4c, B.6), although it lacked the outer membrane iron oxidizing cytochrome (*cyc2*) previously attributed to photoferrotrophy. The conspicuous absence of the *cyc2* gene from the MAG Chlorobi_01 genome thus likely reflects its limited completion (52 %, Table 5.1). The strain KB01 specific *cyc2*, however, was found throughout the water column (Fig. 5.3) and peaked at 12 % of the overall community's metabolic potential at 11 m (Fig. 5.3, B.4). This suggests that the contigs containing the *cyc2* gene did not assemble into MAGs, which is confirmed by the taxonomy of the two *cyc2* genes that were found in non-Chlorobia MAGs being identical to the strain KB01 *cyc2* gene and implies that they represent contamination in those MAGs. Collectively, these data provide evidence that photoferrotrophy is likely the dominant form of primary production and thus provides a significant amount of primary organic carbon to support the growth of the microbial community as a whole.

Other modes of photosynthesis exist at each depth of the Kabuno Bay chemocline, albeit in lower abundances than the those indicated for photoferrotrophy. Functional anchors, or genes that are required for specific processes to occur, that represent photosynthetic pathways such as oxygenic photosynthesis (PSII -– photosystem II) and anoxygenic photosynthesis in the phylum Proteobacteria (*pufM/L* -– photosynthetic reaction center genes specific to Proteobacteria) are present throughout the chemocline (Fig. 5.3, 5.4a). PSII genes found in MAGs that are taxonomically identified as canonical members of the phototrophic phylum Cyanobacteria (e.g. *Pseudanabaena* sp. -– Cyano_02; Fig. 5.4a, B.7, Table 5.1) provide further evidence for oxygenic phototrophs in the chemocline, implying metabolic potential for oxygenic photosynthesis under

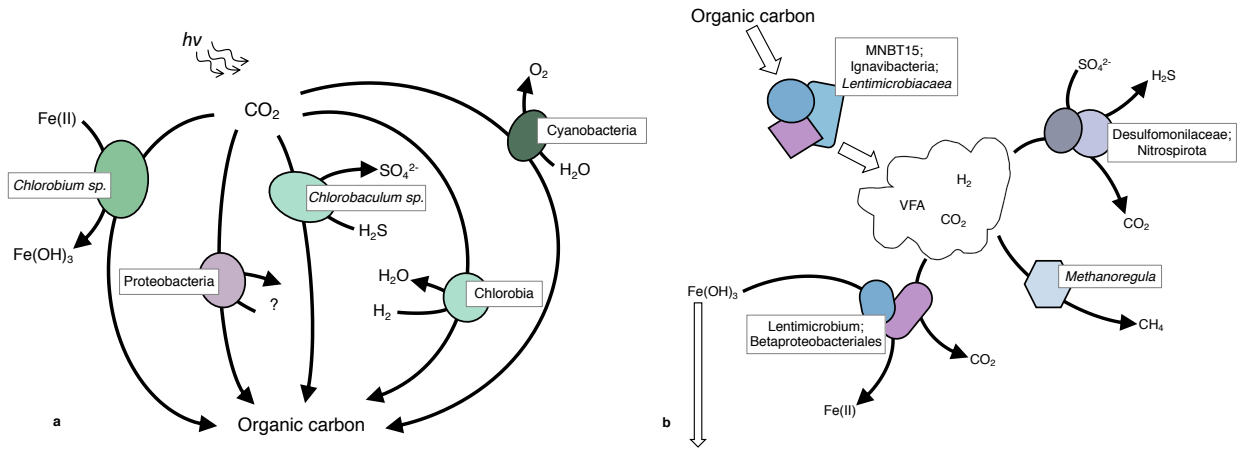

Figure 5.7: *Proposed metabolic model for the primary producing microorganisms present at the chemocline in Kabuno Bay* where *hv* denotes light (a). Proposed metabolic model for the non-primary producing microorganisms present at the chemocline in Kabuno Bay where VFAs are volatile fatty acids (b).

ferruginous conditions. Their presence throughout the water column, even at deeper depths, might infer a lack of the toxicity effects commonly invoked to exclude oxygenic phototrophs from Fe-rich waters [224]. Their less than 1 % abundance implies they are minor members of the total community, while the lack of inhibition of photosynthesis and Fe(II) oxidation by DCMU (Fig. 5.1e) indicates that oxygenic photosynthesis plays little role in Fe(II) oxidation and primary production in Kabuno Bay's chemocline. These cyanobacteria, however, may produce oxygen at low rates, driving a cryptic oxygen cycle or, alternatively, could grow through anoxygenic photosynthesis with electron donors such as H_2S or H_2. Indeed, genes required to oxidize these alternative electron donors are present in the cyanobacterial MAGs (H_2S oxidation genes in *Pseudanabaena* sp. and H_2 in the *Neosynechoccaceae*; Fig. 5.4a). Laboratory strains isolated from anoxic environments, and closely related to the cyanobacteria MAGs from Kabuno Bay, have also been shown to grow through both oxygenic and anoxygenic photosynthesis with their photosynthetic mode controlled by the availability of anoxygenic photosynthetic electron donors: H_2S or H_2 [276–278]. Together, these data provide further evidence for concurrent modes of photosynthesis, including possibly oxygenic photosynthesis (Fig. 5.7a) under ferruginous conditions.

5.5.2 Microbial metabolisms in Kabuno Bay

The majority of the metabolic potential in Kabuno Bay is centered around carbon degradation and fermentation, resulting in an abundant and diverse group of microorganisms who are likely responsible for the partitioning of carbon metabolism across distinct microbial taxa. Glycosyl hydrolases and functional anchors for fermentation pathways are highly abundant throughout the water column (between 40 and 200 % of the overall community metabolic potential; Fig. 5.3, B.4). These same genes, found in most MAGs (93 % contained GH's and 68 % contained fermentation genes and pathways; Fig. 5.6, B.4, B.7), define a group of highly abundant microorganisms that degrade and ferment organic carbon–namely the phyla Bacteroidetes, MBNT15, and Patescibacteria (Fig. 5.2, 5.5, 5.6, 5.7b). Prior studies have shown that members of the phylum Bacteroidetes——specifically members of the class Bacteroidia and Ignavibacteria——can play an active role (as measured through transcriptomics and proteomics) in carbon degradation and fermentation in mineral and organic-rich environments such as the fen regions of peatlands [247]. Members of the phylum Patescibacteria have also been shown to play a role in carbon degradation [279], although their small genomes and general lack of many canonical microbial biosynthetic pathways (e.g. amino acid formation) suggest that these bacteria largely rely on other members of the microbial community to support their growth [279]. Little is known at this stage about the MBNT15 phylum; but our data suggest, however, that they could play an important role in carbon compound hydrolysis and fermentation, at least under ferruginous conditions. The partitioning of carbon degradation and fermentation pathways across these abundant classes of bacteria ultimately supplies small carbon compounds and VFAs to other microbial metabolisms present throughout Kabuno Bay.

Notable, non-iron-based, metabolisms in Kabuno Bay include those involved in sulfur cycling—sulfide oxidation and sulfate reduction. Sulfate reduction, supported by organic carbon compounds produced through carbon degradation and fermentation, peaked at 11.5 m with a rate of 300 nmol L^{-1} d^{-1} (Fig. 5.1c). These rates were accompanied by sulfate reduction genes (*dsrAB*), which were found throughout the water column (Fig. 5.3), albeit at relatively low abundances (peaked at 6 % of the overall metabolic potential at 12 m; B.4). The low abundance

of sulfate reduction genes is supported by the restriction of the sulfate reduction pathway to lesser abundant microorganisms (Desulfobacterota; Fig. 5.6, 5.7b, B.7, B.8). Conversely, sulfide oxidation genes were well represented in the collected MAGs (found in 28 % compared to the 7 % of MAGs that contained sulfate reduction genes) and they represented just less than 20 % of the overall community metabolic potential (B.4). The MAGs that did contain sulfide oxidation genes, however, were those that represented lower abundance phyla (e.g. Omnitrophota). The density of sulfide oxidation genes and the abundance of the phylum Omnitrophota follow the same depth-dependent structure (Fig. 5.2a) of the sulfide concentrations in the chemocline (Fig. 5.1c), thus further supporting the link between these members of the microbial community and sulfide oxidation. Despite the overall lower abundances of the genes implicated in sulfate reduction and sulfide oxidation in Kabuno Bay, minimal pyrite export from the chemocline (6 mmol m^{-2} yr^{-1}) compared to the depth integrated sulfate reduction rates (90 mmol m^{-2} yr^{-1}) demonstrates strong sulfur cycling. Furthermore, the relatively low rates of pyrite export and low rates of sulfate reduction indicate that sulfide production plays a negligible role in Fe(III) reduction, thus directly linking Fe(III) reduction to microbial respiration.

Fe(III) reduction is the most abundant form of respiration in the Kabuno Bay chemocline as the genes required, and the absolute abundance of the micoorganisms likely involved, outnumber those associated with other forms of respiration such as sulfate reduction and, in particular, methanogenesis. Genes implicated in Fe(III) reduction were abundant throughout the water column (up to 30 % throughout the chemocline; Fig. 5.3, B.4) and accompanied high rates of Fe(III) reduction (0.4 ± 0.04 μmol L^{-1} h^{-1}) compared to those of sulfate reduction (0.0125 μmol L^{-1} h^{-1}). These high rates of Fe(III) reduction are conferred by the presence of Fe(III) reduction genes in abundant members of the microbial community (e.g. Bacteroidia and Gammaproteobacteria; Fig. 5.5, 5.6, 5.7b, B.7). Furthermore, the abundance of Fe(III) reduction genes and of phyla that contain Fe(III) reduction genes, such as Bacteriodetes, peak at 11 m (Fig. 5.2a) where concentrations of Fe(III) (oxyhydr)oxides are at their highest (Fig. 5.1b), corroborating the importance of these members of the community in Fe(III) reduction. Conversely, the genes for methanogenesis (*mcrA*) were only found in one MAG (*Methanoregula*; Arch_01, Table 5.1, B.8) and peaked at 2 % of the overall metabolic potential of the microbial community (Fig. B.4). Thus, while both Fe(III)

reduction and methanogenesis appear to be supported by members of the microbial community in Kabuno Bay, those likely capable of Fe(III) reduction far outnumber the methanogens, which may be due to the availability of organic carbon compounds for each metabolism.

5.5.3 Microbial community network and tight carbon and iron coupling

Fe(III) reduction rates and the flux of Fe(III) (oxyhydr)oxides from the Kabuno Bay chemocline indicate that there is a tight coupling between the carbon and iron biogeochemical cycles. Fe(III) reduction rates are sufficiently high that 80 % of the Fe(III) produced through phototrophic Fe(II) oxidation is converted back to Fe(II) in the euphotic portion of the water column. The theoretical flux of Fe(III), calculated from the difference between the Fe(II) oxidation and Fe(III) reduction rates in the water column, indicates that 0.1 to 1.7 mol m^{-2} yr^{-1} Fe(III) will leave the chemocline, which encompasses the measured highly reactive Fe(III) mineral flux captured in sediment traps (0.4 mol m^{-2} yr^{-1}). This appreciable Fe export from the euphotic zone is comparable to those reported from other modern ferruginous lakes, namely Lake Matano (up to 0.1 mol m^{-2} yr^{-1}) and Lake Towuti (up to 0.25 mol m^{-2} yr^{-1}) [273]. In these environments, therefore, the interplay between the microbial mediated rates of iron oxidation and reduction dictates the amount of highly reactive Fe(III) exported from the chemocline. Thus, iron based microbial metabolisms, coupled to organic matter degradation, are likely crucial in maintaining the microbial community under ferruginous conditions.

The partitioning of the metabolic pathways for complex carbon degradation and fermentation coupled to Fe(III) reduction influence the capacity for coupled carbon and iron cycling. One of the most abundant classes of microorganisms in Kabuno Bay, the Bacteroidia ($\sim$7 x 10^3 cells mL^{-1} at each depth), contained pathways for complex carbon degradation, fermentation, and Fe(III) reduction. Specifically, those of the family Lentimicrobiaceae and the genus *Lentimicrobium* (Lenti_01, Lenti_02, Lenti_03; Fig. 5.5, 5.6, Table 5.1) had metabolic potential for complex carbon degradation, fermentation, and Fe(III) reduction (Fig. 5.5, 5.6). Notably, the collection of these pathways within single taxa may enhance the capacity for respiration by minimizing extracellular transport of intermediate organic species. Recent work with newly cultured representatives of the class Bacteroidia indeed suggest that members of this class grow through fermentation but

shuttle a portion of their terminal electrons onto iron (oxyhydr)oxides, effectively reducing iron under laboratory conditions [280]. The pathways found in the Bacteroidia from Kabuno Bay (Fig. 5.5, 5.6, B.7) are similar to those determined through laboratory growth experiments with similar Bacteroidia strains [280], which lends further support to the claim that the Bacteroidia are involved in both fermentation and Fe reduction in Kabuno Bay. The microbial community metabolisms in Kabuno Bay are, thus, dominated by carbon cycling (degradation and fermentation) likely coupled to iron reduction, which has implications for the availability of organic carbon for other forms of respiration.

Coupled C degradation, fermentation, and respiration pathways are also found in some sulfate reducers, suggesting that the lower sulfate reduction rates, compared to Fe(III) reduction rates, is due to alternative factors. Pathway coupling was found in most abundant class of sulfate reducers (Desulfobacterota; Fig. 5.6). The high rate of Fe(III) reduction, however, relative to sulfate reduction ($\sim$40:1), despite the $\sim$600 μM sulfate available in the chemocline, suggests that other facets of the microbial network outweigh the potential increase in sulfate reduction due to pathway coupling. For example, the abundance of recovered MAGs delineated as putative Fe(III) reducers outnumber MAGs with the metabolic potential for sulfate reduction ($\sim$4:1). Differential gene expression of the metabolic potential within these different groups of organisms could also play a role in the differential rates of Fe(III) and sulfate reduction. Further studies which include the use of transcriptomics and proteomics would be necessary to confirm this hypothesis. Thus, while some sulfate reducers in Kabuno Bay have the metabolic potential to couple multiple C degradation and fermentation pathways with sulfate reduction, this coupling does not result in rates that are comparable to the Fe(III) reduction rates.

The tight coupling between C degradation, fermentation, and respiration pathways in single, abundant microorganisms in both the Fe and S cycles restricts the leakage of carbon to alternative respiration pathways, such as methanogenesis. The majority of the most abundant bacteria in the Kabuno Bay chemocline (e.g. phylum Bacteroidetes) exhibit the metabolic potential to couple carbon degradation and fermentation to either Fe(III) or sulfate reduction (Fig. 5.6). As such, the availability of mid-sized carbon compounds or VFAs would depend on either their leakage from these microorganisms or their production by specific carbon degraders, such as the *Ignavibacteria*

(Fig. 5.6). Indeed, methanogenic Archaea that would likely rely on VFAs for growth represent a small portion of the population (a small portion of the 2 % Archaea in Kabuno Bay), while the abundance of the key gene for methanogenesis (*mcrA*) is similarly low (Fig. 5.3, B.4). Thus, the metabolic potential for methanogenesis in Kabuno Bay is low, which is likely due to a lack of carbon leakage from either of the Fe or S cycles, both of which appear to be tightly coupled to carbon degradation and fermentation pathways. Further research, particularly elucidating the rates of microbial methane production are needed to confirm this hypothesis.

5.5.4 Implications for coupled carbon and iron cycling in the Precambrian Eons

The identification of multiple modes of primary production with electron donors, and the metabolic potential for both oxygenic (H_2O) and anoxygenic (Fe(II), H_2S, H_2) photosynthesis (Fig. 5.3, 5.4a, 5.7a) can ultimately be applied to models of primary production for the ferruginous conditions that existed in the Archean and Proterozoic oceans. Prior studies have implicated multiple modes of photosynthesis in large-scale processes, such as the maintenance of a clement climate during the Archean Eon [95]. These studies, however, could be further constrained by using the relationships between multiple modes of photosynthesis as seen in Kabuno Bay. The spatial and temporal coexistence and/or partitioning of these multiple modes of primary production both in the water column and along costal margins or in upwelling zones likely impacted the distribution and circulation of key nutrients to other members of the microbial community when nutrients such as nitrogen or phosphate were scarce or limiting under ferruginous conditions [96, 115]. For example, phosphate is often scarce or limiting under ferruginous conditions [85] due to its absorbance to Fe(III) (oxyhydr)oxides. While phosphate transporters are ubiquitous across the MAGs (Fig. B.7), including in the putative primary producers (Fig. 5.4c, B.7), deeper investigations into number of phosphate acquisition genes in different types of primary producers and how these translate to growth under the natural conditions of ferruginous Kabuno Bay could further constrain future model studies. Furthermore, the antiquity of these genes and the relationship between them could inform on the antiquity of processes vital to primary production and microbial life under ferruginous conditions.

The tight coupling between complex carbon degradation and iron reduction has implications

for the cycling of iron and carbon under the Precambrian ferruginous conditions. As microorganisms evolved and acquired complete C degradation and fermentation pathways coupled to Fe(III) reduction pathways, the efficiency of microbial iron reduction could have increased. The use of a more extensive and varied set of carbon sources that the bacteria themselves produced, rather than relying on a separate population of carbon degraders and fermenters, could have had a number of implications for the early Earth ocean-atmosphere system. For example, coupling the C degradation, fermentation, and respiration pathways in individual bacteria would have limited the concentration of mid-sized carbon compounds and VFAs. Without these intermediate carbon compounds, the rates of alternative respiration pathways that rely on these compounds, such as methanogenesis, may have decreased, ultimately lowering the fluxes of methane to the atmosphere. Thus, the coupling of these pathways in single bacteria may have influenced the degree of climate warming by reducing the concentration of atmospheric methane. Further modeling efforts are required to ascertain the putative effects of the reduction in these methane fluxes. Another potential implication is that as the rates of iron reduction increased, they would approach those of phototrophic Fe(II) oxidation, thus effectively cycling iron in the water column prior to its deposition on the seafloor. This in turn would have precluded the deposition of ferric iron rich deposits, such as banded iron formations. We hypothesize that the evolution of complete carbon degradation and fermentation pathways coupled, in one organism, to iron (oxyhydr)oxide reduction could have begun to alter the magnitude and number of iron depositions, thus reconciling the lower number of these deposits throughout the Proterozoic Eon – despite the ferruginous conditions that likely still existed for much of the Eon [5, 171]. The metabolic potential and process rates of the microbial community found in Kabuno Bay, thus lays the groundwork for the elucidation of the relationships under the naturally complex ferruginous conditions and can be used to inform models of nutrient cycling throughout the Precambrian Eons.

5.6 Supplementary materials

- Table B1: Description of each Fe speciation extraction step
- Table B2: List of genes discussed in the main text and their primary function

- Table B3: % of metagenomic reads that aligned to each set of MAGs
- Fig. B1: The location of Kabuno Bay with the sampling site
- Fig. B2: The relative abundance of the reconstructed 16S rRNA gene for the 16S rRNA genes with a greater than 1 % relative abundance for each depth
- Fig. B3: Reads per kilobase mapped (RPKM) values for taxonomic marker genes related to class Chlorobia and glycosyl hydrolases
- Fig. B4: Gene abundances of the key genes for several pathways
- Fig. B5: The depth integrated absolute abundance of each phyla compared to the number of MAGs recovered from each of those groups
- Fig. B6: Comparison of the Chlorobi_01 MAG to the genome of *Chlorobium phaeoferrooxidans* strain KB01 at the pathway level
- Fig. B7: Comparison of the genomes of several key MAGs at the pathway level
- Fig. B8: Representation of the metabolic potential for two MAGs

Chapter 6

Conclusions

This dissertation creates new knowledge on photoferrotrophy in both laboratory conditions and in the natural environment through data collected on the physiology and metabolic capacity of pelagic photoferrotroph *Chlorobium phaeoferrooxidans* strain KB01, as well as process rate measurements and analyses of the microbial community in ferruginous Kabuno Bay. This new knowledge was subsequently integrated into models to examine the antiquity of nutrient acquisition in the photoferrotrophic Chlorobia, the effect of competition for phosphorus between photoferrotrophs and oxygenic photosynthetic bacteria on the early Earth ocean-atmosphere system, and the role of photoferrotrophs as primary producers during the Archean. These models, developed in this thesis, provide insight on how photoferrotrophs could have sustained the biosphere, deposited BIFs as a by-product of their growth, fueled microbial methanogenesis, and, therefore, helped to stabilize Earth's climate under a dim early Sun.

6.1 Extant photoferrotrophy

This dissertation presents new knowledge on extant photoferrotrophy through a detailed examination of *Chlorobium phaeoferrooxidans* strain KB01, comparing strain KB01 to other known phototrophs, and analyses of microbial community networks supported by photoferrotrophy. Prior to this work, knowledge of extant photoferrotrophs was restricted to benthic isolates, limiting our ability to define characteristic traits of photoferrotrophs and the role of photoferrotrophs in other environmental settings. In Chapter 2, we describe the physiology and metabolic potential of strain KB01 and compare traits, such as its growth response to a range of light intensities, to other known phototrophs. This work created a framework for the remainder of the dissertation by establishing the key aspects of pelagic photoferrotrophy. In Chapter 3, we delve deeper into the growth

of strain KB01 by examining, and biochemically verifying, its metabolic potential for nutrient acquisition—specifically its sulfur and nitrogen requirements. Furthermore, we quantify strain KB01's usage of phosphorus and determine that strain KB01 is capable of acquiring bio-essential phosphorus under very low phosphate conditions [96]. Further knowledge on photoferrotrophy is presented in Chapter 4 where we examine the cell surface chemistry and characteristics of strain KB01 and other photoferrotrophs. These data allow us to elucidate the mechanism by which strain KB01 avoids association with the Fe(III) (oxyhydr)oxides it produces as a by-product of its growth, ultimately causing a physical separation between the cell surface and mineral particles. Conversely, the surface chemistry of strain KB01's benthic relative, strain KoFox, results in cell-mineral association. To further the collective knowledge on photoferrotrophs in complex ferruginous environments, we determine the putative role of a dominant group of photoferrotrophs (related to strain KB01) as primary producers in a modern ferruginous lake (Kabuno Bay) in Chapter 5. Through this work we establish that there is potential for multiple modes of photosynthesis in the Kabuno Bay chemocline, despite the dominant population of photoferrotrophs, and describe the flow of organic carbon the microbial community network, following its production by photoferrotrophs. Specifically, we examine the relationship between primary production and the partitioning of organic carbon between terminal electron processes—namely Fe(III) reduction and methane production.

6.2 Photoferrotrophy during the Archean Eon

This dissertation uses integrated models to connect extant photoferrotrophy to the role that putative photoferrotrophs may have played during the Archean Eon. Prior to this work, photoferrotrophy during the Archean Eon remained largely unconstrained and, in particular, hypotheses were limited by experiments conducted with benthic isolates, which restricts the application of photoferrotrophy to the Archean ocean. In Chapter 2, we establish that strain KB01 is likely analogous to Precambrian photoferrotrophs through a detailed comparison of its key traits to other known phototrophs. The framework established in Chapter 2 is further developed in Chapter 3 where we specifically examine the antiquity of nutrient acquisition in strain KB01 and the

other members of its phylogenetic class—Chlorobia. We determine that the ability to acquire both sulfur and nitrogen under nutrient limiting conditions likely existed in the ancestors of modern Chlorobia and strain KB01. To link nutrient acquisition in extant environments to the Archean oceans we created a competition-based model between photoferrotrophs and oxygenic phototrophs, utilizing phosphorus and light availability, to determine how competition among these phototrophs could have played a role in delaying oxygenation of the Earth [96]. In Chapter 4, we revise the Archean iron budget and delineate a broader range of potential iron fluxes for the Archean oceans using a model constrained by the rock record. We subsequently couple the newly revised iron fluxes with the physical cell-mineral separation of pelagic photoferrotrophs to establish the role of photoferrotrophs in BIF deposition during the Archean Eon. We further utilize this integrated modeling approach to establish that pelagic photoferrotrophs could not only have deposited BIFs, but also fueled microbial methanogenesis, effectively supporting a flux of methane to the atmosphere, which would have contributed to the maintenance of a clement climate under the faint early Sun. In Chapter 5, we establish that a tight coupling exists between Fe(II) oxidation and Fe(III) reduction in a complex modern ferruginous environment. Such a coupling limits the export of Fe(III) (oxyhydr)oxides from the chemocline and the flow of organic carbon to microbial methanogenesis. Thus, the evolution of this coupling could have altered the early Earth ocean-atmosphere system, potentially explaining the lack of BIFs for the majority of the Proterozoic, despite persistent ferruginous conditions.

6.3 Looking ahead

The data and hypotheses generated in this dissertation provide an opportunity to continue to develop and constrain models of the early Earth ocean-atmosphere system. The specific growth kinetics of *Chlorobium phaeoferrooxidans* strain KB01 (Chapter 2, 3) can be further utilized to examine the relationship between nutrient acquisition and BIF deposition. For example, a one-dimensional flux balance model of an Archean ocean could be better constrained with the kinetic equation found in Chapter 2 (Eq. 2.3). Such a model could link ocean driven nutrient fluxes to primary production with the potential to predict the conditions under which BIFs would

form. Furthermore, this type of model could be used to examine some of the remaining enigmas surrounding BIF deposition, such as their banded character [9, 21, 42, 109]. Ultimately, the results gleaned from this small-scale model could be applied to a global modeling system, such as the coupled C-N-P-O_2-S cycles model (CANOPS [96]), to interrogate the impact of nutrient limited primary production on the whole ocean-atmosphere system. Finally, other changes in the rock record throughout the Archean and Proterozoic Eons may be examined in the context of kinetic studies of key types of primary producing phototrophs and further evaluation of the interactions among them. This dissertation takes steps to increase the knowledge of photoferrotrophy and its implications in the Archean oceans. The next stage of investigation will require evaluation of more photoferrotrophs in laboratory cultures, increased kinetic studies on these photoferrotrophs, and the application of these data in informing global models. Integrated research of this type will also provide more constraints on the role of photoferrotrophs during the Precambrian Eon. Additionally, given that isolates do not reflect the natural complexity of a microbial community in a ferruginous environment, continued study of ferruginous environments, analogous to Precambrian oceans, is needed to better constrain the interactions between photoferrotrophs and the microbial communities they often support.

6.4 Closing

Throughout Earth's history, life has shaped the planet's surface chemistry through its propagation and, therefore, transformation of numerous electron donors and acceptors. These interactions between life and Earth's surface have effectively modified the composition of oceans and the rocks deposited within them, shifted redox balances, and, most notably, underpinned biogeochemical cycles. To elucidate both the small- and large-scale implications of the microbial driven biogeochemical cycles throughout Earth's history, in-depth knowledge of individual metabolisms as well as the complexity of microbial community interactions, under conditions relevant to Earth's past, are required. This dissertation adds to the available knowledge on phototrophic Fe(II) oxidation and utilizes this knowledge to develop a more informed modeling framework for phototrophic primary production during the Archean Eon. In particular, this work delineates the likely role of

photoferrotrophs in the deposition of the world's largest iron ore formations, their influence on the Archean biosphere, and the resulting maintenance of a clement climate prior to proliferation of oxygenic phototrophic bacteria. The models generated in this dissertation utilize an integrated approach. For example, micro-scale interactions between a cell surface and an Fe(III) particle, major events in the geologic record, and modern ocean upwelling currents are combined to produce data on the whole ocean-atmosphere system during the Archean Eon. These integrated approaches can be applied to any time in Earth's history, but more importantly, they can be applied to examining Earth's future. As the drivers of biogeochemical cycles have largely shifted from microbial to anthropogenic, it is imperative that we continue to predict and constrain the past to better predict the future. A greater recognition of potential future outcomes provides us with the opportunity to put integrated approaches into action, creating new bio/geoengineering solutions that could maintain a life-sustaining planet.

Bibliography

[1] D. E. Canfield, M. T. Rosing, and C. Bjerrum. Early anaerobic metabolisms. *Philosophical Transactions of the Royal Society B-Biological Sciences*, 361(1474):1819–1834, Oct 2006.

[2] Heinrich D Holland. The oxygenation of the atmosphere and oceans. *Philosophical Transactions of the Royal Society of London B: Biological Sciences*, 361(1470):903–915, 2006.

[3] Paul G Falkowski, Tom Fenchel, and Edward F Delong. The microbial engines that drive earth's biogeochemical cycles. *Science*, 320(5879):1034–1039, 2008.

[4] Cornelis Klein. Some precambrian banded iron-formations (bifs) from around the world: Their age, geologic setting, mineralogy, metamorphism, geochemistry, and origins. *American Mineralogist*, 90(10):1473–1499, 2005.

[5] S. W. Poulton and D. E. Canfield. Ferruginous conditions: A dominant feature of the ocean through earth's history. *Elements*, 7(2):107–112, Apr 2011.

[6] P. Cloud. Paleoecological significance of banded iron formation. *Economic Geology*, 68(7):1135–1143, 1973.

[7] RM Garrels, EA Perry, and FT Mackenzie. Genesis of precambrian iron-formations and the development of atmospheric oxygen. *Economic Geology*, 68(7):1173–1179, 1973.

[8] Kurt O Konhauser, Tristan Hamade, Rob Raiswell, *et al.* Could bacteria have formed the precambrian banded iron formations? *Geology*, 30(12):1079–1082, 2002.

[9] A. Kappler and D. K. Newman. Formation of fe(iii)-minerals by fe(ii)-oxidizing photoautotrophic bacteria. *Geochimica Et Cosmochimica Acta*, 68(6):1217–1226, Mar 2004.

[10] Jin Xiong and Carl E Bauer. Complex evolution of photosynthesis. *Annual Review of Plant Biology*, 53(1):503–521, 2002.

[11] William F Martin, Donald A Bryant, and J Thomas Beatty. A physiological perspective on the origin and evolution of photosynthesis. *FEMS microbiology reviews*, 2017.

[12] C Magnabosco, KR Moore, JM Wolfe, and GP Fournier. Dating phototrophic microbial lineages with reticulate gene histories. *Geobiology*, 16(2):179–189, 2018.

[13] James Farquhar, Huiming Bao, and Mark Thiemens. Atmospheric influence of earth's earliest sulfur cycle. *Science*, 289(5480):756–758, 2000.

[14] AA Pavlov and JF Kasting. Mass-independent fractionation of sulfur isotopes in archean sediments: strong evidence for an anoxic archean atmosphere. *Astrobiology*, 2(1):27–41, 2002.

[15] D. E. Canfield. The early history of atmospheric oxygen: Homage to robert a. garrels. In *Annual Review of Earth and Planetary Sciences*, volume 33 of *Annual Review of Earth and Planetary Sciences*, pages 1–36. Annual Reviews, Palo Alto, 2005.

[16] Sean A Crowe, Lasse N Døssing, Nicolas J Beukes, *et al.* Atmospheric oxygenation three billion years ago. *Nature*, 501(7468):535–538, 2013.

[17] Stefan V Lalonde and Kurt O Konhauser. Benthic perspective on earth's oldest evidence for oxygenic photosynthesis. *Proceedings of the National Academy of Sciences*, 112(4):995–1000, 2015.

[18] Heinrich D Holland and Karl K Turekian. *Treatise on geochemistry*. Elsevier Science, 2004.

[19] Noah Planavsky, Andrey Bekker, Olivier J Rouxel, *et al.* Rare earth element and yttrium compositions of archean and paleoproterozoic fe formations revisited: new perspectives on the significance and mechanisms of deposition. *Geochimica et Cosmochimica Acta*, 74(22):6387–6405, 2010.

[20] F. Widdel, S. Schnell, S. Heising, *et al.* Ferrous iron oxidation by anoxygenic phototrophic bacteria. *Nature*, 362(6423):834–836, Apr 1993.

[21] A. Kappler, C. Pasquero, K. O. Konhauser, and D. K. Newman. Deposition of banded iron formations by anoxygenic phototrophic fe(ii)-oxidizing bacteria. *Geology*, 33(11):865–868, Nov 2005.

[22] Heinrich D Holland. *The chemical evolution of the atmosphere and oceans*. Princeton University Press, 1984.

[23] HEINRICH D Holland. The geologic history of seawater. *Treatise on geochemistry*, 6:583–625, 2003.

[24] SW Poulton and R Raiswell. The low-temperature geochemical cycle of iron: from continental fluxes to marine sediment deposition. *American Journal of Science*, 302(9):774–805, 2002.

[25] Simon W Poulton and Donald E Canfield. Development of a sequential extraction procedure for iron: implications for iron partitioning in continentally derived particulates. *Chemical geology*, 2005.

[26] Louis A Derry and Stein B Jacobsen. The chemical evolution of precambrian seawater: evidence from rees in banded iron formations. *Geochimica et Cosmochimica Acta*, 54(11):2965–2977, 1990.

[27] Sean A Crowe, Guillaume Paris, Sergei Katsev, *et al.* Sulfate was a trace constituent of archean seawater. *Science*, 346(6210):735–739, 2014.

[28] Timothy W Lyons, Christopher T Reinhard, and Noah J Planavsky. The rise of oxygen in earth/'s early ocean and atmosphere. *Nature*, 506(7488):307–315, 2014.

[29] David C Catling, Kevin J Zahnle, and Christopher P McKay. Biogenic methane, hydrogen escape, and the irreversible oxidation of early earth. *Science*, 293(5531):839–843, 2001.

[30] Mojtaba Fakhraee, Sean A Crowe, and Sergei Katsev. Sedimentary sulfur isotopes and neoarchean ocean oxygenation. *Science advances*, 4(1):e1701835, 2018.

[31] Ariel D Anbar, Yun Duan, Timothy W Lyons, *et al.* A whiff of oxygen before the great oxidation event? *Science*, 317(5846):1903–1906, 2007.

[32] Eva E Stüeken, Roger Buick, and Ariel D Anbar. Selenium isotopes support free o2 in the latest archean. *Geology*, 43(3):259–262, 2015.

[33] Robert Frei, Claudio Gaucher, Simon W Poulton, and Don E Canfield. Fluctuations in precambrian atmospheric oxygenation recorded by chromium isotopes. *Nature*, 461(7261):250–253, 2009.

[34] Devon B Cole, Christopher T Reinhard, Xiangli Wang, *et al.* A shale-hosted cr isotope record of low atmospheric oxygen during the proterozoic. *Geology*, 44(7):555–558, 2016.

[35] Woodward W Fischer, James Hemp, and Jena E Johnson. Evolution of oxygenic photosynthesis. *Annual Review of Earth and Planetary Sciences*, 44:647–683, 2016.

[36] Lewis M Ward, Joseph L Kirschvink, and Woodward W Fischer. Timescales of oxygenation following the evolution of oxygenic photosynthesis. *Origins of Life and Evolution of Biospheres*, 46(1):51–65, 2016.

[37] Donald E Canfield, Kirsten S Habicht, and BO Thamdrup. The archean sulfur cycle and the early history of atmospheric oxygen. *Science*, 288(5466):658–661, 2000.

[38] AG Cairns-Smith. Precambrian solution photochemistry, inverse segregation, and banded iron formations. *Nature*, 276:807–808, 1978.

[39] Paul S Braterman, A Graham Cairns-Smith, and Robert W Sloper. Photo-oxidation of hydrated fe(ii): significance for banded iron formations. *Nature*, 1983.

[40] Kurt O Konhauser, Larry Amskold, Stefan V Lalonde, *et al.* Decoupling photochemical fe (ii) oxidation from shallow-water bif deposition. *Earth and Planetary Science Letters*, 258(1):87–100, 2007.

[41] Madeline Vargas, Kazem Kashefi, Elizabeth L Blunt-Harris, and Derek R Lovley. Microbiological evidence for fe (iii) reduction on early earth. *Nature*, 395(6697):65–67, 1998.

[42] KO Konhauser, DK Newman, and A Kappler. The potential significance of microbial fe (iii) reduction during deposition of precambrian banded iron formations. *Geobiology*, 3(3):167–177, 2005.

[43] David Emerson and Craig Moyer. Isolation and characterization of novel iron-oxidizing bacteria that grow at circumneutral ph. *Appl. Environ. Microbiol.*, 63(12):4784–4792, 1997.

[44] Katrina J Edwards, Daniel R Rogers, Carl O Wirsen, and TM McCollom. Isolation and characterization of novel psychrophilic, neutrophilic, fe-oxidizing, chemolithoautotrophic alpha- and gamma-proteobacteria from the deep sea. *Appl. Environ. Microbiol.*, 69(5):2906–2913, 2003.

[45] James J Anderson and Allan H Devol. Deep water renewal in saanich inlet, an intermittently anoxic basin. *Estuarine and Coastal Marine Science*, 1(1):1–10, 1973.

[46] Don E Canfield, Frank J Stewart, Bo Thamdrup, *et al.* A cryptic sulfur cycle in oxygen-minimum–zone waters off the chilean coast. *Science*, 330(6009):1375–1378, 2010.

[47] Sean A Crowe, CarriAyne Jones, Sergei Katsev, *et al.* Photoferrotrophs thrive in an archean ocean analogue. *Proceedings of the National Academy of Sciences*, 105(41):15938–15943, 2008.

[48] Marc Llirós, Tamara García–Armisen, François Darchambeau, *et al.* Pelagic photoferrotrophy and iron cycling in a modern ferruginous basin. *Scientific reports*, 5, 2015.

[49] Katherine Barbeau. Photochemistry of organic iron (iii) complexing ligands in oceanic systems. *Photochemistry and photobiology*, 82(6):1505–1516, 2006.

[50] Debra J Lonergan, Harry L Jenter, John D Coates, *et al.* Phylogenetic analysis of dissimilatory fe (iii)-reducing bacteria. *Journal of bacteriology*, 178(8):2402–2408, 1996.

[51] Armin Ehrenreich and Friedrich Widdel. Anaerobic oxidation of ferrous iron by purple bacteria, a new type of phototrophic metabolism. *Applied and environmental microbiology*, 60(12):4517–4526, 1994.

[52] Silke Heising and Bernhard Schink. Phototrophic oxidation of ferrous iron by a rhodomicrobium vannielii strain. *Microbiology*, 144(8):2263–2269, 1998.

[53] S. Heising, L. Richter, W. Ludwig, and B. Schink. Chlorobium ferrooxidans sp nov., a phototrophic green sulfur bacterium that oxidizes ferrous iron in coculture with a "geospirillum" sp strain. *Archives of Microbiology*, 172(2):116–124, Aug 1999.

[54] Kristina L Straub, Frederick A Rainey, and Friedrich Widdel. Rhodovulum iodosum sp. nov. and rhodovulum robiginosum sp. nov., two new marine phototrophic ferrous-iron-oxidizing purple bacteria. *International Journal of Systematic and Evolutionary Microbiology*, 49(2):729–735, 1999.

[55] F. Hegler, N. R. Posth, J. Jiang, and A. Kappler. Physiology of phototrophic iron(ii)-oxidizing bacteria: implications for modern and ancient environments. *FEMS Microbiology Ecology*, 66(2):250–260, Nov 2008.

[56] Katja Laufer, Annika Niemeyer, Verena Nikeleit, *et al.* Physiological characterization of a halotolerant anoxygenic phototrophic fe (ii)-oxidizing green-sulfur bacterium isolated from a marine sediment. *FEMS microbiology ecology*, 93(5), 2017.

[57] Casey Bryce, Nia Blackwell, Caroline Schmidt, *et al.* Microbial anaerobic fe (ii) oxidation–ecology, mechanisms and environmental implications. *Environmental microbiology*, 20(10):3462–3483, 2018.

[58] S. A. Crowe, A. S. Hahn, C. Morgan-Lang, *et al.* Draft genome sequence of the pelagic photoferrotroph chlorobium phaeoferrooxidans. *Genome Announc*, 5(13), Mar 30 2017.

[59] Yongqin Jiao and Dianne K Newman. The pio operon is essential for phototrophic fe (ii) oxidation in rhodopseudomonas palustris tie-1. *Journal of bacteriology*, 189(5):1765–1773, 2007.

[60] Laura R Croal, Clark M Johnson, Brian L Beard, and Dianne K Newman. Iron isotope fractionation by fe (ii)-oxidizing photoautotrophic bacteria. *Geochimica et cosmochimica acta*, 68(6):1227–1242, 2004.

[61] S Schädler, C Burkhardt, F Hegler, *et al.* Formation of cell-iron-mineral aggregates by phototrophic and nitrate-reducing anaerobic fe (ii)-oxidizing bacteria. *Geomicrobiology Journal*, 26(2):93–103, 2009.

[62] Nicole R Posth, Sonia Huelin, Kurt O Konhauser, and Andreas Kappler. Size, density and composition of cell–mineral aggregates formed during anoxygenic phototrophic fe (ii) oxidation: Impact on modern and ancient environments. *Geochimica et Cosmochimica Acta*, 74(12):3476–3493, 2010.

[63] Tina Gauger, James M Byrne, Kurt O Konhauser, *et al.* Influence of organics and silica on fe (ii) oxidation rates and cell–mineral aggregate formation by the green-sulfur fe (ii)-oxidizing bacterium chlorobium ferrooxidans kofox–implications for fe (ii) oxidation in ancient oceans. *Earth and Planetary Science Letters*, 443:81–89, 2016.

[64] Lidia Romero-Viana, Brendan J Keely, Antonio Camacho, Eduardo Vicente, and M Rosa Miracle. Primary production in lake la cruz (spain) over the last four centuries: reconstruction based on sedimentary signal of photosynthetic pigments. *Journal of Paleolimnology*, 43(4):771–786, 2010.

[65] Corinne Biderre-Petit, Delphine Boucher, Jan Kuever, *et al.* Identification of sulfur-cycle prokaryotes in a low-sulfate lake (lake pavin) using apra and 16s rrna gene markers. *Microbial ecology*, 61(2):313–327, 2011.

[66] SA Crowe, JA Maresca, C Jones, *et al.* Deep-water anoxygenic photosythesis in a ferruginous chemocline. *Geobiology*, 12(4):322–339, 2014.

[67] Xavier A Walter, Antonio Picazo, Maria R Miracle, *et al.* Phototrophic fe (ii)-oxidation in the chemocline of a ferruginous meromictic lake. *Frontiers in microbiology*, 5, 2014.

[68] SL Schiff, JM Tsuji, Lingling Wu, *et al.* Millions of boreal shield lakes can be used to probe archaean ocean biogeochemistry. *Scientific reports*, 7:46708, 2017.

[69] SA Crowe, S Katsev, K Leslie, *et al.* The methane cycle in ferruginous lake matano. *Geobiology*, 9(1):61–78, 2011.

[70] A. Zegeye, S. Bonneville, L. G. Benning, *et al.* Green rust formation controls nutrient availability in a ferruginous water column. *Geology*, 40(7):599–602, Jul 2012.

[71] LB Kuntz, TA Laakso, DP Schrag, and SA Crowe. Modeling the carbon cycle in lake matano. *Geobiology*, 13(5):454–461, 2015.

[72] Cédric Morana, Fleur AE Roland, Sean A Crowe, *et al.* Chemoautotrophy and anoxygenic photosynthesis within the water column of a large meromictic tropical lake (lake kivu, east africa). *Limnology and Oceanography*, 61(4):1424–1437, 2016.

[73] Céline C Michiels, François Darchambeau, Fleur AE Roland, *et al.* Iron-dependent nitrogen cycling in a ferruginous lake and the nutrient status of proterozoic oceans. *Nature GeoScience*, 10(3):217–221, 2017.

[74] Nicolas J Beukes and Cornelis Klein. Geochemistry and sedimentology of a facies transition—from microbanded to granular iron-formation—in the early proterozoic transvaal supergroup, south africa. *Precambrian Research*, 47(1):99–139, 1990.

[75] Alan J Kaufman, JM Hayes, and C Klein. Primary and diagenetic controls of isotopic compositions of iron-formation carbonates. *Geochimica et Cosmochimica Acta*, 54(12):3461–3473, 1990.

[76] A. F. Trendall. The hamersley basin. *Developments in Precambrain Geology*, 6:69–129, 1983.

[77] DE Ayres. Genesis of iron-bearing minerals in banded iron formation mesobands in the dales gorge member, hamersley group, western australia. *Economic Geology*, 67(8):1214–1233, 1972.

[78] ME Baur, JM Hayes, SA Studley, and MR Walter. Millimeter-scale variations of stable isotope abundances in carbonates from banded iron-formations in the hamersley group of western australia. *Economic Geology*, 80(2):270–282, 1985.

[79] Birger Rasmussen, Bryan Krapež, and Daniela B Meier. Replacement origin for hematite in 2.5 ga banded iron formation: Evidence for postdepositional oxidation of iron-bearing minerals. *Bulletin*, 126(3-4):438–446, 2014.

[80] Birger Rasmussen, Janet R Muhling, Alexandra Suvorova, and Bryan Krapež. Dust to dust: Evidence for the formation of "primary" hematite dust in banded iron formations via oxidation of iron silicate nanoparticles. *Precambrian Research*, 284:49–63, 2016.

[81] Nicholas J Tosca, Stephen Guggenheim, and Peir K Pufahl. An authigenic origin for precambrian greenalite: Implications for iron formation and the chemistry of ancient seawater. *Bulletin*, 128(3-4):511–530, 2016.

[82] P Kharecha, J Kasting, and J Siefert. A coupled atmosphere–ecosystem model of the early archean earth. *Geobiology*, 3(2):53–76, 2005.

[83] Ann E Isley and Dallas H Abbott. Plume-related mafic volcanism and the deposition of banded iron formation. *Journal of Geophysical Research: Solid Earth*, 104(B7):15461–15477, 1999.

[84] Heinrich D Holland, B Lazar, and Mark McCaffrey. Evolution of the atmosphere and oceans. *Nature*, 320(6057):27–33, 1986.

[85] C Jones, Suolong Nomosatryo, Sean Andrew Crowe, Christian J Bjerrum, and Donald Eugene Canfield. Iron oxides, divalent cations, silica, and the early earth phosphorus crisis. *Geology*, 43(2):135–138, 2015.

[86] Birger Rasmussen, Daniela B Meier, Bryan Krapež, and Janet R Muhling. Iron silicate microgranules as precursor sediments to 2.5-billion-year-old banded iron formations. *Geology*, 41(4):435–438, 2013.

[87] Birger Rasmussen, Bryan Krapež, Janet R Muhling, and Alexandra Suvorova. Precipitation of iron silicate nanoparticles in early precambrian oceans marks earth's first iron age. *Geology*, 43(4):303–306, 2015.

[88] Leslie J Robbins, Sean P Funk, Shannon L Flynn, *et al.* Hydrogeological constraints on the formation of palaeoproterozoic banded iron formations. *Nature GeoScience*, 12(7):558–563, 2019.

[89] Cornelis Klein and Nicolas J Beukes. Geochemistry and sedimentology of a facies transition from limestone to iron-formation deposition in the early proterozoic transvaal supergroup, south africa. *Economic Geology*, 84(7):1733–1774, 1989.

[90] David Antoine, Jean-Michel André, and André Morel. Oceanic primary production: 2. estimation at global scale from satellite (coastal zone color scanner) chlorophyll. *Global biogeochemical cycles*, 10(1):57–69, 1996.

[91] Paul G Falkowski and John A Raven. *Aquatic photosynthesis*. Princeton University Press, 2013.

[92] Robert E Blankenship. Origin and early evolution of photosynthesis. *Photosynthesis research*, 33(2):91–111, 1992.

[93] Robert E Blankenship, Michael T Madigan, and Carl E Bauer. *Anoxygenic photosynthetic bacteria*, volume 2. Springer Science & Business Media, 2006.

[94] Noah J Planavsky, Dan Asael, Axel Hofmann, *et al.* Evidence for oxygenic photosynthesis half a billion years before the great oxidation event. *Nature GeoScience*, 7(4):283–286, 2014.

[95] Kazumi Ozaki, Eiichi Tajika, Peng K Hong, Yusuke Nakagawa, and Christopher T Reinhard. Effects of primitive photosynthesis on earth's early climate system. *Nature GeoScience*, page 1, 2017.

[96] Kazumi Ozaki, Katharine J Thompson, Rachel L Simister, Sean A Crowe, and Christopher T Reinhard. Anoxygenic photosynthesis and the delayed oxygenation of earth's atmosphere. *Nature communications*, 10(1):1–10, 2019.

[97] Patricia Sánchez-Baracaldo and Tanai Cardona. On the origin of oxygenic photosynthesis and cyanobacteria. *New Phytologist*, 2019.

[98] Wolf-Dieter Schubert, Olaf Klukas, Wolfram Saenger, *et al.* A common ancestor for oxygenic and anoxygenic photosynthetic systems: a comparison based on the structural model of photosystem i. *Journal of molecular biology*, 280(2):297–314, 1998.

[99] Katharine J Thompson, Paul A Kenward, Kohen W Bauer, *et al.* Photoferrotrophy, deposition of banded iron formations, and methane production in archean oceans. *Science Advances*, 5(11):eaav2869, 2019.

[100] David J Des Marais. When did photosynthesis emerge on earth? *Science*, 289(5485):1703–1705, 2000.

[101] J. Xiong, W. M. Fischer, K. Inoue, M. Nakahara, and C. E. Bauer. Molecular evidence for the early evolution of photosynthesis. *Science*, 289(5485):1724–1730, Sep 2000.

[102] John M Olson and Robert E Blankenship. Thinking about the evolution of photosynthesis. In *Discoveries in Photosynthesis*, pages 1073–1086. Springer, 2005.

[103] Antonio Camacho, Xavier A Walter, Antonio Picazo, and Jakob Zopfi. Photoferrotrophy: remains of an ancient photosynthesis in modern environments. *Frontiers in microbiology*, 8:323, 2017.

[104] Genming Luo, Shuhei Ono, Nicolas J Beukes, *et al.* Rapid oxygenation of earth's atmosphere 2.33 billion years ago. *Science advances*, 2(5):e1600134, 2016.

[105] Pascal Philippot, Janaína N Ávila, Bryan A Killingsworth, *et al.* Globally asynchronous sulphur isotope signals require re-definition of the great oxidation event. *Nature communications*, 9(1):2245, 2018.

[106] Stephanie L Olson, Lee R Kump, and James F Kasting. Quantifying the areal extent and dissolved oxygen concentrations of archean oxygen oases. *Chemical Geology*, 362:35–43, 2013.

[107] Nicole R Posth, Florian Hegler, Kurt O Konhauser, and Andreas Kappler. Alternating si and fe deposition caused by temperature fluctuations in precambrian oceans. *Nature GeoScience*, 1(10):703, 2008.

[108] LR Croal, Y Jiao, A Kappler, and DK Newman. Phototrophic fe (ii) oxidation in an atmosphere of h2: implications for archean banded iron formations. *Geobiology*, 7(1):21–24, 2009.

[109] Nicole R Posth, Kurt O Konhauser, and Andreas Kappler. Microbiological processes in banded iron formation deposition. *Sedimentology*, 60(7):1733–1754, 2013.

[110] Pawan K Dadheech, Gernot Glöckner, Peter Casper, *et al.* Cyanobacterial diversity in the hot spring, pelagic and benthic habitats of a tropical soda lake. *FEMS microbiology ecology*, 85(2):389–401, 2013.

[111] Gideon Mazor, Giora J Kidron, Ahuva Vonshak, and Aharon Abeliovich. The role of cyanobacterial exopolysaccharides in structuring desert microbial crusts. *FEMS Microbiology Ecology*, 21(2):121–130, 1996.

[112] Natascha Staats, Ben De Winder, Lucas Stal, and Luuc Mur. Isolation and characterization of extracellular polysaccharides from the epipelic diatoms cylindrotheca closterium and navicula salinarum. *European Journal of Phycology*, 34(2):161–169, 1999.

[113] Juergen Schieber. Microbial mats on muddy substrates-examples of possible sedimentary features and underlying processes. *Atlas of microbial mat features preserved within the siliciclastic rock record*, 2:117e133, 2007.

[114] Martin Schmid, Michel Halbwachs, Bernhard Wehrli, and Alfred Wüest. Weak mixing in lake kivu: new insights indicate increasing risk of uncontrolled gas eruption. *Geochemistry, Geophysics, Geosystems*, 6(7), 2005.

[115] Katharine J Thompson, Rachel L Simister, Aria S Hahn, Steven J Hallam, and Sean A Crowe. Nutrient acquisition and the metabolic potential of photoferrotrophic chlorobi. *Frontiers in Microbiology*, 8:1212, 2017.

[116] Friedrich Widdel and Friedhelm Bak. Gram-negative mesophilic sulfate-reducing bacteria. In *The prokaryotes*, pages 3352–3378. Springer, 1992.

[117] Elmar Pruesse, Christian Quast, Katrin Knittel, *et al.* Silva: a comprehensive online resource for quality checked and aligned ribosomal rna sequence data compatible with arb. *Nucleic acids research*, 35(21):7188–7196, 2007.

[118] Christian Quast, Elmar Pruesse, Pelin Yilmaz, *et al.* The silva ribosomal rna gene database project: improved data processing and web-based tools. *Nucleic acids research*, page gks1219, 2012.

[119] Mark A Larkin, Gordon Blackshields, NP Brown, *et al.* Clustal w and clustal x version 2.0. *Bioinformatics*, 23(21):2947–2948, 2007.

[120] Koichiro Tamura, Glen Stecher, Daniel Peterson, Alan Filipski, and Sudhir Kumar. Mega6: molecular evolutionary genetics analysis version 6.0. *Molecular biology and evolution*, 30(12):2725–2729, 2013.

[121] Sudhir Kumar, Glen Stecher, and Koichiro Tamura. Mega7: Molecular evolutionary genetics analysis version 7.0 for bigger datasets. *Molecular biology and evolution*, page msw054, 2016.

[122] Jared T Simpson, Kim Wong, Shaun D Jackman, *et al.* Abyss: a parallel assembler for short read sequence data. *Genome research*, 19(6):1117–1123, 2009.

[123] Stefan Kurtz, Adam Phillippy, Arthur L Delcher, *et al.* Versatile and open software for comparing large genomes. *Genome biology*, 5(2):R12, 2004.

[124] Jan P Meier-Kolthoff, Alexander F Auch, Hans-Peter Klenk, and Markus Göker. Genome sequence-based species delimitation with confidence intervals and improved distance functions. *BMC bioinformatics*, 14(1):60, 2013.

[125] Doug Hyatt, Gwo-Liang Chen, Philip F LoCascio, *et al.* Prodigal: prokaryotic gene recognition and translation initiation site identification. *BMC bioinformatics*, 11(1):119, 2010.

[126] Takuya Aramaki, Romain Blanc-Mathieu, Hisashi Endo, *et al.* Kofamkoala: Kegg ortholog assignment based on profile hmm and adaptive score threshold. *bioRxiv*, page 602110, 2019.

[127] Minoru Kanehisa, Michihiro Araki, Susumu Goto, *et al.* Kegg for linking genomes to life and the environment. *Nucleic acids research*, 36(suppl 1):D480–D484, 2008.

[128] ED Graham, JF Heidelberg, and BJ Tully. Potential for primary productivity in a globally-distributed bacterial phototroph. *The ISME journal*, 12(7):1861, 2018.

[129] Sara El-Gebali, Jaina Mistry, Alex Bateman, *et al.* The pfam protein families database in 2019. *Nucleic acids research*, 47(D1):D427–D432, 2018.

[130] Vincent Lombard, Hemalatha Golaconda Ramulu, Elodie Drula, Pedro M Coutinho, and Bernard Henrissat. The carbohydrate-active enzymes database (cazy) in 2013. *Nucleic acids research*, 42(D1):D490–D495, 2013.

[131] Tatiana A Tatusova and Thomas L Madden. Blast 2 sequences, a new tool for comparing protein and nucleotide sequences. *FEMS microbiology letters*, 174(2):247–250, 1999.

[132] Sean R Eddy. A new generation of homology search tools based on probabilistic inference. In *Genome Informatics 2009: Genome Informatics Series Vol. 23*, pages 205–211. World Scientific, 2009.

[133] E Viollier, PW Inglett, K Hunter, AN Roychoudhury, and P Van Cappellen. The ferrozine method revisited: Fe (ii)/fe (iii) determination in natural waters. *Applied geochemistry*, 15(6):785–790, 2000.

[134] Niels-Ulrik Frigaard, Kim L Larsen, and Raymond P Cox. Spectrochromatography of photosynthetic pigments as a fingerprinting technique for microbial phototrophs. *FEMS microbiology ecology*, 20(2):69–77, 1996.

[135] DK Button. Nutrient uptake by microorganisms according to kinetic parameters from theory as related to cytoarchitecture. *Microbiol Mol Biol R*, 1998.

[136] CL Woldringh, JS Binnerts, and A Mans. Variation in escherichia coli buoyant density measured in percoll gradients. *Journal of bacteriology*, 148(1):58–63, 1981.

[137] Carles M Borrego, Juan B Arellano, Carles A Abella, Tomas Gillbro, and Jesús Garcia-Gil. The molar extinction coefficient of bacteriochlorophyll e and the pigment stoichiometry in chlorobium phaeobacteroides. *Photosynthesis Research*, 60(2-3):257–264, 1999.

[138] A. K. Manske, J. Glaeser, M. A. M. Kuypers, and J. Overmann. Physiology and phylogeny of green sulfur bacteria forming a monospecific phototrophic assemblage at a depth of 100 meters in the black sea. *Applied and Environmental Microbiology*, 71(12):8049–8060, Dec 2005.

[139] Misha Kudryashev, Aikaterini Aktoudianaki, Dimitrios Dedoglou, Henning Stahlberg, and Georgios Tsiotis. The ultrastructure of chlorobaculum tepidum revealed by cryo-electron tomography. *Biochimica et Biophysica Acta (BBA)-Bioenergetics*, 1837(10):1635–1642, 2014.

[140] CM Borrego, LJ Garcia-Gil, X Vila, *et al.* Distribution of bacteriochlorophyll homologs in natural populations of brown-colored phototrophic sulfur bacteria. *FEMS Microbiology Ecology*, 24(4):301–309, Dec 1997.

[141] Jörg Overmann. The family chlorobiaceae. *The Prokaryotes: Volume 7: Proteobacteria: Delta, Epsilon Subclass*, pages 359–378, 2006.

[142] Donald A Bryant, Zhenfeng Liu, Tao Li, *et al.* Comparative and functional genomics of anoxygenic green bacteria from the taxa chlorobi, chloroflexi, and acidobacteria. In *Functional genomics and evolution of photosynthetic systems*, pages 47–102. Springer, 2012.

[143] Inger Andersson and Anders Backlund. Structure and function of rubisco. *Plant Physiology and Biochemistry*, 46(3):275–291, 2008.

[144] Thomas E Hanson and F Robert Tabita. A ribulose-1, 5-bisphosphate carboxylase/oxygenase (rubisco)-like protein from chlorobium tepidum that is involved with sulfur metabolism and the response to oxidative stress. *Proceedings of the National Academy of Sciences*, 98(8):4397–4402, 2001.

[145] Roman A Barco, David Emerson, Jason B Sylvan, *et al.* The proteomic profile of an obligate iron-oxidizing chemolithoautotroph reveals new insight into microbial iron oxidation. *Applied and Environmental Microbiology*, pages AEM. 01374–15, 2015.

[146] William B Whitman, David C Coleman, and William J Wiebe. Prokaryotes: the unseen majority. *Proceedings of the National Academy of Sciences*, 95(12):6578–6583, 1998.

[147] Christopher T Reinhard, Noah J Planavsky, Benjamin C Gill, *et al.* Evolution of the global phosphorus cycle. *Nature*, 2016.

[148] Niels-Ulrik Frigaard, Aline Gomez Maqueo Chew, Hui Li, Julia A Maresca, and Donald A Bryant. Chlorobium tepidum: insights into the structure, physiology, and metabolism of a green sulfur bacterium derived from the complete genome sequence. *Photosynthesis Research*, 78(2):93–117, 2003.

[149] Evelyn Marschall, Mareike Jogler, Uta Henßge, and Jörg Overmann. Large-scale distribution and activity patterns of an extremely low-light-adapted population of green sulfur bacteria in the black sea. *Environmental microbiology*, 12(5):1348–1362, 2010.

[150] Douglas Cork, Jeremy Mathers, Andrea Maka, and Anna Srnak. Control of oxidative sulfur metabolism of chlorobium limicola forma thiosulfatophilum. *Appl. Environ. Microbiol.*, 49(2):269–272, 1985.

[151] Matthew T Cottrell, Josephine Ras, and David L Kirchman. Bacteriochlorophyll and community structure of aerobic anoxygenic phototrophic bacteria in a particle-rich estuary. *The ISME journal*, 4(7):945, 2010.

[152] Mikhail V Zubkov, Bernhard M Fuchs, Heike Eilers, Peter H Burkill, and Rudolf Amann. Determination of total protein content of bacterial cells by sypro staining and flow cytometry. *Appl. Environ. Microbiol.*, 65(7):3251–3257, 1999.

[153] Hans Van Gemerden. The sulfide affinity of phototrophic bacteria in relation to the location of elemental sulfur. *Archives of microbiology*, 139(4):289–294, 1984.

[154] Sean A Crowe, Raymond P Cox, CarriAyne Jones, *et al.* Decrypting the sulfur cycle in oceanic oxygen minimum zones. *The ISME journal*, page 1, 2018.

[155] J Jeffrey Morris. Black queen evolution: the role of leakiness in structuring microbial communities. *Trends in Genetics*, 31(8):475–482, 2015.

[156] Elena Kazamia, Hjördis Czesnick, Thi Thanh Van Nguyen, *et al.* Mutualistic interactions between vitamin b12-dependent algae and heterotrophic bacteria exhibit regulation. *Environmental microbiology*, 14(6):1466–1476, 2012.

[157] Mak A Saito, Daniel M Sigman, and François MM Morel. The bioinorganic chemistry of the ancient ocean: the co-evolution of cyanobacterial metal requirements and biogeochemical cycles at the archean–proterozoic boundary? *Inorganica Chimica Acta*, 356:308–318, 2003.

[158] I Halevy and A Bachan. The geologic history of seawater ph. *Science*, 355(6329):1069–1071, 2017.

[159] ME Barley, AL Pickard, and PJ Sylvester. Emplacement of a large igneous province as a possible cause of banded iron formation 2.45 billion years ago. *Nature*, 385(6611):55, 1997.

[160] AF Trendall. The significance of banded iron formation (bif) in the precambrian stratigraphic record. *Geoscientist*, 10:4–7, 2000.

[161] Ivan Valiela and Ivan Valiela. *Marine ecological processes*, volume 686. Springer, 1995.

[162] Paul G Falkowski. Evolution of the nitrogen cycle and its influence on the biological sequestration of co 2 in the ocean. *Nature*, 387(6630):272–275, 1997.

[163] Christopher B Field, Michael J Behrenfeld, James T Randerson, and Paul Falkowski. Primary production of the biosphere: integrating terrestrial and oceanic components. *Science*, 281(5374):237–240, 1998.

[164] Robert W Howarth, Roxanne Marino, Judith Lane, and Jonathan J Cole. Nitrogen fixation in freshwater, estuarine, and marine ecosystems. 1. rates and importance. *Limnology and Oceanography*, 33(4part2):669–687, 1988.

[165] D Karl, R Letelier, L Tupas, *et al.* The role of nitrogen fixation in biogeochemical cycling in the subtropical north pacific ocean. *Nature*, 388(6642):533–538, 1997.

[166] Douglas G Capone and Edward J Carpenter. Nitrogen fixation in the marine environment. *Science*, 217(4565):1140–1142, 1982.

[167] Douglas G Capone, James A Burns, Joseph P Montoya, *et al.* Nitrogen fixation by trichodesmium spp.: An important source of new nitrogen to the tropical and subtropical north atlantic ocean. *Global Biogeochemical Cycles*, 19(2), 2005.

[168] Edward J Carpenter and Kristen Romans. Major role of the cyanobacterium trichodesmium in nutrient cycling in the north atlantic ocean. *Science*, 254(5036):1356, 1991.

[169] Andrew D Czaja, Clark M Johnson, Brian L Beard, *et al.* Biological fe oxidation controlled deposition of banded iron formation in the ca. 3770ma isua supracrustal belt (west greenland). *Earth and Planetary Science Letters*, 363:192–203, 2013.

[170] Donald E Canfield, Simon W Poulton, Andrew H Knoll, *et al.* Ferruginous conditions dominated later neoproterozoic deep-water chemistry. *Science*, 321(5891):949–952, 2008.

[171] Noah J Planavsky, Peter McGoldrick, Clinton T Scott, *et al.* Widespread iron-rich conditions in the mid-proterozoic ocean. *Nature*, 477(7365):448–451, 2011.

[172] James CG Walker. Was the archaean biosphere upside down? *Nature*, 329(6141):710–712, 1987.

[173] Hyman Hartman. The evolution of photosynthesis and microbial mats: A speculation on the banded iron formations. *MBL LECT. BIOL. 1984.*, 1984.

[174] CM Moore, MM Mills, KR Arrigo, *et al.* Processes and patterns of oceanic nutrient limitation. *Nature GeoScience*, 6(9):701–710, 2013.

[175] Arpita Bose and Dianne K Newman. Regulation of the phototrophic iron oxidation (pio) genes in rhodopseudomonas palustris tie-1 is mediated by the global regulator, fixk. *Molecular microbiology*, 79(1):63–75, 2011.

[176] L Pereira, IH Saraiva, R Coelho, *et al.* Crystallization and preliminary crystallographic studies of foxe from rhodobacter ferrooxidans sw2, an feii oxidoreductase involved in photoferrotrophy. *Acta Crystallographica Section F: Structural Biology and Crystallization Communications*, 68(9):1106–1108, 2012.

[177] George M Garrity, John G Holt, Jörg Overmann, *et al.* Phylum bxi. chlorobi phy. nov. In *Bergey's Manual® of Systematic Bacteriology*, pages 601–623. Springer, 2001.

[178] Sumedha Sadekar, Jason Raymond, and Robert E Blankenship. Conservation of distantly related membrane proteins: photosynthetic reaction centers share a common structural core. *Molecular biology and evolution*, 23(11):2001–2007, 2006.

[179] Soichirou Satoh, Mamoru Mimuro, and Ayumi Tanaka. Construction of a phylogenetic tree of photosynthetic prokaryotes based on average similarities of whole genome sequences. *PloS one*, 8(7):e70290, 2013.

[180] C. M. Borrego and L. J. Garciagil. Rearrangement of light-harvesting bacteriochlorophyll homologs as a response of green sulfur bacteria to low-light intensities. *Photosynthesis Research*, 45(1):21–30, Jul 1995.

[181] Lea H Gregersen, Kirsten S Habicht, Sandro Peduzzi, *et al.* Dominance of a clonal green sulfur bacterial population in a stratified lake. *FEMS microbiology ecology*, 70(1):30–41, 2009.

[182] Toby Tyrrell. The relative influences of nitrogen and phosphorus on oceanic primary production. *Nature*, 400(6744):525–531, 1999.

[183] Donald E Canfield, Alexander N Glazer, and Paul G Falkowski. The evolution and future of earth's nitrogen cycle. *Science*, 330(6001):192–196, 2010.

[184] Ben Johnson and Colin Goldblatt. The nitrogen budget of earth. *Earth-Science Reviews*, 148:150–173, 2015.

[185] C Mark Moore, Matthew M Mills, Eric P Achterberg, *et al.* Large-scale distribution of atlantic nitrogen fixation controlled by iron availability. *Nature GeoScience*, 2(12):867–871, 2009.

[186] Jacques Meyer, Bruce C Kelley, and Paulette M Vignais. Nitrogen fixation and hydrogen metabolism in photosynthetic bacteria. *Biochimie*, 60(3):245–260, 1978.

[187] Jason Raymond, Janet L Siefert, Christopher R Staples, and Robert E Blankenship. The natural history of nitrogen fixation. *Molecular biology and evolution*, 21(3):541–554, 2004.

[188] Eric S Boyd, Amaya M Garcia Costas, Trinity L Hamilton, Florence Mus, and John W Peters. Evolution of molybdenum nitrogenase during the transition from anaerobic to aerobic metabolism. *Journal of bacteriology*, 197(9):1690–1699, 2015.

[189] Madeline C Weiss, Filipa L Sousa, Natalia Mrnjavac, *et al.* The physiology and habitat of the last universal common ancestor. *Nature Microbiology*, 1:16116, 2016.

[190] JJR Frausto Da Silva and Robert Joseph Paton Williams. *The biological chemistry of the elements: the inorganic chemistry of life*. Oxford University Press, 2001.

[191] James CG Walker and Peter Brimblecombe. Iron and sulfur in the pre-biologic ocean. *Precambrian Research*, 28(3-4):205–222, 1985.

[192] G Paris, JF Adkins, Alex L Sessions, SM Webb, and WW Fischer. Neoarchean carbonate–associated sulfate records positive delta33s anomalies. *Science*, 346(6210):739–741, 2014.

[193] Iadviga Zhelezinskaia, Alan J Kaufman, James Farquhar, and John Cliff. Large sulfur isotope fractionations associated with neoarchean microbial sulfate reduction. *Science*, 346(6210):742–744, 2014.

[194] Niels-Ulrik Frigaard and Donald A Bryant. Genomic insights into the sulfur metabolism of phototrophic green sulfur bacteria. In *Sulfur metabolism in phototrophic organisms*, pages 337–355. Springer, 2008.

[195] Russell L Cuhel, Craig D Taylor, and Holger W Jannasch. Assimilatory sulfur metabolism in marine microorganisms: sulfur metabolism, protein synthesis, and growth of pseudomonas halodurans and alteromonas luteo-violaceus during unperturbed batch growth. *Archives of Microbiology*, 130(1):8–13, 1981.

[196] Kishori M Konwar, Niels W Hanson, Maya P Bhatia, *et al.* Metapathways v2. 5: quantitative functional, taxonomic and usability improvements. *Bioinformatics*, 31(20):3345–3347, 2015.

[197] Kishori M Konwar, Niels W Hanson, Antoine P Pagé, and Steven J Hallam. Metapathways: a modular pipeline for constructing pathway/genome databases from environmental sequence information. *BMC bioinformatics*, 14(1):202, 2013.

[198] Ron Caspi, Tomer Altman, Kate Dreher, *et al.* The metacyc database of metabolic pathways and enzymes and the biocyc collection of pathway/genome databases. *Nucleic acids research*, 40(D1):D742–D753, 2012.

[199] Michael Kaufmann. The role of the cog database in comparative and functional genomics. *Current Bioinformatics*, 1(3):291–300, 2006.

[200] BL Cantarel, PM Coutinho, C Rancurel, *et al.* The carbohydrate-active enzymes database (cazy): an expert resource for glycogenomics. *Nucleic acids research*, 37:233–238, 2009.

[201] R Agarwala, T Barrett, J Beck, *et al.* Database resources of the national center for biotechnology information. *Nucleic Acids Research*, 43:6–17, 2015.

[202] Luis M Rubio and Paul W Ludden. Biosynthesis of the iron-molybdenum cofactor of nitrogenase. *Annu. Rev. Microbiol.*, 62:93–111, 2008.

[203] Rolf D Joerger, Paul E Bishop, and Harold J Evans. Bacterial alternative nitrogen fixation systems. *CRC Critical reviews in microbiology*, 16(1):1–14, 1988.

[204] Eric S Boyd, Trinity L Hamilton, and John W Peters. An alternative path for the evolution of biological nitrogen fixation. *Frontiers in microbiology*, 2:205, 2011.

[205] Basem Soboh, Eric S Boyd, Dehua Zhao, John W Peters, and Luis M Rubio. Substrate specificity and evolutionary implications of a nifdk enzyme carrying nifb-co at its active site. *FEBS letters*, 584(8):1487–1492, 2010.

[206] Zhenfeng Liu, Niels-Ulrik Frigaard, Kajetan Vogl, *et al.* Complete genome of ignavibacterium album, a metabolically versatile, flagellated, facultative anaerobe from the phylum chlorobi. *Frontiers in microbiology*, 3:185, 2012.

[207] Jennifer Hiras, Yu-Wei Wu, Stephanie A Eichorst, Blake A Simmons, and Steven W Singer. Refining the phylum chlorobi by resolving the phylogeny and metabolic potential of the representative of a deeply branching, uncultivated lineage. *The ISME journal*, 10(4):833–845, 2016.

[208] Lawrence A David and Eric J Alm. Rapid evolutionary innovation during an archaean genetic expansion. *Nature*, 469(7328):93–96, 2011.

[209] Eric Boyd and John W Peters. New insights into the evolutionary history of biological nitrogen fixation. *Frontiers in microbiology*, 4:201, 2013.

[210] Jörg Overmann. Mahoney lake: a case study of the ecological significance of phototrophic sulfur bacteria. In *Advances in microbial ecology*, pages 251–288. Springer, 1997.

[211] Mauro Tonolla, Sandro Peduzzi, Antonella Demarta, Raffaele Peduzzi, and Hahb Dittmar. Phototropic sulfur and sulfate-reducing bacteria in the chemocline of meromictic lake cadagno, switzerland. *Journal of Limnology*, 63(2):161–170, 2004.

[212] Ryuji Kondo, Akie Nakagawa, Lisa Mochizuki, *et al.* Dominant bacterioplankton populations in the meromictic lake suigetsu as determined by denaturing gradient gel electrophoresis of 16s rrna gene fragments. *Limnology*, 10(1):63–69, 2009.

[213] KM Meyer, JL Macalady, JM Fulton, *et al.* Carotenoid biomarkers as an imperfect reflection of the anoxygenic phototrophic community in meromictic fayetteville green lake. *Geobiology*, 9(4):321–329, 2011.

[214] Kjell Magne Fagerbakke, Mikal Heldal, and Svein Norland. Content of carbon, nitrogen, oxygen, sulfur and phosphorus in native aquatic and cultured bacteria. *Aquatic Microbial Ecology*, 10(1):15–27, 1996.

[215] Chen-Tung Arthur Chen, Chi-Ming Lin, Being-Ta Huang, and Lei-Fong Chang. Stoichiometry of carbon, hydrogen, nitrogen, sulfur and oxygen in the particulate matter of the western north pacific marginal seas. *Marine Chemistry*, 54(1-2):179–190, 1996.

[216] Yanan Shen, Roger Buick, and Donald E Canfield. Isotopic evidence for microbial sulphate reduction in the early archaean era. *Nature*, 410(6824):77–81, 2001.

[217] Robert P Lowell and Susan M Keller. High-temperature seafloor hydrothermal circulation over geologic time and archean banded iron formations. *Geophysical Research Letters*, 30(7), 2003.

[218] Donald E Canfield. A new model for proterozoic ocean chemistry. *Nature*, 396(6710):450, 1998.

[219] Jeremy B Fein, Christopher J Daughney, Nathan Yee, and Thomas A Davis. A chemical equilibrium model for metal adsorption onto bacterial surfaces. *Geochimica et Cosmochimica Acta*, 61(16):3319–3328, 1997.

[220] Dimitri A Sverjensky and Nita Sahai. Theoretical prediction of single-site surface-protonation equilibrium constants for oxides and silicates in water. *Geochimica et Cosmochimica Acta*, 60(20):3773–3797, 1996.

[221] Kurt O Konhauser. Diversity of bacterial iron mineralization. *Earth-Science Reviews*, 43(3):91–121, 1998.

[222] Kurt O Konhauser, Stefan V Lalonde, Larry Amskold, and Heinrich D Holland. Was there really an archean phosphate crisis? *Science*, 315(5816):1234–1234, 2007.

[223] Vernon R Phoenix, Dave G Adams, and Kurt O Konhauser. Cyanobacterial viability during hydrothermal biomineralisation. *Chemical Geology*, 169(3):329–338, 2000.

[224] Elizabeth D Swanner, Aleksandra M Mloszewska, Olaf A Cirpka, *et al.* Modulation of oxygen production in archaean oceans by episodes of fe (ii) toxicity. *Nature GeoScience*, 8(2):126–130, 2015.

[225] G Saini and CS Chan. Near-neutral surface charge and hydrophilicity prevent mineral encrustation of fe-oxidizing micro-organisms. *Geobiology*, 11(2):191–200, 2013.

[226] Oleg Stukalov, Anton Korenevsky, Terry J Beveridge, and John R Dutcher. Use of atomic force microscopy and transmission electron microscopy for correlative studies of bacterial capsules. *Applied and environmental microbiology*, 74(17):5457–5465, 2008.

[227] Carel J Van Oss. *Interfacial forces in aqueous media*. CRC press, 2006.

[228] Nathan Yee and Jeremy Fein. Cd adsorption onto bacterial surfaces: a universal adsorption edge? *Geochimica et Cosmochimica Acta*, 65(13):2037–2042, 2001.

[229] Ann E Isley. Hydrothermal plumes and the delivery of iron to banded iron formation. *The Journal of Geology*, 103(2):169–185, 1995.

[230] Lee R Kump and William E Seyfried. Hydrothermal fe fluxes during the precambrian: effect of low oceanic sulfate concentrations and low hydrostatic pressure on the composition of black smokers. *Earth and Planetary Science Letters*, 235(3):654–662, 2005.

[231] Jun Korenaga. Archean geodynamics and the thermal evolution of earth. *Archean geodynamics and environments*, pages 7–32, 2006.

[232] Norman H Sleep, K Zahnle, and PS Neuhoff. Initiation of clement surface conditions on the earliest earth. *Proceedings of the National Academy of Sciences*, 98(7):3666–3672, 2001.

[233] John H Martin, George A Knauer, David M Karl, and William W Broenkow. Vertex: carbon cycling in the northeast pacific. *Deep Sea Research Part A. Oceanographic Research Papers*, 34(2):267–285, 1987.

[234] Allan H Devol and Hilairy E Hartnett. Role of the oxygen-deficient zone in transfer of organic carbon to the deep ocean. *Limnology and Oceanography*, 46(7):1684–1690, 2001.

[235] Jillian F Banfield, Susan A Welch, Hengzhong Zhang, Tamara Thomsen Ebert, and R Lee Penn. Aggregation-based crystal growth and microstructure development in natural iron oxyhydroxide biomineralization products. *Science*, 289(5480):751–754, 2000.

[236] David Kadko. Upwelling and primary production during the us geotraces east pacific zonal transect. *Global Biogeochemical Cycles*, 31(2):218–232, 2017.

[237] Christian J Bjerrum and Donald E Canfield. Ocean productivity before about 1.9 gyr ago limited by phosphorus adsorption onto iron oxides. *Nature*, 417(6885):159, 2002.

[238] Alexander A Pavlov, Lisa L Brown, and James F Kasting. Uv shielding of nh3 and o2 by organic hazes in the archean atmosphere. *Journal of Geophysical Research: Planets*, 106(E10):23267–23287, 2001.

[239] Eugene L Madsen. Identifying microorganisms responsible for ecologically significant biogeochemical processes. *Nature Reviews Microbiology*, 3(5):439–446, 2005.

[240] Kurt O Konhauser. *Introduction to geomicrobiology*. John Wiley & Sons, 2009.

[241] Jizhong Zhou, Kai Xue, Jianping Xie, *et al.* Microbial mediation of carbon-cycle feedbacks to climate warming. *Nature Climate Change*, 2(2):106–110, 2012.

[242] Thomas W Crowther, Stephen M Thomas, Daniel S Maynard, *et al.* Biotic interactions mediate soil microbial feedbacks to climate change. *Proceedings of the National Academy of Sciences*, 112(22):7033–7038, 2015.

[243] Mónica Torres-Beltrán, Alyse K Hawley, David W Capelle, *et al.* Methanotrophic community dynamics in a seasonally anoxic fjord: Saanich inlet, british columbia. *Frontiers in Marine Science*, 3:268, 2016.

[244] J Schieber. Pyritic shales and microbial mats: Significant factors in the genesis of stratiform pb-zn deposits of the proterozoic? *Mineralium Deposita*, 25(1):7–14, 1990.

[245] Celia Méndez-García, Ana I Peláez, Victoria Mesa, *et al.* Microbial diversity and metabolic networks in acid mine drainage habitats. *Frontiers in microbiology*, 6:475, 2015.

[246] Alyse K Hawley, Mónica Torres-Beltrán, Elena Zaikova, *et al.* A compendium of multi-omic sequence information from the saanich inlet water column. *Scientific data*, 4:170160, 2017.

[247] Ben J Woodcroft, Caitlin M Singleton, Joel A Boyd, *et al.* Genome-centric view of carbon processing in thawing permafrost. *Nature*, 560(7716):49–54, 2018.

[248] Elena Zaikova, David A Walsh, Claire P Stilwell, *et al.* Microbial community dynamics in a seasonally anoxic fjord: Saanich inlet, british columbia. *Environmental microbiology*, 12(1):172–191, 2010.

[249] Jody J Wright, Kishori M Konwar, and Steven J Hallam. Microbial ecology of expanding oxygen minimum zones. *Nature Reviews Microbiology*, 10(6):381–394, 2012.

[250] Stilianos Louca, Alyse K Hawley, Sergei Katsev, *et al.* Integrating biogeochemistry with multiomic sequence information in a model oxygen minimum zone. *Proceedings of the National Academy of Sciences*, 113(40):E5925–E5933, 2016.

[251] Steven J Robbins, Paul N Evans, Donovan H Parks, Suzanne D Golding, and Gene W Tyson. Genome-centric analysis of microbial populations enriched by hydraulic fracture fluid additives in a coal bed methane production well. *Frontiers in microbiology*, 7:731, 2016.

[252] Inka Vanwonterghem, Paul D Jensen, Korneel Rabaey, and Gene W Tyson. Genome-centric resolution of microbial diversity, metabolism and interactions in anaerobic digestion. *Environmental microbiology*, 18(9):3144–3158, 2016.

[253] Kurt O Konhauser, Noah J Planavsky, Dalton S Hardisty, *et al.* Iron formations: A global record of neoarchaean to palaeoproterozoic environmental history. *Earth-Science Reviews*, 172:140–177, 2017.

[254] Mirna Daye, Vanja Klepac-Ceraj, Mihkel Pajusalu, *et al.* Light-driven anaerobic microbial oxidation of manganese. *Nature*, pages 1–4, 2019.

[255] Klaus Grasshoff, Klaus Kremling, and Manfred Ehrhardt. *Methods of seawater analysis*. John Wiley & Sons, 2009.

[256] Derek R Lovley and Elizabeth JP Phillips. Availability of ferric iron for microbial reduction in bottom sediments of the freshwater tidal potomac river. *Applied and Environmental Microbiology*, 52(4):751–757, 1986.

[257] Bo Thamdrup, Henrik Fossing, and Bo Barker Jørgensen. Manganese, iron and sulfur cycling in a coastal marine sediment, aarhus bay, denmark. *Geochimica et Cosmochimica Acta*, 1994.

[258] B Cusack, T Stanton, and E Richelson. acid guanidinium thiocyanate-phenol-chloroform extraction. *Anal biochem*, 162:156–159, 1987.

[259] Dinghua Li, Chi-Man Liu, Ruibang Luo, Kunihiko Sadakane, and Tak-Wah Lam. Megahit: an ultra-fast single-node solution for large and complex metagenomics assembly via succinct de bruijn graph. *Bioinformatics*, 31(10):1674–1676, 2015.

[260] Heng Li and Richard Durbin. Fast and accurate long-read alignment with burrows–wheeler transform. *Bioinformatics*, 26(5):589–595, 2010.

[261] Christopher S Miller, Brett J Baker, Brian C Thomas, Steven W Singer, and Jillian F Banfield. Emirge: reconstruction of full-length ribosomal genes from microbial community short read sequencing data. *Genome biology*, 12(5):R44, 2011.

[262] Christopher S Miller. Assembling full-length rrna genes from short-read metagenomic sequence datasets using emirge. In *Methods in enzymology*, volume 531, pages 333–352. Elsevier, 2013.

[263] Benjamin J Callahan, Paul J McMurdie, Michael J Rosen, *et al.* Dada2: high-resolution sample inference from illumina amplicon data. *Nature methods*, 13(7):581, 2016.

[264] Matthew Kearse, Richard Moir, Amy Wilson, *et al.* Geneious basic: an integrated and extendable desktop software platform for the organization and analysis of sequence data. *Bioinformatics*, 28(12):1647–1649, 2012.

[265] Jordan A Fish, Benli Chai, Qiong Wang, *et al.* Fungene: the functional gene pipeline and repository. *Frontiers in microbiology*, 4:291, 2013.

[266] Yu-Wei Wu, Blake A Simmons, and Steven W Singer. Maxbin 2.0: an automated binning algorithm to recover genomes from multiple metagenomic datasets. *Bioinformatics*, 32(4):605–607, 2016.

[267] Donovan H Parks, Michael Imelfort, Connor T Skennerton, Philip Hugenholtz, and Gene W Tyson. Checkm: assessing the quality of microbial genomes recovered from isolates, single cells, and metagenomes. *Genome research*, 25(7):1043–1055, 2015.

[268] Pierre-Alain Chaumeil, Aaron J Mussig, Philip Hugenholtz, and Donovan H Parks. Gtdb-tk: a toolkit to classify genomes with the genome taxonomy database. *Bioinformatics*, 2018.

[269] Norman I Bishop. The influence of the herbicide, dcmu, on the oxygen-evolving system of photosynthesis. *Biochimica et biophysica acta*, 27(1):205, 1958.

[270] Donald E Canfield. Reactive iron in marine sediments. *Geochimica et Cosmochimica Acta*, 53(3):619–632, 1989.

[271] Christelle Hyacinthe, Steeve Bonneville, and Philippe Van Cappellen. Reactive iron (iii) in sediments: chemical versus microbial extractions. *Geochimica et cosmochimica acta*, 70(16):4166–4180, 2006.

[272] Kurt O Konhauser, Andreas Kappler, and Eric E Roden. Iron in microbial metabolisms. *Elements*, 7(2):89–93, 2011.

[273] Kohen Bauer, James Byrne, Paul Kenward, *et al.* Magnetite biomineralization in ferruginous waters and early earth evolution. 2020.

[274] Donald A Bryant and ZF Liu. Green bacteria: insights into green bacterial evolution through genomic analyses. *Adv Bot Res*, 66:99–150, 2013.

[275] Johannes F Imhoff. Taxonomy, phylogeny, and general ecology of anoxygenic phototrophic bacteria. In *Photosynthetic Prokaryotes*, pages 53–92. Springer, 1992.

[276] Y Cohen, BB Jørgensen, E t PADAN, and M Shilo. Sulphide-dependent anoxygenic photosynthesis in the cyanobacterium oscillatoria limnetica. *Nature*, 257(5526):489–492, 1975.

[277] Shimshon Belkin and Etana Padan. Hydrogen metabolism in the facultative anoxygenic cyanobacteria (blue-green algae) oscillatoria limnetica and aphanothece halophytica. *Archives of Microbiology*, 116(1):109–111, 1978.

[278] Judith M Klatt, Mohammad AA Al-Najjar, Pelin Yilmaz, *et al.* Anoxygenic photosynthesis controls oxygenic photosynthesis in a cyanobacterium from a sulfidic spring. *Appl. Environ. Microbiol.*, 81(6):2025–2031, 2015.

[279] RE Danczak, MD Johnston, Christopher Kenah, *et al.* Members of the candidate phyla radiation are functionally differentiated by carbon-and nitrogen-cycling capabilities. *Microbiome*, 5(1):112, 2017.

[280] Verona Vandieken, Ian PG Marshall, Helge Niemann, Bert Engelen, and Heribert Cypionka. Labilibaculum manganireducens gen. nov., sp. nov. and labilibaculum filiforme sp. nov., novel bacteroidetes isolated from subsurface sediments of the baltic sea. *Frontiers in microbiology*, 8:2614, 2018.

[281] Anton Korenevsky and Terry J Beveridge. The surface physicochemistry and adhesiveness of shewanella are affected by their surface polysaccharides. *Microbiology*, 153(6):1872–1883, 2007.

[282] D Suter, C Siffert, B Sulzberger, and W Stumm. Catalytic dissoluion of iron (iii)(hydr) oxides by oxalic acid in the presence of fe (ii). *Naturwissenschaften*, 75(11):571–573, 1988.

[283] Eric E Roden and John M Zachara. Microbial reduction of crystalline iron (iii) oxides: Influence of oxide surface area and potential for cell growth. *Environmental Science & Technology*, 30(5):1618–1628, 1996.

[284] Raul E Martinez, D Scott Smith, Karsten Pedersen, and F Grant Ferris. Surface chemical heterogeneity of bacteriogenic iron oxides from a subterranean environment. *Environmental Science & technology*, 37(24):5671–5677, 2003.

[285] D Scott Smith and F Grant Ferris. Proton binding by hydrous ferric oxide and aluminum oxide surfaces interpreted using fully optimized continuous p k a spectra. *Environmental Science & technology*, 35(23):4637–4642, 2001.

[286] Raul E Martinez, D Scott Smith, Ezra Kulczycki, and F Grant Ferris. Determination of intrinsic bacterial surface acidity constants using a donnan shell model and a continuous pk a distribution method. *Journal of Colloid and Interface Science*, 253(1):130–139, 2002.

[287] JP Cowen. Morphological study of marine bacterial capsules: implications for marine aggregates. *Marine Biology*, 114(1):85–95, 1992.

[288] CJ Van Oss. Hydrophobicity of biosurfaces—origin, quantitative determination and interaction energies. *Colloids and Surfaces B: Biointerfaces*, 5(3-4):91–110, 1995.

[289] Derick G Brown and Peter R Jaffé. Effects of nonionic surfactants on the cell surface hydrophobicity and apparent hamaker constant of a sphingomonas sp. *Environmental science & technology*, 40(1):195–201, 2006.

[290] Willem Norde and J Lyklema. Protein adsorption and bacterial adhesion to solid surfaces: a colloid-chemical approach. *Colloids and surfaces*, 38(1):1–13, 1989.

[291] Joseph N Ryan and Philip M Gschwend. Effects of ionic strength and flow rate on colloid release: Relating kinetics to intersurface potential energy. *Journal of colloid and interface Science*, 164(1):21–34, 1994.

[292] Scott M McLennan and SR Taylor. Continental freeboard, sedimentation rates and growth of continental crust. *Nature*, 306(5939):169–172, 1983.

[293] DR Lowe. Major events in the geological development of the precambrian earth. *The Proterozoic Biosphere: A Multidisciplinary Study*, pages 67–75, 1992.

[294] Kent C Condie. Chemical composition and evolution of the upper continental crust: contrasting results from surface samples and shales. *Chemical geology*, 104(1-4):1–37, 1993.

[295] Keith D Stolzenbach, Kathleen A Newman, and Charles S Wong. Aggregation of fine particles at the sediment-water interface. *Journal of Geophysical Research: Oceans*, 1992.

[296] William S Reeburgh. Oceanic methane biogeochemistry. *Chemical reviews*, 107(2):486–513, 2007.

[297] Paul R Craddock and Nicolas Dauphas. Iron and carbon isotope evidence for microbial iron respiration throughout the archean. *Earth and Planetary Science Letters*, 303(1-2):121–132, 2011.

[298] Donald E Canfield. Sulfate reduction and oxic respiration in marine sediments: implications for organic carbon preservation in euxinic environments. *Deep Sea Research Part A. Oceanographic Research Papers*, 36(1):121–138, 1989.

Appendix A

Chapter 4: supplemental material

- Materials and Methods
- Section 1: Cell surface features and acid-base chemistry
- Section 2: Cell-iron surface interaction and extended DVLO modeling
- Section 3: Iron concentration and supply
- Section 4: Physical separation of ferric iron oxyhydroxides and cellular biomass in an ocean setting
- Section 5: Box model of Archean marine carbon and iron cycles
- Section 6: Organic carbon burial and diagenesis
- Table A1: Media concentrations
- Table A2: Cell surface characteristics
- Table A3: Modern and Archean Fe fluxes
- Table A4: Physical separation model results
- Table A5: Data compilations for Fig. 4.1 and Figure S1
- Fig. A1: BIF redox state
- Fig. A2: Growth curve for *Chlorobium phaeoferrooxidans* strain KB01
- Fig. A3: Additional SEM and TEM images of strains KB01 and KoFox
- Fig. A4: Surface charge of strains KB01 and KoFox
- Fig. A5: Additional cell surface characteristics
- Fig. A6: Fe particle aggregation and physical separation model results
- Fig. A7: Modelled weight % organic carbon
- Fig. A8: Iron and carbon box model sensitivity results

A.1 Supplementary materials and methods

A.1.1 Experimental and growth media

The basal media was prepared after Hegler et. al., 2008 [55] and allocated into serum bottles (100 mL media, 160 mL total volume), with 0.3 g L^{-1} NH_4Cl, 0.5 g L^{-1} $MgSO_4{\cdot}7H_2O$, 0.1g L^{-1} $CaCl_2{\cdot}2H_2O$. After autoclaving, 22 mmol L^{-1} bicarbonate, trace elements, mixed vitamin solution, selenate-tungstate and vitamin B12 were added and the pH was adjusted to 6.8-6.9 under an N_2:CO_2 atmosphere (80:20). KH_2PO_4, Fe(II), and silica were added in a range of concentrations depending on the specific experiment (see Table A.1).

All experiments were initially conducted using the standard media with 10 mM Fe(II) and 4.4 mM KH2PO4. In subsequent experiments, the media composition was adjusted to test the impact of a range of concentrations of Fe(II), $PO_4{}^{3-}$, and Si (Table A.1) on the percentage of cells that remain suspended as

opposed to depositing. This same range of Fe(II), PO_4^{3-}, and Si concentrations was further used to test the surface charge of the Fe(III) oxyhydroxides precipitated under these conditions (Fig. 4.2, Fig. A.5a). The range of Fe(II), PO_4^{3-}, and Si concentrations was used to create a range of P:Fe(III) and Si:Fe(III) ratios (Fig. 4.2b). Specifically, Si concentrations were chosen to reflect the likely Si concentrations of the Precambrian oceans based on Jones et. al., 2015 [85].

A.1.2 Fe(II) oxidation and cell growth

To track the growth kinetics of *Chlorobium phaeoferrooxidans* strain KB01 and *Chlorobium ferrooxidans* strain KoFox, sub-samples were taken from the serum bottles at the time of inoculation and every day thereafter. The first of these sub-samples were analyzed for Fe(II) and Fe(III) concentrations using spectrophotometric analyses. Specifically, Fe(II) and Fe(III) concentrations were measured using the ferrozine method and samples were measured directly as well as after being fixed in 1 N HCl – after Voillier et. al., 2000 [133]. Fe(II) and Fe(III) concentrations were further used to identify when all of the Fe(II) had been oxidized to Fe(III) oxyhydroxides and therefore the appropriate time to determine the percentage of cells that remained suspended. Additional sub-samples were taken from these same serum bottles to measure the pigment concentrations. Pigments were measured spectrophotometrically after 24 hour extractions of 1 mL of pelleted cells in acetone:methanol (7:2 v/v) [134]. Pigment concentrations were then used as a proxy for cell abundance for both strains. To further confirm the growth of the strains, sub-samples were taken from the serum bottles and cells were fixed in gluteraldehyde (final concentration of 0.1 %). After the cells were fixed they were subsequently stained with SYBR green (0.25 % final concentration) and directly counted in a 96 well plate using a Miltenyi Biotec MACSQuant, with a flow rate of medium. Pigment concentrations were also used to determine the fraction of cells that remained suspended. An example of a growth curve for strain KB01 is shown in Fig. A.2 where the decrease in Fe(II) concentrations and an increase in cell counts confirm the growth of the strain.

A.1.3 Determination of cellular association to Fe(III)

C. phaeoferrooxidans strain KB01, *C. ferrooxidans* strain KoFox, and *Synechococcus* sp. were grown to late log phase in standard growth media (Fig. A.2). The bottles were gently shaken by inversion to mix cells and Fe(III) oxyhydroxides and allowed to settle for 24 hours. Mixing was done to resuspend cells that had settled out of the water column as a result of Stokes settling without any association to Fe(III) oxyhydroxides, and to allow maximum potential exposure of cell surfaces to Fe(III) oxyhydroxide particles. Sub-samples for Fe(II)/Fe(III) and pigments were taken from the upper portion of the serum bottle, avoiding settled Fe(III) oxyhydroxides. A second set of sub-samples was taken from each bottle after the bottle had been well mixed. Fe(II)/Fe(III) and pigment concentrations were measured as described above. The fraction of cells associated with Fe(III) oxyhydroxides was calculated by dividing pigment concentrations, a proxy for cell density (6.3×10^{-10} pigment/cell/mL for *C. phaeoferrooxidans* and 5.8×10^{-10} pigment/cell/mL for *C. ferrooxidans*), from the water column by the fully mixed suspensions. These measurements were conducted in 5 replicates and across a range of conditions (Table A.1) Fig. 4.2, Fig. A.5a. Association between both organisms and Fe(III) oxyhydroxide particles was further assessed through electron microscopy (described above). Images of strain KB01 are shown in the main text (Fig. 4.3a, b), while images of KoFox and more TEM images of KB01 are shown below (Fig. A.3).

A.1.4 Zeta potential

To assess the surface charge of Fe(III) oxyhydroxides and cells, we determined the zeta potential of both using a Particle Metrix: ZetaView©. To prepare the Fe(III) oxyhydroxides for zeta potential measurements, they were first concentrated through centrifugation at 14 g for 10 seconds. The supernatant was then discarded and the Fe(III) oxyhydroxides were sonicated for 1 minute to loosen any cells from the Fe(III) oxyhydroxide particles. The Fe(III) oxyhydroxides were subsequently rinsed once in sterile MQ water and concentrated again via centrifugation. This process was repeated three times to reduce the numbers of cells

associated with the Fe(III) oxyhydroxides to low (<100 cells mL^{-1}, counted through flow cytometry as described above) numbers. We confirmed that such low cell numbers had no impact on the surface charge of the Fe(III) oxyhydroxide particles by determining the zeta potential of Fe(III) oxyhydroxides produced through abiotic Fe(II) oxidation in sterile 1.0 mM Si growth media. The zeta potential of these Fe(III) oxyhydroxides was the same as those produced in our experiments (data not shown). Fe(III) oxyhydroxides that we precipitated abiotically in sterile MQ water and in 0.7 M NaCl exhibited a positive surface charge, as generally observed [220]. The surface charges of biotically precipitated Fe(III) oxyhydroxides under the range of media compositions tested (described above) are shown in Fig. 4.2.

To determine the surface charge of the photoferrotrophic strains *C. phaeoferrooxidans* strain KB01 and *C. ferrooxidans* strain KoFox, both strains were grown to late log phase in 400 μM Fe(II), 1.0 mM Si, 3 μM PO_4^- media. The bottles were shaken and allowed to settle for 24 hours until all the Fe(III) oxyhydroxides had reached the bottom serum bottle. Cells were then collected from water column and suspensions of Fe(III) oxyhydroxides and cells after mixing. The samples from the water column were centrifuged (10000 g) for 7 minutes and washed three times (7 minutes centrifugation at 10000 g between washes) in either Fe free growth media or 0.1 N NaCl. Each sample was then diluted 1/10 with filter-sterilized dH_2O (to lower the conductivity of the sample to <2000 $\mu S\ cm^{-1}$) and measured in triplicate using a Particle Metrix: ZetaView©. The samples of mixed cell-Fe(III) oxyhydroxide suspensions were first treated with pH 7 dithionite to reduce the Fe(III) to Fe(II). Fe(II) and Fe(III) concentrations were measured (as described above) before and after the dithionite treatments and the subsequent rinses to confirm that any residual Fe had been effectively removed (<2.5 μM) (data not shown). Following dithionite treatment, the mixed suspensions were measured in the same manner as the water column samples. Zeta potentials for each strain are summarized in Fig. A.4, while the zeta potentials for cells and Fe(III) oxyhydroxides measured in growth media and used in DVLO modeling are in Table A.2.

A.1.5 Surface contact angles

To calculate the interfacial forces between the *C. phaeoferrooxidans* strain KB01, *C. ferrooxidans* strain KoFox, and the Fe(III) oxyhydroxides formed as by-product of their growth, we measured static contact angles for strain KB01, strain KoFox, and Fe(III) oxyhydroxides precipitated abiotically from silica-rich media. These measurements were conducted following Korenevsky and Beveridge, 2007 [281] and Saini and Chan, 2013 [225] and the contact angle data are summarized in Table A.2. To conduct these measurements, cells and Fe(III) oxyhydroxides were collected onto a 0.22 μm polycarbonate filter until there was a thick lawn of cells or Fe(III) oxyhydroxides coating the entire filter. The filters were subsequently dried for 45-60 minutes to remove excess liquid prior to measurement. Contact angle measurements were conducted using a contact angle goniometer with three liquids that have known surface tension properties: water, glycerol, and diiodomethane (Table A.2). 1 μL of each liquid was placed on the sample, 30 images were taken over the course of one and a half minutes, and contact angles were measured and averaged from these 30 images. This process was repeated three times for each of the reference liquids.

A.1.6 Cell surface titrations

To determine the acid-base chemistry and interrogate cell-surface functional groups, both strains *C. phaeoferrooxidans* strain KB01 and *C. ferrooxidans* strain KoFox were grown in 1.0 mM silica-rich media as described above. The cells were then removed from the media and pelleted through centrifugation. To remove residual Fe(III) oxyhydroxides the pelleted cells were treated for 10 minutes with 10 mL of oxalate/oxalic acid (pH 3) and 1 mL of 100 mM Fe(II) for every 1 mL of cells [256, 282, 283]. To remove residual Fe(II) the cells were rinsed with anoxic iron-free growth media [55]. Finally, the cells were resuspended in 200 mL of that same anoxic iron-free media. Cell suspensions were acid/base titrated following the protocol detailed in Martinez et. al. 2003 [284]. Cells were centrifuged four times for 8 minutes at 6200 x g. In between these centrifugations the cells were rinsed three times with degassed MQ water and once with sterile, degassed 0.1 M KNO_3. The final pellet was resuspended in 0.1 M KNO_3. Sub-samples of 1 mL from this cell suspension were then used for each acid-base titration. The pH of the 1

mL sub-sample was lowered to 3.5 using 200 μL of a 0.2 M sterile HNO_3 stock. These sub-samples were then placed inside a Metrohm glass titration vessel and covered with a Metrohm lid that was fit with a pH electrode and N_2 gas line. The pH meter was calibrated at three points — 4, 7, and 10 — prior to each experiment and the system was allowed to reach equilibrium by maintaining a constant pH reading for at least 180 minutes. Titrant additions occurred at a rate of less than 0.1 mV/min based on the settings of the autotitrator, which is adjusted to maintain a fixed interval of 0.15 pH units. These titrations were conducted between the pH values of 3.5 and 11 and were subsequently modelled [284–286]. Results from the cell surface titrations are shown in Table A.2.

A.1.7 Electron microscopy (SEM, TEM)

Cells for SEM were grown up to late log-early stationary phase in regular growth media (10 mM Fe(II), 4.41 mM phosphate). The cell-Fe(III) oxyhydroxide suspensions were gently shaken and allowed to settle for 24 hours. A 1 mL sub-sample was collected from either the upper portion of the serum bottle, avoiding settled Fe(III) oxyhydroxides, or from the mixed suspension after gentle shaking. The samples were placed on a Nucleopore Track-Etched Membrane from Whatman©. The cells were then fixed with 2.5 % gluteraldehyde buffered with 0.1 M PIPES at pH of 7.4. The external cellular structures were preserved using a 1 % osmium tetroxide solution buffered with 0.1 M PIPES at pH 6.8. Filters were rinsed gently with MQ water and then dried using an ethanol dehydration series. The filters were critical-point-dried using a Samdri795 from Toosimis Research Corporation. Finally, the filters were attached to a stub and coated with 5 nm of iridium to ensure conductivity. The filters were imaged on a Helios SEM. Fe(III) oxyhydroxides and cells were confirmed through energy-dispersive X-ray spectroscopy (EDS) measurements of carbon and iron abundances and multiple points were measured for each surface found. SEM images are shown in Fig. 4.3 and Fig. A.3. Cells for TEM were concentrated through centrifugation. The cells were then frozen rapidly using a LEICA EM HPM100. The cellular water was replaced with an alcohol mix while in liquid nitrogen; the samples were sliced as thin sections from an epoxy block and placed onto a copper grid. The samples were imaged on an Osiris S/TEM at the 4D labs imaging facility at Simon Fraser University. TEM images are shown in Fig. 4.3 and Fig. A.3.

A.1.8 Particle size

To assess the particle-size distribution of Fe(III) oxyhydroxides formed during photoferrotrophy, Fe(III) oxyhydroxides produced by strains KB01 and KoFox in standard media containing 3 μM PO_4^{3-} and 1.0 mM Si were concentrated and rinsed as described for zeta potential measurements above, and particle sizes determined using a Mastersizer2000. To reduce artificial clumping during measurement, the Fe(III) oxyhydroxide particles were sonicated for 1 minute in the Mastersizer2000 prior to their measurement. The particles were then stirred continuously during measurement to reduce aggregation. The particle size distribution data are shown in Fig. A.6.

A.2 Supplementary text

A.2.1 Cell surface features and acid-base chemistry

To quantify the observed differences between strain KB01 and strain KoFox we determined the acid-base chemistry of the cell surfaces of both strains using titrations, as described above. Results of these experiments (Table A.2) indicate a clear difference between the surface functional groups of these organisms with strain KB01 having proportionally more amine groups than carboxyl. The surface of strain KoFox, conversely, is dominated by carboxyl functional groups, which are present at much higher density on the surface of strain KoFox than KB01 and have different pKa values, notably the functional group on KoFox with pKa of 4.05 $\pm$ 0.12 (Table A.2). These additional surface functional groups on strain KoFox cells have strong potential to bind metals like Fe(III), which by binding with anionic surface species would offset the overall negative surface charge. To test the possible role of Fe(III) in reducing surface charge

on strain KoFox, we treated cells with dithionite to reduce surface bound Fe(III) to Fe(II) and liberate it from cell surfaces. Dithionite treated KoFox cells became more negatively charged, as expected. Dithionite treatments had correspondingly little effect on the surface charge of strain KB01 cells indicating a lack of Fe(III) binding to KB01 cell surfaces. The presence of functional groups that bind Fe(III) on strain KoFox surfaces thus appears to explain the different charges on the two strains. Notably, benthic microorganisms often develop surface layers rich in such anionic functional groups to facilitate particle adherence. We explore this in more detail below.

Detailed electron microscopy revealed that strain KB01 cells were almost exclusively free of Fe(III) oxyhydroxides and characterized by a surface texture that was free of any obvious extracellular features (Fig. 4.3a, b; Fig. A.3g, h). While cells of strain KoFox clearly avoided encrustation by Fe oxyhydroxides, they were almost invariably associated with Fe(III) oxyhydroxide particles and situated in multicellular aggregates with Fe(III) oxyhydroxides (Fig. A.3a, b, c, e, f). Unlike the rather featureless surfaces of strain KB01 cells, KoFox cell surfaces are characterized by long (20-100 nm), thin (<5 nm) tendrils (Fig. A.3d, e, f), which can be observed under iron-free (Fig. A.3d) and iron-rich conditions (Fig. A.3e, f). Furthermore, under iron-rich conditions tendrils appear to be directly associated with Fe(III) oxyhydroxides (Fig. A.3e, f). These tendrils are reminiscent of bacterial capsules observed on other organisms including *Escherichia coli* K30, *Pseudomonas aeruginosa* FRD1, and *Shewanella oneidensis* [226, 287]. Bacterial capsules are commonly excreted by benthic microorganisms as a mode of cellular defense, and to adhere to mineral surfaces or bind particles [226, 287]. Such capsules are commonly comprised of EPS and are thus rich in carboxyl surface groups as we observed for strain KoFox. We thus attribute the difference in surface properties between strains KB01 and KoFox to the excretion of this capsule-like surface coating by the latter. Such a capsule-like extracellular feature likely sets benthic photoferrotrophic Chlorobi apart from their pelagic counterparts given the obvious advantages of capsule formation to a benthic lifestyle and the challenges it would present to a pelagic lifestyle.

A.2.2 Cell-iron surface interaction and extended DVLO modeling

To assess the biophysical controls on the association between Fe(III) oxyhydroxides and cell surfaces, we conducted Derjaguin, Landau, Verwey and Overbeek (DVLO) and extended DVLO modeling [225, 227, 281, 288]. DVLO modeling allows us to describe both short range interactions, such as Lewis acid-base forces, as well as long range interactions, such as electrostatic forces, which combine to control the association between bacterial cell surfaces and Fe(III) oxyhydroxides. To determine the individual forces and thus the sum force (total) or interaction energy between cell surfaces and Fe(III) oxyhydroxides, we calculate the surface tension properties for the cell surfaces and Fe(III) oxyhydroxides as:

$$\gamma^{TOT} = \gamma^{LW} + \gamma^{AB} \tag{A.1}$$

where γ represents surface tension (in mJ m^{-2}) and TOT is the total surface tension, LW is the apolar Lifshitz-van der Waals surface tension, and AB is the polar Lewis acid-base surface tension. The AB component of equation A.1 can be further broken down into electron donating (γ^-) and electron accepting (γ^+) components:

$$\gamma^{AB} = 2\sqrt{\gamma^+\gamma^-} \tag{A.2}$$

These values can be determined for a given surface (S) through measurements of surface contact angles (θ) between the solid and three liquids (L) with known surface tensions (Table A.2). Using these contact angles, Young's equation can be solved for the unknown surface tension (S) of the cells and Fe(III)

oxyhydroxides [227, 288].

$$(1+cos\theta)*\gamma^{TOT}=2\left(\sqrt{\gamma_S^{LW}\gamma_L^{LW}}+\sqrt{\gamma_S^{+}\gamma_L^{-}}+\sqrt{\gamma_S^{-}\gamma_L^{+}}\right) \tag{A.3}$$

The calculated surface properties for *Chlorobium phaeoferrooxidans* strain KB01, *Chlorobium ferrooxidans* strain KoFox, and abiotically precipitated iron oxyhydroxides are shown in Table A.2. These surface properties can then be used to calculate the Gibbs free energy for an interaction between two identical particles '*i*' in water '*w*' (ΔG_{iwi}) [Eq.A.4] and two different particles '*i*' and '*j*' in water '*w*' (ΔG_{iwj}) [Eq.A.5]:

$$\begin{aligned}\Delta G_{iwi} &= \Delta G_{iwi}^{AB}+\Delta G_{iwi}^{LW}\\ &= -2*\left(\sqrt{\gamma_i^{LW}}-\sqrt{\gamma_w^{LW}}\right)^2-4*\left(\sqrt{\gamma_i^{+}\gamma_i^{-}}+\sqrt{\gamma_w^{+}\gamma_w^{-}}-\sqrt{\gamma_i^{+}\gamma_w^{-}}-\sqrt{\gamma_w^{+}\gamma_i^{-}}\right)\end{aligned}$$

and

$$\Delta G_{iwj}=\Delta G_{iwj}^{AB}+\Delta G_{iwj}^{LW} \tag{A.4}$$

and

$$\begin{aligned}\Delta G_{iwi} &= \Delta G_{iwi}^{AB}+\Delta G_{iwi}^{LW}\\ &= -2*\left(\sqrt{\gamma_i^{LW}}-\sqrt{\gamma_w^{LW}}\right)^2-4*\left(\sqrt{\gamma_i^{+}\gamma_i^{-}}+\sqrt{\gamma_w^{+}\gamma_w^{-}}-\sqrt{\gamma_i^{+}\gamma_w^{-}}-\sqrt{\gamma_w^{+}\gamma_i^{-}}\right)\end{aligned}$$

and

$$\Delta G_{iwj}=\Delta G_{iwj}^{AB}+\Delta G_{iwj}^{LW} \tag{A.5}$$

Here, a positive ΔG indicates a thermodynamically unfavorable interaction (repulsion) between the two particles, while a negative ΔG indicates a thermodynamically favorable interaction (attraction).

Using this modeling approach, both strain KB01 and strain KoFox had low electron-accepting (<2.2 mJ m^{-2}) and high electron donating (>44 mJ m_{-2}) attributes, which is consistent with surface tensions reported for other bacterial strains such as *S. putrefaciens* [281] and *M. ferrooxydans* strain PV-1 [225]. These properties suggest that the cell surfaces of both strain KB01 and strain KoFox are monopolar and hydrophilic [227]. Furthermore, when the free energy of interaction was calculated for both strains, strain KB01 and strain KoFox had large positive ΔG_{iwj}^{AB} (Table A.2) conferring a large repulsive force that overwhelmed a much

smaller attraction arising from Lifshitz-van der Waals forces, resulting in a positive overall ΔG_{iwj} of 33.3 mJ m^{-2} and 24.1 mJ m^{-2} respectively, and net repulsion (Table A.2). The total interaction energy between two surfaces, however, also includes an electrostatic force and the combination of all 3 forces can vary depending on the distance between two surfaces. Extended DVLO modeling can be used to determine how these forces vary with distance and thus assess net attraction or repulsion.

Extended DVLO modeling determines the contribution of each individual force — Lewis acid-base (AB), Lifshitz-van der Waals (LW), and electrostatic (EL) — over a specified distance between surfaces by summing the three individual interaction energies:

$$\Delta G^{TOT} = \Delta G^{AB} + \Delta G^{LW} + \Delta G^{EL} \tag{A.6}$$

To calculate each of these individual ΔG's, an assumption has to be made regarding the geometry between the interacting cell surface and the iron particle. For all calculations we assumed, therefore, that the cell surface was equivalent to a semi-infinite plate, and the diameter of the Fe(III) oxyhydroxide particle was 1 nm (Fig. 4.2c, Fig. A.5c) or 10 nm (data not shown). Additionally, all free energies are calculated as a function of the distance between the cell surface and the iron oxyhydroxide particle over a distance of 5nm. Using the assumed geometry and distances, the Lewis acid-base (ΔG^{AB}) interaction energy equation is:

$$\Delta G^{AB}(d) = 2\pi r\lambda * \Delta G_{iwj}^{AB} * e^{\frac{[d_0 - d]}{\lambda}} \tag{A.7}$$

where r is the radius of the iron oxyhydroxide particle, λ is the correlation length of the molecules in the liquid medium ($\sim$0.6 nm), d is the separation distance, do is the distance of closest approach between the cell surface and the Fe(III) oxyhydroxide particle (0.157 nm) [227] and ΔG_{iwj}^{AB} is the AB component of the cell-Fe(III) oxyhydroxide free energy of interaction (Table A.2).

The Lifshitz-van der Waals interaction energy (ΔG^{LW}) equation is:

$$\Delta G^{LW}(d) = -\frac{A}{6}\left[\frac{2r(d+r)}{d(d+2r)} - \ln\left(\frac{d+2r}{d}\right)\right] \tag{A.8}$$

where r is the radius of the Fe(III) oxyhydroxide particle, d is the separation distance, A is the Hamakar constant. The Hamakar constant between two identical particles is given as:

$$A_{ii} = 24\pi b_0^2 \gamma_i^{LW} \tag{A.9}$$

where d_0 is the minimum separation distance between two semi-infinite planar surfaces in van der Waals contact (average of 0.157 nm) [289] and γ_i^{LW} represents the LW surface tension component of the particle in question (Table A.2). The Hamakar constant can then be calculated separately for each photoferrotrophic strain by calculating the individual Hamakar constants for the bacteria 'b' and the Fe(III) oxyhydroxide surface 's' in water 'w' through the following equation:

$$A_{bws} = \left(\sqrt{A_{bb}} - \sqrt{A_{ww}}\right) * \left(\sqrt{A_{ss}} - \sqrt{A_{ww}}\right) \tag{A.10}$$

Finally, the electrostatic interaction as a function of the separation distance between the cell surface and

the Fe(III) oxyhydroxide particle can be calculated as follows:

$$\Delta G^{EL}(d) = \pi\varepsilon\varepsilon_0 r(\phi_b^2 + \phi_s^2) * \left\{\frac{2\phi_b\phi_s}{\phi_b^2+\phi_s^2} * \ln\left[\frac{1+e^{(-\kappa d)}}{1-e^{(-\kappa d)}}\right] + \ln\left[1 - e^{(-2\kappa d)}\right]\right\} \tag{A.11}$$

where ε is the dielectric constant of the interacting medium (80), ε_0 is the permittivity of a vacuum (8.854 x 10^{-12} C2 J^{-1} m^{-1}), r is the radius of the Fe(III) oxyhydroxide particle, ϕ_b and ϕ_s are the zeta potentials of the bacteria and Fe(III) oxyhydroxide respectively (in JC^{-1}; Table A.2 — reported in mV, conversion factor of 10^{-3}), d is the separation distance, and κ is the reciprocal Debye length [290]. The reciprocal Debye length can be calculated as follows:

$$\kappa = \sqrt{\frac{2000*N_a*I*e^2*Z^2}{\varepsilon*\varepsilon_0*\kappa*T}} \tag{A.12}$$

where N_a is Avogadro's number (6.022 x 10^{23}), I is the ionic strength of the medium (0.001 M in our experiments), e is the elementary charge (1.6 x 10^{-19} C), Z is the valence of the electrolyte medium (2), κ is Boltzmann's constant (1.38 x 10^{-23} m^2 Kg s^{-2} K^{-1}), and T is temperature (K) [227, 291].

Results for the extended DVLO modelling indicate that both strain KB01 and strain KoFox have positive primary maxima (20 kT and 15 kT respectively) that are dominated by a strong Lewis acid-base repulsion (Fig. 4.2, Fig. A.5c). At a distance of 3 nm, however, the electrostatic interaction force becomes the dominant force under all conditions. In the case of strain KB01, the electrostatic force maintains a strong positive interaction energy (repulsion between cell surface and Fe(III) oxyhydroxide), which results a consistently positive overall interaction energy with no negative minimum for strain KB01 (Fig. 4.2c). This result corroborates the results of the cell separation experiments, described above and shown in Fig. 4.2a, b, demonstrating that a repulsive electrostatic force maintains the separation between the cell surface of strain KB01 and the negatively charged Fe(III) oxyhydroxides. When the charge of the Fe(III) oxyhydroxides is positive, however, the extended DVLO modelling generates a negative minimum at approximately 3nm that continues over the remaining distance (data not shown), which suggests a weak attraction between strain KB01 and the Fe(III) oxyhydroxides and explains the much higher numbers (50 %) of strain KB01 cells seen in the sediments when the strain is grown in medium with low P and Si concentrations that leads to positively charged Fe(III) oxyhydroxides (Fig. 4.2a). The *AB* interaction force, for strain KoFox, leads to a primary positive maximum, which is similar albeit a bit lower in magnitude than that of strain KB01. Regardless of whether the Fe(III) oxyhydroxides are negative (Fig. A.5c) or positive (data not shown), however, the electrostatic interaction energy creates a weakly negative minimum between 4 and 4.5nm (Fig. A.5c). This weak attractive interaction force supports the results of the cell separation experiment (Fig. 4.2a, Fig. A.5a) and the association between strain KoFox cells and Fe(III) oxyhydroxides seen in the SEM and TEM images of strain KoFox (Fig. A.3). The extended DVLO modelling demonstrates that both forces that arise from acid-base and electrostatic interactions lead to repulsion between strain KB01 and Fe(III) oxyhydroxides, allowing this pelagic photoferrotroph to physically separate itself from its growth byproduct and thus remain suspended. DVLO modeling thus reveals differences between *Chlorobium phaeoferrooxidans* strain KB01, which does not interact with Fe(III) oxyhydroxides and *Chlorobium ferrooxidans* strain KoFox, which forms a weak association with Fe(III) oxyhydroxides. The association between KoFox and Fe(III) oxyhydroxides is, however, weak and only appears at a distance of 3nm or more between surfaces.

A.2.3 Iron concentration and supply

To address an apparent deficiency in global Fe(II) fluxes to the oceans required to sustain BIF deposition during the Archean Eon, we re-evaluated both modern and Precambrian global Fe budgets with new

information on material and energy fluxes for modern and Precambrian hydrothermal and weathering systems. Previous estimates for Fe(II) fluxes in the modern oceans are based on the product of hydrothermal fluid fluxes of 3 x 10^{13} kg yr^{-1} ± 1.5 x 10^{13} kg yr^{-1} [24] and Fe(II) concentrations measured in these fluids, ∼6 mmol kg^{-1} [24], which yield a global flux of Fe(II) from hydrothermal vents of 0.3 ± 0.1 Tmol yr^{-1} [5]. Fe(II) is also delivered to modern oceans through extensive, yet poorly quantified, low temperature off-axis hydrothermal venting [24], where measurements of fluid flow (2.5 x 10^{15} kg yr^{-1} [24]) and Fe(II) concentrations (∼0.75 mmol kg^{-1} [24]) suggest these systems contribute 6 times more Fe(II) to the global oceans, at rates of 1.88 Tmol yr^{-1}. Combining on- and off-axis estimates yields a total Fe(II) hydrothermal flux of ∼2 Tmol Fe yr^{-1} to the modern oceans and this is insufficient to sustain BIF deposition (Table A.3, part 1). These previous estimates of Fe(II) fluxes to the modern oceans, however, may still underestimate total hydrothermal leaching of Fe(II) from ocean crust due, in-part, to the poorly quantified off-axis hydrothermal circulation. We thus re-estimated the modern hydrothermal Fe leaching with new fluid flow estimates from a recent compilation, as described in the main text [158]. While the on-axis Fe concentration remains unchanged, the off-axis hydrothermal Fe leaching increases to 10.5 Tmol Fe yr^{-1} (Table A.3, part 2). Combining on and off-axis fluxes gives a new upper estimate on modern hydrothermal Fe leaching of ∼11 Tmol yr^{-1}, and while we use this value as a point of departure for reconstructing Fe fluxes in the Precambrian Eons, it should be further tested through direct measurements in the modern. Including the new estimates of off-axis hydrothermal Fe(II) flux increases the overall Fe(II) flux to the global oceans to values that could sustain BIF deposition without depleting the oceans of Fe(II) for hundreds of millions of years.

Given that global Fe fluxes would have been much different in the Archean Eon due to conditions that differ from the modern, such as pervasively anoxic oceans, reduced seawater sulfate [27, 230], and enhanced hydrothermal activity [229, 230], we sought to further reconcile the global Fe budget during the Archean Eon. To account for the enhanced Archean hydrothermal fluid flow, we scaled modern fluid flow by the ratio of past to modern lithospheric heat loss. We calculated the global lithospheric heat loss (Q) for any age lithosphere (t), at geologic time (τ), using the following equation:

$$Q(t,\tau) = 2\left(\frac{2A}{t_m}\right)(t_m)^{\frac{1}{2}}\left[\left(\frac{t}{t_m}\right)^{\frac{1}{2}} - \left(\frac{1}{3}\right)\left(\frac{t}{t_m}\right)^{\frac{3}{2}}\right] \tag{A.13}$$

where

$$t_m = 180 - 38.2\tau \tag{A.14}$$

t is 1 m.y., and A is a calculated ratio for continental growth. We utilized a linear continental growth model [292, 293] and calculated A as follows:

$$A = \frac{C_m}{(-0.1\tau+1)} \tag{A.15}$$

where C_m is the size of the modern continents as a fraction of the Earth's surface size, and τ is the geologic time. To calculate the heat loss ratio for each geologic time, we normalized each calculated Q to the Q value calculated for the modern (Table A.3). Finally, we used this ratio to scale hydrothermal fluid flow, calculating past on- and off-axis hydrothermal fluid flow for the Proterozoic and Archean Eons as seen in the main text and in Table A.3.

To assess the delivery flux of Fe(II) to Archean oceans from continental weathering we scaled the modern rate of Fe delivery to the Archean. Reactive Fe is delivered to the modern oceans as Fe(III) (oxyhydr)oxides at a rate of 6.5 ± 1.7 Tmol yr^{-1}, as mineral bound Fe(II) is oxidized during weathering under the well oxygenated modern atmosphere. Under the low oxygen Archean atmosphere, a fraction of

the reactive Fe would have been weathered as Fe(II). While the concentration of Fe(II) in the Precambrian crust was likely higher than it is in the modern [294], which would result in a larger flux of Fe(II) to the oceans, the total continental area was smaller. To estimate the weathering flux of Fe(II) to the oceans in the Archean Eon, we used an estimate for Mg_2^+ [85] weathering fluxes (5.5 Tmol yr^{-1}) and multiplied these by the ratio of Mg to Fe in the Precambrian crust (1.2) [294], for an Fe(II) flux of 6.6 Tmol y^{-1}. Recognizing that weathering rates are proportional to continental area, we scaled this number by 0.75 to account for smaller continents at 2.5 Ga although this value may have been as much as a factor of two smaller during the early Archean [231], resulting in an Fe(II) weathering flux of 5 Tmol yr^{-1} to the oceans.

A.2.4 Physical separation of ferric iron oxyhydroxides and cellular biomass in an ocean setting

To evaluate the impact of the physical separation of pelagic photoferrotrophs from their Fe(III) oxyhydroxide byproducts in an ocean upwelling setting we created a model detailing the impact of horizontal ocean current velocities on the deposition of Fe(III) oxyhydroxides and cellular biomass to the seafloor. To calculate the distance that an Fe(III) oxyhydroxide particle or cell travels prior to deposition, we first calculated the settling velocity for the Fe(III) oxyhydroxide particles and cells. Settling velocity was calculated according to Stokes law:

$$S_v = \frac{(P_p - P_w) * g * d^2}{18\eta} \tag{A.16}$$

where P_p is the density of the particle (Fe(III) oxyhydroxide or cell), P_w is the density of seawater at 20 ∘C (1.025 g cm^{-3}), g is gravitational acceleration (9.8 m s^{-2}), d is the diameter of the particle (Fe(III) oxyhydroxide or cell), and η is the dynamic viscosity of seawater at 20 ∘C (0.00108 kg m^{-1} s^{-1}). For this model, the density of ferrihydrite (3.8 g cm^{-1}) was used to simulate biogenic Fe(III) oxyhydroxides [8, 63], while the density of an *E. coli* cell (average of 1.08 g cm^{-1}) was taken from the literature [136]. To represent a realistic range of Fe(III) oxyhydroxide particle diameters, particle sizes were measured (as described above) and the measured sizes fit with a lognormal probability distribution according to:

$$p(x) = \frac{e^{\frac{-(\ln(x)-\mu)^2}{2\sigma^2}}}{\sigma * \sqrt{2\pi} * x} \tag{A.17}$$

where the value of μ is 1.9 and the value of σ is 1.1 based on the data. We then applied a simple aggregation factor to the lognormal distribution where the smallest particle (0.01 μm) grew to be twice its size, and particles greater than 28.6 μm remained the same size, and the growth rate of all particles in between was scaled linearly [295] (Fig. A.6). The diameters of strain KB01 and strain KoFox range from 250 nm to 1 μm with a median of 500 nm. The distribution of cell sizes was also modelled using a lognormal probability distribution (equation 17; μ is 0.5 and σ is 1.012) based on cell imaging (data not shown). The particle sizes for both the Fe(III) oxyhydroxides and cells were then used to calculate the Stokes settling velocity for each individual particle. We then calculated the distance that each particle would travel given a 150 meter deep water column (typical depth of a coastal shelf) using horizontal water velocities typical for coastal margin settings [233, 236]. Results of this model illustrate the effective physical separation of the Fe(III) oxyhydroxides and cellular biomass produced in upwelling provinces under all reasonable conditions (Fig. A.6 and Table A.4). Furthermore, the cellular biomass travels distances that are similar to the width of modern oceans, indicating that the biomass produced through photoferrotrophy in an upwelling province would have been dispersed throughout all oceanic provinces.

A.2.5 Box model of Archean marine carbon and iron cycles

To evaluate the global rates of photoferrotrophy, iron oxyhydroxide deposition, and methane production we constructed an oceanic box model. To create the box model, we split the upper ocean into the three oceanic provinces [233] — upwelling, coastal, and open-ocean — and subsequently added the pertinent carbon and iron fluxes as the inputs and outputs of each box (Fig. 4.4). We treated the upper ocean of each province separately and calculated primary production for each of these provinces as:

$$PP_p = [Fe(II)]_D * A_p \tag{A.18}$$

where A_p is the upwelling rate (m y^{-1}) in the oceanic province of interest, $[Fe(II)]_D$ is the deep ocean Fe(II) concentration, and PP_p is the primary production specific to that province. We tested a range of deep ocean Fe(II) concentrations (0-100 μM; Fig. 4.5c) and upwelling rates specific to each province as guided by relevant values from the modern ocean (0-1500 m y^{-1} — upwelling province; Fig. 4.5d, 0-100 m y^{-1} — coastal province; Fig. A.8a, 0-5 m y^{-1} — open ocean; Fig. A.8b) [233, 236]. Once the primary production (in mol m^{-2} y^{-1}) for each province has been calculated, global primary production was calculated by multiplying each province by its areal extent:

$$PP_G = \left[\left(\frac{S_{Up}}{S_G}\right) * PP_{Up}\right] + \left[\left(\frac{S_{Cp}}{S_G}\right) * PP_{Cp}\right] + \left[\left(\frac{S_{Op}}{S_G}\right) * PP_{Op}\right] \tag{A.19}$$

where S_{Up}, S_{Cp}, and S_{Op} are the areal extents of the upwelling, coastal, and open ocean provinces respectively (m^2), and S_G is the area of the whole ocean (m^2). We tested the effect of continental growth (0-100 % of modern continental size; Fig. 4.5a) by reducing the area of the ocean in response to increasing continental areas while maintaining a fixed ratio of upwelling and coastal province area to continental area (i.e. with larger continents come larger upwelling and coastal provinces). Thus, changing the size of the continents changes the contribution that each province makes to total ocean area and global primary production (Fig. 4.5a). Rates of other biogeochemical processes were calculated in a similar fashion by replacing the PP in equation A.19 with the biogeochemical process of interest.

Organic carbon produced during primary production was distributed into two pools: 1) Fe(III) oxyhydroxide associated biomass, and 2) free, unassociated biomass. Fe(III) associated biomass settled and was deposited within the oceanic province in which it was produced, whereas given the broad dispersal of cellular material, the unassociated biomass was evenly distributed across the global ocean. Settling rates of Fe(III) oxyhydroxides are sufficiently rapid that we ignored degradation of biomass associated with Fe(III) oxyhydroxides in the water column. Settling of unassociated biomass is much slower and is thus subject to degradation within the water column. To calculate the organic carbon that is degraded through iron reduction and methanogenesis as it sinks to the ocean floor, we used a power law [233]:

$$F = F_{100} * \left(\frac{z}{100}\right)^b \tag{A.20}$$

where F is the amount of organic carbon degraded (in mol m^{-2} y^{-1}), z is the depth of the oceanic province, the exponent, b, is the log-log slope scaled for anaerobic respiration (0.36 [234]), and F_{100} is the log-log of the carbon degradation rate data [233]. F_{100} is dependent on the rate of primary production and is calculated, therefore, using the relationship between F_{100} and the primary production in a given province [233]:

$$F_{100} = 0.0677 * (PP_G)^{1.3041} \tag{A.21}$$

where PP_G is global primary production (as calculated above). Finally, we calculated the final value for F by integrating the values for F over two different depth intervals -– 150 m for the upwelling and coastal provinces and 3000 m for the open ocean — using 12.5 m intervals for z. Given that iron reduction is generally thermodynamically more favorable than methanogenesis [296], we channeled biomass degradation first through Fe-reduction until Fe(III) oxyhydroxides were entirely reduced and then through methanogenesis, once Fe(III) oxyhydroxides were exhausted. Rates of degradation were calculated for individual provinces and global rates calculated by summing the 3 provinces (Equation A.19). Residual organic carbon and Fe(III) oxyhydroxides — if not quantitatively degraded in the water column — were deposited in the sediments of each province. The organic carbon that reaches the sediments is the sum of Fe(III) oxyhydroxide associated carbon for that province and residual mean global unassociated carbon that escaped degradation in the water column. We, thus, calculated the organic carbon that reaches the sediments in a specific province using the following equation:

$$C_s = \{[PP_G * (1 - A)] - WC_d\} + \left(PP_p * A\right) \tag{A.22}$$

where C_s (in mol m^{-2} y^{-1}) is the biomass carbon that reaches the sediments, PP_G is the global primary production, A is the fraction of cells that are associated with Fe(III) oxyhydroxides, WC_d is the amount of carbon degraded in the water column of that province, and PP_p is the primary production of the specific province. Furthermore, given the strain dependent differences in cell-Fe(III) oxyhydroxide association discussed in the main text (Fig. 4.2a, Figure A.5a), we used equation A.22 to test the impact of cell-Fe(III) oxyhydroxide associations (between 0-100 %: Fig. 4.5b) on the outputs of the model.

The flux of biomass carbon that reaches the sediments in each of the three provinces was calculated with Equation A.22 but some of this carbon is subject to degradation during diagenesis. We estimated that the fraction of carbon buried is 15 % of that deposited, based on carbon burial in modern ferruginous lakes [27, 47, 69]. We further tested the impact of this burial efficiency by changing efficiency from 0-50 % (Fig. A.8c). The biomass carbon not buried was again used to fuel Fe(III) reduction and methanogenesis in that order. If the biomass carbon delivered to the sediment (less carbon buried) exceeded Fe(III) supply, then the remaining biomass carbon was channeled through methanogenesis. Given that the greatest area specific rates of primary production, and therefore Fe(III) oxyhydroxide formation, occurred in the upwelling province, and that much of the corresponding biomass was exported to other provinces, all biomass carbon deposited in sediments underlying the upwelling province was channeled through Fe(III) reduction. Methanogenesis, on the other hand, occurred when all the Fe(III) oxyhydroxides were consumed in the coastal and open ocean provinces. Given the formation of Fe(III) oxyhydroxides in each province, we calculated the rate of Fe(III) oxyhydroxide deposition (in mol m^{-2} y^{-1}) through the following equation:

$$Fe(III)_p = \left(PP_p * 4\right) - \left(WC_{dFe} * 4\right) - \left(S_{dFe} * 4 * R_{IR}\right) \tag{A.23}$$

where the water column carbon degradation channeled through iron reduction (WC_{dFe}), multiplied by the 4:1 Fe:C ratio of photoferrotrophy, and the sediment carbon degradation channeled through iron reduction (S_{dFe}) (multiplied by the 4:1 ratio) are subtracted from the total primary production in a given province (PP_p) (multiplied by the 4:1 ratio). R_{IR} is the fraction of the Fe(III) oxyhydroxide Fe that is reduced in the sediments and re-enters the water column by diffusion as dissolved Fe(II). We used a fraction of 0.25, constrained by the rates of recycling observed in modern Archean ocean analogues [71], and then further tested the impact of Fe(III) oxyhydroxide recycling on the model output by running fractions between 0 and 0.5 (Fig. A.8d).

Finally, to calculate global rates of Fe(III) reduction and methanogenesis, we tallied the water column and sediment rates and multiplied them by the size of the global ocean (in m2) to calculate the global rate in Tmol yr^{-1} (Table **??**). Global rates of total Fe(III) oxyhydroxide production, Fe(III) deposition, Fe recycling, and primary production were calculated in Tmol yr^{-1} (Table **??**). Overall the model illustrates the magnitude of the coupled Fe and carbon biogeochemical cycles that could have been supported by an

Archean Earth system in which primary production is driven by photoferrotrophy.

A.2.6 Organic carbon burial and diagenesis

Siderite is an important component of BIF, and at least some of the siderite in BIF is diagenetic. For example, carbon isotopes can be used to estimate the amount of diagenetic siderite in BIF. The isotopic composition of carbon in BIF siderite varies from -5 ‰ to -10 ‰ across different units with an approximate average of -7 ‰ [75, 297], while the carbon isotopic composition of seawater is estimated at 0 ‰ and the isotopic composition of organic carbon is estimated at -30 ‰. Assuming that carbon in siderite is a mixture of carbon from seawater carbonate and carbonate produced during diagenetic respiration of organic matter, the fraction of diagenetic carbon in siderite can be estimated through isotopic mass balance. Based on the values above then, we estimate 30 % of the carbon in BIF siderite is diagenetic.

This example places constraints on the amount of organic carbon that needs to be deposited in BIF in order to support diagenetic siderite. Again, for example, assuming our benchmark model parameters with 15 % cell-Fe(III) association — 1.2 mol C m^{-2} yr^{-1} reaches sediments underlying the upwelling province. 15 % of which is considered unreactive and is buried, leaving a reactive carbon flux of 1 mol C m^{-2} yr^{-1} to support siderite formation. In the benchmark scenario, 30.8 mol Fe m^{-2} yr^{-1} Fe(III) deposited and the 1 mol C m^{-2} yr^{-1} supports the reduction of 4 mol Fe m^{-2} yr^{-1}, leaving 27 mol Fe(III) m^{-2} yr^{-1}. 25 % of the Fe(II) produced through reduction is recycled into the water column, leaving 3 mol Fe m^{-2} yr^{-1} to form diagenetic siderite. Assuming that 30 % of the siderite is diagenetic based on carbon isotopes (see above) this leads to 10 mol Fe(II) m^{-2} yr^{-1} siderite deposition. In this example then, BIFs contain 27 % iron as siderite and the remainder as ferric iron phases, which results in a mean redox state of 2.7. This redox state is similar to many units found in Neoarchean BIFs (Fig. A.1, Table A.5).

Finally, to compare carbon deposition rates from our model with the geologic record we estimated the fractional contribution of organic carbon to total sedimentation rates by assuming total sedimentation rates similar to those determined for a range of modern environments (Fig. A.7). The resulting organic carbon concentrations at the lower sedimentation rates characteristic of modern deep water environments are similar to those found in organic carbon-rich Precambrian shales (Fig. A.77; Fig. 4.1; Table A.5), while higher sedimentation rates lead to organic carbon contents similar to typical coastal margin sediments.

A.3 Supplementary figures

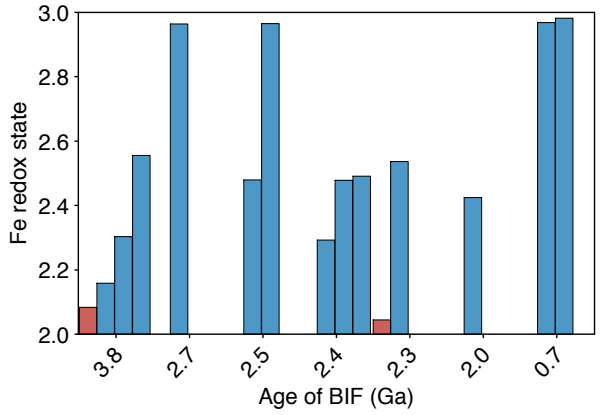

Figure A.1: *The redox state of iron in BIF through time where the red bars indicate the siderite rich BIFs.* The overall average redox state of BIFs is 2.4, whereas the average redox state of Archean Eon BIFs, excluding the anomalous siderite rich units is 2.6. References for this figure can be found in Table S5.

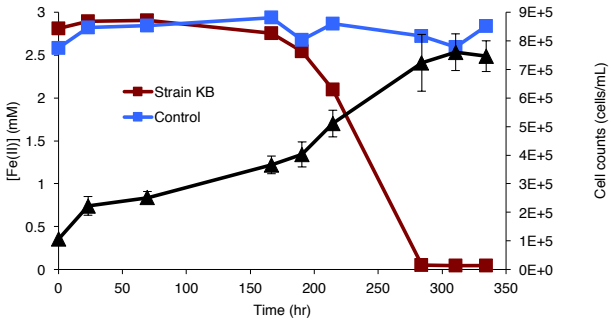

Figure A.2: *Growth curve for Chlorobium phaeoferrooxidans strain KB01.* Fe(II) oxidation by Chlorobium phaeoferrooxidans strain KB01 (red squares) compared to a non-inoculated control (blue squares) on the left vertical axis. On the right vertical axis, cell counts in cells mL^{-1} for the strain KB01 bottle are shown in black triangles. Strain KB01 was capable of oxidizing Fe(II) at rates up to 27 μM/hr.

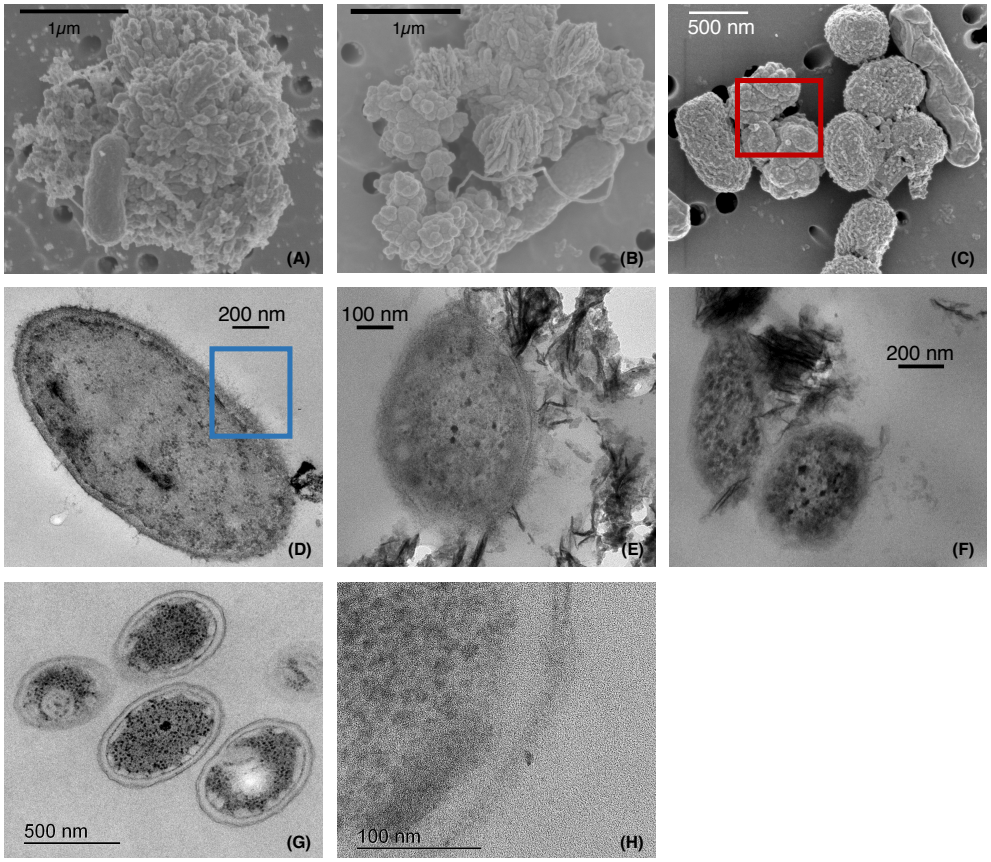

Figure A.3: *Additional SEM and TEM images of strains KB01 and KoFox.* SEM (a,b,c) and TEM (d,e,f,g,h) images showing KoFox cells forming a loose association with Fe(III) particles, but no encrustation (a,b,c). Note the area with the red square in image c denotes iron particles confirmed through EDS spectrum. TEM images (d,e,f) showing KoFox cells forming a loose association with Fe(III) particles. Note the area with the blue square in image d denotes the bacterial capsule. Finally, TEM images (g,h) show multiple KB01 cells without any visible Fe(III) present (g) and a KB01 cell with an Fe(III) nanoparticle noted with the orange square (h).

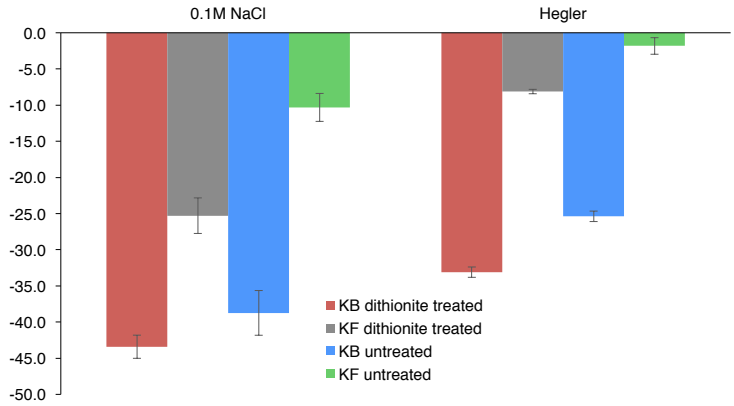

Figure A.4: *Surface charge of strains KB01 and KoFox under two conditions.* Zeta potential of strain KB01 and strain KoFox (dithionite treated -– red and grey; untreated -– blue and green) with two different wash solutions: 0.1 M NaCl and Fe free standard media (as described in materials and methods).

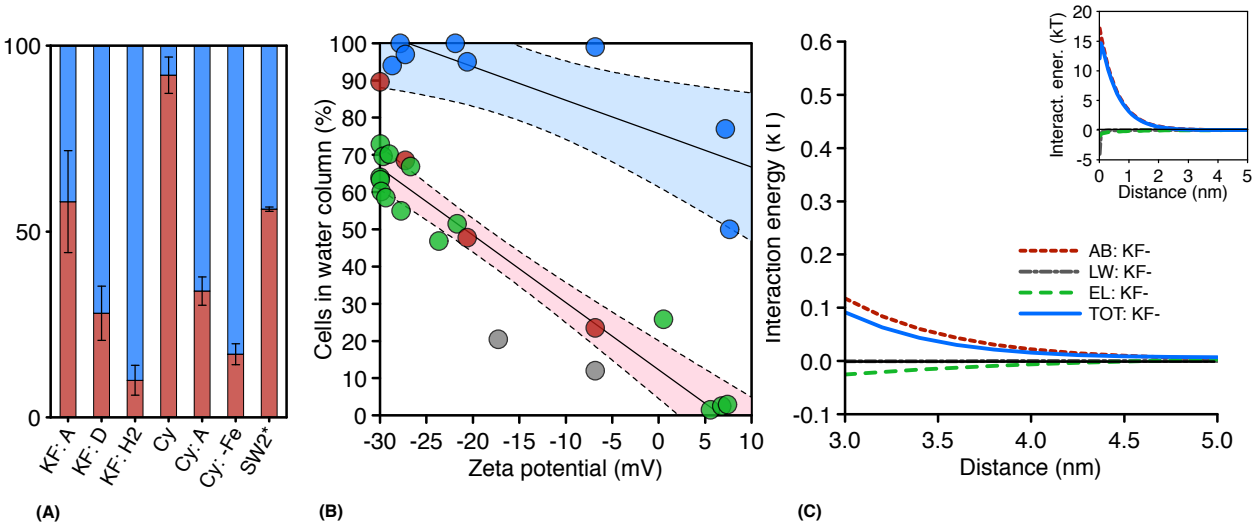

Figure A.5: *Additional cell surface characteristics for strain KoFox (A and C) and the relationship between the number of planktonic cells and the Fe(III) surface charge (B).* The fractions of planktonic (blue) versus sedimented (red) cells (A) for treatments not shown in the main text. The following conditions are represented for the following strains: 400 μM Fe, low P (3 μM), with 0.6 mM Si [A] for strain KoFox and *Synechococcus*, 10 mM Fe, 4.4 mM P [D] and Hydrogen gas with 4.4 mM P [H2] for strain KoFox, 400 μM Fe with low P (3 μM) [unmarked] and no Fe with low P (3 μM) [-Fe] for *Synechococcus*, and 0.8-2 mM Fe with 4.4 mM P [*] for strain SW2 [62]. The relationship between the percentage of cells in the water column and the surface charge of the Fe(III) particles (B) with KoFox (red), Cyanobacteria (green), and SW2 (grey) following a strong downward trend while KB01 (blue) only decreases once Fe(III) particles become positive. The shaded areas represent a 95 % confidence interval. Finally, the extended DVLO modeling for strain KoFox (C) with the main graph depicting the interaction energies of the 3 forces and the total for those forces from 3 nm-5 nm, while the inset depicts the forces from 0 nm-5 nm. AB refers to the acid-base force, LW the Lifshitz-van der Waals force, EL the electrostatic force, and TOT the total of all three forces.

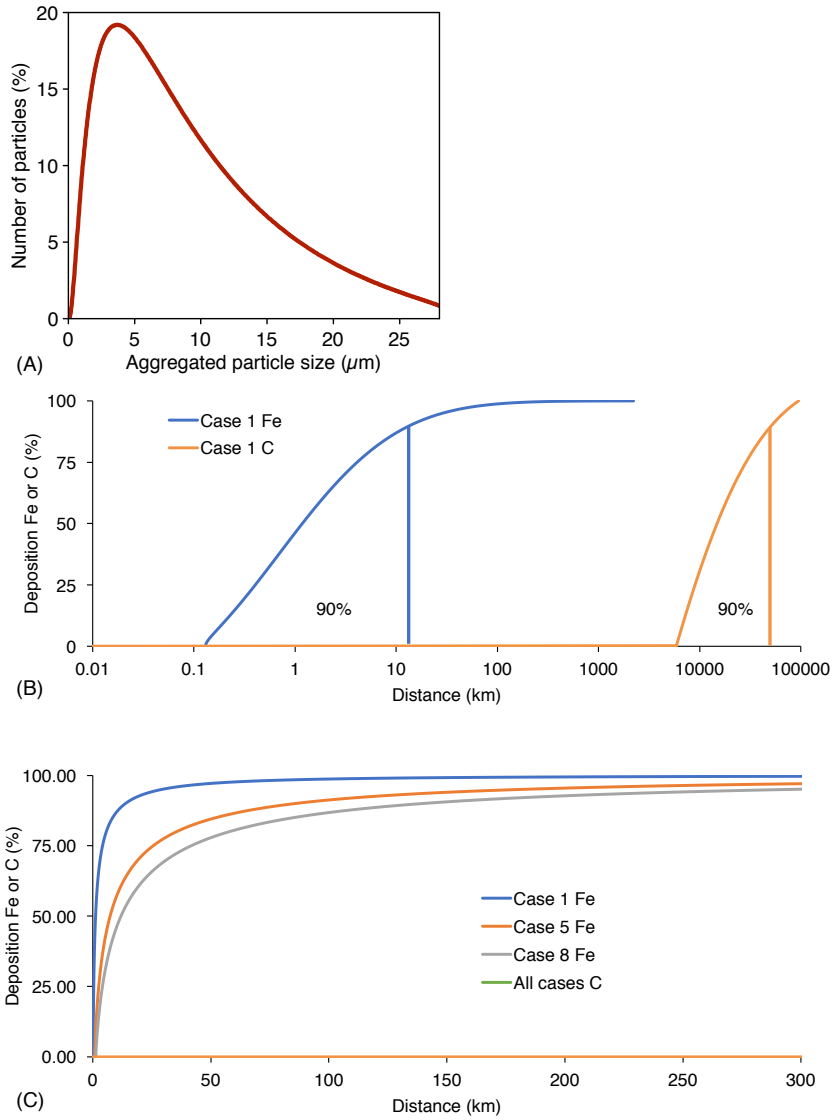

Figure A.6: *Modeling the settling velocity of carbon and iron using a range of horizontal current velocities.* Percentage of Fe(III) particles (A) that are present at each particle size, in μm, when Fe(III) oxyhydroxides are precipitated abiotically in media with 1.0 mM Si and measured using a Mastersizer2000. These data were used to inform the deposition of iron oxyhydroxides in the iron-biomass separation model. The distance over which iron oxyhydroxides (blue curve) and carbon particles (orange curve) deposit for case 1 (B) when an outflow rate of 3.6 m y^{-1} is applied to the particles of iron oxyhydroxides and carbon respectively. The distance that 90 % of the Fe(III) oxyhydroxides or carbon travels is denoted under each curve. The distance over which iron oxyhydroxides particles deposit for cases 1, 5, and 8 (C) with the distance that the carbon particles travel not shown in the distance covered by the graph.

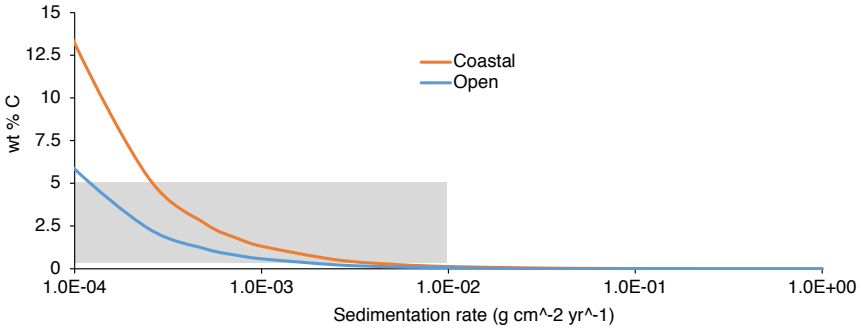

Figure A.7: *Modeled weight % organic carbon in the coastal and open ocean sediments.* This figure depicts the weight % organic carbon using the values generated in the benchmark model run (2.5 Ga mid, Table 4.1). The grey box indicates the range of modern marine sedimentation rates for coastal and open ocean sediments [298] on the x-axis and the range of wt % C found in Precambrian shales (Fig. 4.1, Table S5) on the y-axis.

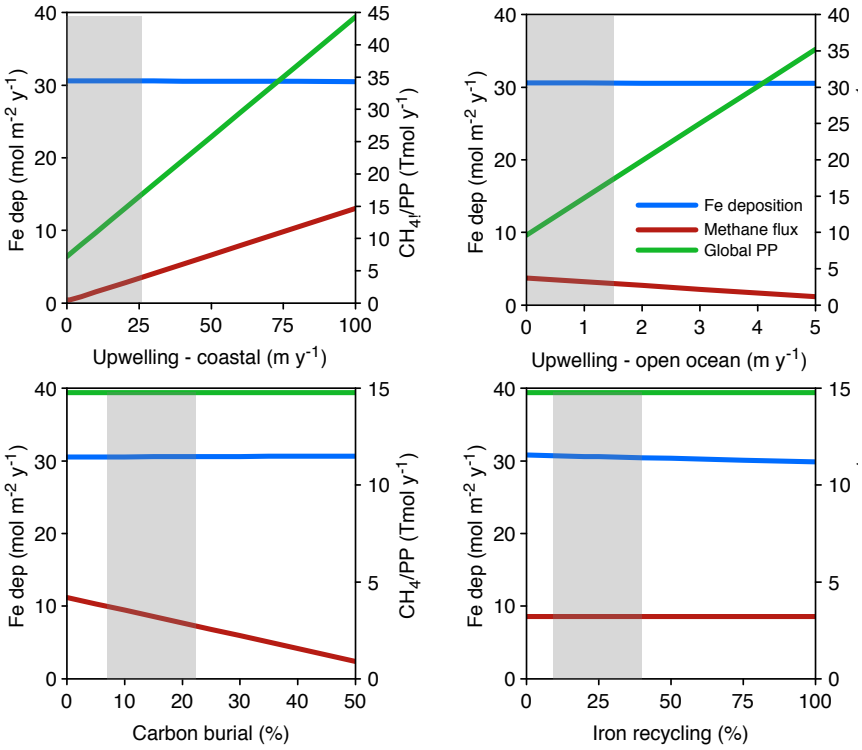

Figure A.8: *Iron and carbon box model sensitivity results.* Model sensitivity results for varying upwelling rates in the coastal provinces (a), varying upwelling rates in the open ocean provinces (b), varying percentages of carbon burial (c), and varying percentages of iron recycling (d). Iron deposition rates in the upwelling provinces are depicted on the left y-axis, while global rates of primary production and methane production are both shown on the right y-axis in Tmol yr^{-1}.

A.4 Supplementary tables

Table A.1: Range of concentrations in the growth media used throughout experiments.

	$FeCl_2$	**Silica**	**KH_2PO_4**
Standard growth media	10 mM	0 mM	4.4 mM
Low P	250 µM-500 µM	0 mM	3-6 µM
Low P, low Si	250 µM-500 µM	0.6 mM	3-6 µM
Low P, middle Si	250 µM-500 µM	1.0 mM	3-6 µM
Low P, high Si	250 µM-500 µM	1.5 mM	3-6 µM

Table A.2: Cell surface characteristics and cell-mineral interaction modelling.

Part 1: Summary of pKa and site concentration values from Langmuir isotherm/LPM optimization

Site	****pK_a**	****Site concentration (mol/g) x 10^{-4}**	**Suggested functional group assignment***
Strain **KB01** - 1	6.14 ± 0.26	2.63 ± 0.26	Carboxyl or phosphoryl
Strain **KB01** - 2	7.27 ± 0.17	2.21 ± 0.04	Amine
Strain **KB01** - 3	8.70 ± 0.37	1.76 ± 0.41	Amine
Strain **KoFox** - 1	4.05 ± 0.12	4.25 ± 0.08	Carboxyl or phosphoryl
Strain **KoFox** - 2	6.55 ± 0.23	25.1 ± 0.28	Carboxyl***
Strain **KoFox** - 3	8.70 ± 0.11	5.15 ± 0.13	Amine

Footnote: *Functional group assignments derived from FTIR spectra analysis of the same samples. **pKa and site concentration values represent the average of 4 replicate experiments. ***Needs confirmation by FTIR.

Part 2: DVLO modeling – zeta potential and surface contact angle data summary

	Zeta potential (mV)	**θ- water (°)**	**θ- Glycerol (°)**	**θ- Diiodomethane (°)**
Strain KB01 (water column in Hegler media)	-25.4 ± 3.7	29.3 ± 4.1	53.5 ± 5.0	50.4 ± 2.9
Strain KoFox (water column in Hegler media)	-4.5 ± 2.3	20.8 ± 3.0	33.4 ± 4.7	52.2 ± 3.1
Abiotic Fe(III) oxyhydroxides precipitated with 1.0 mM Si	-30 ± 2	12.6 ± 1.8	18.7 ± 2.7	0 ± 0

Part 3: DVLO modeling – surface tensions components for the three known liquids, photoferrotrophic cells, and abiotic iron minerals (eq.3).

(in mJ m^{-2})	γ^{TOT}	$\boldsymbol{\gamma^{LW}}$	$\boldsymbol{\gamma^{AB}}$	$\boldsymbol{\gamma^{+}}$	$\boldsymbol{\gamma^{-}}$
Water	72.8	21.8	51.0	25.5	25.5
Diiodomethane	50.8	50.8	0.0	0.0	0.0
Glycerol	64.0	34.0	30.0	3.9	57.4
Strain KB01	36.8	34.1	2.7	0.03	62.8
Strain KoFox	53.8	33.1	20.8	2.1	51.6
Abiotic Fe(III) oxyhydroxides precipitated with 1.0 mM Si	64.1	50.8	13.3	1.0	44.3

Part 4: DVLO modeling – surface free energies for cell-cell (eq.4) and cell-Fe(III) oxyhydroxide (eq.5) interactions.

	Cell-Cell			**Cell-Fe(III) oxyhydroxide**		
(in mJ m^{-2})	ΔG_{iwi}	ΔG_{iwi}^{AB}	ΔG_{iwi}^{LW}	ΔG_{iwj}	ΔG_{iwj}^{AB}	ΔG_{iwj}^{LW}
Strain KB01	53.34	56.07	-2.73	33.30	38.91	-5.61
Strain KoFox	28.41	30.75	-2.33	24.07	29.25	-5.19
Abiotic Fe(III) oxyhydroxides precipitated with 1.0 mM Si	14.45	-12.09	26.54			

Table A.3: Modern and Archean Fe fluxes.

Part 1: BIF deposition, demonstrating the depletion of the Fe(II) reservoir

	Individual BIF (*5*)	**Global Fe(II) to deposit BIFs**	**High estimate deep ocean Fe(II) (*76*)**	**Approx. L in ocean based on 75% modern continents**	**Global inventory of Fe(II)**	**Years to deplete Fe(II) from oceans**	**Modern hydro. input: on-axis and off-axis (*41*)**	**Years to deplete with modern hydro. input resupply**
Units	mol/m^2y	$Tmol\ yr^{-1}$	mmol/L	L	Tmol	y	$Tmol\ yr^{-1}$	y
Values	45	4.5	1	$1.12x10^{21}$	$1.12x10^{6}$	249,000	2.18	482,000

Part 2: Newly calculated Fe(II) fluxes to the Archean oceans

Time	**Litho-sphere heat loss ratio**	**Hydro. fluid flow: on-axis**	**Hydro. Fe(II) flux: on-axis***	**Hydro. fluid flow: off-axis**	**Hydro. Fe(II) flux: off-axis****	**Total hydro. Fe(II) flux**	**Total Fe(II) flux: hydro. + continental weathering*****
Ga	N/A	$kg\ yr^{-1}$	$Tmol\ yr^{-1}$	$kg\ yr^{-1}$	$Tmol\ yr^{-1}$	$Tmol\ yr^{-1}$	$Tmol\ yr^{-1}$
4.0	10.9	5.5E+14	32.7	1.5E+17	114.5	147.2	160.3
3.5	5.9	3.0E+14	17.7	8.3E+16	62.0	79.7	89.1
3.0	3.9	2.0E+14	11.7	5.5E+16	41.0	52.7	60.6
2.5	2.8	1.4E+14	8.4	3.9E+16	29.4	37.8	44.9
2.0	2.2	1.1E+14	6.6	3.1E+16	23.1	29.7	36.4
1.5	1.7	8.5E+13	0.51	2.4E+16	17.9	18.4	24.6
1.0	1.4	7.0E+13	0.42	2.0E+16	14.7	15.1	21.2
0.5	1.2	6.0E+13	0.36	1.7E+16	12.6	13.0	18.9
0.0	1.0	5.0E+13	0.30	1.4E+16	10.5	10.8	16.6

Footnote: *On-axis [Fe(II)]: 0-1.5 Ga 6 mmol/kg, 2-4 Ga 60 mmol/kg; **Off-axis [Fe(II)]: 0-4 Ga 0.75 mmol/kg; ***Continental weathering Fe(II) flux: 0-1.5 Ga 0 $Tmol\ yr^{-1}$, 2-4 Ga 5 $Tmol\ yr^{-1}$.

Table A.4: Different scenarios of the physical separation model, with each case using a different water velocity.

	Horizontal water velocity*	**Distance to deposit 50% of the Fe(III) oxyhydroxides****	**Distance to deposit 90% of the Fe(III) oxyhydroxides**
Units	m yr^{-1}	km	km
Case 1	**31536**	**1.2**	**13.4**
Case 2	72533	2.7	30.9
Case 3	113530	4.2	48.3
Case 4	154526	5.8	65.7
Case 5	**195523**	**7.3**	**83.2**
Case 6	236520	8.8	100.6
Case 7	277517	10.4	118.1
Case 8	**318514**	**11.9**	**135.5**

Footnote: *Water velocity based on modern ocean current velocities (*52, 55*); **Density of iron for this calculation was 3.8g mL^{-1}; [3]An upwelling rate of 375m y^{-1} and deep water [Fe] of 37μM were used to calculate the iron deposition rates; [4]Density of carbon for this calculation was 1.075g mL^{-1}. Bold and underlined cases are shown in Figure S6.

Table A.5: Data compilations for Figure 1 and S1.

Part 1: Data for Figure 1 of main text

Banded Iron formation location	% Weight OM	Reference	Deposit Age (Ga)
Fe-rich carbonates (Transvaal supergroup, RSA) 1	0.041	Klein and Buekes, 1989 (*25*)	2.3
Fe-rich carbonates (Transvaal supergroup, RSA) 2	0.36	"	2.3
Siderite-rich BIFs and chert (Transvaal supergroup, RSA)1	0.052	"	2.3
Siderite-rich BIFs and chert (Transvaal supergroup, RSA)2	0.047	"	2.3
Siderite-rich BIFs and chert (Transvaal supergroup, RSA)3	0.11	"	2.3
Siderite-rich BIFs and chert (Transvaal supergroup, RSA)4	0.06	"	2.3
Siderite-rich BIFs and chert (Transvaal supergroup, RSA)5	0.06	"	2.3
Siderite-rich BIFs and chert (Transvaal supergroup, RSA)6	0.144	"	2.3
Siderite-rich BIFs and chert (Transvaal supergroup, RSA)7	0.065	"	2.3
Siderite-rich BIFs and chert (Transvaal supergroup, RSA)8	0.101	"	2.3
Siderite-rich BIFs and chert (Transvaal supergroup, RSA)9	0.041	"	2.3
Siderite-rich BIFs and chert (Transvaal supergroup, RSA)10	0.084	"	2.3
Siderite-rich BIFs and chert (Transvaal supergroup, RSA)11	0.062	"	2.3
Siderite-rich BIFs and chert (Transvaal supergroup, RSA)12	0.203	"	2.3

Siderite-rich BIFs and chert (Transvaal supergroup, RSA)13	0.062	"	2.3
Siderite-rich BIFs and chert (Transvaal supergroup, RSA)14	0.059	"	2.3
Siderite-rich BIFs and chert (Transvaal supergroup, RSA)15	0.065	"	2.3
Siderite-rich BIFs and chert (Transvaal supergroup, RSA)16	0.061	"	2.3
Siderite-rich BIFs and chert (Transvaal supergroup, RSA)17	0.673	"	2.3
Siderite-rich BIFs and chert (Transvaal supergroup, RSA)18	0.104	"	2.3
Siderite-rich BIFs and chert (Transvaal supergroup, RSA)19	0.146	"	2.3
Magnetite-rich, oxide Ifs (Transvaal supergroup, RSA) 1	0.01	"	2.3
Magnetite-rich, oxide Ifs (Transvaal supergroup, RSA) 2	0.017	"	2.3
Magnetite-rich, oxide Ifs (Transvaal supergroup, RSA) 3	0.008	"	2.3
Magnetite-rich, oxide Ifs (Transvaal supergroup, RSA) 4	0.015	"	2.3
Magnetite-rich, oxide Ifs (Transvaal supergroup, RSA) 5	0.013	"	2.3
Magnetite-rich, oxide Ifs (Transvaal supergroup, RSA) 6	0.015	"	2.3
Magnetite-rich, oxide Ifs (Transvaal supergroup, RSA) 7	0.008	"	2.3
Magnetite-rich, oxide Ifs (Transvaal supergroup, RSA) 8	0.008	"	2.3
Magnetite-rich, oxide Ifs (Transvaal supergroup, RSA) 9	0.013	"	2.3
Magnetite-rich, oxide Ifs (Transvaal supergroup, RSA) 10	0.015	"	2.3
Transition zone Kuruman & Griquatown (Transvaal supergroup, RSA) 1	0.017	Beukes and Klein 1990 (*87*)	2.4
Transition zone Kuruman & Griquatown (Transvaal supergroup, RSA) 2	0.019	"	2.4
Transition zone Kuruman & Griquatown (Transvaal supergroup, RSA) 3	0.012	"	2.4
Transition zone Kuruman & Griquatown (Transvaal supergroup, RSA) 4	0.017	"	2.4
Transition zone Kuruman & Griquatown (Transvaal supergroup, RSA) 5	0.015	"	2.4
Transition zone Kuruman & Griquatown (Transvaal supergroup, RSA) 6	0.016	"	2.4
Transition zone Kuruman & Griquatown (Transvaal supergroup, RSA) 7	0.017	"	2.4
Transition zone Kuruman & Griquatown (Transvaal supergroup, RSA) 8	0.018	"	2.4
Transition zone Kuruman & Griquatown (Transvaal supergroup, RSA) 9	0.019	"	2.4
Transition zone Kuruman & Griquatown (Transvaal supergroup, RSA) 10	0.011	"	2.4
Transition zone Kuruman & Griquatown (Transvaal supergroup, RSA) 11	0.016	"	2.4

Transition zone Kuruman & Griquatown (Transvaal supergroup, RSA) 12	0.017	"	2.4
Transition zone Kuruman & Griquatown (Transvaal supergroup, RSA) 13	0.034	"	2.4
Transition zone Kuruman & Griquatown (Transvaal supergroup, RSA) 14	0.012	"	2.4
Transition zone Kuruman & Griquatown (Transvaal supergroup, RSA) 15	0.016	"	2.4
Transition zone Kuruman & Griquatown (Transvaal supergroup, RSA) 16	0.015	"	2.4
Transition zone Kuruman & Griquatown (Transvaal supergroup, RSA) 17	0.022	"	2.4
Transition zone Kuruman & Griquatown (Transvaal supergroup, RSA) 18	0.022	"	2.4
Transition zone Kuruman & Griquatown (Transvaal supergroup, RSA) 19	0.017	"	2.4
Transition zone Kuruman & Griquatown (Transvaal supergroup, RSA) 20	0.024	"	2.4
Transition zone Kuruman & Griquatown (Transvaal supergroup, RSA) 21	0.02	"	2.4
Transition zone Kuruman & Griquatown (Transvaal supergroup, RSA) 22	0.018	"	2.4
Transition zone Kuruman & Griquatown (Transvaal supergroup, RSA) 23	0.02	"	2.4
Transition zone Kuruman & Griquatown (Transvaal supergroup, RSA) 24	0.014	"	2.4
Transition zone Kuruman & Griquatown (Transvaal supergroup, RSA) 25	0.043	"	2.4
Transition zone Kuruman & Griquatown (Transvaal supergroup, RSA) 26	0.025	"	2.4
Transition zone Kuruman & Griquatown (Transvaal supergroup, RSA) 27	0.015	"	2.4
Transition zone Kuruman & Griquatown (Transvaal supergroup, RSA) 28	0.039	"	2.4
Transition zone Kuruman & Griquatown (Transvaal supergroup, RSA) 29	0.03	"	2.4
Transition zone Kuruman & Griquatown (Transvaal supergroup, RSA) 30	0.022	"	2.4
Transition zone Kuruman & Griquatown (Transvaal supergroup, RSA) 31	0.012	"	2.4
Transition zone Kuruman & Griquatown (Transvaal supergroup, RSA) 32	0.015	"	2.4
Transition zone Kuruman & Griquatown (Transvaal supergroup, RSA) 33	0.015	"	2.4
Transition zone Kuruman & Griquatown (Transvaal supergroup, RSA) 34	0.018	"	2.4
Quartz-rich Dales Gorge Member BIF (Dales Gorge, AUS) 1	0.067	Kaufman *et. al*. 1990 (*24*)	2.5
Quartz-rich Dales Gorge Member BIF (Dales Gorge, AUS) 2	0.032	"	2.5
Quartz-rich Dales Gorge Member BIF (Dales Gorge, AUS) 3	0.08	"	2.5
Quartz-rich Dales Gorge Member BIF (Dales Gorge, AUS) 4	0.082	"	2.5
Quartz-rich Dales Gorge Member BIF (Dales Gorge, AUS) 5	0.108	"	2.5

Marra Mamba IF (Pilbara/Hammersley, AUS) 1	0.3	Baur *et. al.* 1985 (*88*)	2.5
Marra Mamba IF (Pilbara/Hammersley, AUS) 2	0.2	"	2.5
Marra Mamba IF (Pilbara/Hammersley, AUS) 3	0.4	"	2.5
Macroband BIF 4 (Dales Gorge Member, AUS) 1	0.3	"	2.5
Macroband BIF 4 (Dales Gorge Member, AUS) 2	0.2	"	2.5
Macroband BIF 4 (Dales Gorge Member, AUS) 3	0.4	"	2.5
Macroband BIF 4 (Dales Gorge Member, AUS) 4	2.6	"	2.5
Macroband BIF 4 (Dales Gorge Member, AUS) 5	2.1	"	2.5
Macroband BIF 4 (Dales Gorge Member, AUS) 6	3.1	"	2.5
Siliceous manganese formations (Urucum, BRA) 1	0.05	Klein and Laderia 2004 (*89*)	0.75
Siliceous manganese formations (Urucum, BRA) 2	0.06	"	0.75
Siliceous manganese formations (Urucum, BRA) 3	0.06	"	0.75
Siliceous manganese formations (Urucum, BRA) 4	0.08	"	0.75
Siliceous manganese formations (Urucum, BRA) 5	0.04	"	0.75
Siliceous manganese formations (Urucum, BRA) 6	0.07	"	0.75
Siliceous manganese formations (Urucum, BRA) 7	0	"	0.75
Siliceous manganese formations (Urucum, BRA) 8	0.06	"	0.75
Quartz-magnetite IF (Isua, GRN) 1	0.06	Dymek and Klein 1988 (*90*)	3.8
Quartz-magnetite IF (Isua, GRN) 2	0.05	"	3.8
Quartz-magnetite IF (Isua, GRN) 3	0.01	"	3.8
Quartz-magnetite IF (Isua, GRN) 4	0.02	"	3.8
Quartz-magnetite IF (Isua, GRN) 5	0.02	"	3.8
Quartz-magnetite IF (Isua, GRN) 6	0.01	"	3.8
Magnesian IF (Isua, GRN) 1	0.11	"	3.8
Magnesian IF (Isua, GRN) 2	0.06	"	3.8
Magnesian IF (Isua, GRN) 3	0.05	"	3.8
Magnesian IF (Isua, GRN) 4	0.03	"	3.8
Aluminous IF (Isua, GRN) 1	0.16	"	3.8
Aluminous IF (Isua, GRN) 2	0.01	"	3.8
Graphitic IF (Isua, GRN) 1	2.98	"	3.8
Graphitic IF (Isua, GRN) 2	1.54	"	3.8
Graphitic IF (Isua, GRN) 3	0.7	"	3.8
Graphitic IF (Isua, GRN) 4	2.09	"	3.8
Carbonate-rich IF (Isua, GRN) 1	1.92	"	3.8
Carbonate-rich IF (Isua, GRN) 2	1.38	"	3.8
Carbonate-rich IF (Isua, GRN) 3	0.27	"	3.8
Carbonate-rich IF (Isua, GRN) 4	1.17	"	3.8
Carbonate-rich IF (Isua, GRN) 5	1.44	"	3.8
Carbonate-rich IF (Isua, GRN) 6	2.13	"	3.8
Carbonate-rich IF (Isua, GRN) 7	1.35	"	3.8
Hematite bearing IF (Riptan, CAN) 1	0.165	Klein and Beukes 1993 (*91*)	0.75
Hematite bearing IF (Riptan, CAN) 2	0.131	"	0.75
Hematite bearing IF (Riptan, CAN) 3	0.147	"	0.75

Proterozoic Minas Supergroup, BIF, Aguas Claras, Carb rich (SE Brazil) 1	0.023	Klein and Laderia 2000 (*92*)	2.5
Proterozoic Minas Supergroup, BIF, Aguas Claras, Carb rich (SE Brazil) 2	0.019	"	2.5
Proterozoic Minas Supergroup, BIF, Aguas Claras, Carb rich (SE Brazil) 3	0.019	"	2.5
Proterozoic Minas Supergroup, BIF, Mutuca (SE Brazil) 1	0.023	"	2.5
Proterozoic Minas Supergroup, BIF, Mutuca (SE Brazil) 2	0.027	"	2.5
Proterozoic Minas Supergroup, BIF, Mutuca (SE Brazil) 3	0.509	"	2.5
Ancient sediments and non-IF rocks			
Shales averages through time 1	0.6	Holland and Schidlowski 1984 p. 103 (*93*)	3.4
Shales averages through time 2	0.85	"	2.7
Shales averages through time 3	1.5	"	2.1
Shales averages through time 4	0.3	"	1.9
Shales averages through time 5	0.4	"	1.1
Shales averages through time 6	0.67	"	0.5
Sediments averages through time 1	0.6	"	3.8
Sediments averages through time 2	0.5	"	3.4
Sediments averages through time 3	1.3	"	2.5
Sediments averages through time 4	0.2	"	2.1
Sediments averages through time 5	0.15	"	1.1
Sediments averages through time 6	0.4	"	0.5
Black Shale, Carajas, overlying BIF (Brazil) 1	1.58	Cabral *et. al.* 2013 (*94*)	2.7
Black Shale, Carajas, overlying BIF (Brazil) 2	1.64	"	2.7
Black Shale, Carajas, overlying BIF (Brazil) 3	0.85	"	2.7
Black Shale, Carajas, overlying BIF (Brazil) 4	2.69	"	2.7
Black Shale, Carajas, overlying BIF (Brazil) 5	2.56	"	2.7
Black Shale, Carajas, overlying BIF (Brazil) 6	3.21	"	2.7
Black Shale, Carajas, overlying BIF (Brazil) 7	2.59	"	2.7
Black Shale, Carajas, overlying BIF (Brazil) 8	3.27	"	2.7
Black Shale, Carajas, overlying BIF (Brazil) 9	2.36	"	2.7
Black Shale, Carajas, overlying BIF (Brazil) 10	1.14	"	2.7
Black Shale, Carajas, overlying BIF (Brazil) 11	1.2	"	2.7
Black Shale, Carajas, overlying BIF (Brazil) 12	0.98	"	2.7
Black Shale, Carajas, overlying BIF (Brazil) 13	1.26	"	2.7
Black Shale, Carajas, overlying BIF (Brazil) 14	1.27	"	2.7
Black Shale, Carajas, overlying BIF (Brazil) 15	1.11	"	2.7
Black Shale, Carajas, overlying BIF (Brazil) 16	1.27	"	2.7
Silverton, Kaapvaal shales, underestimate due to metamosphsis (RSA)	0.9	Watanabe *et. al*., 1997 (*95*)	2.2
Timeball Hill, Kaapvaal shales, underestimate due to metamosphsis (RSA) 1	0.94	"	2.2
Timeball Hill, Kaapvaal shales, underestimate due to metamosphsis (RSA) 2	1.22	"	2.2
Timeball Hill, Kaapvaal shales, underestimate due to metamosphsis (RSA) 3	1.07	"	2.2

Timeball Hill, Kaapvaal shales, underestimate due to metamosphsis (RSA) 4	0.81	"	2.2
Black Reef, Kaapvaal shales, underestimate due to metamosphsis (RSA) 1	1.56	"	2.6
Black Reef, Kaapvaal shales, underestimate due to metamosphsis (RSA) 2	1.72	"	2.6
Black Reef, Kaapvaal shales, underestimate due to metamosphsis (RSA) 3	1.33	"	2.6
Black Reef, Kaapvaal shales, underestimate due to metamosphsis (RSA) 4	1.69	"	2.6
Selati, Kaapvaal shales, underestimate due to metamosphsis (RSA)	0.2	"	2.6
K-8, Kaapvaal shales, underestimate due to metamosphsis (RSA) 1	0.21	"	2.8
K-8, Kaapvaal shales, underestimate due to metamosphsis (RSA) 2	0.23	"	2.8
Carbonaceous shale, Wilpena Group, (South Australia)	1.51	McKirdy 1974 (*96*)	0.65
Shale, Pertatataka Formation (Nothern Territory Australia)	0.89	"	0.7
Shale, Bitter Springs Formation (NT Australia)	0.66	"	0.85
Upper Shale member, Nonesuch shale (Michigan, USA)	0.4	"	1.1
Shale, Muhos Formation, Jotnian Series (Finland)	0.41	"	1.3
Calcereous shale, McMinn Formation, Roper Group (NT Australia)	1.04	"	1.4
HYC Pyritic shale, McArthur Group (NT Australia)	1.85	"	1.6
Carbonaceous , dolomite shale, Gooparla Group (NT Australia)	2.25	"	1.9
Carbonaceous shale, Soudan Iron Formation (Minnesota, USA)	3.2	"	2.7
Hematite mudstone (Rapitan IF, surrounding lithologies) 1	0.128	Klein and Beukes 1993 (*91*)	0.75
Hematite mudstone (Rapitan IF, surrounding lithologies) 2	0.134	"	0.75
Volcaniclastic mudstone (Rapitan IF, surrounding lithologies) 1	0.189	"	0.75
Shale (Rapitan IF, surrounds lithologies) 1	0.23	"	0.75
Shale (Rapitan IF, surrounds lithologies) 2	0.261	"	0.75
Shale (Rapitan IF, surrounds lithologies) 3	0.522	"	0.75
Shale (Transvaal supergroup, RSA) 1	5.33	Klein and Beukes 1989 (*25*)	2.3
Shale (Transvaal supergroup, RSA) 2	3.77	"	2.3
Shale (Transvaal supergroup, RSA) 3	2.62	"	2.3
Shale (Transvaal supergroup, RSA) 4	2.73	"	2.3
Shale (Transvaal supergroup, RSA) 5	4.95	"	2.3
Shale (Transvaal supergroup, RSA) 6	6.36	"	2.3
Shale (Transvaal supergroup, RSA) 7	3.84	"	2.3
Shale (Transvaal supergroup, RSA) 8	4.19	"	2.3
Shale (Transvaal supergroup, RSA) 9	2.79	"	2.3
Shale (Transvaal supergroup, RSA) 10	2.52	"	2.3
Modern environments			

Molenplaat, Schelde estuary, intertidal (Netherlands) 1	0.309	Middelburg *et. al.* 1999 (*97*)	
Molenplaat, Schelde estuary, intertidal (Netherlands) 2	0.372	"	
Molenplaat, Schelde estuary, intertidal (Netherlands) 3	0.158	"	
Molenplaat, Schelde estuary, intertidal (Netherlands) 4	0.093	"	
Molenplaat, Schelde estuary, intertidal (Netherlands) 5	0.108	"	
Iberian Margin, 175m-4909m depth (Atlantic Ocean) 1	0.407	"	
Iberian Margin, 175m-4909m depth (Atlantic Ocean) 2	0.24	"	
Iberian Margin, 175m-4909m depth (Atlantic Ocean) 3	0.22	"	
Iberian Margin, 175m-4909m depth (Atlantic Ocean) 4	0.63	"	
Iberian Margin, 175m-4909m depth (Atlantic Ocean) 5	0.51	"	
13m-1997m (Northwestern Black Sea) 1	1.262	"	
13m-1997m (Northwestern Black Sea) 2	0.783	"	
13m-1997m (Northwestern Black Sea) 3	1.638	"	
13m-1997m (Northwestern Black Sea) 4	2.147	"	
13m-1997m (Northwestern Black Sea) 5	1.111	"	
13m-1997m (Northwestern Black Sea) 6	2.997	"	
13m-1997m (Northwestern Black Sea) 7	4.459	"	
13m-1997m (Northwestern Black Sea) 8	5.26	"	
13m-1997m (Northwestern Black Sea) 9	2.288	"	
2.7m-270m (North Sea) 1	2.093	"	
2.7m-270m (North Sea) 2	2.424	"	
2.7m-270m (North Sea) 3	0.559	"	
2.7m-270m (North Sea) 4	0.078	"	
2.7m-270m (North Sea) 5	0.219	"	
2.7m-270m (North Sea) 6	0.055	"	
5400m (Madeira Abyssal Plain) 1	0.182	"	
5400m (Madeira Abyssal Plain) 2	0.228	"	
5400m (Madeira Abyssal Plain) 3	0.361	"	
5400m (Madeira Abyssal Plain) 4	1.139	"	
5400m (Madeira Abyssal Plain) 5	1.137	"	
2539m (Eastern Mediterranean) 1	0.417	"	
2539m (Eastern Mediterranean) 2	0.222	"	
2539m (Eastern Mediterranean) 3	2.598	"	
Western continental slope India OMZ, 85m-2297m (Arabian Sea) 1	0.14	Paropkari *et. al.* 1993 (*98*)	
Western continental slope India OMZ, 85m-2297m (Arabian Sea) 2	1.1	"	
Western continental slope India OMZ, 85m-2297m (Arabian Sea) 3	2.81	"	
Western continental slope India OMZ, 85m-2297m (Arabian Sea) 4	2.07	"	

Western continental slope India OMZ, 85m-2297m (Arabian Sea) 5	2.51	"	
Western continental slope India OMZ, 85m-2297m (Arabian Sea) 6	0.57	"	
Western continental slope India OMZ, 85m-2297m (Arabian Sea) 7	3.4	"	
Western continental slope India OMZ, 85m-2297m (Arabian Sea) 8	4.14	"	
Western continental slope India OMZ, 85m-2297m (Arabian Sea) 9	0.79	"	
Western continental slope India OMZ, 85m-2297m (Arabian Sea) 10	5.88	"	
Western continental slope India OMZ, 85m-2297m (Arabian Sea) 11	3.33	"	
Western continental slope India OMZ, 85m-2297m (Arabian Sea) 12	2.76	"	
Western continental slope India OMZ, 85m-2297m (Arabian Sea) 13	5.06	"	
Western continental slope India OMZ, 85m-2297m (Arabian Sea) 14	5.47	"	
Western continental slope India OMZ, 85m-2297m (Arabian Sea) 15	6.18	"	
Western continental slope India OMZ, 85m-2297m (Arabian Sea) 16	2.33	"	
Western continental slope India OMZ, 85m-2297m (Arabian Sea) 17	1.9	"	
Western continental slope India OMZ, 85m-2297m (Arabian Sea) 18	2.07	"	
Western continental slope India OMZ, 85m-2297m (Arabian Sea) 19	3.21	"	
Western continental slope India OMZ, 85m-2297m (Arabian Sea) 20	1.35	"	
Western continental slope India OMZ, 85m-2297m (Arabian Sea) 21	0.98	"	
Western continental slope India OMZ, 85m-2297m (Arabian Sea) 22	0.66	"	
Western continental slope India OMZ, 85m-2297m (Arabian Sea) 23	0.79	"	
Western continental slope India OMZ, 85m-2297m (Arabian Sea) 25	0.59	"	
Western continental slope India OMZ, 85m-2297m (Arabian Sea) 25	0.69	"	
Chilean continental slope OMZ (Pacific Ocean) 1	5	Niggemann *et. al*. 2007 (*99*)	
Chilean continental slope OMZ (Pacific Ocean) 2	5.25	"	
Chilean continental slope OMZ (Pacific Ocean) 3	6	"	
Chilean continental slope OMZ (Pacific Ocean) 4	5.5	"	
Chilean continental slope OMZ (Pacific Ocean) 5	5.5	"	
Chilean continental slope OMZ (Pacific Ocean) 6	6	"	
Chilean continental slope OMZ (Pacific Ocean) 7	2	"	
Chilean continental slope OMZ (Pacific Ocean) 8	1.9	"	
Chilean continental slope OMZ (Pacific Ocean) 9	1.8	"	
Chilean continental slope OMZ (Pacific Ocean) 10	3.4	"	
Chilean continental slope OMZ (Pacific Ocean) 11	3.7	"	

Chilean continental slope OMZ (Pacific Ocean) 12	4.4	"	
Chilean continental slope OMZ (Pacific Ocean) 13	4.1	"	
Chilean continental slope OMZ (Pacific Ocean) 14	4.1	"	
Chilean continental slope OMZ (Pacific Ocean) 15	4.1	"	
Chilean continental slope OMZ (Pacific Ocean) 16	2.9	"	
Chilean continental slope OMZ (Pacific Ocean) 17	3	"	
Chilean continental slope OMZ (Pacific Ocean) 18	3	"	
Chilean continental slope OMZ (Pacific Ocean) 19	2.1	"	
Chilean continental slope OMZ (Pacific Ocean) 20	2.1	"	
Chilean continental slope OMZ (Pacific Ocean) 21	2	"	
Chilean continental slope OMZ (Pacific Ocean) 22	2.6	"	
Chilean continental slope OMZ (Pacific Ocean) 23	2.5	"	
Chilean continental slope OMZ (Pacific Ocean) 24	2.5	"	

Part 2: Data for SI Figure 1

Age (Ga)	**Iron redox state**	**BIF type**	**Reference**	**% Fe_2O_3**	**% FeO**
3.8	2.56	Isua QM IF	Dymek and Klein 1988 (*90*)	18.17	13.03
3.8	2.16	Isua Al IF	"	4.98	23.5
3.8	2.30	Isua G IF	"	11.98	24.65
3.8	2.08	Isua C IF	"	1.87	18.19
2.7	2.96	Carajas BIF	Klein and Ladeira 2002 (*100*)	58.95	1.97
2.5	2.48	Dales Gorge	Kaufman et al 1990 (*24*)	12.91	13.97
2.5	2.97	Minas BIF	Klein and Ladeira 2000 (*92*)	36.61	1.17
2.4	2.29	RSA Ste IF	Beukes and Klein 1990 (*87*)	9.16	19.8
2.4	2.49	RSA K IF	"	17.42	16.16
2.4	2.48	RSA G IF	"	17.72	17.29
2.3	2.05	RSA Sid IF	Klein and Beukes 1989 (*25*)	1.196	22.58
2.3	2.54	RSA Ox IF	"	22.72	17.56
2	2.43	Labrador BIF	Klein 1966 (*101*)	9.23	11.2
0.75	2.98	Rapitan whole BIF	Klein and Beukes 1993 (*91*)	43.78	0.69
0.75	2.97	Urucum BIF	Klein and Ladeira 2004 (*89*)	37.73	1.08

Appendix B

Chapter 5: supplemental material

- Table B1: Description of each Fe speciation extraction step
- Table B2: List of genes discussed in the main text and their primary function
- Table B3: % of metagenomic reads that aligned to each set of MAGs
- Fig. B1: The location of Kabuno Bay with the sampling site
- Fig. B2: The relative abundance of the reconstructed 16S rRNA gene for the 16S rRNA genes with a greater than 1 % relative abundance for each depth
- Fig. B3: Reads per kilobase mapped (RPKM) values for taxonomic marker genes related to class Chlorobia and glycosyl hydrolases
- Fig. B4: Gene abundances of the key genes for several pathways
- Fig. B5: The depth integrated absolute abundance of each phyla compared to the number of MAGs recovered from each of those groups
- Fig. B6: Comparison of the Chlorobi_01 MAG to the genome of *Chlorobium phaeoferrooxidans* strain KB01 at the pathway level
- Fig. B7: Comparison of the genomes of several key MAGs at the pathway level
- Fig. B8: Representation of the metabolic potential for two MAGs

B.1 Supplemental figures

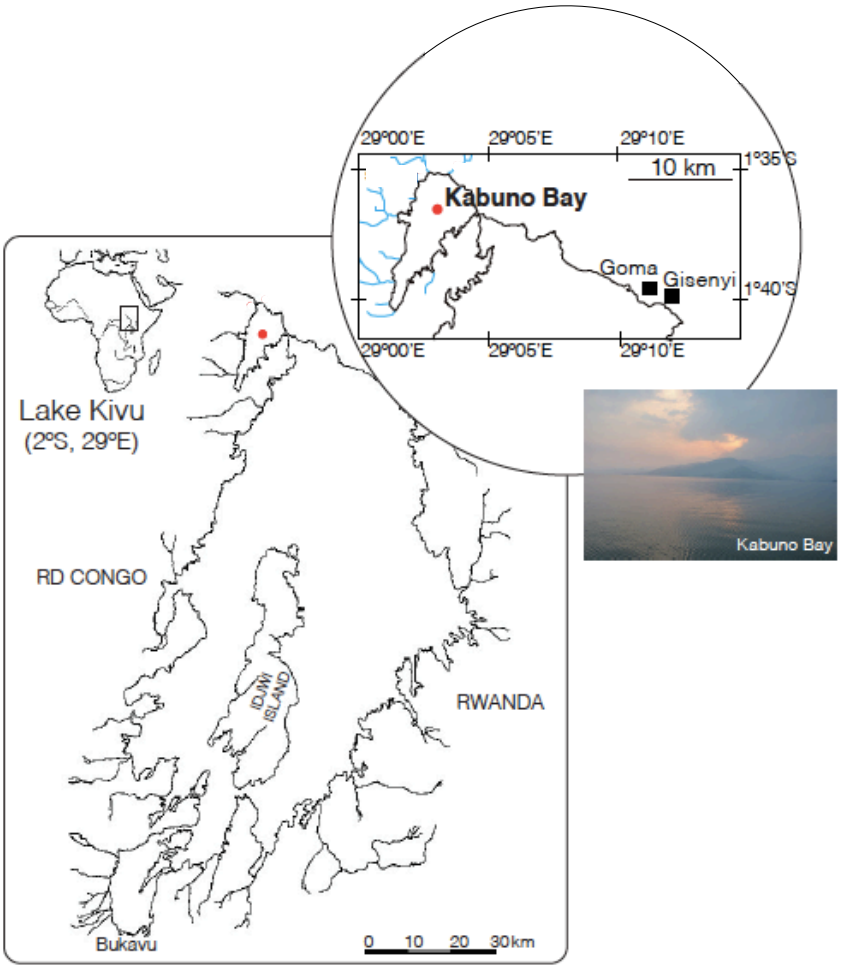

Figure B.1: *The location of Kabuno Bay with the sampling site* (marked in red) and surrounding rivers, adapted from Lliros et. al. [48].

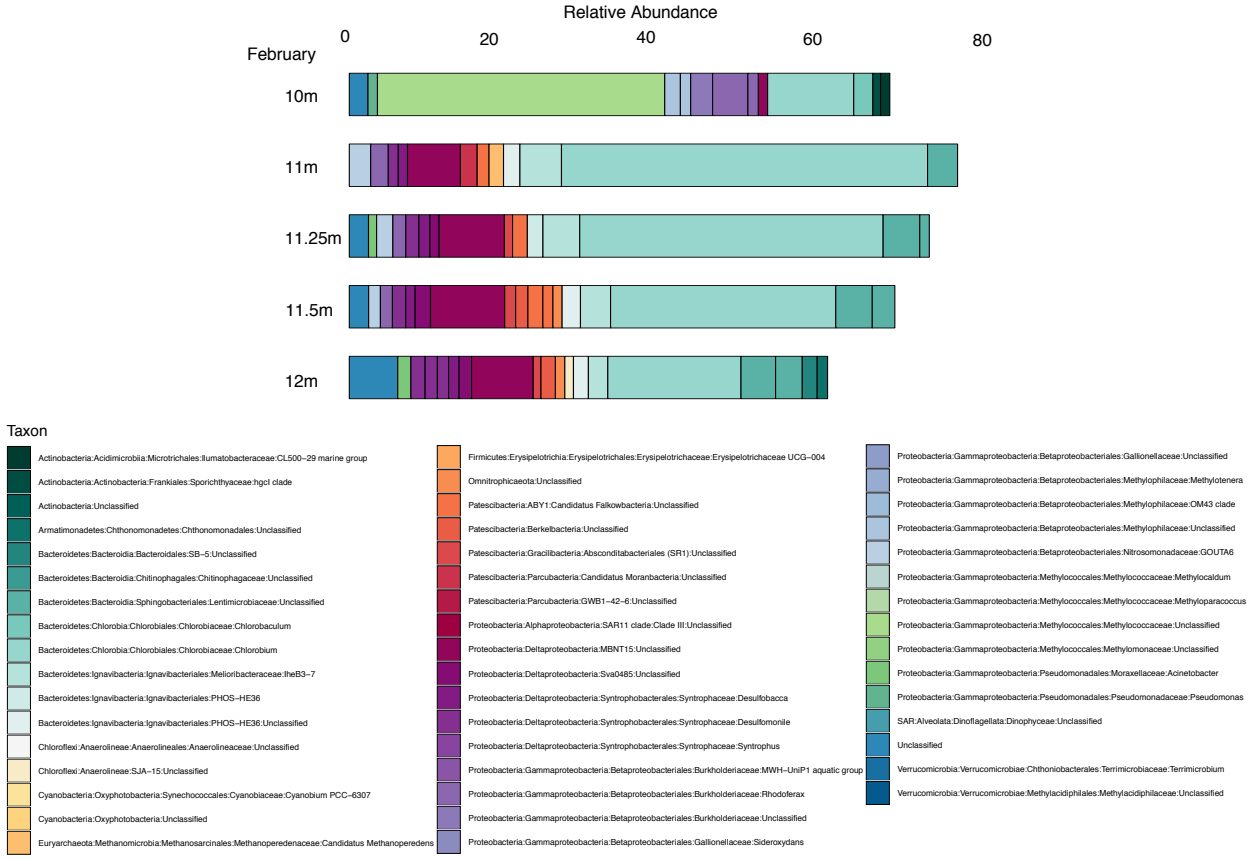

Figure B.2: *The relative abundance of the reconstructed 16S rRNA gene* for the 16S rRNA genes with a greater than 1 % relative abundance for each depth.

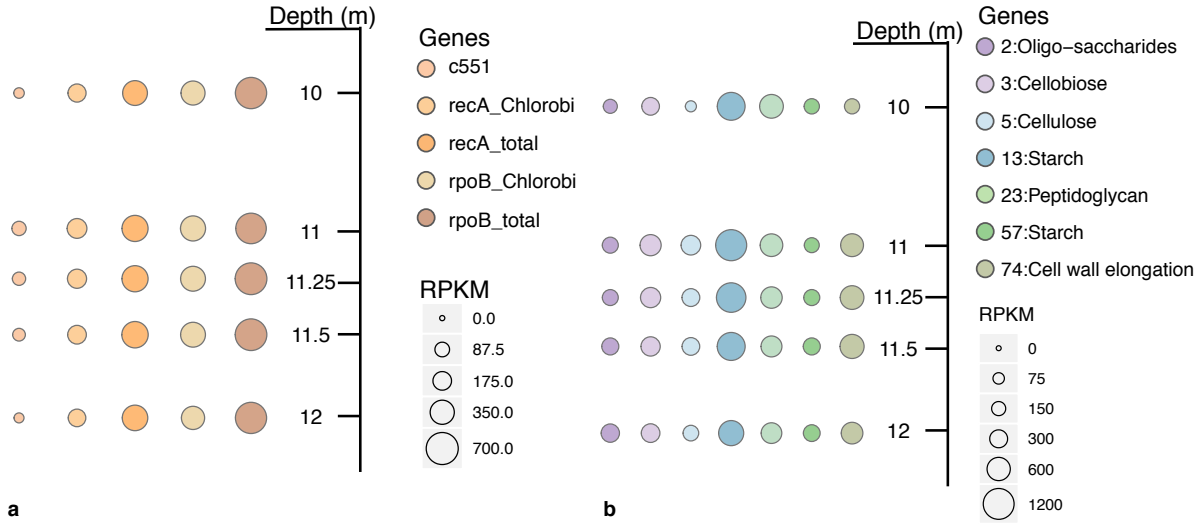

Figure B.3: *Reads per kilobase mapped (RPKM) values for taxonomic marker genes related to class Chlorobia (a) and glycosyl hydrolases (b).* The size of each bubble represents the total RPKM for that gene at the specified depth for each month, while the colors delineate each gene.

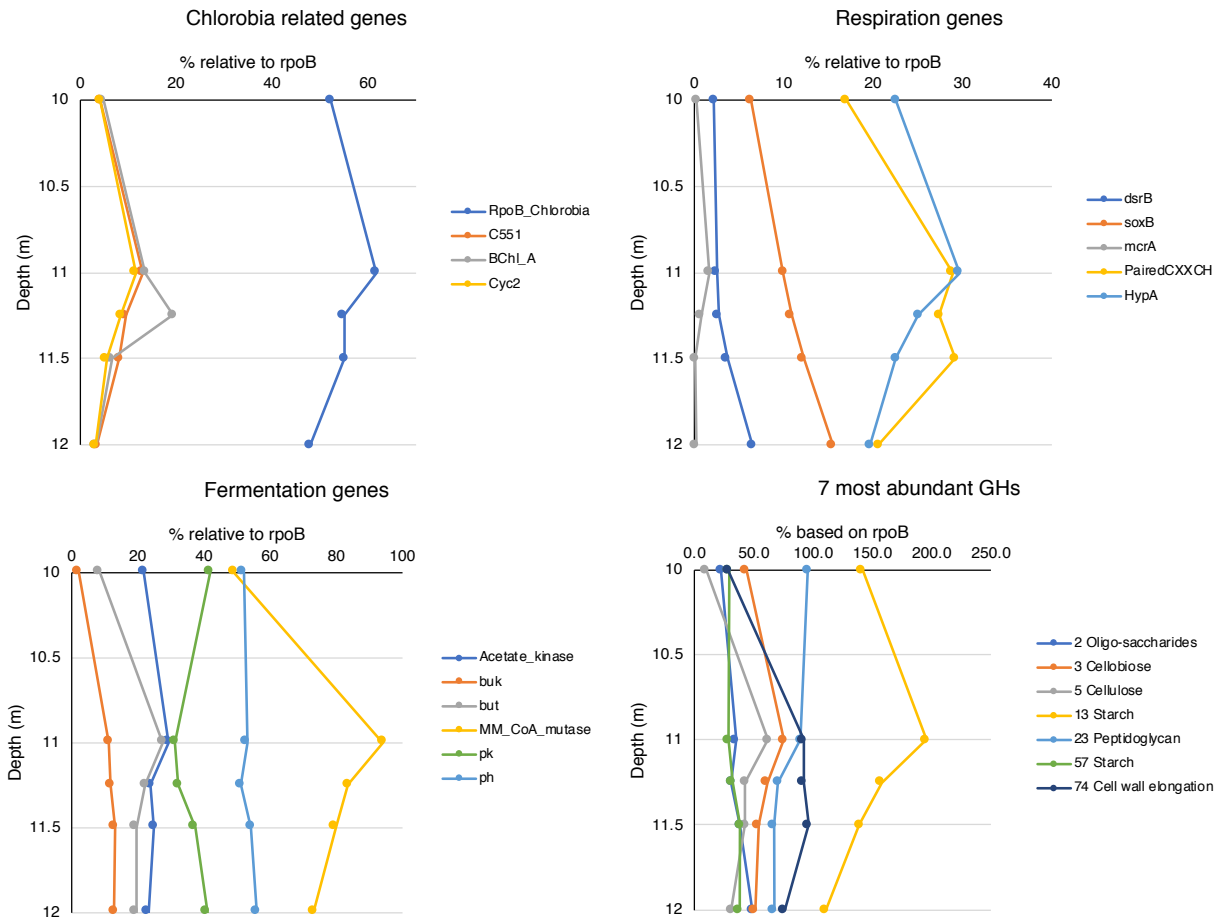

Figure B.4: *Gene abundances of the key genes for several pathways* compared to the abundance of the single copy marker gene *rpoB* at each depth, reported as a percent.

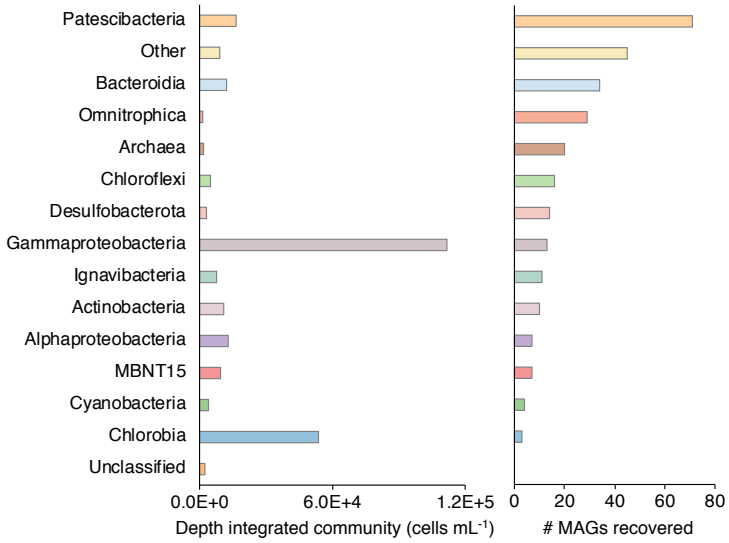

Figure B.5: *The depth integrated absolute abundance of each phyla (Bacteroidetes and Proteobacteria split into their representative classes: Bacteroidia/Ignavibacteria/Chlorobia and Alphaproteobacteria/Gammaproteobacteria respectively) compared to the number of MAGs recovered from each of those groups.*

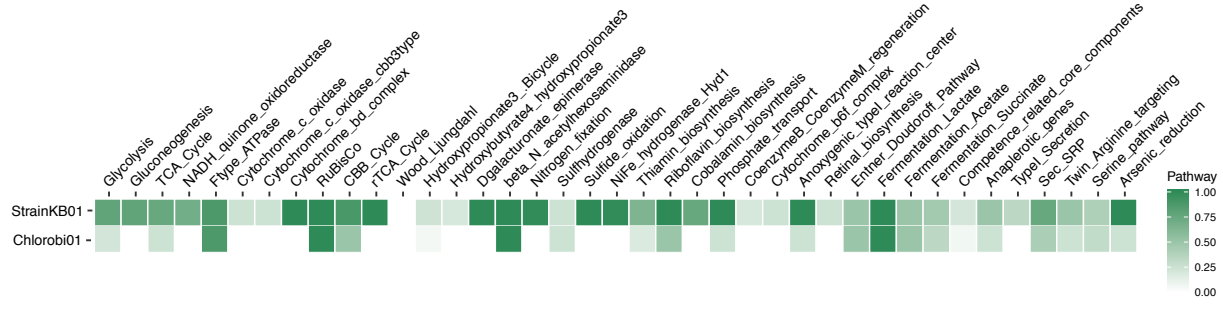

Figure B.6: *Comparison of the Chlorobi_01 MAG to the genome of* Chlorobium phaeoferrooxidans *strain KB01 at the pathway level.*

Figure B.7: *Comparison of the genomes of several key MAGs at the pathway level.*

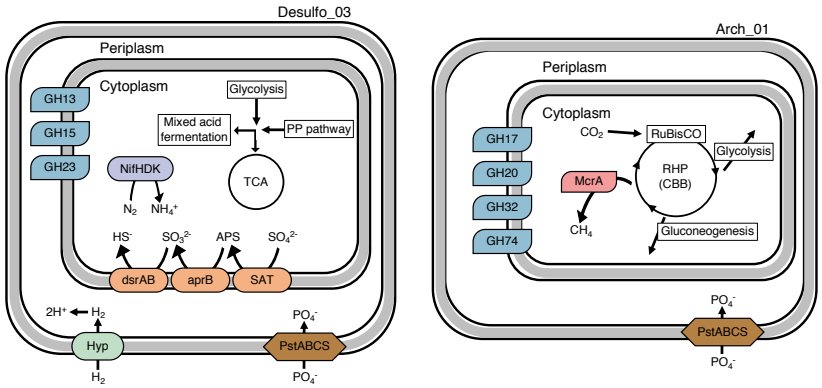

Figure B.8: *Representation of the metabolic potential for two MAGs*: a putative sulfate reducer (Desulfo_03) and a methanogen (Arch_01). The description of each gene listed in found in Table B.2.

B.2 Supplemental tables

Table B.1: Description of each Fe speciation extraction step where reactive Fe (Fe_{HR}) refers to the sum of Fe_{Aca}, $Fe(II)_{HCl}$, $Fe(III)_{HCl}$, Fe_{Dith}, and Fe_{Oxa} pools. Unreactive Fe (Fe_{NR}) refers to the Fe_{Sil} pool.

Operationally defined Fe – mineral phases	**Extractant**
Siderite, Lepidocrocite, Ferrihydrite, Fe(II) and $Fe(III)_{HCl}$	0.5 M HCl, 1 h (Thamdrup et al., 1994)
Goethite, Hematite, Fe_{Dith}	0.35 M acetic acid/0.2 M Na-citrate Na-dithionite, 2 h (Poulton and Canfield, 2005)
Magnetite, Fe_{Oxa}	0.2 M ammonium oxalate/0.17 M oxalic acid, 6 h (Poulton and Canfield, 2005)
Silicate Fe, Fe_{Sil}	Near boiling 6 M HCl, 24 h (Poulton and Canfield, 2005)

Table B.2: List of genes discussed in the main text and their primary function.

Gene Abbreviation	Full name	Function
BChl_A	bacteriochlorophyll a	Anoxygenic photosynthesis
BChl_e	bacteriochlorophyll e	Anoxygenic photosynthesis
pufM	photosynthetic reaction center subunit M	Anoxygenic photosynthesis
RuBisCo	ribulose-1,5-bisphosphate carboxylase	Carbon fixation
GH1	cellobiose glycosyl hydrolase	Complex carbon degradation
GH13	starch glycosyl hydrolase	Complex carbon degradation
GH15	oligo-saccharide glycosyl hydrolase	Complex carbon degradation
GH17	cellobiose glycosyl hydrolase	Complex carbon degradation
GH2	oligo-saccharide glycosyl hydrolase	Complex carbon degradation
GH20	oligo-saccharide glycosyl hydrolase	Complex carbon degradation
GH23	peptidoglycan glycosyl hydrolase	Complex carbon degradation
GH3	cellobiose glycosyl hydrolase	Complex carbon degradation
GH32	oligo-saccharide glycosyl hydrolase	Complex carbon degradation
GH5	cellulose glycosyl hydrolase	Complex carbon degradation
GH74	cellulose glycosyl hydrolase	Complex carbon degradation
cytC	outer membrane cytochrome; multiple paired CXXCH binding motifs	Fe(III) reductase
buk	butyrate kinase	Fermentation
but	butyrate-CoA transferase	Fermentation
MM-CoA mutase	methylmalonyl-CoA mutase	Fermentation
pd	pyruvate dehydrogenase	Fermentation
pk	pyruvate kinase	Fermentation
ack	acetate kinase	Fermentation
PP pathway	Pentose phosphate pathway	Glucose to NADPH
Glycolysis	Glycolysis pathway	Glucose to pyruvate
hypA	NiFe hydrogenase subunit A	Hydrogen production or oxidation
mcrA	methyl-coenzyme M reductase subunit A	Methanogenesis
narGH	nitrate reductase subunit G, H	Nitrate reduction to nitrite
nxrAB	nitrite oxidoreductase subunit A, B	Nitrite oxidation to nitrate
nifHDK	nitrogenase subunits H, D, and K	Nitrogen fixation
coxABCD	cytochrome c oxidase subunit A, B, C, D	Oxidative phosphorylation
cydABX	cytochrome bd ubiquinol subunit A, B, X	Oxidative phosphorylation
PSII	photosystem II	Oxygenic photosynthesis
pstABCS	phosphate transport system subunit A, B, C, S	Phosphate transport
phnDEC	phosphonate transport system subunit D, E, C	Phosphonate transport
cyc2	outer membrane cytochrome	Putative Fe(II) oxidase
TCA	Tricarboxylic citric acid cycle	Pyruvate to CO2 and ATP
aprB	adenylylsulfate reductase subunit B	Sulfate reduction pathway
dsrAB	dissimilatory sulfite reductase subunits A, B	Sulfate reduction pathway
SAT	sulfate adenylyltransferase	Sulfate reduction pathway
fccAB	sulfide dehydrogenase subunit A, B	Sulfide oxidation
sorB	sulfite dehydrogenase subunit B	Sulfite oxidation
soxB	sulfur-oxidizing protein SoxB	Thiosulfate oxidation

Table B.3: % of metagenomic reads that aligned to each set of metagenomic assembled genomes (MAGs) that had a Q-score greater than 50.

Depth (m)	# of quality MAGs	% reads aligned to quality bins
10	42	16.1
11	20	3.2
11.25	54	35.7
11.5	78	36.2
12	90	34.1